Doctoral thesis submitted for the degree of Doctor of Philosophy in Telecommunication Engineering

Postgraduate Programme: Communication Technology

Characterization of Wireless Propagation in Complex Indoor Environments

Presented by:

Leyre Azpilicueta Fernández de las Heras

Supervised by:

Dr. Francisco Falcone Lanas and Dr. Antonio J. López Martín

Pamplona, June 2015

To my family

Contents

Abstract

In this research work, a novel deterministic approach for radio propagation prediction in complex environments is presented. First, an in-depth analysis of the recent propagation models used in the technical literature is made. Conclusions show that deterministic methods based on ray tracing or ray launching techniques achieve a trade-off between accuracy results and inherent computational time. Because of that, a deterministic method has been implemented in this work based on the ray launching technique. The algorithm is explained in detail and a convergence analysis of the algorithm is done. Besides, two novel acceleration techniques are presented achieving accurate results with a significant reduction in simulation computational time.

Finally, several applications of the proposed method are presented and simulation results are compared with real measurements achieving good results with very low levels of difference errors.

Acknowledgements

I would first like to express my sincere gratitude to my supervisors Dr. Francisco Falcone and Dr. Antonio López Martín, for their support and dedication over the last years. I truly appreciate all their contributions of time and ideas. Thanks also to all those people of the Electrical and Electronic Engineering Department of the Public University of Navarra (UPNA) who have helped me eventually during this work, especially my team-mates, Erik and Peio, always ready to give you a hand when you need it.

Besides, I want to thank Prof. César Vargas, from the Instituto Tecnológico de Estudios Superiores de Monterrey (ITESM), México, for his attention during my pre-doctoral stay in 2014.

I would also like to mention the following Institutions, whose financial support have made this thesis possible:

- Government of Navarre, through the project FASTER.

- Public University of Navarra, through its PhD. Grants Program.

- IEEE Antennas and Propagation Society, through its Doctoral Research Awards.

- Banco Santander, through its Research Mobility Awards.

- All people and Institutions I have collaborate with and which have made possible the work of this thesis.

Finally, I would like to thank my friends and family, especially my parents and brothers, for their encouragement to always pursue my dreams. And lastly Mikel, I could never thank you enough for your ongoing patience and support towards me.

List of Acronyms

1G	First Generation
2D	Two-Dimensional
2G	Second Generation
3D	Three-Dimensional
3G	Third Generation
3GPP	Third Generation Partnership Project
4G	Fourth Generation
5G	Fifth Generation
ACK	Acknowledgement
AP	Access Point
AWGN	Additive White Gaussian Noise
AZB	Angular Z-Buffer
B4G	Beyond Fourth Generation
BAN	Body Area Network
BER	Bit Error Rate
BLE	Bluetooth Low Energy
BSS	Basic Service Set
CDF	Cumulative Distribution Function
CF	Collaborative Filter
CPU	Central Processing Unit
DE	Diffusion Equation
DSSS	Direct Sequence Spread Spectrum
EPA	Effective Propagation Area

ESS	Extended Service Set
FDTD	Finite Difference Time Domain
FFD	Full Function Device
FFNN	Feed-Forward Neural-Network
FHSS	Frequency-Hopping Spread-Spectrum
GO	Geometrical Optics
GO-DE	Geometrical Optics and Diffusion Equation
GO-PO	Geometrical Optics and Physical Optics
GO-UTD	Geometrical Optics and Uniform Theory of Diffraction
GO-UTD-DE	Geometrical Optics and Uniform Theory of Diffraction and Diffusion Equation
GPS	Global Positioning System
GRIMM	Geometrical Ray Implementation for Mobile Propagation Modeling
GSM	Global System for Mobile Communication
GTD	Geometrical Theory of Diffraction
IBSS	Independent Basic Service Set
IEEE	Institute of Electrical & Electronic Engineers
IMTA	International Mobile Telecommunications Advanced
IP	Internet Protocol
ISM	Industrial, Scientific and Medical
ITS	Intelligent Transportation Systems
LAN	Local Area Network
LoS	Line of Sight
LTE	Long Term Evolution
LTE-A	Long Term Evolution-Advanced
MAC	Medium Access Control
MIMO	Multiple Input Multiple Output

MMSE	Minimum Mean Square Error
MoM	Method of Moments
NLoS	Non Line of Sight
NMSE	Normalized Mean Square Error
NN	Neural Network
OEM	Original Equipment Manufacturer
OFDM	Orthogonal Frequency Division Multiplexing
PAN	Personal Area Network
PC	Personal Computer
PDF	Probability Density Function
PDP	Power Delay Profile
PDT	Physical Theory of Diffraction
PER	Packet Error Rate
PHY	Physical
PL	Path Loss
PO	Physical Optics
QoS	Quality of Service
QPSK	Quadrature Phase Shift Keying
RAM	Random Access Memory
RBFNN	Radial Basis Function Neural Network
RCS	Radar Cross Section
RF	Radio Frequency
RFD	Reduced Function Device
RFID	Radio Frequency Identification
RL	Ray Launching
RL-CF	Ray Launching and Collaborative Filter
RL-DE	Ray Launching and Diffusion Equation

RL-NN	Ray Launching and Neural Network
RMS	Root Mean Square
RT	Ray Tracing
RX	Receiver
SBR	Shooting and Bouncing Ray
SD	Standard Deviation
SIG	Special Interest Group
SNR	Signal to Noise Ratio
SoC	System-on-Chip
STA	Station
TX	Transmitter
UAT	Uniform Asymptotic Theory
UHF	Ultra High Frequency
UMTS	Universal Mobile Telecommunication System
USB	Universal Serial Bus
UTD	Uniform Theory of Diffraction
V2I	Vehicle to Infrastructure
V2V	Vehicle to Vehicle
VPL	Vertical Plane Launch
WBAN	Wireless Body Area Network
WLAN	Wireless Local Area Network
WMAN	Wireless Metropolitan Area Network
WPAN	Wireless Personal Area Network
WWAN	Wireless Wide Area Network

Chapter 1

Introduction

T HE aim of this introductory chapter is to present the framework of the thesis. Section 1.1 is focused on the motivation of the thesis, emphasizing the growing demand of electromagnetic propagation analysis before the implementation of wireless communication systems. General objectives of the thesis are covered in Section 1.2 and, finally, a summary of the structure of the work is provided in Section 1.3.

1.1 Motivation

The significant growth of wireless communications systems over the last years has led to the necessity of adequate and efficient tools to predict radio wave propagation in different environments. The capability of determining optimum base-station locations, as well as predicting their coverage without carrying out a series of measurements, which are really expensive and time consuming, has been in high demand in the past two decades. It is therefore essential to develop an effective propagation model to assist wireless system design and determine the coverage range of a cellular base station in a metropolitan area or the required transmit power of a wireless network in a typical office environment [Jan01].

Traditionally, empirical methods such as COST-231, Walfish-Bertoni and Okumura-Hata, were used for initial coverage estimation [Hat80, Ike84, Pha09]. These empirical methods have the advantage of rapidity with the drawback that

they need calibration based on measurements using regression methods. On the other hand, deterministic methods [Lee09, Lee00, Tan96, Kan97, Dim06, Fra04, Pri09] can be based on either full-wave simulation techniques, such as Method of Moments (MoM) and Finite Difference Time Domain (FDTD) [Sch97], or, geometrical approximations such as Ray Launching (RL) [Sei94] and Ray Tracing (RT) [Yan98]. Previously, RL and RT were both classified as ray tracing methods, although more recently both methods are distinguished. The differences are mainly due to the different approaches followed. RL technique principle is that the transmitter launches thousands of test rays in a solid angle and the true path is determined by looking for the rays arriving at the receiver, whereas in classical RT methods the paths reflected by walls and furniture are found by computing the image of the transmitter or of the receiver. The advantage of these methods is accuracy, but the computational time could be prohibitive depending of the scenario's complexity. When combined with the Uniform Theory of Diffraction (UTD) [Gen09], they are the most frequently applied to predict radio coverage [Son99, Tay09, Son09]. The RT and RL approaches potentially are the most accurate and functional methods for multipath propagation characterization in urban and indoor environments.

In the light of the above survey of different propagation methods, it is highly important to adopt deterministic approaches which lead to accurate results with an affordable computational simulation time. The achievement of this goal is the main original contribution of this thesis, which presents a deterministic propagation model based on the RL technique for the characterization of complex indoor environments.

1.2 Objectives

The general purpose of this thesis is to develop a new and efficient propagation prediction model based on deterministic approaches for the characterization of wireless communications in complex indoor scenarios. In particular, the objectives of this work are the following:

- The first objective is to summarize the state of the art on wireless path loss prediction models employed so far in the literature, focusing especially in RT methods, which achieve a good trade-off between simulation results and inherent computational time.

- With the aim to achieve an adequate propagation prediction in complex indoor scenarios with an affordable computational time, the second objective is to develop a 3D RL code based on Geometrical Optics (GO) and the Uniform Theory of Diffraction (UTD).

- To perform a convergence analysis of the algorithm which leads to the optimal parameters to be used as inputs in the simulation of complex environments, with the goal of maximizing the efficiency of the algorithm.

- To develop new hybrid acceleration techniques with the aim of reducing the simulation time with accurate results, in order to make it more practical and better adapted to current demands.

- To validate the proposed method comparing simulation results with experimental measurements in complex environments and use it for radio planning purposes before the deployment of wireless communication systems in different scenarios.

By fulfilling these objectives, this thesis tries to contribute to the characterization of the electromagnetic propagation in the physical channel with a new and efficient deterministic approach. This contribution is one of the most important requirements nowadays with the growing demand of wireless communication systems everywhere.

1.3   Structure of the Thesis

This thesis is organized in seven chapters and two appendixes, being the first one the present introductory chapter. It has been focused on explaining the motivation of this work, along with the objectives of the thesis. Figure 1.1 shows a general scheme of the main contributions achieved during the work of this thesis. It is shown that the RL technique can be used for a broad range of applications. Channel characterization of different complex environments can be assessed, as well as dosimetric analysis estimation, interference source modeling and computational electromagnetics performance. Figure 1.2 shows a scheme of the work done and the following paragraphs provide a summary of the other six chapters of this work.

Figure 1.1. General scheme of the main contributions of this thesis.
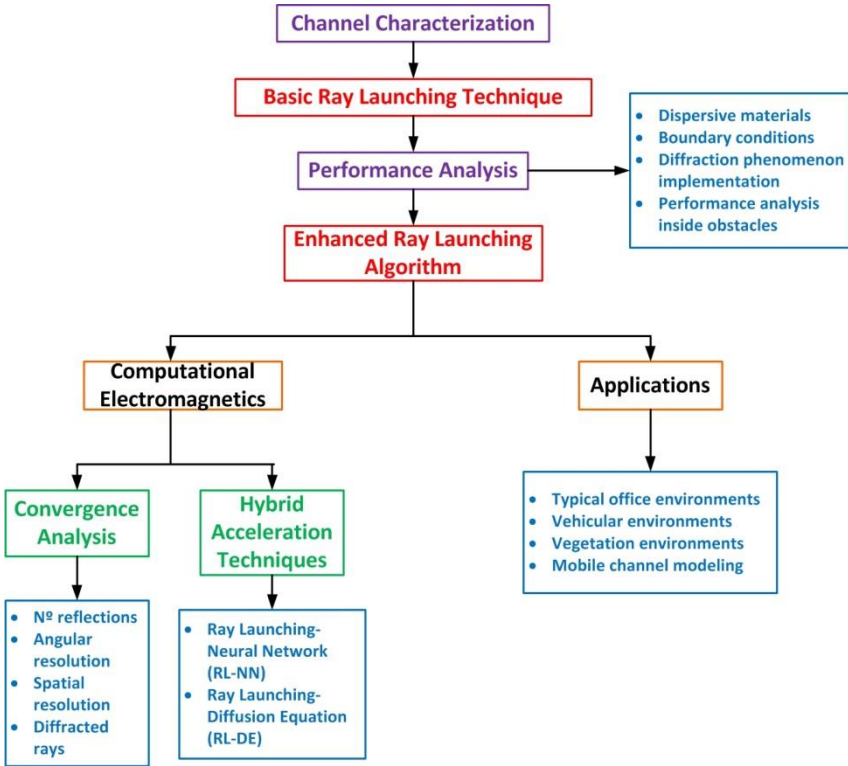
Figure 1.2. Description of the work presented in this thesis.

Chapter 2 covers a technology overview of wireless communication systems, with special emphasis in short-range technologies which are the most relevant ones for the work developed in this thesis. After that, the second part of the chapter presents a survey of wireless path loss prediction models, from theoretical to site-specific methods, focusing especially in RT methods, which achieve a good trade-off between simulation results accuracy and inherent computational time.

Chapter 3 is devoted to present in detail the in-house developed RL algorithm. It presents the initial conditions of the algorithm, with its challenges and the development of the enhanced RL algorithm. This chapter is particularly relevant for this thesis, because it is the basis of the work developed in the following chapters.

5

In Chapter 4, focused on the RL technique, a convergence analysis of the algorithm is presented. This analysis leads to the optimal parameters which allow modeling the radio wave propagation in complex environments with accurate results and affordable simulation computational time. The comparison between the Geometrical Optics (GO) only approach, the Geometrical Optics and Uniform Theory of Diffraction (GO-UTD) approach and real measurements has also been presented in this chapter. This comparison proves that the proposed hybrid GO-UTD technique yields excellent results and that the UTD extension definitely improves the simulation of the RL algorithm for realistic environments.

Chapter 5 is devoted to present two novel hybrid acceleration techniques, which combined with the RL approach yields to significant reduction of computational time with accurate results. On one hand, a new hybrid Ray Launching-Neural Network (RL-NN) technique is presented for joint prediction of radio wave propagation using RL and NN. This technique uses NN for modeling and storing the RL results for coverage prediction. On the other hand, a novel Ray Launching-Diffusion Equation (RL-DE) approach for electromagnetic propagation analysis in complex indoor environments is proposed in the second part of this chapter. This technique combines the 3D RL algorithm based on GO and UTD with the DE method based on the equation of transfer.

In Chapter 6, different applications of the proposed technique are presented. First, an in-depth analysis of electromagnetic propagation in a typical office environment is provided. After that, the work has been focused in more complex indoor environments, such as vehicular environments. Radio planning analysis within vegetation environments is also presented in this chapter, evidencing the complexity of this type of scenarios. The last part of the chapter is focused in mobile channel characterization, and a Vehicle to Infrastructure (V2I) system based on Radio Frequency IDentification (RFID) has been presented.

Finally, Chapter 7 provides a compilation of the most significant results and general conclusions of this work. Besides, future research lines related to this thesis are proposed and briefly analyzed.

Two appendixes are introduced at the end of the thesis, being the first one a catalog of material properties used in the simulations, and the second one, the measurement equipment specification of the hardware used during the work of the thesis.

Bibliography of the Chapter

[Dim06] A. G. Dimitriou and G. D. Sergiadis, "Architectural features and urban propagation", *IEEE Trans. Antennas and Propag.*, vol 54, no. 3, pp. 774-784, 2006.

[Fra04] M. Franceschetti, J. Bruck and L. J. Schulman, "A random walk model of wave propagation", *IEEE Trans. Antennas and Propag.*, vol. 52, no. 5, pp. 1304-1317, 2004.

[Gen09] G. Gennarelli and G. Riccio, "A uapo-based model for propagation prediction in microcellular environments", *Progress in Electromagnetics Research B*, vol 17, pp. 101-116, 2009.

[Hat80] M. Hata, "Empirical formula for propagation loss in land mobile radio services", *IEEE Trans. Antennas and Propag.*, vol. 29, no. 3, pp. 317-325, 1980.

[Ike84] F. Ikegami, S. Yoshida, T. Takeuchi, and M. Umehira, "Propagation factors controlling mean field strength on urban streets", *IEEE Trans. Antennas and Propag.*, vol. 32, no. 8, pp. 822-829, 1984.

[Jan01] R. Janaswamy, *Radiowave Propagation and Smart Antennas For Wireless Communications*, Norwell, MA: Kluwer Academic, 2001.

[Kan97] A. G. Kanatas, I. D. Kountouris, G. B. Kostaras and P. Constantinou, "A UTD propagation model in urban microcellular environments", *IEEE Trans. Veh. Tech.*, vol. 46, no. 1, pp. 185-193, 1997.

[Lee00] D. J. Y. Lee and W. C. Y. Lee, "Propagation prediction in and through buildings", *IEEE Trans. Veh. Tech.*, vol. 49, no. 5, pp. 1529-1533, 2000.

[Lee09] S. H. Lee, "A photon modeling method for the characterization of indoor optical wireless communication", *Progress in Electromagnetics Research*, vol. 92, pp. 121-136, 2009.

[Pha09] S. Phaiboon and P. Phokharatkul, "Path loss prediction for low-rise buildings with image classification on 2-D aerial photographs", *Progress in Electromagnetics Research*, vol. 95, pp. 135-152, 2009.

[Pri09]   J. Blas Prieto, R. M. Lorenzo Toledo, P. Fernández Reguero, E. J. Abril, A. Bahillo Martínez, S. Mazuelas Franco, and D. Bullido, "A new metric to analyze propagation models", *Progress in electromagnetics research*, vol. 91, pp. 101-121, 2009.

[Sch97] J. W. Schuster and R. J. Luebbers, "Comparison of GTD and FDTD predictions for UHF radio wave propagation in a simple outdoor urban environment", *IEEE Antennas and Propag. Society International Symposium*, vol 3, pp. 2022-2025, 1997.

[Sei94]   S. Y. Seidel, T. S. Rappaport, "Site-Specific Propagation Prediction for Wireless In-Building Personal Communication System Design", *IEEE Transactions on Vehicular Technology*, vol. 43, no. 4, pp. 879-891, 1994.

[Son09] H. B. Song, H. G. Wang, K. Hong and L. Wang, "A novel source localization scheme based on unitary esprit and city electronic maps in urban environments", *Progress In Electromagnetics Research*, vol. 94, pp. 243-262, 2009.

[Son99] H. W. Son and N. H. Myung, "A deterministic ray tube method for microcellular wave propagation prediction model", *IEEE Trans. Antennas and Propag.*, vol 47, no. 8, pp. 1344-1350, 1999.

[Tan96] S. Y. Tan and H. S. Tan, "A microcellular communications propagation model based on the uniform theory of diffraction and multiple image theory", IEEE Trans. Antennas and Propag., vol 44, no.10, pp. 1317-1326, 1996.

[Tay09] A. Tayebi, J. Gómez, F. S. de Adana and O. Gutierrez, "The application of arrival and received signal strength in multipath indoor environments", *Progress In Electromagnetics Research*, vol. 91, pp. 1-15, 2009.

[Yan98] C. F. Yang, "A Ray-Tracing Method for Modeling Indoor Wave Propagation and Penetration", *IEEE Transactions on Antennas and Propagation*, vol. 46, no. 6, pp. 907-919, 1998.

Chapter 2

Wireless Communications

THE significant growth of wireless communications over the past two decades, has led to an intense interest in understanding and predicting radio wave propagation characteristics in both indoor and outdoor environments. This makes it really valuable to have the capability of determining optimum base-station locations, and predicting their coverage, without carrying out a series of measurements, which are very expensive and time consuming. It is therefore fundamental to develop an effective propagation model for wireless communication, in order to provide accurate design guidelines for wireless systems. In the first part of this chapter, a technology overview of wireless communication systems is given, with special emphasis in short-range technologies which are the most relevant for the work developed in this thesis. After that, the second part of the chapter presents a survey of wireless path loss prediction methods, from theoretical models to site-specific models, focusing especially in Ray Tracing (RT) methods, which achieve a good trade-off between simulation results accuracy and inherent computational time.

2.1 Overview of Wireless Communication Systems

Recent advancements in information technology and continued miniaturization of mobile communication devices have increased the use of wireless communications. Because of this tremendous growth, wireless networks

have witnessed rapid changes and the development of new applications. Recently, wireless networks have come into prominence, and the impact of wireless networks has been and will continue to be profound because they hold the potential to revolutionize many segments of our economy and life, from environmental monitoring and conservation to manufacturing and business asset management and to automation in the transportation and health care industries. Due to this success in the adoption of wireless communications, an increasing number of different systems and diverse applications are being adopted. In this sense, several wireless links can be operating simultaneously, with different requirements in terms of coverage as well as capacity.

Wireless communication networks can be classified into Wireless Body Area Networks (WBANs), Wireless Personal Area Networks (WPANs), Wireless Local Area Networks (WLANs), Wireless Metropolitan Area Networks (WMANs), and Wireless Wide Area Networks (WWANs) based on the communication range (Figure 2.1).

A Wireless Body Area Network (WBAN) is characterized by having only a few meters of coverage, which usually comprises the immediate proximity of a person. For instance, it may be formed by an ad hoc topology connecting several wireless sensors distributed inside, on, and/or near the human body to monitor physical or biometric parameters.

A WPAN is used for communication among data devices that are relatively close, usually within the workspace of a person. It is sometimes assumed that radio links are less than 10m, although nowadays the most employed WPAN technologies such as Bluetooth or Zigbee have much wider coverage areas. It is also relatively common to include WBANs into the WPAN concept.

A WLAN is employed for wireless connectivity of devices such as computers, smartphones, tablets, PDAs, printers, etc., featuring radio coverage of around 100m. It is commonly named as WiFi network. The most popular WLANs today are those based on extensions of the IEEE 802.11 standard.

A WMAN provides connectivity in a metropolitan area of several kilometers. It may provide connectivity for instance to different buildings of a large campus or a city, and may be an alternative or backup solution to typical copper or fiber networks. An example of WMAN networks is WiMAX based on the IEEE 802.16-2004 standard.

A WWAN features wider coverage areas. It includes for instance cellular networks (GSM, UMTS, LTE, etc.).

Although there is not an exact boundary, typically short-range communications comprise radio coverage of less than around 100 m, including WLAN, WPAN and WBAN networks. They are common networks deployed in indoor scenarios. The most relevant standards concerning short-range wireless communications are the family of IEEE 802.11 standards for WLAN, and the family of IEEE 802.15 standards for WPAN and WBAN. In the remainder of this section, the main technologies employed for short-range and large-range communications are described, with special emphasis in short-range communications, which are the most frequently used in the work of this thesis.
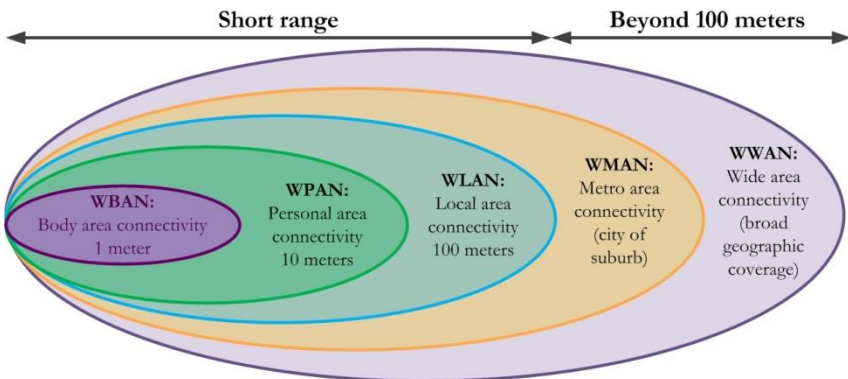

Figure 2.1. Categories in wireless communication.

2.1.1 Different technologies

2.1.1.1. Bluetooth

Bluetooth technology was developed by the Bluetooth Special Interest Group (SIG), which was initially created by 5 large companies in 1998, where the brand name was formally adopted. Bluetooth can be used to form WPANs having a short range of communication. Some of the features of Bluetooth technology are that it is robust, consumes less power, and costs less to manufacture. Bluetooth can be found in a number of devices, including computer peripherals, digital cameras, and GPS devices. It can be configured as a piconet or scatternet. In a piconet, up to eight devices communicate with each other using Frequency-Hopping Spread Spectrum (FHSS). Among them, one device acts as master device and the remaining devices connect to this master device. Collisions

do not occur in a piconet as the master device assigns a communication slot for each of the seven slave devices. A scatternet is made up of clusters of piconets. A master device in one piconet can act as a slave in another piconet. The master device plays the role of a bridge in connecting two piconets. Bluetooth operates at the 2.4GHz ISM frequency band and its maximum data rate achievable is up to 1Mbps (higher in recent versions of Bluetooth).

Bluetooth technology is basically designed for low-power consumption with a short range based on low-cost transceiver microchips in each device. The Bluetooth specification defines three transmitter power classes based on the modulation mode with the highest output power, as shown in Table 2.1. The most commonly used radio is Class 2. Bluetooth devices can adapt the transmitted power to the radio link employed, saving power and reducing interference. A power class 1 device shall support such power control techniques, according to the Bluetooth specification, while it is optional for class 2 and class 3 devices.

Bluetooth Low Energy (BLE) is the distinguishing feature of the latest Core Version, Bluetooth v4.0 developed by the Bluetooth SIG for short-range communication. In contrast with previous Bluetooth flavors, BLE has been designed as a low-power solution for control and monitoring applications. BLE is Bluetooth SIG's response to the convergence of several key trends in wireless connectivity: wireless everywhere, portability and low-cost [Blu10]. BLE substantially reduces classic Bluetooth's peak, average, and idle mode power consumption, with energy efficiencies that can be 20 times higher than Classic Bluetooth.

Table 2.1 shows the difference between Classic Bluetooth and BLE in terms of output power, operational range and sensitivity. The data has been taken from the literature [Gom12].

Table 2.1. Differences between Classic Bluetooth and Bluetooth Low Energy.

		Output Power (dBm)	Operational Range (m)	Sensitivity (typical)(dBm)
Classic Bluetooth	Class 1	20	~ 100	-90
	Class 2	4	~ 10	-90
	Class 3	0	~ 1	-90
Bluetooth Low Energy		-20 to 10	~ 100	-87 to -93

2.1.1.2. ZigBee

ZigBee is a technology for low-data rate short-range wireless communications. It is mainly targeted for battery-powered devices requiring low cost, low data rate, and long battery lifetime. These devices are typically used in low-latency applications, where the percentage of time the device is active performing any sensing or data transmission task is very small, spending most of the time in sleep mode to save power. Examples of such applications are wireless sensor networks for distributed monitoring of parameters such as temperature, humidity, blood pressure, heart rate, etc. Thus they can be applied in scenarios such as health and fitness monitoring, home control of heat, ventilation and air conditioning systems, structural health monitoring of buildings or infrastructures, etc.

The ZigBee specifications are developed by the ZigBee Alliance, which was created in 2002 and that in 2012 has more than 600 member companies, ranging from semiconductor companies and software developers to installers and original equipment manufacturers (OEMs).

ZigBee-based devices operate in the 868MHz, 915MHz and 2.4GHz bands and the maximum transmission speed in 250kbps. ZigBee was designed for low data rate, low cost and low energy consumption. The ZigBee standard adopted the physical and MAC (Medium Access Control) layers from the IEEE 802.15.4 standard. Thus, a ZigBee compliant device is compatible with IEEE 802.15.4.
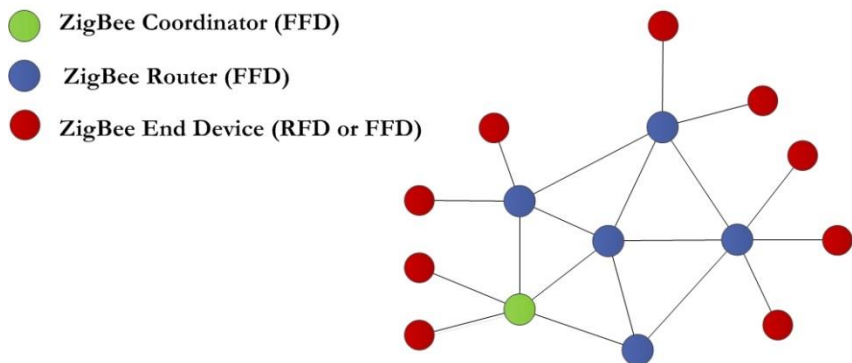

Figure 2.2. ZigBee network architecture.

Figure 2.2 shows a typical architecture of a ZigBee network. There are two types of devices, as in any other IEEE 802.15.4 based network:

- Full Function Device (FFD). This device is able to perform all the tasks described in the IEEE 802.15.4 standard, and can play any role in the network. In particular, it can be Coordinator, Router or End Device.
- Reduced Function Device (RFD). It has limited capabilities that make it able to operate only as an End Device. As a consequence, they can only communicate with FFDs, but not with other RFDs. Typically RFDs are very simple devices with less hardware and software complexity than FFDs and aimed to simple tasks such as sensing a temperature value or turning on or off a switch. This device usually can be in sleep mode most of the time.

The three different roles that a Zigbee FFD can play in an IEEE 802.15.4 based network are:

- Coordinator: it is the controller of the WPAN network
- Router: it has network routing capabilities, so that it is capable of relaying messages.
- End Device: it only has capability to communicate with its parent FFD (either router or coordinator)

A slightly different terminology is used in the IEEE 802.15.4 standard. The Zibgee coordinator is the IEEE 802.15.4 PAN coordinator, a Zibgee router is a device that can act as an IEEE 802.15.4 coordinator, and a ZigBee end device is an IEEE 802.15.4 device that is neither a router nor a coordinator.

There are various network topologies that ZigBee supports: point-to-point, star topology, tree topology and mesh topology.

In the point-to-point and star topologies, a FFD becomes the ZigBee coordinator and is responsible of initializing the network. The other(s) device(s) communicate directly with the coordinator. The first thing the coordinator does is choosing a unique PAN identifier not used by any other network in its radio coverage area.

In the tree and mesh topologies, the ZigBee coordinator initializes the network and sets the network parameters, but other FFDs acting as routers may extend the initial network established by the ZigBee coordinator by participating in message routing.

In any of the topologies, the ZigBee coordinator selects a unique PAN identifier, allocates a unique (16-bit or 64-bit) address to each device of the network and initiates, terminates and routes messages throughout the network.

2.1.1.3. Wi-Fi

The most popular short-range communications systems today are WLANs. A WLAN allows wireless data transfer between devices in relatively large areas such as a campus or a building. Devices usually connect using unlicensed RF bands to an access point which provides internet access. Typical WLAN users are static or move at pedestrian speed. The IEEE 802.11 Wireless LAN working group was founded in 1987 to begin standardization of spread spectrum WLANs for use in the ISM bands. Despite the unrestricted spectrum allocation and intense industry interest, the WLAN movement did not gain momentum until the late 1990s when the phenomenal popularity of the Internet combined with wide scale acceptance of portable, laptop computers finally caused WLAN to become an important and rapidly growing segment of the modern wireless communications marketplace. IEEE 802.11 was finally standardized in 1997 and provided interoperability standards for WLAN manufacturers. In 1999, the 802.11 High Rate standard (called IEEE 802.11b) was approved, thereby providing new user data rate capabilities of 11Mbps and 5.5Mbps in addition to the original 2Mbps and 1Mbps user rates of IEEE 802.11, which were retained.

Figure 2.3 illustrates the evolution of IEEE 802.11 Wireless LAN standards. It is shown how both frequency hopping and direct sequence approaches were used in the original IEEE 802.11 standard, but as of late 2001 only Direct Sequence Spread Spectrum (DS-SS) modems had thus far been standardized for high rate (11Mbps). The DS-SS IEEE 802.11b standard has been named Wi-Fi by the Wireless Ethernet Compatibility Alliance, a group that promotes adoption of 802.11b DS-SS WLAN equipment and interoperability between vendors.

The family of IEEE 802.11 Wi-Fi standards defines the Physical (PHY) and Medium Access Control (MAC) layers of the WLAN. They allow peer-to-peer connections between devices and multiple device connections to an access point. In the first case, which is not very used, the stations form an ad hoc network.

Figure 2.4 shows the typical architecture of a Wi-Fi network of the second type, according to the IEEE 802.11 standards. The main network elements are:
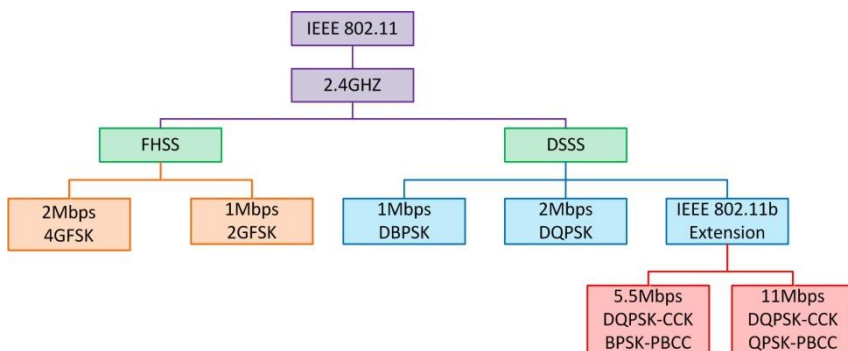

Figure 2.3. Overview of the IEEE 802.11 Wireless LAN standard.

- Station (STA). They are devices that have an IEEE 802.11 network interface (laptop computers, smartphones, tablets, etc.). They are typically powered by batteries. However, many desktop computers are now sold with IEEE 802.11 network interfaces, to reduce the number of cables.
- Access Point (AP). They perform, among other tasks, the bridging connection between the wireless medium and the wired infrastructure.
- Distribution system. Allows connection of the access points, forwarding frames to their destination. It typically includes the bridging elements and the backbone network. This backbone network is usually a wired Ethernet LAN.

The elementary building block of an IEEE 802.11 network is the Basic Service Set (BSS), shown in Figure 2.4, which corresponds to the group of stations that communicate to a given AP. In this case it is called infrastructure BSS, since communications rely on the AP. The BSSs corresponding to the APs of the same WLAN network form an Extended Service Set (ESS). When stations form an ad hoc network, an independent BSS (IBSS) is established. Figure 2.5 illustrates this case.
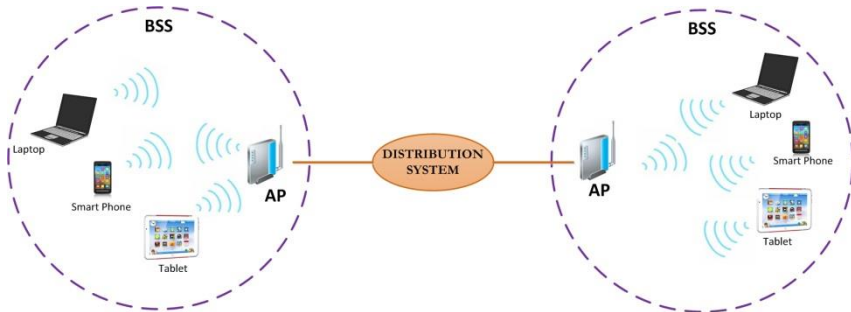
Figure 2.4. Typical architecture of an IEEE 802.11 WLAN network.

Figure 2.5. Ad hoc IEEE 802.11 network forming an Independent BSS.

2.1.1.4. Mobile Systems: From 1G to 5G

Mobile networks have evolved through more than three generations, starting with the analogue or first-generation (1G) networks deployed in the early 1980s, and moving on to the digital second-generation (2G) networks deployed in the early 1990s. Third-generation (3G) networks were deployed in 2000 and the fourth-generation (4G) systems since around 2010. The wireless mobile network has experienced a huge transformation, from a pure telephony system to a network that can transport rich multimedia contents. The 4G wireless systems were designed to fulfill the requirements of the International Mobile Telecommunications-Advanced (IMT-A) requirements using IP for all services [Has08]. In 4G systems, an advanced radio interface is used with Orthogonal Frequency-Division Multiplexing (OFDM), Multiple-Input Multiple-Output

(MIMO), and link adaptation technologies. 4G wireless networks can support data rates of up to 1Gbps for low mobility, such as nomadic/local wireless access, and up to 100 Mbps for high mobility, such as mobile access. LTE and its extension, LTE-Advanced (LTE-A) systems, as practical 4G systems, have recently been deployed around the world.

However, the large increase in the number of users who subscribe to mobile broadband systems every year has led to more people craving faster Internet access on the move, trendier mobiles, and, in general, instant communication with others or access to information. This fact, together with the fact that more powerful smartphones and laptops are becoming more popular nowadays, demanding advanced multimedia capabilities, has resulted in an explosion of wireless mobile devices and services. Because of that, many research challenges need to be addressed. One of the most crucial challenges is the physical scarcity of RF spectra allocated for cellular communications. There are also other challenges like, for example, high data rate and high mobility, seamless coverage, diverse Quality of Service (QoS) requirements, and fragmented user experience (incompatibility of different wireless devices/interfaces and heterogeneous networks), to mention only a few.

One of the main problems of 4G networks is that they have just almost reached the theoretical limit on the data rate with current technologies and therefore, they are not sufficient to accommodate the aforementioned challenges. In this sense, the necessity of groundbreaking wireless technologies to solve the above problems caused by trillions of wireless devices has increased in the last years, and researchers have already started to investigate beyond 4G (B4G) or 5G wireless techniques.

The 5G network is expected to be standardized by around 2020. It is now too early to define this with any certainty. However, it is widely agreed that compared to the 4G network, the 5G network should achieve 1000 times the system capacity, 10 times the spectral efficiency, energy efficiency and data rate (i.e., peak data rate of 10Gbps for low mobility and peak data rate of 1Gbps for high mobility), and 25 times the average cell throughput. A proposed 5G heterogeneous cellular architecture is illustrated in Figure 2.6 [Wan14]. The aim is to connect the entire world, and achieve seamless and ubiquitous communications between anybody (people to people), anything (people to machine, machine to machine), wherever they are (anywhere), whenever they need (anytime), by whatever electronic devices/services/networks they wish (anyhow). This means that 5G networks should be able to support

communications for some special scenarios not supported by 4G networks (e.g., for high-speed train users). High-speed trains can easily reach 350 up to 500 km/h, while 4G networks can only support communication scenarios up to 250 km/h.
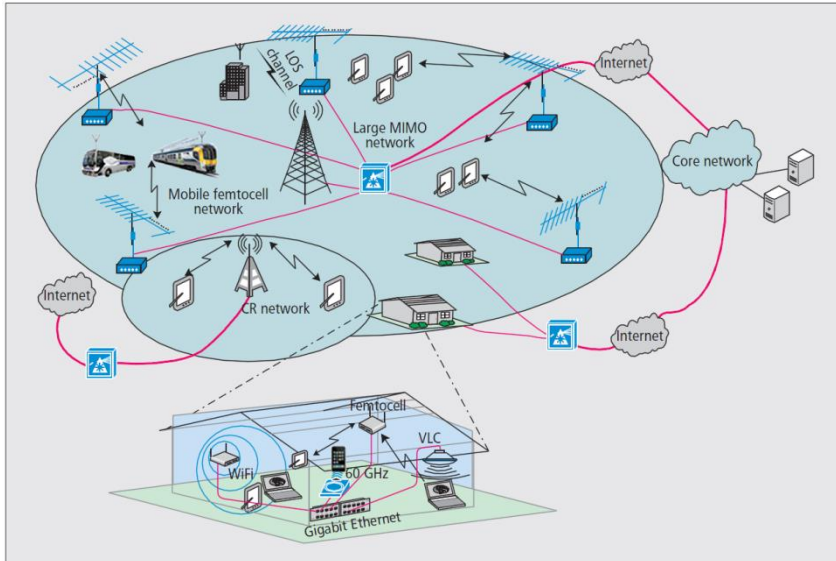

Figure 2.6. A proposed 5G heterogeneous wireless cellular architecture [Wan14].

The network architecture of 5G is really complex, as it is illustrated in Figure 2.7, which represents the Release 13 of the 3rd Generation Partnership Project (3GPP), the group responsible for standards related to mobile communication technologies. This network architecture must be able to support heterogeneous networks, which is a non-trivial task. Like all wireless networks the performance of 4G and beyond networks depend for a major part on the channel, that is, how the signal propagates between emitters and users. That is why channel modelling and propagation is very important and must have full consideration. Indeed, in order to study the performance of future wireless networks, it is very important to be able to characterize the wireless channel into different scenarios and to be able to take into account the new situations introduced by future networks.
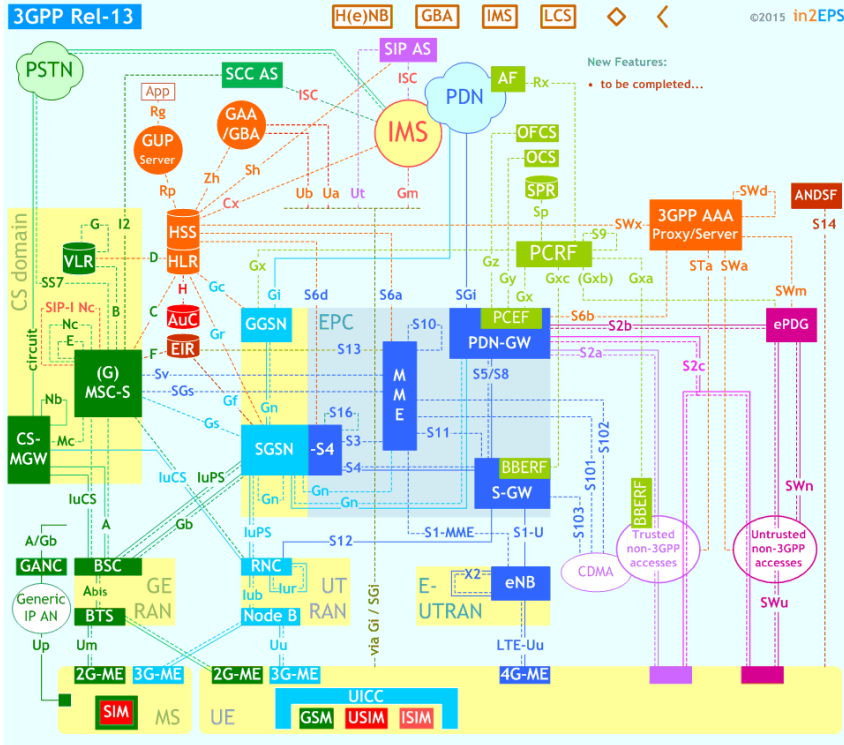
Figure 2.7. 3GPP Release 13 Network Architecture [Int15].

2.2 Propagation Models in Wireless Communications

Before implementing designs and confirming planning of wireless communications systems, accurate propagation characteristics of the environment should be known. Propagation prediction usually provides two types of parameters corresponding to the large-scale path loss and small-scale fading statistics. The path-loss information is vital for determining optimum base-station locations, as well as predicting their coverage without carrying out a series of measurements, which are really expensive and time consuming.

2.2.1 Classification of propagation models

A propagation model is a set of mathematical expressions, diagrams and algorithms used to represent the radio propagation characteristics of an

environment. The path-loss prediction models can be roughly divided into three types, i.e., theoretical, empirical and site-specific models.

The purely theoretical treatment of suburban or urban propagation is basically an intractable electromagnetic problem because of the general non-availability of a detailed geometric description of the coverage area, together with the numerous boundary conditions. Theoretical models are derived physically assuming some ideal conditions, for example the diffracting screens model is derived using physical optics assuming uniform heights and spacing of buildings.

Empirical or statistical models are based on measurements while deterministic models are based on the fundamental principles of radio waves propagation and they are not based on extensive measurements. They consider environment details that may estimate the signal propagation.

Empirical models are usually a set of equations derived from extensive field measurements. They are simple, efficient to use and accurate for environments with the same characteristics as those where the measurements were made. Important models in this group are Okumura model, who is one of the most widely used in urban areas, and Hata model, which is an empirical formula of the graphical model Okumura [Oku68, Hat80]. These models are recommended when high accuracy is not required. One of the main drawbacks of empirical models is that they cannot be used for different environments without modification; for example, the empirical model for macro-cells cannot be used for indoor pico-cells. They have a large big dependence with the measurement environment and some conditions to the validity of the models, linked to the regressive process used to obtain them. The input parameters for the empirical models are usually qualitative and not very specific, e.g., a dense urban area, a rural area, and so on. The output parameters are basically range-specific, not site-specific.

In order to increase accuracy and minimize the dependence of measurements, deterministic methods for estimating coverage of wireless systems are developed. These site-specific methods are based on numerical methods. They use Maxwell's equations to calculate the full electromagnetic propagation characteristics. Some examples are the Ray-Tracing (RT) method [Sae00], the Finite-Difference Time-Domain (FDTD) method or the Method of Moments (MoM). The input parameters can be very detailed and accurate. The disadvantages of the deterministic methods are the large computational overhead that may be prohibitive for some complex environments.

The propagation prediction has been more challenging because of the fast evolution of wireless communications and the trend to use higher frequency bands, smaller cell sizes and smart antenna systems. In macro-cells, simple empirical and statistical models are widely used with satisfactory accuracy because the transmitting antenna is usually located on a high tower. However, for the microcells and especially for picocells, the height of the transmitting antenna may be lower than the average height of the buildings in the regions involved, and this could greatly affect the propagation of the radio waves because of the geometry of the buildings and terrains, causing wide shadow regions due to the reflections from vertical walls and ground, diffractions from vertical and horizontal edges of buildings, scattering from non-smooth surfaces and all possible combinations.

To deal with the new complex propagation environments, deterministic models have been developed based on ray-tracing techniques. In a basic ray-tracing algorithm, the fundamental task is to determine the path of a ray launched from a transmitting antenna. This procedure involves the calculation of the intersection of a ray with a surface (in three-dimensional, 3D, cases) or a ray with an edge segment (in two-dimensional, 2D, cases). The computation efficiency is then the biggest obstacle against the application of ray-tracing methods. Since more types of rays can be taken into account (such as reflected, transmitted, diffracted and scattered rays), an efficient ray-tracing procedure is really important for improving the prediction accuracy.

Figure 2.8 represents the trade-off between accuracy and simulation time for different propagation models. It can be seen, as stated above, that the ray tracing techniques achieve a good trade-off between precision and simulation time. In the remainder of this section, the main propagation prediction models have been described, from theoretical models to deterministic models. Special emphasis has been given to ray tracing methods due to the fact that this thesis is focused in the implementation of a 3D Ray Launching algorithm for coverage prediction, which is described in detail in Chapter 3.
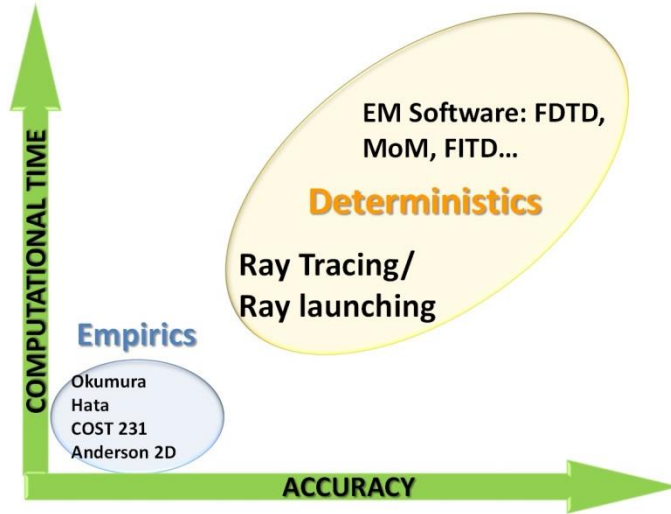
Figure 2.8. Overview of the different propagation prediction methods.

2.2.1.1. Theoretical Models

The theoretical models considered here are by no means exhaustive. There are many excellent models, including the Longley-Rice model [Lon68, Huf82], the Bullington model [Bul57, Bul77] and Lee's model [Lee90, Lee97]. We will begin here with the Free Space Model, based on the Friis formula, and the Diffracting Screens Model, which considers propagation from a fixed-site antenna in a city made of buildings of nearly uniform height organized into rows of streets to a final diffraction of the rooftop field down to a street-level mobile or portable radio.

Free Space Model

In free space, the radiated energy by an omnidirectional antenna spreads as the surface of a sphere centered on the antenna. The model of free space propagation is used to predict the power of the signal between the transmitter and receiver when there is a clear line of sight. Satellite communication systems and microwave links can be modeled as free-space propagation links.

Basic free space propagation attenuation is due to the geometric spherical expansion of waves, so attenuation is inversely proportional to the distance d squared, and the power density at distance d is

$$P_r(d) = \frac{P_t G_t G_r \lambda^2}{(4\pi)^2 d^2 L} \qquad (2.1)$$

Where:

- $P_r(d)$ is the power at distance d
- P_t is the transmitter power
- G_t is the transmitter antenna gain
- G_r is the reception antenna gain
- L are the system losses not related with the propagation

Antenna gain and effective aperture area are related by

$$A = \frac{G \lambda^2}{4\pi} \qquad (2.2)$$

The Friis transmission formula [Fri46] states the ratio of the received power to transmitted power in terms of the free space propagation law and the transmitting and receiving antenna effective apertures A_t and A_r, respectively. So,

$$\frac{P_r}{P_t} = \frac{A_r A_t}{\lambda^2 d^2} \qquad (2.3)$$

The Friis equation is only valid for predicting P_r values in the region of the far field of the transmitting antenna. The far-field region or Fraunhofer region of a transmitting antenna is defined as the distance beyond the distance d_f, which is related to the largest dimension of the numerical aperture transmitting antenna. Fraunhofer distance is given by

$$d_f = \frac{2D^2}{\lambda} \qquad (2.4)$$

Where D is the largest physical dimension of the antenna. Besides, to be in the far field region, it must be satisfied $d_f \gg D$ and $d_f \gg \lambda$. Furthermore, it is clear that this equation is not valid for $d = 0$.

Diffracting Screens Model

The theoretical model described here is based on a geometrical generalization based in the J.Walfisch and H. L. Bertoni [Wal88] model. This model considers the rows of city buildings as a series of absorbing diffracting screens of uniform height. An overall propagation model is given for the case of an elevated fixed antenna above the building roofline to a location at street level due to the forward diffraction, along the screens, with a final diffraction down to street level, as we can see in Figure 2.9.
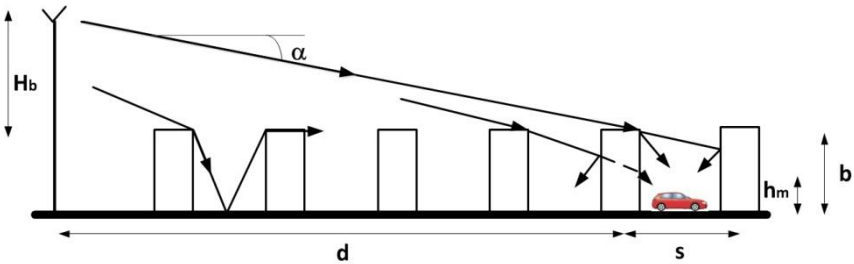

Figure 2.9. Wave propagation in a homogeneous urban region.

An extended Walfisch-Bertoni model is L. R. Maciel, Bertoni and H. H. Xia [Mac93] which allow the fixed-site antenna to be below, as well as above, the rooftop level, but the restriction of a nearly homogeneous neighborhood of uniform-height still applies. The resulting expression for path propagation L_{ds} is written in terms of the free space loss F, excess losses L_{e2} due to diffraction along the rooftops, and a final diffraction L_{e1} down below roof-top level. A correction term is included to account for Earth curvature, provided that the distance does not approach the radio horizon.

$$L_{ds} = -F - L_{e1} - L_{e2} - 18log\left[\frac{17H_b + d^2}{17H_b}\right] \qquad (2.5)$$

Where:

- L_{ds} is the diffracting screens propagation, average signal (dB)
- H_b is the fixed-site antenna height (m)

25

- H_m is the mobile antenna height (m)
- b is the building height
- s is the separation between rows of buildings (m)
- w is the distance from mobile to building on street (m)
-   is the range (Km) (not beyond radio horizon)
- f is the frequency (MHz)

The first term F is free space propagation loss:

$$F = 32.4479 + 20log(fd) \tag{2.6}$$

The loss L_{e1} is:

$$L_{e1} = -10log\left[\frac{G_m(\theta)}{\pi k \sqrt{(b-H_m)^2 + w^2}}\left[\frac{1}{\theta} - \frac{1}{2\pi + \theta}\right]^2\right] \tag{2.7}$$

Where $G_m(\theta)$ is the mobile antenna gain in the roof edge direction, k is the wave number, and θ is the angle from the roof edge to the mobile found from

$$\theta = atan\left[\frac{b - H_m}{w}\right] \tag{2.8}$$

L_{e2} in the roof direction is (with G_b the fixed-site antenna gain usually taken to be unity):

$$L_{e2} = -10log[G_b Q^2] \tag{2.9}$$

Q is either Q_E or Q_L, depending on whether the fixed-side antenna is above or below the rooftop level. Q_E is chosen when the fixed-site antenna height H_b is more than $\sqrt{\lambda s}$ above the rooftop level b, and Q_L is chosen when H_b is below rooftop level by more than $0.5\sqrt{\lambda s}$ [Wal88]. Q_L is given by

$$Q_L = \frac{\frac{s}{1000d - s}}{\sqrt{2\pi k \sqrt{(b - H_b)^2 + s^2}}}\left[\frac{1}{atan\left[\frac{b - H_b}{s}\right]} - \frac{1}{2\pi + atan\left[\frac{b - H_b}{s}\right]}\right] \tag{2.10}$$

Above the rooftop level, the expression Q_E is

26

$$Q_E = 2.35 \left[atan \left[\frac{H_b}{1000d} \right] \sqrt{\frac{s}{\lambda}} \right]^{0.9} \tag{2.11}$$

The results are not valid close to, or beyond, the radio horizon. At distances beyond 20km, the Earth's curvature begins to have an effect. Beyond the radio horizon, losses are greater than predicted by the model. Personal communications systems that are likely to use antennas at heights below rooftop level are also likely to be low-power microcellular systems that tend to be interference rather than propagation limited.

2.2.1.2. Empirical Models

Empirical methods provide a quick estimate of the loss basic propagation or, alternatively, the field strength at any point around a transmitter. They are quick and easy to use, but obviously they have not a lot of accuracy. The mean square error between the estimated value of one of these methods and the measured value may be around 10 to 14dB.

Several empirical models have been developed based on measured data and use curve-fit equations to model propagation in areas of urbanization. Often empirical models are city specific and tied to urban land-use maps. The London model of M. F. Ibrahim and J. D. Parsons [Par89, Par00] is an example of such a model. Another, more generalized, hence more commonly used, empirical model is that of Y. Okumura [Oku68]. Their model is based on extensive measurements in Tokyo, Japan, environs. Because the Okumura data is well documented and widely known, the model has been extensively adopted around the world using "correction factors" to force-fit applicability to regions other than Tokyo.

Okumura Prediction Method

The Okumura model [Oku68] is an empirical model based on extensive measurements made in Japan over wide a range of frequencies, from 150-1920MHz (behavior was extrapolated and interpolated to frequencies between 100 and 3000MHz). Measurements were made at several fixed-site and mobile antenna heights (between 30-1000m), and over various irregular terrains and environmental clutter conditions. The basic prediction formula is as follows

$$L_{mean}(dB) = L_{free} + A_{mu}(f,d) - G(h_{te}) - G(h_{re}) - G_{correction} \tag{2.12}$$

27

Where $L_{mean}(dB)$ is the median value of the propagation path loss, L_{free} is the free-space path loss, A_{mu} is the median attenuation value relative to free space in an urban area, $G(h_{te})$ and $G(h_{re})$ are the height gain factors of fixed-site and mobile antennas, and $G_{correction}$ is the correction factor due to the environment.

Curves were generated in several environments, including the distance dependence of field strength in open and urban areas, the frequency dependence of field strength in urban areas, and urban versus suburban differences. This led to curves giving a suburban correction factor. Additionally, corrections were extracted for various types of terrain and foliage. Illustrative examples using the Okumura model can be found in, e.g., [Rap96, Her99].

Hata Prediction Method

The Hata model [Hat80] is a formula-based model based in the graphics of the Okumura model which can be used more effectively. Hata's formula was limited to a frequency range of 100 to 1500MHz, distances of between 1 and 20km, base antenna heights between 30m and 200m, and vehicle antenna heights from 1m to 100m. The basic formula for the median path loss in this model is

$$L_{mean}(dB) = [69.55 + 26.16\,log(f) - 13.82\,log(H_b) \\ + [44.9 - 6.55\,log(H_b)]\,log(d) + a_x(H_m)] \qquad (2.13)$$

Where f is the frequency in MHz, d is the distance in km, and H_b is the base station height in meters. $a_x(H_m)$ is a mobile height correction function for mobile antenna heights which takes the following form

$$a_m(H_m) = [0.7 - 1.1\log(f)]H_m + 1.56\log(f) - 0.8 \qquad (2.14)$$

In suburban areas, Hata gives the path loss as $L_{mean} - L_{ps}$, where

$$L_{ps} = -2log^2\left[\frac{f}{28}\right] - 5.4 \qquad (2.15)$$

And in open areas, as $L_{mean} - L_{po}$, where

$$L_{po} = -4.78log^2(f) + 18.33\,log(f) - 40.94 \qquad (2.16)$$

Hata's model is a good approximation to Okumura when d>1km. It is a good model to the first generation of mobile phones, but it does not work very accurately with current technologies with smaller cell sizes and higher frequencies.

2.2.1.3. Deterministic Models

Deterministic methods [Lee09, Lee00, Tan96, Kan97, Dim06, Fra04, Bla09] are based on numerical approaches involving either solution of Maxwell's equations using full-wave simulation techniques, such as MoM and FDTD [Sch97], or, using geometrical approximations such as RL [Sei94] and RT [Yan98]. Previously, RL and RT were both classified as ray tracing methods, although more recently both methods are distinguished. The differences are mainly due to different approaches. RL technique principle is that the transmitter launches thousands of test rays in a solid angle and the true path is determined by looking for the rays arriving at the receiver, whereas in classical RT methods the reflected paths by walls and furniture are found by computing the image of the transmitter or of the receiver. These methods are precise but are time-consuming due to inherent computational complexity. When combining with the Uniform Theory of Diffraction (UTD) [Kou74] they are the most frequently applied to radio coverage prediction [Gen09, Son99, Tay09, Son09]. The RT and RL models potentially represent the most accurate and versatile methods for urban and indoor, multipath propagation characterization or prediction. In the rest of this section, different deterministic methods are explained, within which the ray tracing methods are explained in more detail.

FDTD Models

The FDTD method solves Maxwell's equation and provides a complete solution of all the spatial points giving signal-coverage information throughout a given area. FDTD method fully explains the effects of reflection, diffraction and radiation. This method is suitable for studying the wave interaction in the medium and its main advantage is the accuracy. However, it requires plenty of storage space and huge computation to keep track of the solution at all locations, and extensive calculations to update the solution at successive instants of time. Because of this, FDTD is useful only for a small part of the entire modeling environment, due to the computational resources required.

Considering the RT or RL techniques, and FDTD techniques, several advantages and disadvantages can be presented. In the literature, some works have been found combining these two technologies for wireless communication channel modeling. In [Wan00] a hybrid technique is proposed, based on combining a RT method with an FDTD method. The philosophy was to use RT to analyze wide areas, and FDTD to study areas near structures with complex material properties, where ray-based solutions are not sufficiently accurate. In [Thi09], a full 3-D hybrid method is presented which combines full-wave techniques which are used for the analysis of one unit cell of inhomogeneous periodic walls with a RF field calculation for the interaction between the walls. Reference [Thi08] presents the same work for a hybrid method for indoor wave propagation modeling where the theory and the implementation are presented for the 2D case.

Moment-Method Models (MoM)

The MoM model is appropriate when high precision is required and when the size of the buildings is small. The solutions determined by the MoM are numerically exact, as long as the segmentation of the objects is small enough. Due to the limitations of the computer memory and CPU time, the MoM is usually applied for analyzing smaller objects in wavelengths. In the literature, it can be found the combination of MoM with RT methods exploiting the advantages of each of them [Yan98, Bac96]. In [San97], a hybrid approach is presented, combining the RT method and the MoM for material objects, which was developed to study indoor wave propagation, penetrations, and also scattering due to periodic structures in buildings.

Ray Tracing Methods

Ray theory is an accurate site-specific method which is emerging as a highly promising technique to obtain useful simulation results. Ray tracing is a technique based on Geometrical Optics (GO) and Geometrical Theory of Diffraction (GTD) that can easily be applied as an approximate method for estimating the levels of high-frequency electromagnetic fields. GO principle is that energy can be considered to be radiated through infinitesimally small tubes, often called rays. These rays are normal to the surface of equal signal power. They lie along the direction of propagation and travel in straight lines. Therefore, signal propagation can be modeled via ray propagation. By using the concept of ray tracing, rays can be launched from a transmitter location, and the interaction of the rays can be described using the well-known theory of refraction and reflection and

interactions with the neighboring environment. The rays considered in GO are only direct, reflected and refracted rays. Because of this, abrupt transition areas may occur, corresponding to the boundaries of the regions where these rays exist. To complement the GO theory, the diffracted rays can be introduced with the GTD and its uniform extension, the Uniform GTD (UTD). The purpose of these rays is to remove the field discontinuities and to introduce proper field corrections, especially in the zero-field regions predicted by GO.

The advantage of this model is that it is very accurate, but it is relatively slow in operation, so that preprocessing and simplification must be applied. The details of the location geometry of obstacles and the electromagnetic parameters of all the materials are required accurately. The deterministic ray modeling approach is based generally on putting the transmitter and receiver as a reference point in the three-dimensional coordinate system. The indoor walls, ceilings and floors are defined as a plane with dielectric constant and thickness, whose surfaces are processed as plane sections. The simulation path is composed by those rays emitted from the transmitter through walls, ceilings, floors, tables and other objects, reflected and reaching the receiver through these objects. In Chapter 3, a detailed description of the in-house developed 3D ray launching algorithm employed to perform coverage predictions in complex indoor environments is given.

The image method is a simple and accurate method for determining the ray trajectory between the transmitter and the receiver. Figure 2.10 represents the basic idea of the image method [Isk02]. For this simple case, firstly the image of the transmitter 1 (Tx1) due to the Wall1 (W1) is determined. Then, it is calculated the image of Tx1 due to Wall2 (W2), (Tx2). A reflection point (P2) can be found connecting Rx and Tx2. Connecting P2 and Tx1 another reflection point (P1) can be found. The image method is efficient, but it can only handle simple environments. Many environments with which we are concerned in our daily life are complicated, and the conventional image method is not adequate. For realistic applications, special techniques such as the hybrid and acceleration methods have to be used to reduce the computation time.
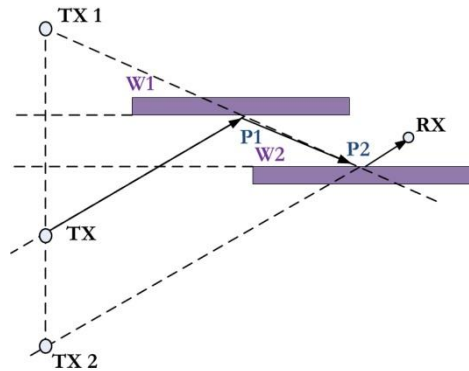
Figure 2.10. Illustration of the Image Method.

The ray-tracing method is simple and it is most widely used in the area of site-specific propagation prediction. However, it can be very computationally inefficient, leading to efforts focused on the acceleration of ray-tracing algorithms. In [Kel62] ray tracing is accelerated considerably by using the Angular Z-Buffer (AZB) technique. The philosophy behind this method consists in reducing the number of rigorous tests that have to be made by reducing the number of facets that each ray has to treat. The AZB consists in dividing in angular regions the space seen from the source and storing the facets of the model in the regions where they belong. In this way, for each ray, only the facets stored in its region need to be analyzed. This method can accelerate the ray-tracing algorithm, but, when multiple reflections are needed, the preprocessing is not easy. Liang and Bertoni proposed in [Lia98] the Vertical-Plane-Launch (VPL) technique for approximating a full three dimensional (3D) site-specific ray trace. The VPL technique employs the standard shoot and bounce method [Lin89] in the horizontal plane while using a deterministic approach to find the vertical displacement of the unfolded ray paths. This approximation is valid since buildings walls are almost always vertical. The method consists on employing the usual 2D ray tracing in the horizontal plane and each ray in the 2D case represents a vertical propagation plane. When a ray hits a vertical wall, reflection from the vertical wall and diffraction from the rooftop horizontal edge can occur. When the ray hits a vertical edge, diffraction also occurs. The over-rooftop diffraction creates two vertical propagation planes, one in the same direction as the incident ray and the other in the direction of reflection. Diffraction from the vertical edges creates a new source and many new rays in 2D planes should be launched.

The work in [Lia98] introduces the scale-level concept to assess some criteria for a useful and interesting comparison between measurement and ray-tracing simulation. They analyze the validity domain of the ray-tracing tool and the degree of accuracy of the prediction as a function of the scale level. The scale levels are related to the extent of the spatial regions representing the basic elements from which propagation parameters are extracted. The basic spatial regions can be grouped according to their characteristics at any scale level, from the smaller (a point at space) to a whole class of buildings. In [Lin89], an enhanced ray-launching model is proposed to improve the efficiency and the speed of computation of propagation characteristics. Two methods are used to obtain the improvements: the first one is the effective propagation area method, which restricts the propagation region to be considered when the wave propagation characteristics are predicted. This method considers only the buildings included in the effective propagation area, which is defined as the region where the buildings which have dominant effects on the propagation characteristics are distributed. In the suggested model, the boundary of the effective propagation area (EPA) is defined in terms of the average delay time and the RMS delay spread of the received signal. The second method is the dominant corner extraction method, which is used to diminish the amount of the diffraction ray computation by considering only the particular building corners which have a significant influence on the received power. In the ray-tracing process of the ray-launching model, each building corner operates as a diffraction wedge and the corresponding diffracted ray paths are obtained by applying the ray-launching method in which the corners are regarded repeatedly as new transmitters and receivers. As a result, the actual number of base stations to be considered increases with the number of the building corners. However, there exist dominant rays which provide most of the power and have a significant influence on the delay spread. In the dominant corner extraction method, the corners on which the dominant rays are diffracted are picked out and taken into calculation. Rappaport and colleagues explain in [Rap96] a new 3D ray tracing technique that reduces kinematic errors associated with ray launching algorithms based on the reception sphere and distributed wave fronts methods. In their method, a sphere, centered on a candidate receiver location and sized according to the angular separation of the incoming rays, collects the rays that contribute to the overall electric field. The radius for a reception sphere sweeps out a circular area across the adjacent rays, but sometimes two rays fall within the sphere, which lead to double count errors. Distributed wave front methods increase the accuracy of 3D ray tracing by eliminating the kinematic errors of double-counting while maintaining simplicity and speed.

The main drawback of ray propagation modeling is lengthy computation time due to 3D space analysis. This has given rise to the proposal of hybrid methods which are a combination of different methods to accelerate and improve efficiency of ray-tracing models. In [Ros02] Rossi and Gabillet presents the Geometrical Ray Implementation for Mobile Propagation Modeling (GRIMM). In their approach, the ray construction mixes two techniques by splitting the 3D problem into two successive 2D stages, without loss of generality compared with the full 3D techniques. The first stage uses the basis of ray launching while the second stage uses ray tracing. A Shooting-and-Bouncing-Ray (SBR) and image method is proposed in [Mac93]. A deterministic approach using a modified SBR technique denoted as the SBR/Image method is developed in the work to deal with the radio wave propagation in furnished rooms which are composed of triangular facets. Conceptually, they use the SBR method to trace triangular ray tubes (not rays) bouncing in the room. If the Rx is within a ray tube, the ray tube will have a contribution to the received field at Rx and the corresponding equivalent source (image) can be determined. Besides, the first-order wedge diffraction from furniture is included, and the diffracted rays also can be attributed to the corresponding images. By summing all contributions of these images, the total received field at Rx can be obtained.

2.3 Summary

In the first part of this chapter, an overview of different short-range wireless communication systems has been presented. It has been explained the reasons why before the deployment of a wireless network, radio-planning analysis with an efficient propagation prediction approach becomes necessary. After that, a complete survey of different propagation models which have been used in the literature has been presented. A summary of various propagation models dealing with path loss is shown in Table 2.2, showing that Ray Tracing methods lead to a reasonable trade-off between accuracy and computational time of simulations.

Table 2.2. Comparison of different Path Loss Propagation models.

Model Name	Suitable Environment	Complexity	Details of Environment	Accuracy	Time
Free Space Model	Macrocell	Simple	No	Good	Little
Diffracting Screens Model	Macrocell	Simple	No	Good	Little
Okumura Model	Macrocell	Simple	No	Good	Little
Hata Model	Macrocell (early cellular)	Simple	No	Good	Little
COST-231	Microcell (outdoor)	Simple	No	Good	Little
Ray-Tracing	Outdoor and Indoor	Complex	Yes	Very good	Very much
FDTD	Indoor (small)	Complex	Every detail	Best	Very much
MoM	Indoor (small)	Complex	Every detail	Best	Very much

35

Bibliography of the Chapter

[Bac96] B. De Backer, H. Borjeson, F. Olyslager and D. De Zutter, "The study of wave-propagation through a windowed wall at 1.8GHz," *IEEE 46th Vehicular Technology Conference, Mobile Technology for the Human Race*, vol. 1, pp. 165-169, 1996.

[Bla09] J. Blas Prieto, R. M. Lorenzo Toledo, P. Fernández Reguero, E. J. Abril, A. Bahillo Martínez, S. Mazuelas Franco, and D. Bullido, "A new metric to analyze propagation models", *Progress in electromagnetics research*, vol. 91, pp. 101-121, 2009.

[Blu10] *Specification of the Bluetooth System, Covered Core Package*, Version 4.0; The Bluetooth Special Interest Group: Kirkland, WA, USA, 2010.

[Bul57] K. Bullington, "Radio propagation fundamentals," *Bell Syst. Tech. J.*, 36: 593, 1957.

[Bul77] K. Bullington, "Radio Propagation for vehicular communications," *IEEE Transactions on Vehicular Technology*, vol. 26, nº 4, pp. 295-308, 1977.

[Dim06] A. G. Dimitriou and G. D. Sergiadis, "Architectural features and urban propagation", *IEEE Trans. Antennas and Propag.*, vol 54, no. 3, pp. 774-784, 2006.

[Fra04] M. Franceschetti, J. Bruck and L. J. Schulman, "A random walk model of wave propagation", *IEEE Trans. Antennas and Propag.*, vol. 52, no. 5, pp. 1304-1317, 2004.

[Fri46] H. T. Friis, "A note on a simple transmission formula," *proc. IRE*, 34(5): 254-256, 1946.

[Gen09] G. Gennarelli and G. Riccio, "A uapo-based model for propagation prediction in microcellular environments", *Progress in Electromagnetics Research B.*, vol 17, pp. 101-116, 2009.

[Gom12] C. Gomez, J. Oller, J. Paradells, "Overview and Evaluation of Bluetooth Low Energy: An Emerging Low Power Wireless Technology," *Sensors,* 2012, nº 9, pp. 11734-11753.

[Has08] A. Hashimoto, H. Yourshino and H. Atarashi, "Roadmap of IMT-Advanced Development," *IEEE Microwave Magazine*, vol. 9, nº 4, pp. 80-88, 2008.

[Hat80] M. Hata, "Empirical formula for propagation loss in land mobile radio services," *IEEE Transactions on Vehicular Technology*, vol. 29, nº 3, pp. 317-325, 1980.

[Her99] J. M. Hernando and F. Pérez-Fontán, "Introduction to mobile communications engineering," *Artech House*, 1999.

[Huf82] G. A. Hufford, A. G. Longley, W. A. Kissick, "A Guide to the Use of the ITS Irregular Terrain Model in the Area Prediction Mode," *US Dept. of Commerce, National Telecommunications and Information Administration*, United States, 1982.

[Int15] Into the 3GPP Evolve Packet System. Available online (2015, March 25): http://www.in2eps.com/3g0/tk-3gpp-netarch-113.html

[Isk02] M. F. Iskander and Z. Yun, "Propagation prediction models for wireless communication systems," *IEEE Microwave Theory and Techniques*, vol. 50, nº 3, pp. 662-673, 2002.

[Kan97] A. G. Kanatas, I. D. Kountouris, G. B. Kostaras and P. Constantinou, "A UTD propagation model in urban microcellular environments", *IEEE Trans. Veh. Tech.*, vol. 46, nº 1, pp. 185-193, 1997.

[Kel62] J. B. Keller, "Geometrical Theory of Diffraction," *Journal of the Optical Society of America*, vol. 52, nº 2, pp. 116-130, 1962.

[Kou74] R. G. Kouyoumjian and P. H. Pathak, "A uniform theory of diffraction for an edge in a perfectly conducting surface", IEEE *Proc.*, vol. 62, nº 4, pp. 1448-1462, 1974.

[Lee00] D. J. Y. Lee and W. C. Y. Lee, "Propagation prediction in and through buildings", *IEEE Trans. Veh. Tech.*, vol. 49, nº 5, pp. 1529-1533, 2000.

[Lee09] S. H. Lee, "A photon modeling method for the characterization of indoor optical wireless communication", *Progress in Electromagnetics Research*, vol. 92, pp. 121-136, 2009.

[Lia98]   G. Liang and H. L. Bertoni, "A new approach to 3D ray tracing for propagation prediction in cities," *IEEE Transactions on Antennas and Propagation*, vol. 46, nº 6, pp. 853-863, 1998.

[Lin89]   H. Ling, R. C. Chou and S. W. Lee, "Shooting and Bouncing rays: calculating the RCS of an arbitrary shaped cavity," *IEEE Transactions on Antennas and Propagation*, vol. 37, nº 2, pp. 194-205, 1989.

[Lon68]   A. G. Longley and P. L. Rice, "Prediction of tropospheric radio transmission loss over irregular terrain, a computer method," *ESSA Technical Report, ERL-79-ITS67*, Boulder, Colorado, 1968.

[Mac93]   L. R. Maciel, H. L. Bertoni and H. N. Xia, "Unified approach to prediction of propagation over buildings for all ranges of base station antenna height," *IEEE Transactions on Vehicular Technology*, vol. 42, nº 1, pp. 42-45, 1993.

[Oku68]   Y. Okumura, E. Ohmori, T. Kawano and K. Fukuda, "Field strength and its variability in VHF and UHF land-mobile radio service," *Rev. Elec. Commun. Lab*, vol. 16, nº 9, pp. 825-873, 1968.

[Par00]   J. D. Parsons and P. J. D. Parsons, "The mobile radio propagation channel," vol. 81, *Wiley Online Library*, 2000.

[Par89]   J. D. Parsons and J. G. Gardiner, "Mobile communication systems," *Halsted Press*, 1989.

[Rap96]   T. S. Rappaport, "Wireless communications: principles and practice," *Prentice Hall PTR,* New Jersey, 2996.

[Ros02]   J. P. Rossi and Y. Gabillet, "A mixed ray launching/tracing method for full 3D UHF propagation modeling and comparison with wide-band measurements," *IEEE Transactions on Antennas and Propagation*, vol. 50, nº 4, pp. 517-523, 2002.

[Sae00]   F. Saez de Adana, G. Blanco, G. Diego, P. Arriaga and M. F. Cátedra, "Propagation model based on ray tracing for the design of personal communication systems in indoor environments," *IEEE Transactions on Vehicular Technology*, vol. 49, nº6, pp. 2105-2112, 2000.

[San97] Z. Sandor, L. Nagy, Z. Szabo and T. Csaba, "3D Ray Launching and moment method for indoor radio propagation purposes," *The 8th IEEE International Symposium on Personal, Indoor and Mobile Radio Communications*, vol. 1, pp. 130-134, 1997.

[Sch97] J. W. Schuster and R. J. Luebbers, "Comparison of GTD and FDTD predictions for UHF radio wave propagation in a simple outdoor urban environment", *IEEE Antennas and Propag. Society International Symposium*, vol. 3, pp. 2022-2025, 1997.

[Sei94] S. Y. Seidel, T. S. Rappaport, "Site-Specific Propagation Prediction for Wireless In-Building Personal Communication System Design", *IEEE Transactions on Vehicular Technology*, vol. 43, nº 4, pp. 879-891, 1994.

[Son09] H. B. Song, H. G. Wang, K. Hong and L. Wang, "A novel source localization scheme based on unitary esprit and city electronic maps in urban environments", *Progress In Electromagnetics Research*, vol. 94, pp. 243-262, 2009.

[Son99] H. W. Son and N. H. Myung, "A deterministic ray tube method for microcellular wave propagation prediction model", *IEEE Trans. Antennas and Propag.*, vol 47, nº 8, pp. 1344-1350, 1999.

[Tan96] S. Y. Tan and H. S. Tan, "A microcellular communications propagation model based on the uniform theory of diffraction and multiple image theory", *IEEE Trans. Antennas and Propag.*, vol 44, nº 10, pp. 1317-1326, 1996.

[Tay09] A. Tayebi, J. Gómez, F. S. de Adana and O. Gutierrez, "The application of arrival and received signal strength in multipath indoor environments", *Progress In Electromagnetics Research*, vol. 91, pp. 1-15, 2009.

[Thi08] M. Thiel and K. Sarabandi, "A hybrid method for indoor wave propagation modeling," *IEEE Transactions on Antennas and Propagation*, vol. 56, nº 8, pp. 2703-2709, 2008.

[Thi09] M. Thiel and K. Sarabandi, "3D wave propagation analysis of indoor wireless channels utilizing hybrid methods," *IEEE Transactions on Antennas and Propagation*, vol. 57, nº 5, pp. 1539-1546, 2009.

[Wal88] J. Walfisch and H. L. Bertoni, "A theoretical model of UHF propagation in urban environments," *IEEE Transaction on Antennas and Propagation*, vol. 36, nº 12, pp. 1788-1796, 1988.

[Wan00] Y. Wang, S. Safavi-Naeini and S. K. Chaudhuri, "A hybrid technique based on combining ray tracing and FDTD methods for site-specific modeling of indoor radio wave propagation," *IEEE Transactions on Antennas and Propagation*, vol. 48, nº 5, pp. 743-754, 2000.

[Wan14] C. X. Wang, F. Haider, X. Gao, X. H. You, Y. Yang, D. Yuan, H. M. Aggoune, H. Haas, S. Fletcher, E. Hepsaydir, " Cellular Architecture and Key Technologies for 5G Wireless Communication Networks," *IEEE Communications Magazine*, vol. 52, nº 2, pp. 122-130, 2014.

[Yan98] C. F. Yang, B. C. Wu and C. J. Ko, "A ray-tracing method for modeling indoor wave propagation and penetration," *IEEE Transactions on Antennas and Propagation*, vol. 46, nº 6, pp. 907-919, 1998.

Chapter 3

The Ray Launching Technique

With the growing demand of wireless communication systems, an efficient and accurate tool to assist wireless system design and determine the coverage range of a cellular base station in a metropolitan area or the required transmit power of a wireless network in a typical office environment, becomes highly necessary. Because of that, a deterministic approach has been developed in this thesis with the aim to achieve an adequate propagation prediction in complex indoor scenarios with an affordable computational time. For this purpose, a 3D Ray Launching (RL) code has been developed based on Geometrical Optics (GO) and the Uniform Theory of Diffraction (UTD). A detailed description of the algorithm, together with a brief history of its principle and its implementation, are presented in this chapter.

3.1 Geometrical Optics and Uniform Theory of Diffraction (GO/UTD)

The first study of light phenomenon was originated in Greece, with an attempt to find a mathematical and geometrical explanation to the propagation using observation [Har61]. With the development of optical instruments and significant discoveries, such as the refraction law (Snell) and Fermat's principle [Kel85], the optics field expanded greatly in the sixteenth century and at the beginning of the seventeenth century. Based on these theories, all the

mathematics underlying optics were established and are called classical GO [Bor75].

The appearance of Maxwell's equations in 1864 marks a clear evolution in electromagnetic theory, and their results are applicable to wave propagation and consider light to be a high-frequency electromagnetic wave. Sommerfield and Range, based on mathematical and physical concepts derived from Poincaré's work [Poi86], were the pioneers who linked Maxwell's equations with the GO laws by introducing the notion of an asymptotic series. The extension of this work to vector fields by Luneberg [Lun44] and Kline [Kli51] led to the modern version GO, which proves that GO expressions correspond to the first term of an asymptotic series.
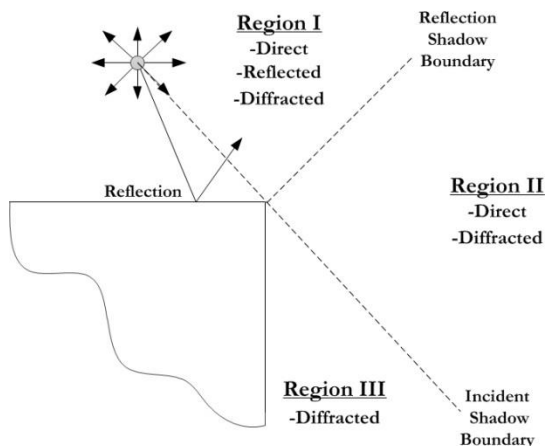
Figure 3.1. Example of the different regions defined by GO rays.

However, GO only approach presents the problem of shadow areas created by edges and discontinuities because it is unable to predict the field in these areas, as it is shown in Figure 3.1. This is because the rays considered in GO are only direct, reflected and refracted rays, leading to the existence of abrupt areas, corresponding to the boundaries of the regions where these rays exist. This problem was initially solved by Keller [Kel62, Kel56] by introducing diffraction phenomenon. Keller stated that the diffracted rays behave as GO rays once they leave the edge, and their path can be obtained by generalizing Fermat's principle [Kel85]. Nevertheless, the original formulation developed by Keller presented some problems in the shadow and reflection boundaries where the GO fields present discontinuities. These problems were solved with uniform solutions to

the asymptotic expressions that Keller used to develop his theory. The first one is the UTD developed by Kouyoumjian and Pathak [Kou74] from the asymptotic expansion by Pauli Clemmow [Cle50], whereas the second one is the Uniform Asymptotic Theory (UAT) obtained by Lee and Deschamps [Lee76]. The main benefit of the UTD is that it is numerically easier to implement compared to the UAT because the UAT obtains the fields by subtracting two terms whose values are infinite at the shadow boundaries. Thus, the UTD has been, historically, more widely used, and therefore, it has been selected to be implemented in the in-house developed 3D RL code.

3.2   The Algorithm

The development of the work of this thesis starts with a basic 3D RL algorithm implemented in the Public University of Navarre (UPNA). This basic algorithm is based in GO and considers only reflection and refraction phenomenon. Figure 3.2 represents the starting point and the performance analysis developed during the work of this thesis to achieve an enhanced 3D RL algorithm.

The main challenges of the RL performance analysis and the solutions adopted in this thesis are presented in Table 3.1, following by the detailed description of the algorithm in next paragraphs.
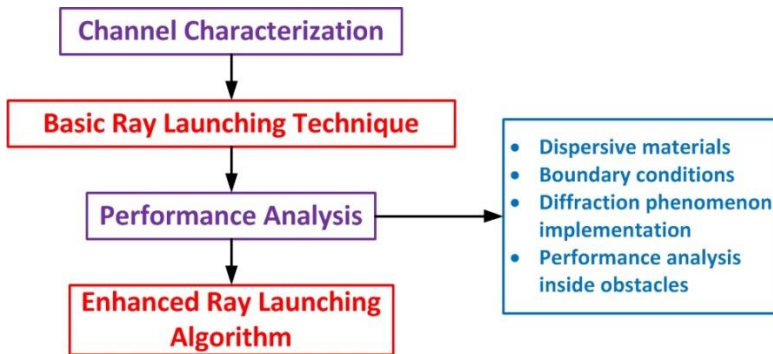
Figure 3.2. Development of the Enhanced RL algorithm.

Table 3.1. Challenges and Solutions of the RL Performance Analysis.

Ray Launching Performance Analysis	
Challenges	**Solutions**
-To achieve a commitment between accuracy results and computational time.	-Convergence analysis to find the optimal input parameters of angular and spatial resolution, number of reflections and number of diffracted rays.
-Characterization of the dispersive nature of different materials.	-Creation of a material properties catalog with the conductivity and dielectric constant of each material for different frequencies.
-Implementation of more electromagnetic phenomena in the algorithm.	-Diffraction phenomenon implementation. -Scattering by water surfaces implementation. -Scattering for environments with high obstacles density.
-Dosimetric analysis.	-Modularization to save the parameters of the electromagnetic waves within the obstacles (human beings) with the consideration of several reflections inside the obstacles.
-Acceleration techniques to obtain accurate results with affordable computational time.	-New hybrid acceleration techniques: RL-NN and RL-DE.
-Mobile channel modeling.	-Implementation of a new module which capture the non-stationarity of the channel.

The enhanced 3D RL algorithm is based on GO and Geometrical Theory of Diffraction (GTD)[Azp14]. Different applications of this algorithm can be found in the literature, like the analysis of wireless propagation in closed environments [Azp12, Mor12, Naz12, Ses14, Led13], interference analysis [Itu12] or electromagnetic dosimetry evaluation in wireless systems [Agu12]. The ray-launching method considers a bundle of transmitted rays that may or may not reach the receiver. The available spatial resolution and the accuracy of the model are determined by the number of rays considered and the distance from the transmitter to the receiver location. The basic idea is that a finite sample of the possible directions of the propagation from the transmitter is chosen and a ray is launched for each such direction. If a ray hits an object, then a reflecting ray and a refracting ray are generated. If a ray impact with an edge, then a family of diffractive rays is generated.

The algorithm has been designed for evaluating the wireless communication in an indoor environment. Hence, this algorithm has the following features:

- Recreation of a realistic multipath scenario.
- Three-dimensional modeling of all types of rooms with different shapes and sizes.
- Creating of complex environments as large as desired, with multiple plants and multiple buildings.
- Characterization and modeling of any objects (windows, tables, chairs, walls, etc.) through its three-dimensional shape and dielectric constant.
- Modeling of reflection, refraction and diffraction.
- Calculation of the interaction between rays and objects taking into account the polarization wave.
- Modeling of any transceiver.
- Duration of the simulation of a ray determined by the number of reflections and the maximum delay.
- Analysis of the scenario by extracting parameters such as electric field strength, signal/interference, power delay, dispersion, and so on.

The use of advanced radioplanning tools, such as the 3D RL algorithm is usually divided into three phases:

1. **Phase 1**: Creating the scenario. This phase sets the scenario, consisting in rooms with objects and the transmitters and receivers.
2. **Phase 2**: Simulation of ray tracing in three dimensions. In this phase, the rays are launched from each transmitter, keeping the parameters in each position in space.
3. **Phase 3**: Analysis of the results. In this phase, the values are obtained from the simulation to calculate the desired parameters.

3.2.1   Creation of the scenario

The scenario is created with the information which characterized the room and the objects in it, the interconnections of the different rooms and all the information which characterizes the transmitters and receivers.

45
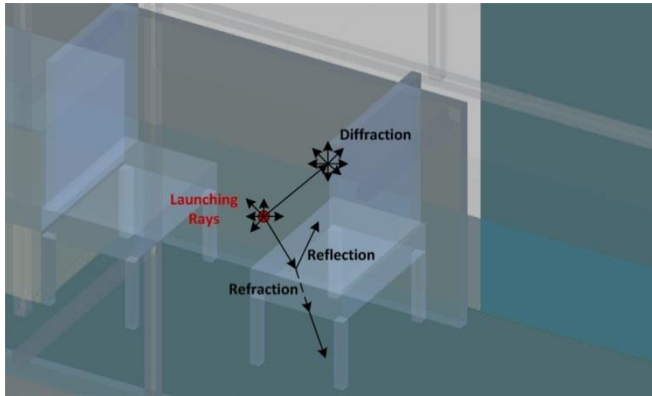
Figure 3.3. Typical scenario with the rays launched from the transmitter

The room's characterization is given by its size. In this algorithm, the rooms are defined as different hexahedra with different dimensions in the x-axis, y-axis and z-axis. Besides, the material which is in the room can be defined. Normally, this material is air, but it is possible to consider any material for the room.

Complex forms can be created by interconnection of several hexahedral. Moreover, the fact of dividing an environment in multiple hexahedra gives the possibility to analyze each room with different resolution, providing more flexibility. Each room is divided into multiple hexahedra and the parameters of the ray that arrive to each hexahedron are stored. Thus, the resolution in each axis of each room is defined as the number of hexahedra of that axis. So, each room is divided into multiple equi-dimensional hexahedra and the precision of each axis can be chosen. Figure 3.3 represents a typical office with the rays launched from the transmitter.

Objects are defined as different hexahedra in the algorithm. By this basic geometric shape it is very easy to form another objects much more complex, such as tables, chairs and shelves, and placing them into the room. In a generic room, walls can be formed by windows, doors, frames, etc. Therefore, to characterize the walls of a room, each discontinuity on the wall must be characterized. This will define each part of the wall like an object by its central position on the wall, the width in each dimension and the material that is made of. Rooms are created individually and they are interconnected with the interconnection matrix, which defines the portion of wall of a room that is connected with the wall portion of another room.

In the creation of the scenario, transmitters are defined in a generic way. Thus, performing a single simulation of phases 1 and 2, the parameters of the transceiver, like the radiated power and the directivity of the antennas, can vary in phase 3, saving a lot of calculation time. Therefore, each transceiver can be defined with the following parameters:

- Location: Room and coordinates.
- Number of launching rays and directions.
- Maximum number of reflections of the rays.
- Maximum delay of the rays.
- Frequency of emission fc.
- Radiated power P_r)
- Directivity $D(\theta, \emptyset)$
- Polarization $X^\perp, X^\parallel)$

A receiver is modeled taking into account that it absorbs the rays that come to it in certain directions. Therefore, to define a receiver the following parameters are characterized:

- Location: room and coordinates.
- Angular range in which the receiver absorbs the rays.

Besides, in this phase of simulation there are several options to be chosen like the calculation of parameters inside the obstacles. This option is useful to analyze the radiated power inside a certain object, for example, a human body. Nevertheless, the different materials of the objects are always taken into account. Consideration of diffraction or not can also be chosen in this phase of the algorithm. A trade-off between computational time and accuracy of results must be chosen to obtain best results of the simulation.

3.2.2   3D Ray Launching Simulation

In this phase, the rays are launched from each transmitter. These rays propagate through the space interacting with the obstacles in their path, causing physical phenomena such as reflection, refraction and diffraction. The parameters of these rays are stored as they enter to each hexahedron until the ray has a certain number of reflections or it has exceeded the pre-propagation time set. RL techniques are based on identifying a single point on the wave front of the

radiated wave with a ray that propagates along the space following a combination of optics and electromagnetic theories, as it is illustrated in Figure 3.4.

The algorithm works in an iterative manner, considering a ray and its reflections, storing the created ray for processing later the phenomenon of diffraction.

The 3D RL algorithm has three recurrent steps. The first step is to take all the antennas of the same room and introduce them to simulate. The second step is to simulate the room, and the third step is to transform the rays coming out of the room in new antennas in other rooms.
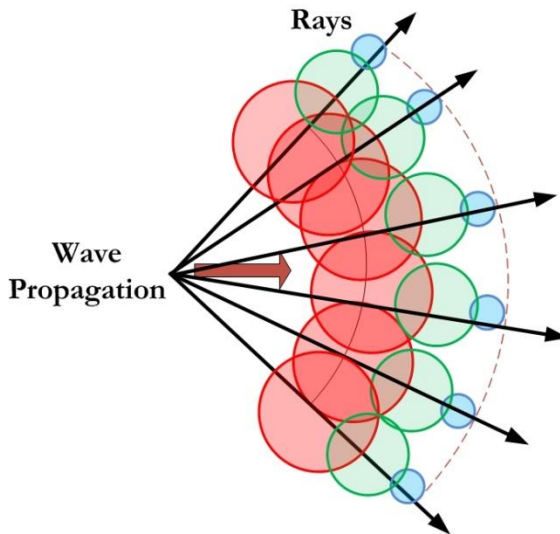
Figure 3.4. Wave front propagation with rays associated with single wave front points.

Figure 3.5 shows the different steps of the algorithm. The most important ones are the following:

- Calculating the impact point.
- Tour starting at the initial point to the point of impact storing the parameters.
- Calculation of the reflected ray.
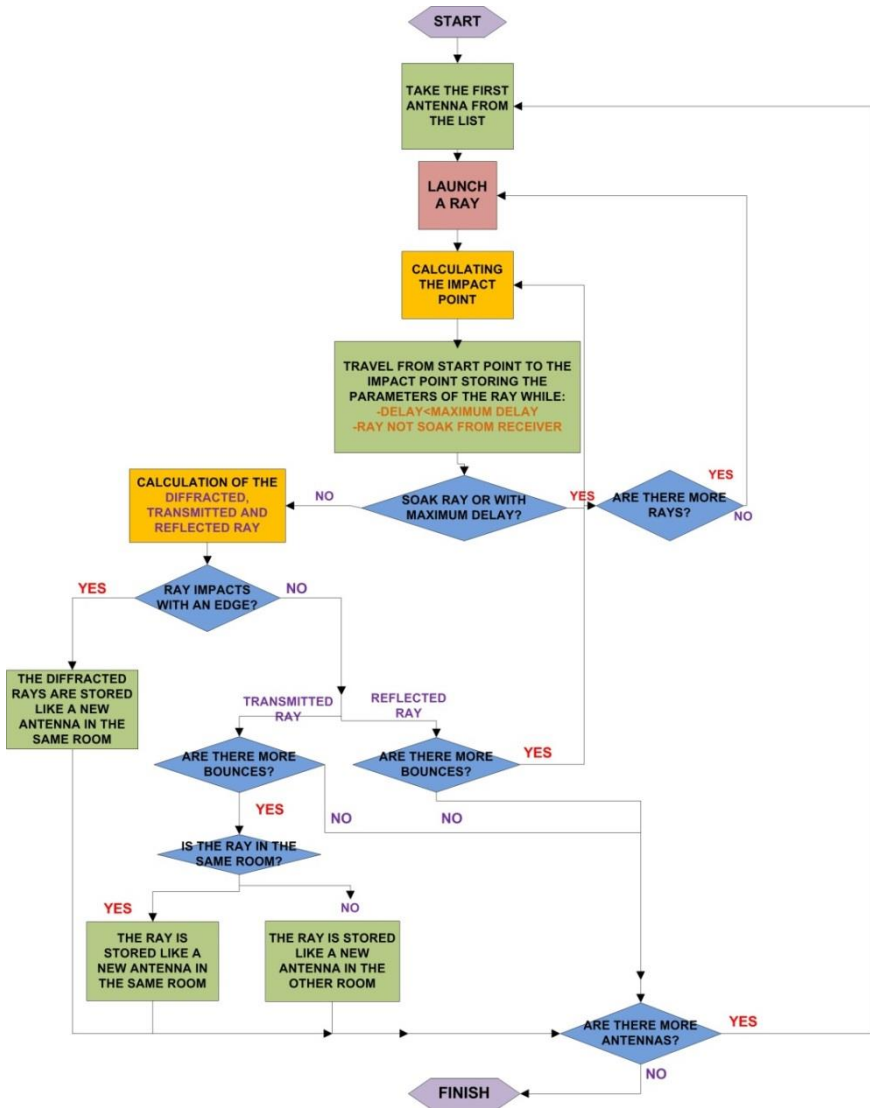
Figure 3.5. Functional diagram of the 3D Ray Launching Algorithm.

- Calculation of the transmitted ray.
- Calculation of the diffractive rays.

The calculation of the impact point has been done decomposing the three-dimensional problem in one dimensional problems, calculating the propagation velocities in each axis.

$$V_x = V_p \, sin(\theta_0) \, cos(\emptyset_0)$$

$$V_y = V_p \, sin(\theta_0) \, cos(\emptyset_0)$$

$$V_z = V_p \, cos(\theta_0)$$

(3.1)

where $V_p = c/n$. The impact happens in the first instant of time that the three projections are in the range of the projection of the obstacle. If it does not impact with any obstacles, the algorithm calculates in the same way the point of impact with the wall.

Once the point of impact is calculated, it is necessary to follow the straight line joining the initial point (x_i, y_i, z_i) and the final impact point (x_f, y_f, z_f) saving the parameters of each ray. It is important to emphasize that a grid is defined in the space to save the parameters of each ray. Accordingly, the environment is divided into a number of cuboids of a fixed size. When a ray enters a specific hexahedron, its parameters are saved in a matrix. Parameters such as frequency of operation, radiation patterns of the antennas, number of multipath reflections, separation angle between rays and cuboid dimension can be modified in the algorithm. The information stored in each hexahedron that the ray passes in its trajectory is:

- Time taken from the ray to arrive τ)
- Distance traveled by the ray d)
- Loss coefficient in each polarization $L^{\perp}, L^{\parallel}$)
- Ray direction in the transmitter θ_t, ϕ_t)
- Ray direction in the receiver θ_r, ϕ_r)
- Transmitting antenna n)
- Diffraction
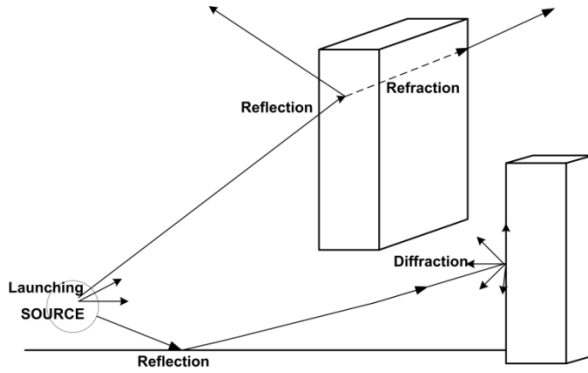
Figure 3.6. Principle of RL method: reflection, transmission and diffraction.

Figure 3.6 represents the phenomena of reflection and transmission when the ray impacts with an obstacle and the diffraction phenomena when the ray impacts with an edge.
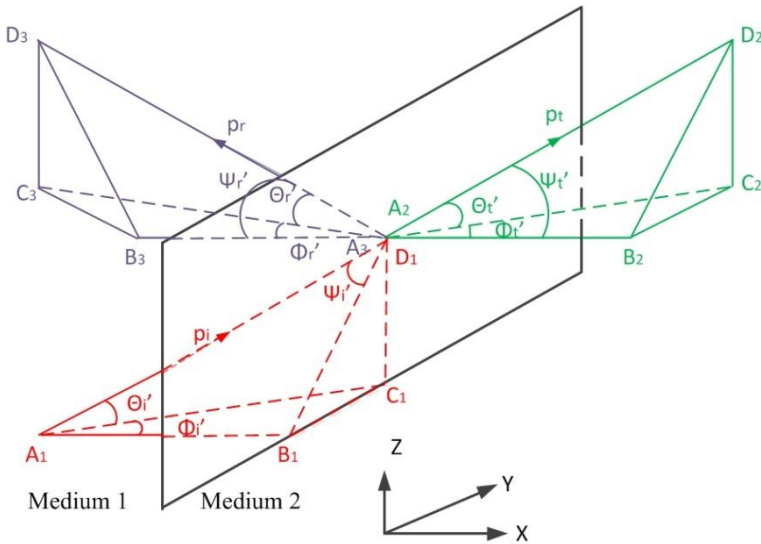
Figure 3.7. Reflection and transmission by plane interface at the oblique wave incidence.

A plane electromagnetic wave falling to the planar interface between two regular semi-infinite media 1 and 2 gives rise to two plane waves: reflected and

transmitted (or refracted). According to the Snell's law [Hri00], the reflection coefficient $R^\perp$ and transmission coefficient $T^\perp$ are calculated by

$$T^\perp = \frac{E_t^\perp}{E_i^\perp} = \frac{2\eta_2 cos(\psi_i)}{\eta_2\,cos(\psi_i) + \eta_1 cos(\psi_t)} \tag{3.2}$$

$$R^\perp = \frac{E_r^\perp}{E_i^\perp} = \frac{\eta_2\,cos(\psi_i) - \eta_1\,cos(\psi_t)}{\eta_2\,cos(\psi_i) + \eta_1 cos(\psi_t)} \tag{3.3}$$

where $\eta_1 = 120\pi/\sqrt{\varepsilon_{r1}}$, $\eta_2 = 120\pi/\sqrt{\varepsilon_{r2}}$, and ψ_i, ψ_r and ψ_t are the incident, reflected and transmitted angles respectively. For the parallel (or magnetic) polarization the magnetic field vector of the incident wave is perpendicular to the plane of incidence. Then, the reflection and transmission coefficients $R^\parallel$ and $T^\parallel$ can be calculated by

$$R^\parallel = \frac{E_r^\parallel}{E_i^\parallel} = \frac{\eta_1\,cos(\psi_i) - \eta_2\,cos(\psi_t)}{\eta_1\,cos(\psi_i) + \eta_2 cos(\psi_t)} \tag{3.4}$$

$$T^\parallel = \frac{E_t^\parallel}{E_i^\parallel} = \frac{2\eta_2\,cos(\psi_i)}{\eta_1\,cos(\psi_i) + \eta_2 cos(\psi_t)} \tag{3.5}$$

Once the parameters of transmission T and reflection R are calculated, and the angle of incidence ψ_i and ψ_t, the new angles (θ_r, ϕ_r) of the reflected wave and $\theta_t, \phi_t)$ of the transmitted wave can be calculated. A general case where a ray impinges with an obstacle with $(\theta_i', \emptyset_i')$ angles is represented in Figure 3.7. Taking into account all the possible angles of incidence, the new angles for the reflected and transmitted wave are calculated, as it is shown for a general case in Figure 3.7.
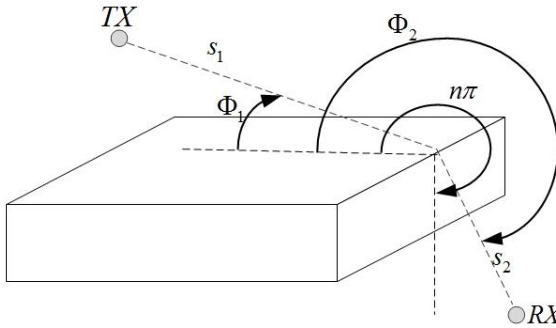
Figure 3.8. Geometry for wedge diffraction coefficients.

The finite conductivity two-dimensional diffraction coefficients are given by [Lue89, Lue98] as

$$D^{\parallel \perp} = \frac{-e^{-j\pi/4}}{2n\sqrt{2\pi k}} \left\{ \begin{array}{l} cot\left(\dfrac{\pi + (\Phi_2 - \Phi_1)}{2n}\right) F(kLa^+ \ \Phi_2 - \Phi_1)) \\ + cot\left(\dfrac{\pi - (\Phi_2 - \Phi_1)}{2n}\right) F(kLa^- \ \Phi_2 - \Phi_1)) \\ + R_0^{\parallel \perp} cot\left(\dfrac{\pi - (\Phi_2 + \Phi_1)}{2n}\right) F(kLa^- \ \Phi_2 + \Phi_1)) \\ + R_n^{\parallel \perp} cot\left(\dfrac{\pi + (\Phi_2 + \Phi_1)}{2n}\right) F(kLa^+ \ \Phi_2 + \Phi_1)) \end{array} \right\} \qquad (3.6)$$

where $n\pi$ is the wedge angle, F, L and a_-^+ are defined in [Lue89], $R_{0,n}$ are the reflection coefficients for the appropriate polarization for the 0 face or n face, respectively. The Φ_2 and Φ_1 angles in (3.6) would refer to the angles in Figure 3.8.

3.2.3   Analysis of Radioplanning Results

In the third phase of the simulation procedure, the results are analyzed using the stored parameters of each ray. The electric field $\vec{E}$ created by an antenna with a radiated power P_{rad} in (θ, ϕ) directions with a directivity $D(\theta, \phi)$ and polarization ratio $X^\perp, X^\parallel)$ at distance d in the free space is calculated by [Agu12]

$$E_i^\perp = \sqrt{\frac{P_{rad}D_t \ \theta_t, \emptyset_t)\eta_0}{2\Pi}} \ \frac{e^{-j\beta_0 r}}{r} \ X^\perp L^\perp \qquad (3.7)$$

$$E_i^\parallel = \sqrt{\frac{P_{rad}D_t \ \theta_t, \emptyset_t)\eta_0}{2\Pi}} \ \frac{e^{-j\beta_0 r}}{r} \ X^\parallel L^\parallel \qquad (3.8)$$

where $\beta_0 = 2\pi f_c\sqrt{\varepsilon_0 \mu_0}$, ε_0=8.854*10^{-12} F/m, μ_0=4π*10^{-7} H/m and η_0=120π Ohms. $L^{\perp \parallel}$ are the path loss coefficients for each polarization ratio $X^\perp, X^\parallel)$. P_{rad} is the radiated power and $D_t(\theta_t, \emptyset_t)$ the transmitter directivity.

The diffracted field is calculated by [Hri00]

$$E_{UTD} = e_0 \frac{e^{-jks_1}}{s_1} D^{\perp \parallel} \sqrt{\frac{s_1}{s_2 \ s_1 + s_2)}} e^{-jks_2} \qquad (3.9)$$

where $D^{\perp\|}$ are the diffraction coefficients in (3.5) and s_1, s_2 are the distances represented in Figure 3.8, from the source to the edge and from the edge to the receiver point.

The received power is calculated at each point taking into account the losses of propagation through a medium (ε, μ, σ) at a distance d, with the attenuation constant α (Np/m), and the phase constant β (rad/m). The received power is calculated with the sum of incident electric vector fields in an interval of time Δt inside each cuboid of the defined mesh. Based on the above theory, the main characteristic of the ray-launching technique is that it provides the impulse response of the channel h (t, f_c ,Δf, d) for each transmitter, at a given carrier frequency, f_c, at a given bandwidth ($f_c \pm \Delta f$), where the materials have a similar response and at a given position. With this information, a stationary channel can be wholly characterized.

3.3 Summary

This chapter presents a detailed description of the in-house developed 3D RL code. The basis and its principle have been explained explicitly. This approach permits radio planning analysis prior to the implementation of a wireless system, leading to accurate results without an expensive campaign of measurements. In the following chapters, results and different applications of the algorithm are presented, achieving good performance when compared with real measurements.

Bibliography of the Chapter

[Agu12] E. Aguirre, J. Arpón, L. Azpilicueta, S. de Miguel, V. Ramos and F. Falcone, "Evaluation of electromagnetic dosimetry of wireless systems in complex indoor scenarios within body human interaction," *Progress In Electromagnetics Research B*, vol. 43, pp. 189-209, 2012.

[Azp12] L. Azpilicueta, F. Falcone, J. J. Astráin, J. Villadangos, I. J. García Zuazola, H. Landaluce, I. Angulo, A. Perallos, "Measurement and modeling of a UHF-RFID system in a metallic closed vehicle," *Microwave and Optical Technology Letters*, vol. 54, Issue 9, pp. 2126-2130, 2012.

[Azp14] L. Azpilicueta, M. Rawat, K. Rawat, F. Ghannouchi and F. Falcone, "Convergence analysis in deterministic 3D Ray Launching radio channel estimation in complex environments," *The Applied Computational* Electromagnetic Society Journal, vol. 29, nº 4, April 2014.

[Bor75] M. Born and E. Wolf. Principles of Optics. *Pergamon*, 1975.

[Cle50] P. C. Clemmow, "Some extensions to the method of integration by steepest descents," *Quart. J. Mech. App. Math.*, 3:241-256, 1950.

[Har61] R. F. Harrington. *Time-Harmonic Electromagnetic Fields*. McGraw-Hill, 1961.

[Hri00] Hristov, Hristo D. "Fresnel Zones in wireless links, zone plate lenses and antennas", *Artech House, Inc.*, 2000.

[Itu12] P. L. Iturri, J. A. Nazábal, L. Azpilicueta, P. Rodriguez, M. Beruete, C. Fernández-Valdivielso and F. Falcone, "Impact of High Power Interference Sources in Planning and Deployment of Wireless Sensor Networks and Devices in the 2.4GHz frequency band in Heterogeneous Environments," *Sensors*, 2012, vol. 12, issue 11, pp. 15689-15708.

[Kel56] J. B. Keller, "Diffraction by a convex cylinder," *IRE Transactions on Antennas and Propagation*, AP-24: 312-321, 1956.

[Kel62] J. B. Keller, "Geometrical theory of diffraction," *J. Opt. Soc. Amer.*, 52: 116-130, 1962.

[Kel85] J. B. Keller, "One hundred years of diffraction theory," *IEEE Transactions on Antennas and Propagation*, vol. 33, nº 2, pp. 123-136, February 1985.

[Kel85] J. B. Keller, "One hundred years of diffraction theory," *IEEE Transactions on Antennas and Propagation*, AP-33(2):123-136, February 1985.

[Kli51] M. Kline, "An asymptotic solution of Maxwell's equations," *Communications on Pure Applied Mathematics*, vol. 4, pp. 225-262, 1951.

[Kou74] R. C. Kouyoumjian and P. H. Pathak, "A geometrical theory of diffraction for an edge in a perfectly conducting surface," *Proceedings of IEEE*, 62(11): 1448-1461, November 1974.

[Led13] S. Led, L. Azpilicueta, E. Aguirre, M. Martínez de Espronceda, L. Serrano, F. Falcone, "Analysis and Description of HOLTIN Service Provision for AECG monitoring in Complex Indoor Environments," *Sensors*, 2013, vol. 13, Issue 4, pp. 4947-4960.

[Lee76] S. W. Lee and G. A. Deschamps, "A uniform asymptotic theory of electromagnetic diffraction by a curved wedge," *IEEE Transactions on Antennas and Propagation*, AP-24:25-34, January 1976.

[Lue89] Luebbers, Raymond J, "A Heuristic UTD Slope Diffraction Coefficient for Rough Lossy Wedges", *IEEE Transactions on Antennas and Propagation*, February, Vol. 37, 1989

[Lue98] Luebbers, Raymond J., "Comparison of Lossy Wedge Diffraction Coefficients with Application to Mixed Path Propagation Loss Prediction", *IEEE Transactions on Antennas and Propagation*, Vol. 36, July 1998.

[Lun44] R. M. Luneberg, "Mathematical Theory of Optics," *Brown University Press*, 1944.

[Mor12] A. Moreno, I. Angulo, A. Perallos, H. Landaluce, I. J. G. Zuazola, L. Azpilicueta, J. J. Astráin, F. Falcone, J. Villadangos, "IVAN: Intelligent Van for the Distribution of Pharmaceutical Drugs," *Sensors*, 2012, vol. 12, pp. 6587-6609.

[Naz12] J. A. Nazábal, P. Iturri López, L. Azpilicueta, F. Falcone and C. Fernández-Valdivielso, "Performance Analysis of IEEE 802.15.4 Compliant Wireless Devices for Heterogeneous Indoor Home Automation Environments," *International Journal of Antennas and Propagation*, Hindawi Publishing Corporation, 2012.

[Poi86] H. Poincaré, "Sur les intégrales irréguliéres des équations linéaires," *Acta Mathematica*, vol. 8, pp. 295-344, 1886.

[Ses14] I. Sesma, L. Azpilicueta, J.J. Astráin, J. Villadangos, F. Falcone, "Analysis of challenges in the application of deterministic Wireless cannel modelling in the implementation of WLAN-based indoor location system in large complex scenarios," *Int. J. Ad Hoc and Ubiquitous Computing*, vol. 15, Nos. 1/2/3, 2014.

Chapter 4

Numerical Convergence Study of the Algorithm in Complex Environments

A prerequisite to the modeling of complex environments with standard computer equipment, is achieving an outstanding reduction of memory efforts preserving at the same time enough accuracy. For that purpose, it is necessary to have knowledge about the optimal parameters to be used as inputs in the simulation of complex environments. In this chapter, an analysis of the convergence of the in-house developed 3D Ray Launching (RL) algorithm with respect to the computational time, the angular resolution of the shooting rays and the number of reflections considered, is presented. Besides, the numerical convergence study to obtain the optimal calculation parameters for the diffracted rays is also provided. This analysis leads to the optimal parameters which allow modeling the radio wave propagation channel in complex environments with accurate results and affordable simulation computational time. In addition, a comparison with the Geometrical Optics (GO) only approach, the Geometrical Optics and Uniform Theory of Diffraction (GO-UTD) approach and real measurements has been done. This comparison proves that the proposed hybrid GO-UTD algorithm yields excellent results and that the UTD extension definitely improves the simulation of the RL algorithm for realistic environments.

4.1   Related work

RT and RL models potentially represent the most accurate and versatile methods for urban and indoor multipath propagation characterization. Nevertheless, the computational time in conventional RL defined by the Shooting-and-Bouncing-Ray (SBR) method [Lin89], can be very large depending on the required accuracy of the results.

In [Wei06], Weinmann presents a new efficient approach in order to assess the simulation of scattered fields from arbitrary metallic objects with a ray tracing algorithm which combines the principles of Physical Optics (PO) and the Physical Theory of Diffraction (PTD). The paper demonstrates that both, CPU time and accurate results depend strongly on the number of rays N and the accuracy of the geometric model. The treatment of multiple interactions in a GO-PO approach has been studied in [Gri87], showing that, on one hand, the multiple PO approach is indeed more accurate. On the other hand, the simulation efforts increase exponentially with the order of the reflection, which makes multiple PO not applicable to more than double reflections. In [Wei09], a description of a novel implementation of diffracted rays according to the Uniform Theory of Diffraction (UTD) concept into a SBR code is presented, describing a numerical convergence study with respect to the number of diffracted rays and in terms of multiple diffractions. In [Ros02], a Geometrical Ray Implementation for Mobile Propagation Modeling (GRIMM) is presented, which splits the 3D ray construction problem into two successive 2D stages without loss of generality and with a great gain in time and simplicity. This permits to take into account reflections and diffractions in any order to meet convergence. In [Cho13], a numerical convergence study of a Refined Ray-Tracing Algorithm is carried out with respect to the propagation time and the number of bounces.

It is proved that an increase of the number of rays and angular resolution in a SBR approach achieves satisfying results but leads to the significant drawback of higher computational time [Wei06]. Therefore, it is relevant to study the convergence of the results when using RT methods.

With the aim of achieve accurate results with an affordable computational time, a numerical convergence study has been done in this chapter in the in-house developed 3D RL code. First, the GO only approach has been analyzed in relation with the number of reflections and the angular resolution of the launching rays. It is highly important to analyze the convergence versus the

number of reflections because it is shown that it converges for a certain number of them, and it is not worthy to increment this number because it does not lead to more accurate results, but to a great rise of computational time. This work has been published in the literature and can be found in [Azp14a].

After that, the numerical convergence study versus the angular resolution of diffracted rays has been done for the GO-UTD approach. An analysis considering diffracted obstacles of different size is presented, always taking into account the required trade-off between accuracy of the results and simulation computational time. The accuracy of the results has been evaluated by comparison with real measurements.

Finally, subsection 4.5 emphasizes on the outcomes when large and complex scenarios are analyzed. It is shown that depending on the angular resolution of the launching rays, for a fixed mesh of cuboids, there is a certain distance *d* from which the rays do not reach any cuboid and lead to neglecting significant contributions. Because of that, it is highly necessary to analyze this divergence of the launching rays when assessing radio wave propagation in large scenarios. An adaptive meshing has been presented for these cases leading to accurate results when compared with real measurements.

4.2   Numerical convergence study of the GO only approach

4.2.1 Definition of the considered scenario

In principle, it can be stated that simulation results tend to be more accurate when more rays are launched and more reflections are considered. However, computational time has to be taken into account in order to obtain accurate results within an acceptable time span.

In this section, the influence of considering different number of reflections and launching rays is evaluated. For that purpose, two different angular resolutions of launching rays have been considered and analyzed versus the number of reflections. Afterwards, once the optimal number of reflections has been obtained, the assessment of the most accurate angular resolution of launching rays has been done taking into account the computational time.

The scenario under consideration is a complex environment, which corresponds to several rooms of the iRadio Laboratory of the University of Calgary. A schematic view of the scenario is represented in Figure 4.1.
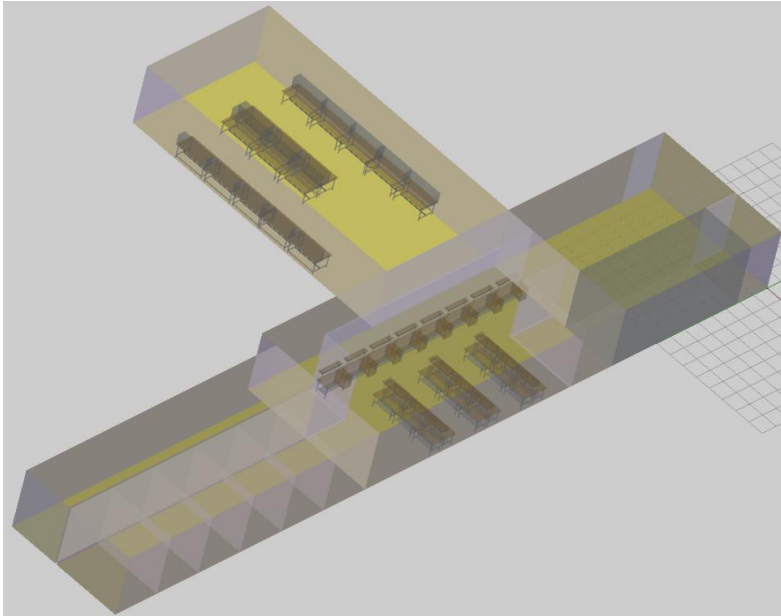
Figure 4.1. Complete scenario of iRadio Laboratory of University of Calgary.
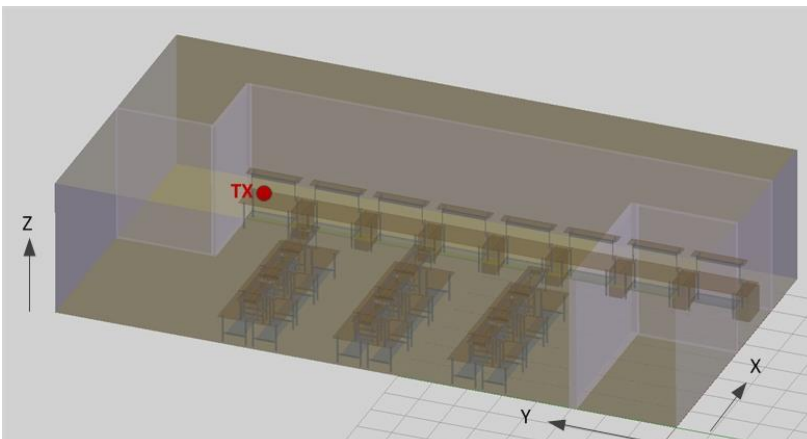
Figure 4.2. Detail of Room 2 of the complete scenario representing the iRadio Laboratory.

Within the complete scenario, only one room has been chosen to be analyzed exhaustively, i.e., Room 2, which is depicted in detail in Figure 4.2. The red point in this figure corresponds to the location of the transmitter antenna, with coordinates (X=6.24m, Y=16.94m, Z=0.96m). All the elements within the scenario have been taken into account, i.e. the different dimension and distribution of desks, chairs and walls. The material parameters used in the simulation models are shown in Table 4.1 [Bal89, Cui02].

Table 4.1. Material Parameter Definition.

Material	Air	Aluminum	Glass	Wood	Brick wall
Permittivity (ε_r)	1	4.5	6.06	3	5.2
Conductivity (σ) [S/m]	0	4×10^7	10^{-12}	0.0006	0.028

4.2.2 Convergence versus the number of reflections

First, a numerical convergence study of the algorithm versus the number of reflections that the ray could experience with the obstacles and walls has been obtained. Different cases have been considered varying the number of reflections. These cases correspond to different angular resolutions when the rays are launched, as shown in Table 4.2.

Table 4.2. Different cases considered for simulation versus the number of reflections.

	$N_{launching\ rays}$	$\Delta\Phi = \Delta\theta$
Case 0	16200	2º
Case 1	64800	1º
Case 2	259200	0.5º

Table 4.3. Simulation Parameters

Ray Launching Parameters	
Frequency	2.4GHz
Transmitted Power	20dBm
Cuboids resolution	12 x 12 x 12cm³
Transmitter Point	(X=6.24m, Y=16.94m, Z=0.96m)

Case 1 and Case 2 have been analyzed versus the number of reflections, and simulation parameters for both cases are shown in Table 4.3.

Figures 4.4, 4.5, 4.6 and 4.7 depict simulation results for Case 1. The mean value and the Standard Deviation (SD) of Power (dBm) for different X and Z, along the Y-axis are presented. These lines of received power correspond to the red lines in Figure 4.3a and 4.3b. The mean power values exhibit large variability due to the influence of the morphology and topology of the scenario. Therefore, the way in which the elements within the indoor scenario are configured and the different material properties play a fundamental role in the overall performance of the network.

The standard deviation of power decreases as the number of reflections increases and converges approximately for six reflections in all cases, which implies that the maximum efficiency of the algorithm will be reached when six reflections are considered.

Figure 4.5 shows the linear regression lines of the received power for different locations in the X axis, along the Y-axis and for different heights. It is demonstrated that when the number of reflections considered in the algorithm has been increased, the algorithm tends to converge and it exhibits the same behavior from a threshold value for the number of reflections, corresponding to six reflections. In all cases the trend is to decrease over distance, and it is observed that with more reflections the slope of the lines is smaller.

Figure 4.6 shows the mean and the SD of Power (dBm) for different Y and Z locations, along the X-axis (green lines in Figure 4.3a). It is observed that mean power converges as the number of reflections increases. Besides, the SD of the received power decreases and also converges at approximately six reflections.

Figure 4.7 shows the linear regression lines of the received power for different values in Y axis and heights, along de X-axis. It is observed that, for smaller values in the Y axis, the slope of the lines is smaller as the number of reflections increases. From Y=6m, figures of smaller heights show more variability due to the obstacles within the ray path. Lines converge as the number of reflections is increased. From Y=12m, power increases along the X-axis due to the proximity of the transmitter antenna.

(a)   (b)
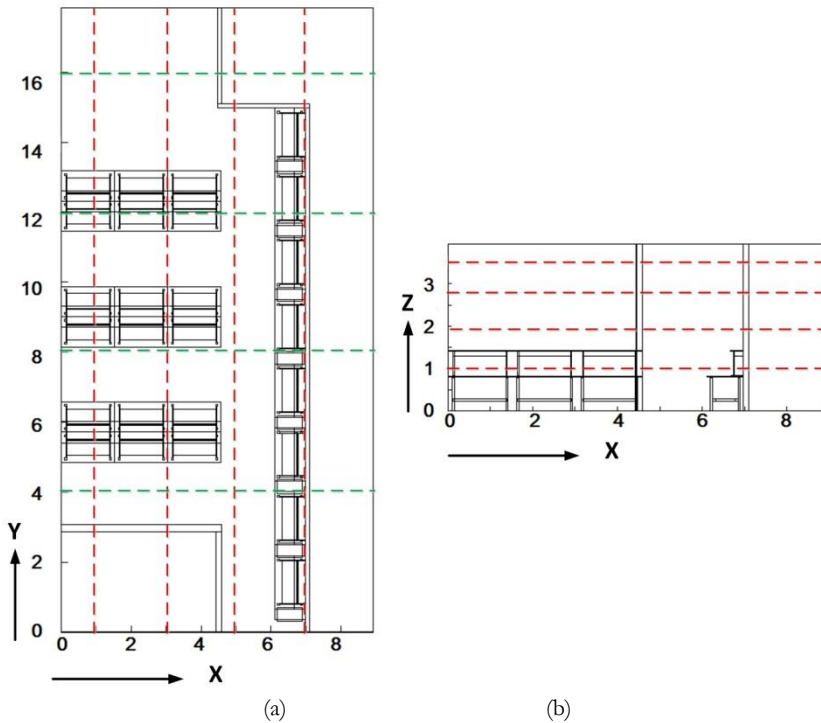
Figure 4.3. Schematic representation of the linear TX-RX distances chosen for the numerical convergence study of the algorithm (a) along the X-axis and the Y-axis (b) different heights in the Z-axis.
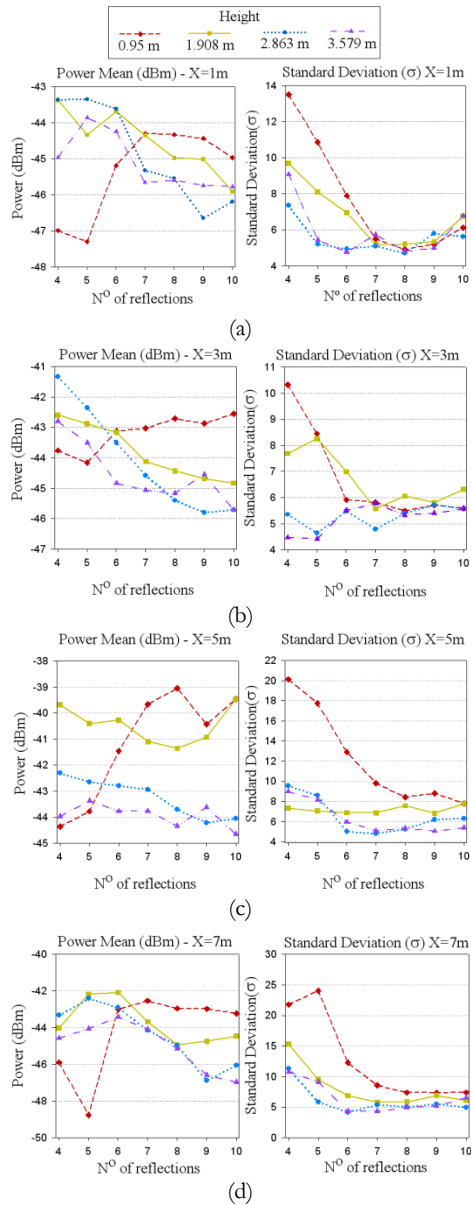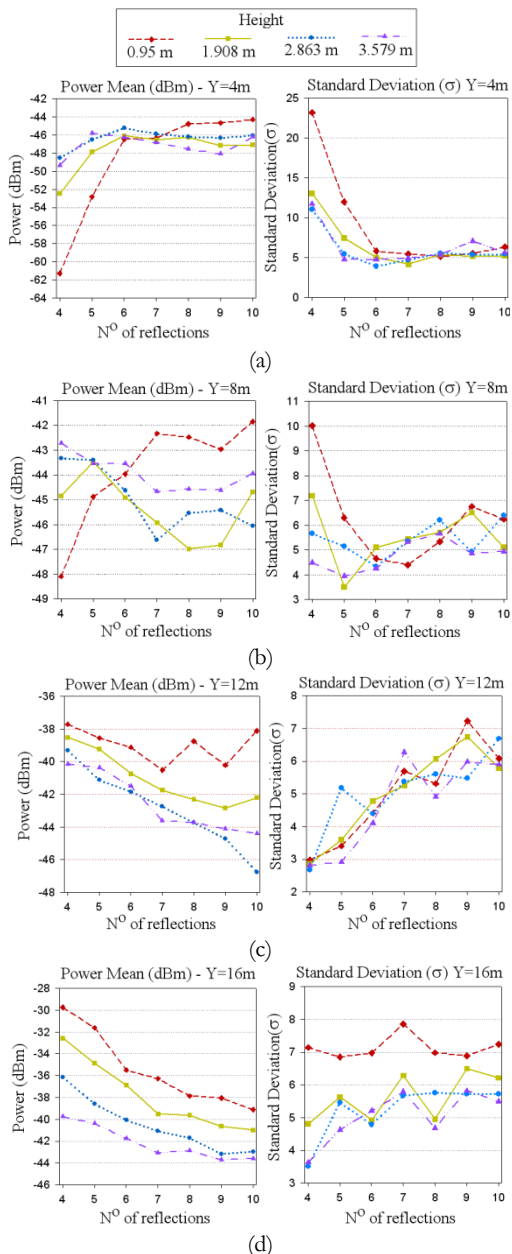
Figure 4.4. Mean (dBm) and Standard Deviation (dB) of Power for different X and Z versus the number of reflections with $N_{launching\ rays}$=64800 (a) X=1m (b) X=3m (c) X=5m (d) X=7m.
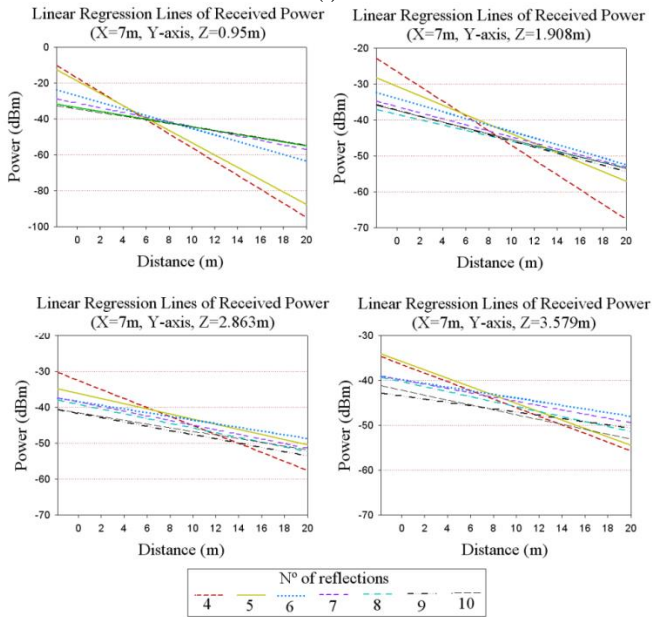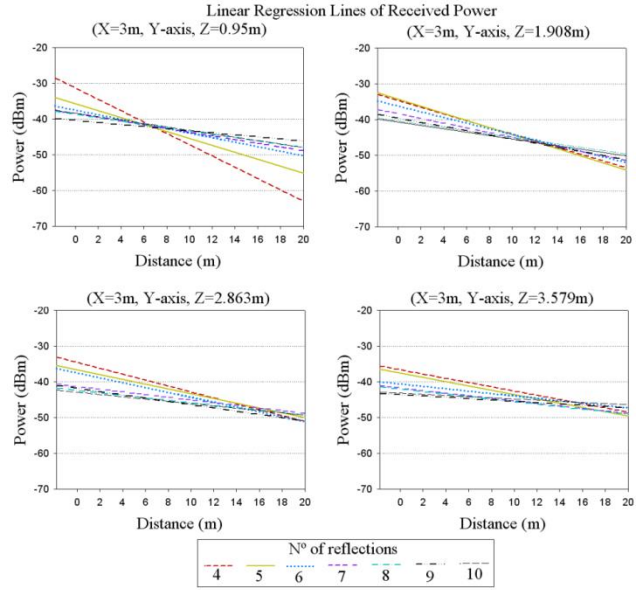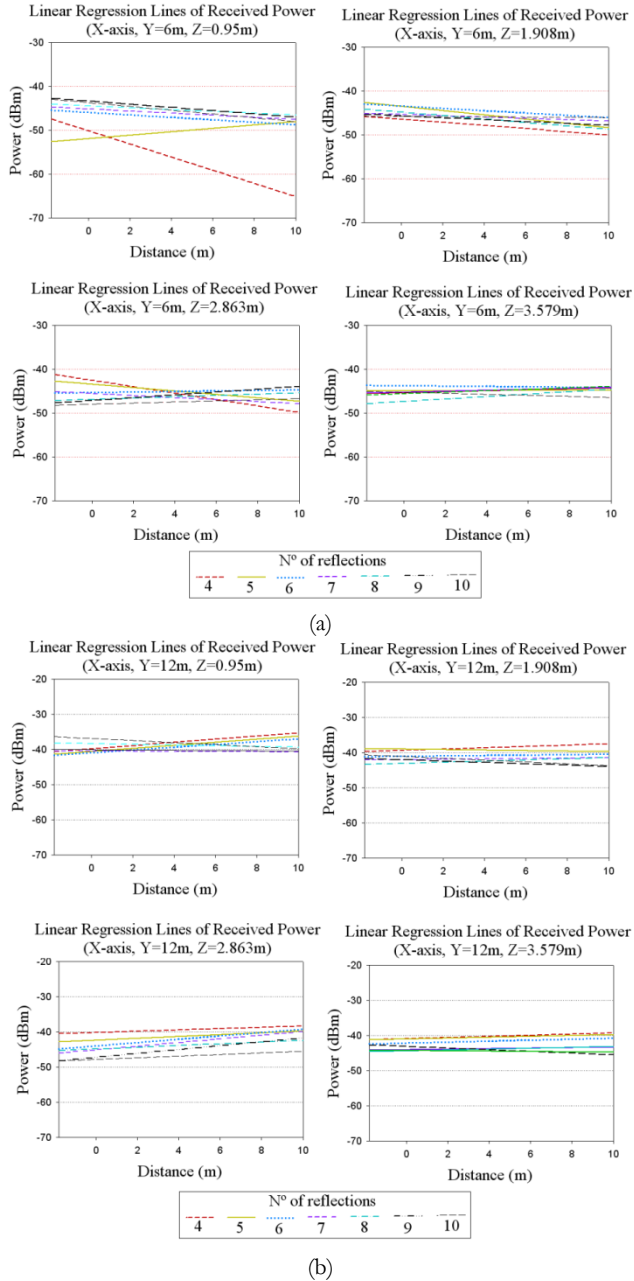
Figure 4.5. Linear regression lines of Received Power for different X, along the Y-axis and for different heights, with $N_{launching\ rays}$=64800 (a) X=3m (b) X=7m.
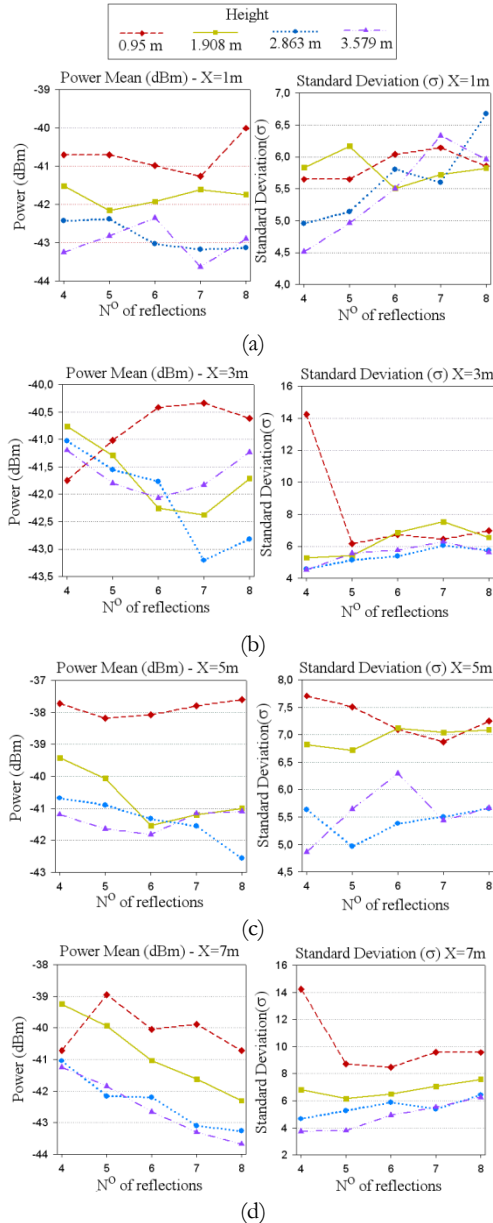
Figure 4.6. Mean and Standard Deviation of Power for different Y and Z versus the number of reflections with $N_{launching\ rays}$=64800 (a) Y=4m (b) Y=8m (c) Y=12m (d) Y=16m

Figure 4.7. Linear regression lines of Received Power for different Y, along the X-axis and for different heights, with $N_{launching\ rays}$=64800 (a) Y=6m (b) Y=12m.

In order to validate previous results, which conclude that six reflections should be considered in complex indoor scenarios, the same analysis has been done with a lower angular resolution (Case 2 in Table 4.2). This implies that the number of shooting rays is increased to test if the number of rays has an influence in the algorithm convergence. Simulation parameters are shown in Table 4.3.

Figure 4.8 represents the mean and the SD of Power (dBm) for different X and Z, along the Y-axis, with $\Delta\Phi = \pi/360$ and $\Delta\theta=\pi/360$. As in the previous case, large variability in the mean of the received power is observed due to the influence of the morphology and topology of the scenario, and multipath fading which is a relevant phenomenon in this type of indoor scenarios. The SD of the power does not converge as clearly as in the previous case. However, Figures 4.8b and 4.8d depict convergence of the algorithm.

The linear regression lines of the received power for different X, along the Y-axis, and for different heights, with angular resolution of launching rays of 0.5°, are presented in Figure 4.9. It is observed that in all cases the received power decreases with the distance and the slope of the lines are smaller as the number of reflections increases. In Case 2, the algorithm converges with one reflection less considered because of the rise of launching rays. The slope of the regression lines in Figure 4.9 and Figure 4.11 are, for every height, smaller than Case 1, therefore the number of considered reflections to achieve the convergence is smaller.

However, the computational time is also deeply important. Simulations have been performed in an Intel Xeon CPU X5650 @2.67GHz 2.66GHz, with 64GB of RAM memory. In Case 2, the computational complexity is increased overall. Figure 4.12 shows the simulation time of the considered scenario depending of the number of reflections and the number of launching rays. Computational time with angular resolution of 0.5° (Case 2) is hugely greater than Case 1, with angular resolution of 1° for each number of reflections considered. It can be seen that the optimal parameters to achieve accurate results with an acceptable computational time is to consider six reflections and angular resolution of launching rays of 1°.

Figure 4.8. Mean and Standard Deviation of Power for different X and Z versus the number of reflections with $N_{launching\ rays}$=259200 (a) X=1m (b) X=3m (c) X=5m (d) X=7m.
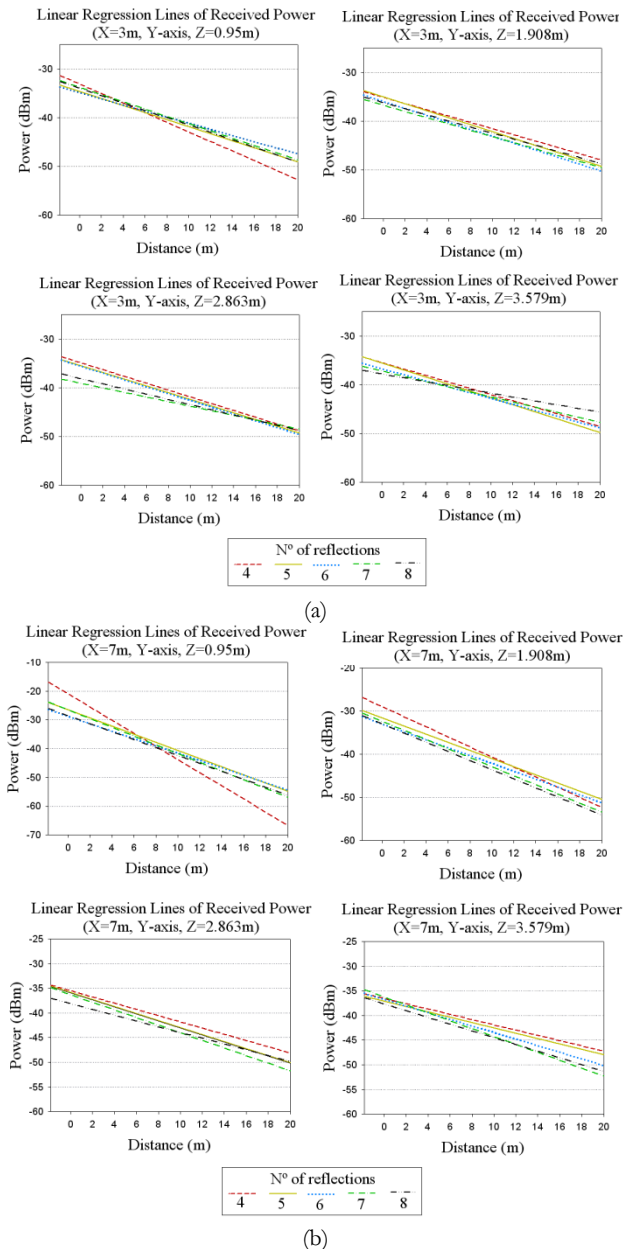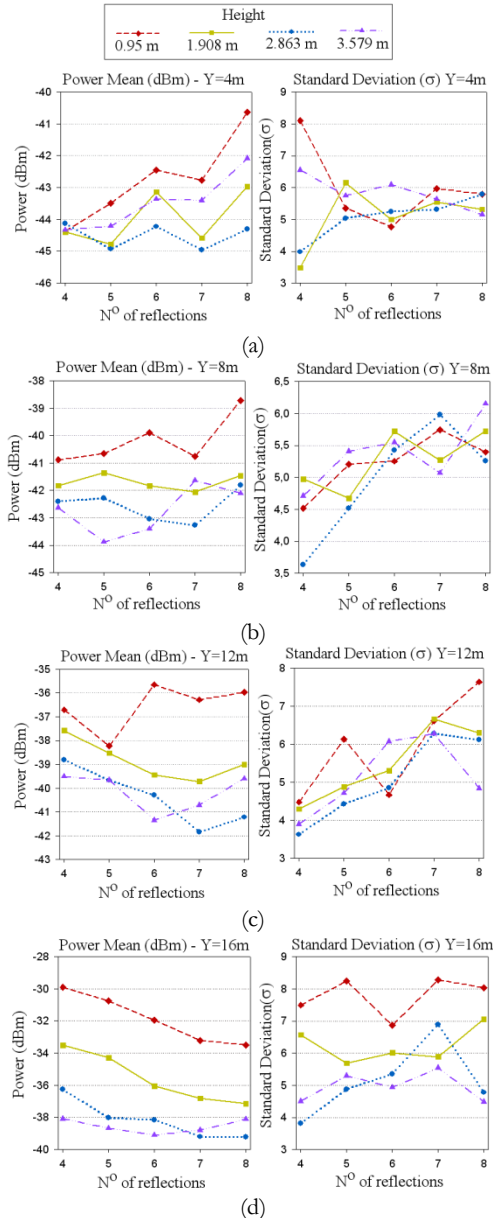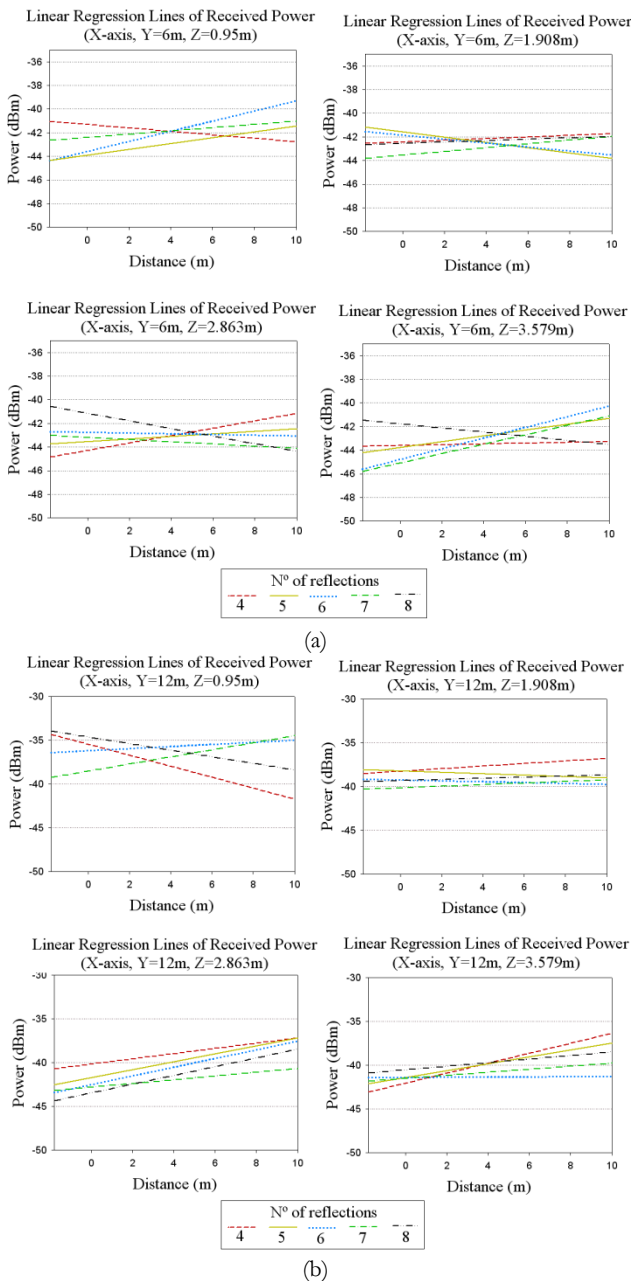
Figure 4.9. Linear regression lines of the Received Power for different X, along the Y-axis and for different heights, with $N_{launching\ rays}$=259200 (a) X=3m (b) X=7m.
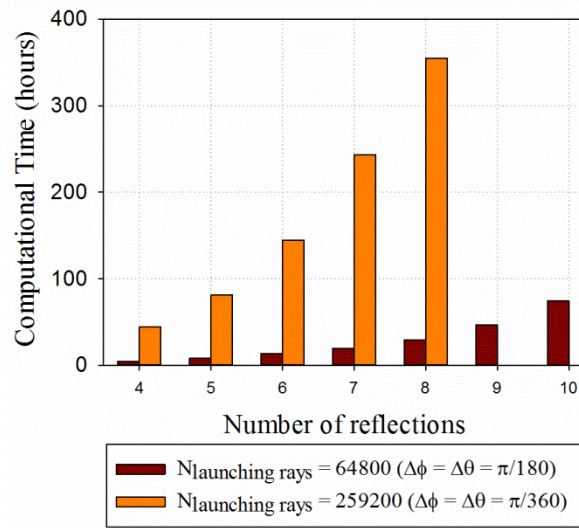
Figure 4.10. Mean and Standard Deviation of Power for different Y and Z versus the number of reflections with $N_{launching\ rays}$=259200 (a) Y=4m (b) Y=8m (c) Y=12m (d) Y=16m.

Figure 4.11. Linear regression lines of the Received Power for different Y, along the X-axis and for different heights, with $N_{launching\ rays}$=259200 (a) Y=6m (b) Y=12m.

Figure 4.12. Comparison of Computational Time versus different number of launching rays and different number of reflections considered in the algorithm. Simulations have been performed in an Intel Xeon CPU X5650 @2.67GHz 2.66GHz, with 64GB of RAM memory.

4.2.3 Convergence versus the number of launching rays

In order to validate the results obtained in the previous section, an analysis of the convergence of the algorithm versus the number of launching rays has been performed considering six reflections. Figure 4.13 and Figure 4.14 show the mean and the SD of power for different locations in the X, Y axis and heights, in comparison with the three cases shown in Table 4.2. It can be seen that the mean value of received power increases as the number of shooting rays is increased, which is in agreement with previous results in the sense that the algorithm is more accurate with more shooting rays. Alternatively, the SD of power decreases sharply for Case 0 to Case 1, and converges in all cases in Case 1, which corresponds to angular resolutions of 1º. Accordingly, these results validate the previous statements taking into account the high amount of CPU-time required to analyze the large amount of rays of Case 3, which is shown in Figure 4.15.
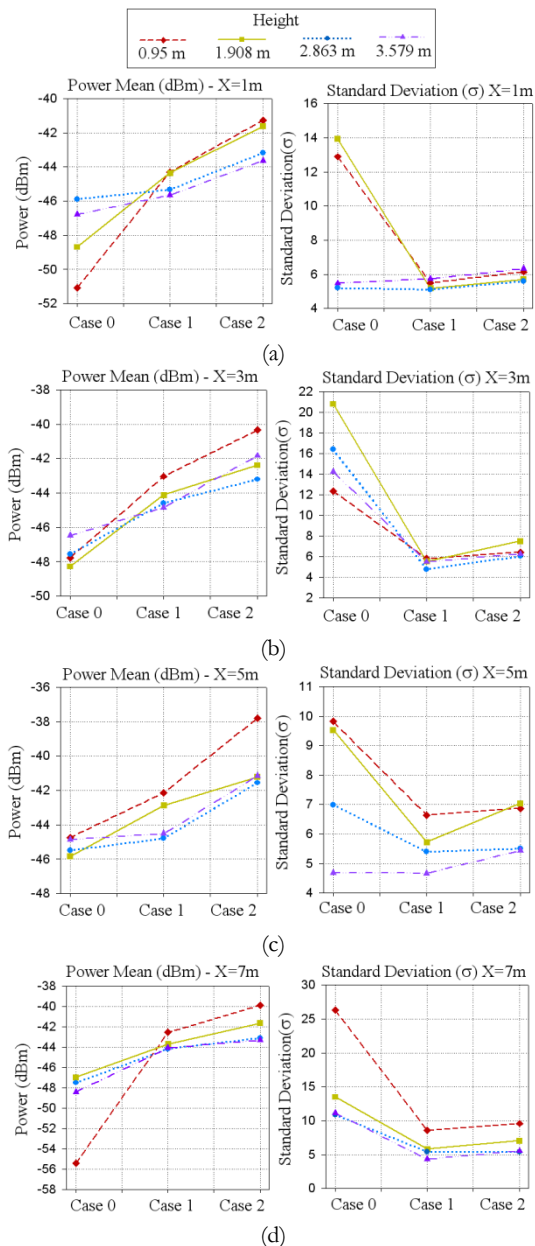
Figure 4.13. Mean and Standard Deviation of Power in Room 2 versus different cases of shooting rays for different X.
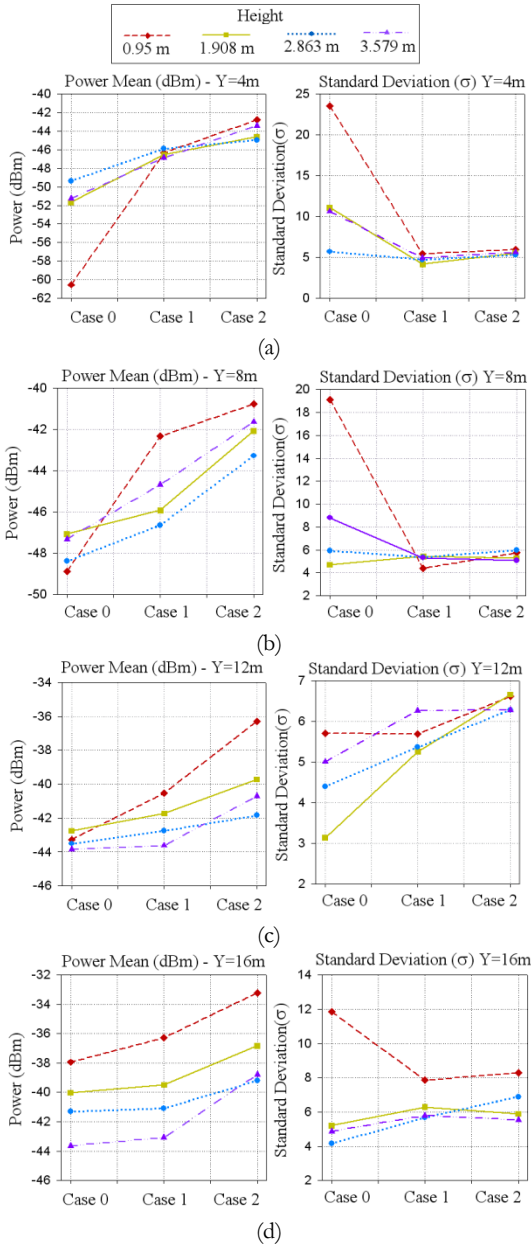
Figure 4.14. Mean and Standard Deviation of Power in Room 2 versus different cases of shooting rays for different Y.
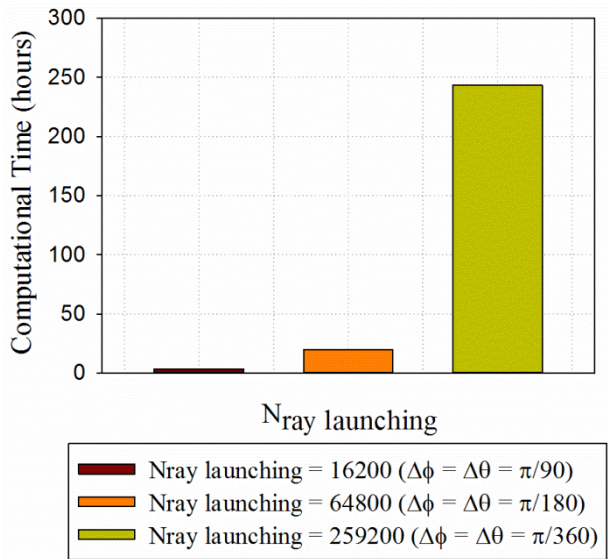
Figure 4.15. Comparison of Computational Time versus different number of launching rays. Simulations have been performed in an Intel Xeon CPU X5650 @2.67GHz 2.66GHz, with 64GB of RAM memory.

4.3 Numerical convergence study of the hybrid GO-UTD approach

In this section, the analysis of the impact in the accuracy of the results of considering different number of diffracted rays and obstacles of different size for diffractive objects has been done taking into account the computational time for the GO-UTD approach.

4.3.1 Definition of the considered scenario

The scenarios under consideration have been three different environments represented in Figure 4.16. The first one is a typical complex indoor environment, which corresponds to an office of our campus (Figure 4.16a). The dimensions of the scenario are 13m by 7m by 4.2m and the obstacle density is 1.24%. The obstacle density has been defined as the number of cuboids occupied with obstacles per total cuboids in the whole scenario. The red point in this figure corresponds to the transmitter antenna, which is placed at the point (X= 9.94m,

Y=4.5m, Z=0.60m). The second environment (Figure 4.16b) is bigger and it has more clutter within it. The transmitter and receiver measurement points are represented in the figure. The dimensions of this scenario are 12.37m by 15.82m by 3.2m and the obstacle density is 2.78%. It has been also considered a third scenario (Figure 4.16c), which corresponds to the basement floor of the Mathematics and Computer Building of the Public University of Navarre. This third scenario is really complex because it is bigger (55.3m by 27.85m by 3.8m) and it has a lot of obstacles with different material properties within it. The obstacle density of this third scenario is 3.52%. For all the cases, each element within the scenario have been taken into account (i.e. the different dimension and distribution of desks, chairs and walls). The material parameters used in the simulation models are provided in Table 4.4 [Bal89, Cui02].

Table 4.4. Material properties in the GO-UTD approach.

Material	Permittivity (ε_r)	Conductivity (σ) [S/m]
Air	1	0
Plywood	2.88	0.21
Brick wall	4.11	0.0364
Glass	6.06	10^{-12}
Concrete	5.66	0.142
Metal	4.5	$4*10^7$
Polycarbonate	3	0.2

Table 4.5 shows the selected parameters for the GO-UTD simulation. The transmitter and receiver antennas are omnidirectional, with 5dBi gain respectively. The angular resolution in the horizontal ($\Delta\Phi$) and vertical plane ($\Delta\theta$) for the launching rays is 1°. The number of reflections considered in the simulation is six and the cuboids resolution is 5cm, 10cm and 0.5m respectively for each scenario.

Table 4.5. Ray Launching Simulation Parameters in the GO-UTD approach

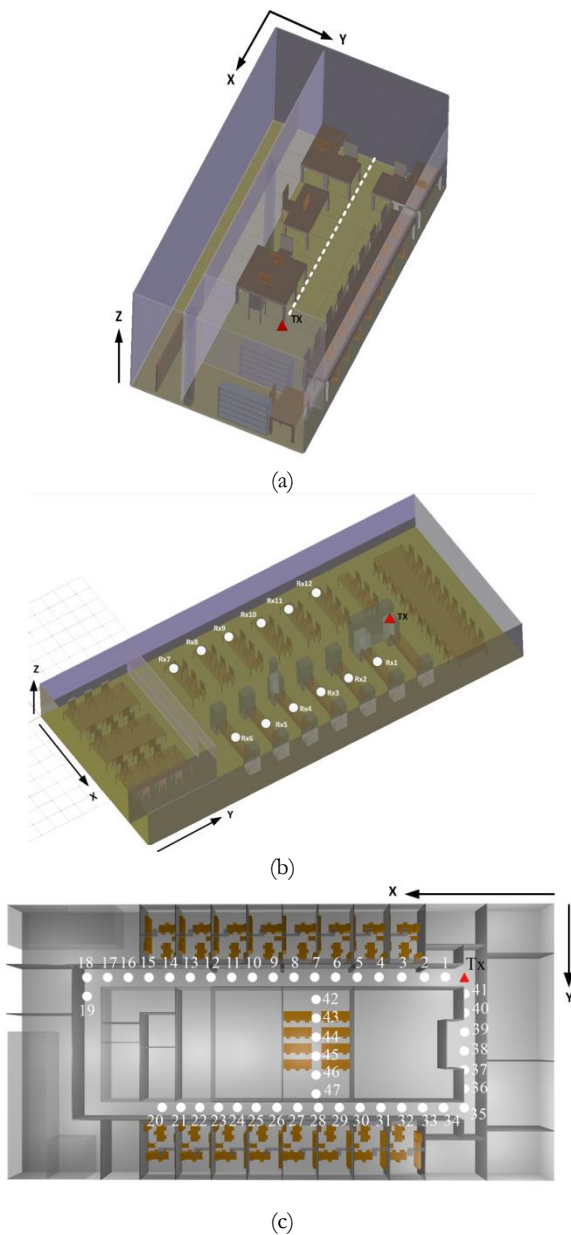| Ray Launching Parameters	
Frequency	2.4GHz
Transmitted Power	0dBm
Antenna gain	5dBi
Horizontal plane angle resolution ($\Delta\Phi$)	1°
Vertical plane angle resolution ($\Delta\theta$)	1°
Reflections	6
Cuboids resolution	5cm / 10cm /0.5m

(a)

(b)

(c)

Figure 4.16. Schematic view of the considered scenario. Ceiling has not been shown for illustration. a) Scenario 1 b) Scenario 2 c) Scenario 3.

4.3.2 Angular resolution of diffracted rays

An analysis of the convergence of the algorithm has been done comparing the accuracy of the model versus the computational time depending of the diffracted rays launched for the first scenario considered. The diffraction phenomenon has been taken into account considering the three different cases shown in Table 4.6, which illustrate the different size considered for diffractive obstacles.

Table 4.6. Different cases considered for the size of diffractive obstacles.

Case 1	Diffractive objects $\geq \lambda/2$
Case 2	Diffractive objects $\geq 4\lambda$
Case 3	Diffractive objects $\geq 8\lambda$

Two different angular resolutions for the diffracted rays have been considered, $\Delta\zeta_1=\pi/180$ and $\Delta\zeta_2=\pi/20$, selected taking into account the wide range of possible angular resolutions, being one of them very accurate ($\Delta\zeta_1$) and the other one less accurate ($\Delta\zeta_2$). The purpose of this choice is to analyze the influence of the diffracted launching rays in the convergence of the results accuracy. Mean and standard deviation for the three different cases stated above have been calculated taking into account both angular resolutions of diffractive rays ($\Delta\zeta_1$ and $\Delta\zeta_2$). As it can be seen from Table 4.7, there is not a lot of variation in the mean and the standard deviation of both cases. However, as it is shown in Figure 4.17 the overall computational time increases significantly with an angular resolution of diffractive rays of $\Delta\zeta_1$. Accordingly, to achieve a good trade-off between results accuracy and inherent computational time, the $\Delta\zeta_2$ angular resolution for diffracted rays has been chosen.

Table 4.7. Mean and Standard Deviation for the different cases considered.

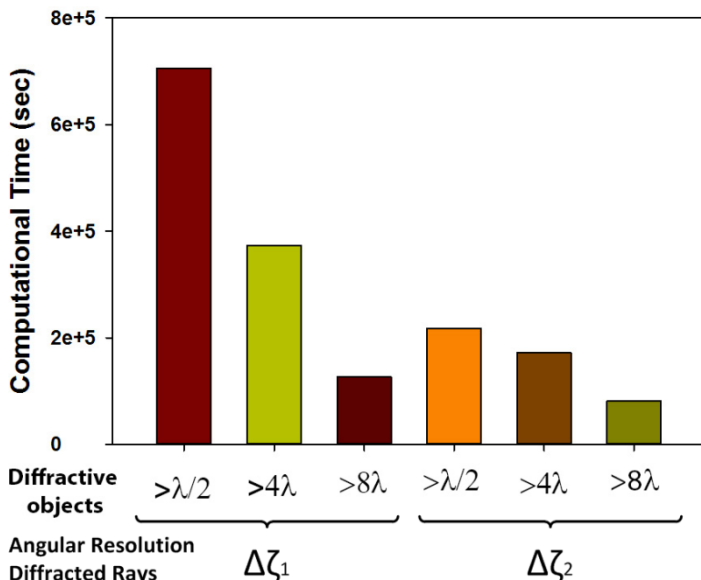| Angular Resolution Diffracted Rays	Diffractive objects considered	Power Mean (dBm)	Standard Deviation (dB)
$\Delta\zeta_1$	Case 1	-61.95	7.75
	Case 2	-61.95	7.75
	Case 3	-61.62	7.51
$\Delta\zeta_2$	Case 1	-61.41	7.32
	Case 2	-64.40	7.32
	Case 3	-61.33	7.37

Figure 4.17. Computational time versus the diffractive obstacles size and the selected angular resolution for the diffracted rays. Simulations have been performed in an Intel Xeon CPU X5650 @2.67GHz 2.66GHz, with 64GB of RAM memory.

4.3.3 Diffractive obstacles size

For the radial of received power which corresponds to Y=5.75 meters along the X-axis, an analysis of the received power has been done considering different sizes of diffracted objects in the scenario. The influence of considering the three different cases shown in Table 4.6 for the diffractive objects has been analyzed. Figure 4.18 shows the comparison of received power for the radial which corresponds with Y=5.75 meters along the X-axis in Figure 4.16, considering different sizes of diffractive objects.

It can be seen from Figure 4.18 that there is not a lot of variability between the three cases considered because in this particular scenario there is not much variation within the elements in the environment. However, it is shown that in the particular interval which is zoomed in, a bigger decay of the signal can be observed when considering smaller diffractive obstacles. Nevertheless, the difference is very small for this particular indoor environment, showing that the

influence of diffractive obstacles size is not decisive to obtain better results. It must be pointed out that for this particular radial in the considered scenario, the obstacle density of edges is 8.46%. Thus, it can be concluded that for this edges obstacle density, the diffractive obstacles size has not a lot of influence, so the Case 3 in Table 4.6 can be used leading to smaller simulation computational times with accurate results.

To better understand this assumption, the Power Delay Profile (PDP) of the point which has a bigger decay in the zoomed part of Figure 4.18 is represented in Figure 4.19 comparing the three cases. As it can be seen, there are not significant variations because as stated above, in this particular scenario, the sizes of the objects do not have a relevant variance.
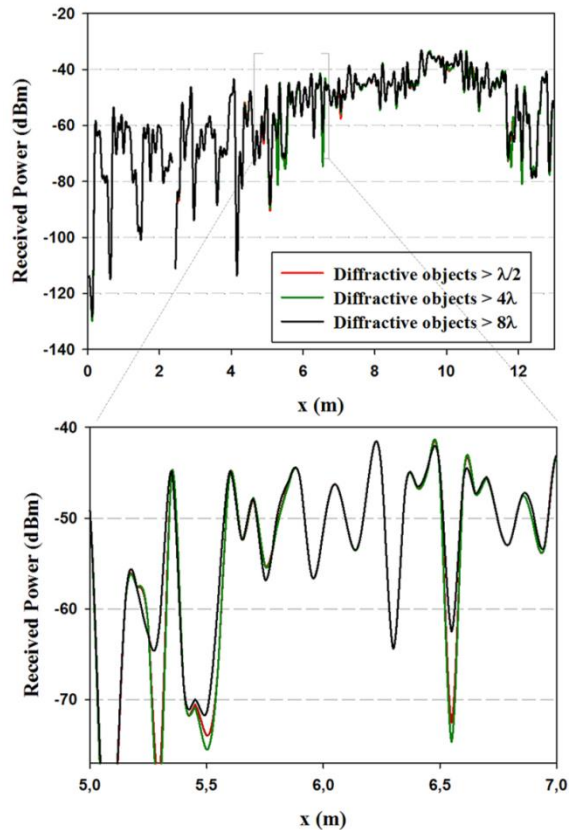
Figure 4.18. Radial of received power (dBm) for Y=5.75m along the X-axis considering different sizes of diffractive objects.

Figure 4.20 and Figure 4.21 represent the difference in received power between different cases. It can be observed that Figure 4.21 has more variations than Figure 4.20, and this means that the variability of the results taking into account different sizes of diffracted obstacles has influence in the accuracy of the model. Table 4.8 represents the mean and SD for the difference in received power of Case 1 and Case 2, and Case 1 and Case 3, showing a larger standard deviation in the second case. Nevertheless, as stated above, for this particular case, the differences are very small, and they are not decisive in the accuracy of the results.
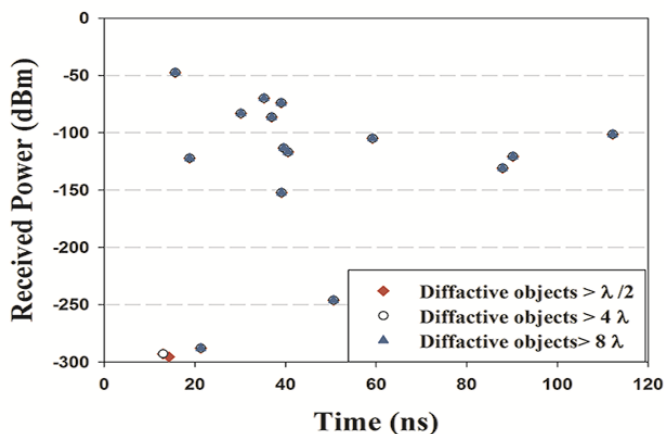
Figure 4.19. Comparison of Power Delay Profile for the zoom point represented in Figure 4.18.
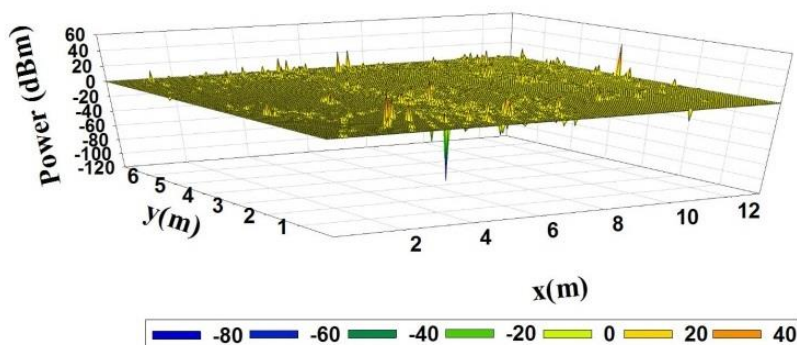
Figure 4.20. Comparison of Received Power (dBm) between Case 1 and Case 2.
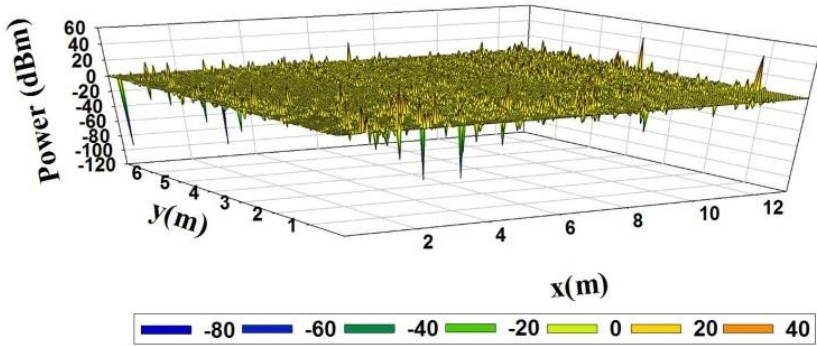
Figure 4.21. Comparison of Received Power (dBm) between Case 1 and Case 3.

Table 4.8. Mean and Standard Deviation for the different cases represented in Figure 4.20 and Figure 4.21.

	Difference Mean (dBm)	Standard Deviation (dB)
Case 1 and Case 2	0.01	1.11
Case 1 and Case 3	0.10	2.38

4.4 Comparison between GO only approach and GO-UTD approach

A comparison between 3D RL only approach (based only in GO) and 3D RL with edge contributions (based in GO and UTD) approach has been made. Figures 4.22, 4.23, 4.24, 4.25, 4.26 and 4.27 show the results for different radials of received power along the scenario for a height of 0.8 meters. The red dashed line in the small cut plane of the scenario of each figure corresponds to the radial of received power depicted in that figure. The radial of received power represented in Figure 4.22 does not have any obstacles in its way; therefore power doesn't have as much variations as the other cases. Figures 4.23, 4.24, 4.26 and 4.27 have more elements in the radials depicted in the figures and the vertical black dashed lines in the pictures represent the different positions of the obstacles. It can be seen that these obstacles have a clear influence in the received power, showing more variability around the objects.
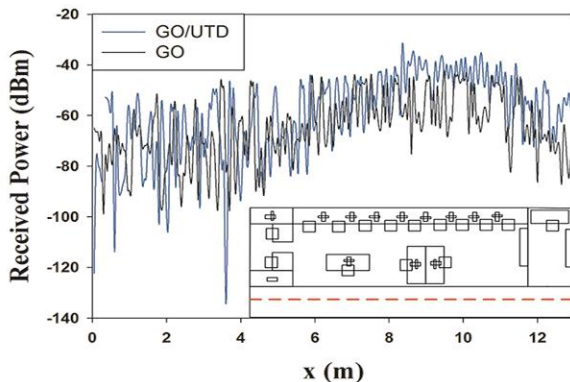
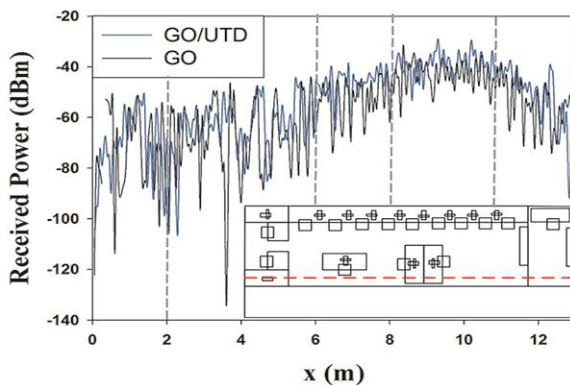**Figure 4.22.** Radial of received power (dBm) for Y=1.5m along the X-axis.

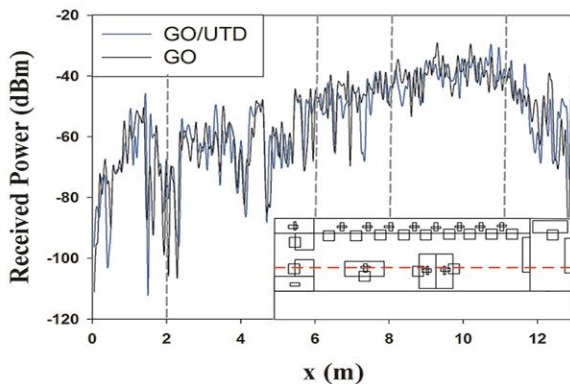**Figure 4.23.** Radial of received power (dBm) for Y=2.5m along the X-axis.

Figure 4.24. Radial of received power (dBm) for Y=3.75m along the X-axis.

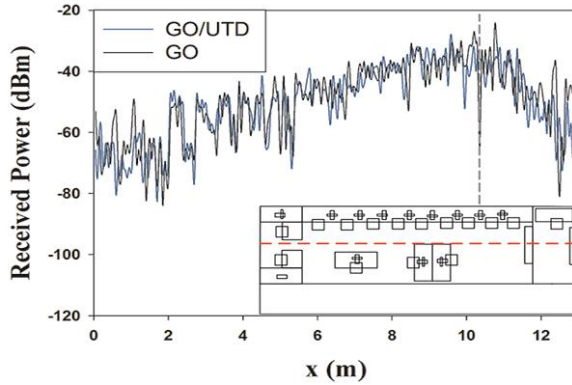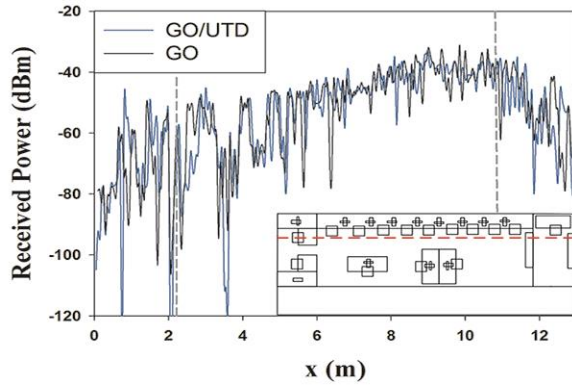**Figure 4.25.** Radial of received power (dBm) for Y=4.5m along the X-axis.

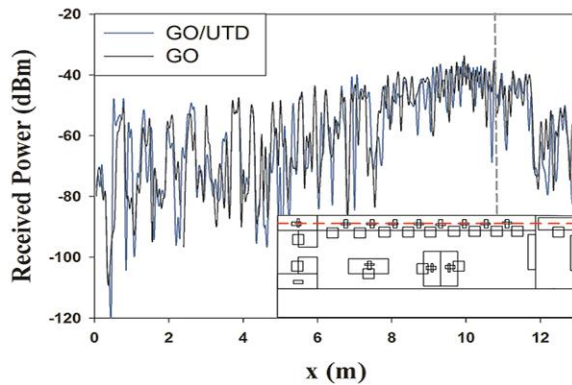**Figure 4.26**. Radial of received power (dBm) for Y=5.25m along the X-axis.

Figure 4.27. Radial of received power (dBm) for Y=6.5m along the X-axis.

4.4.1 Impact of furniture

Furniture has a great influence in the decay of the signal in radio wave propagation in indoor scenarios. With the aim of representing this impact, different simulations have been done for three different cases: with all the furniture considered, with only tables, and without furniture. Figures 4.28, 4.29 and 4.30 show the bi-dimensional planes of received power for a height of 0.8 meters in the 3D scenario. For these simulations, the GO-UTD approach has been used, and results show that furniture in the environment has a significant influence in the propagation of the signal showing a bigger interference with distance when more obstacles are included.

Figure 4.31 shows the radial of received power for the three different cases of considered obstacles, for Y=5.75 meters along the X-axis. It can be seen in the trend lines that the predicted power is lower when all the furniture is taken into account.
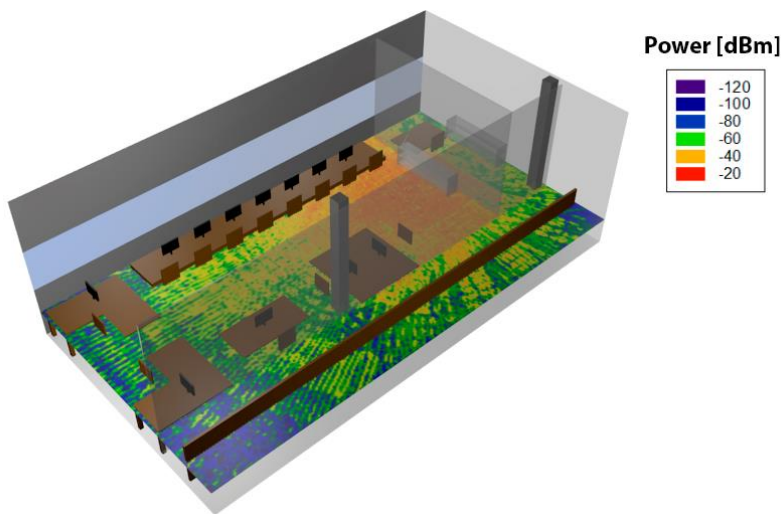
Figure 4.28. Bi-dimensional plane of received power (dBm) for 1 meter high considering all the furniture in the scenario.
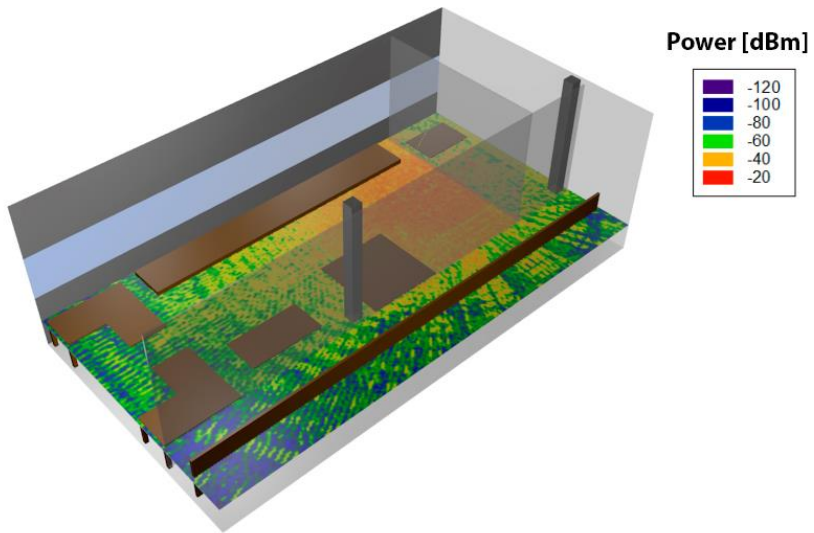
Figure 4.29. Bi-dimensional plane of received power (dBm) for 1 meter high considering only the tables in the scenario.
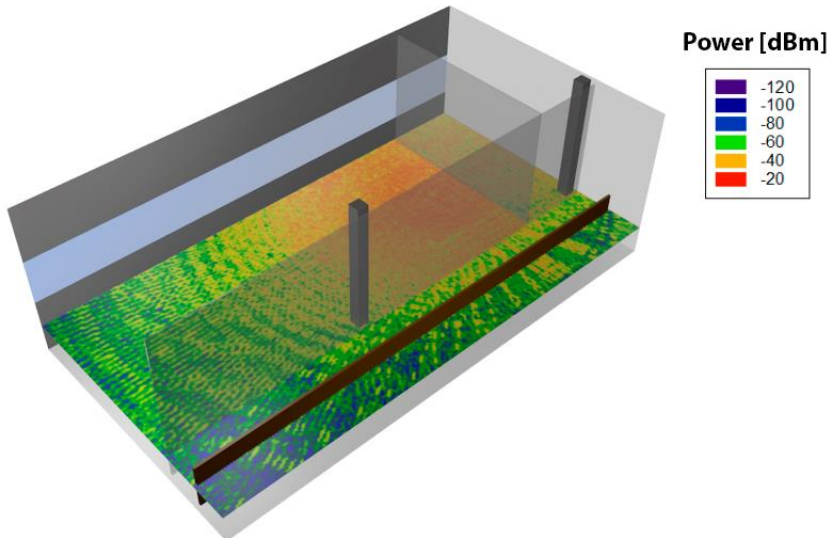

Figure 4.30. Bi-dimensional plane of received power (dBm) for 1 meter high without furniture in the scenario.
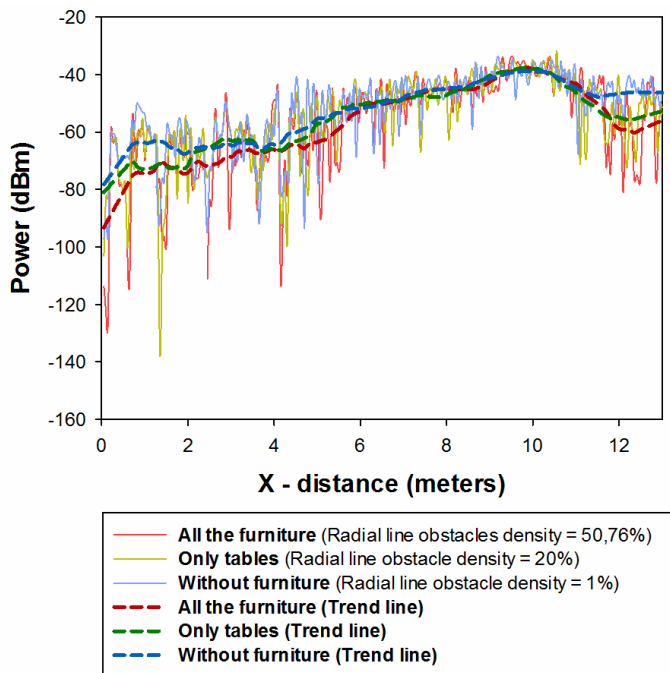
Figure 4.31. Comparison between radials of received power for the three cases considered: with all the furniture in the room, with only tables and without furniture.

4.4.2 Measurement results

In order to validate the results previously obtained, real measurements for the three different scenarios depicted in Figure 4.16 have been obtained and compared with simulations. For that purpose, a signal generator connected to a transmitter antenna at 2.4GHz frequency has been located at the coordinates of the transmitter point for each scenario. The signal generator which has been employed is a portable Agilent N1996A and the spectrum analyzer is an Agilent N9912 Field Fox. The antennas used are Picea 2.4GHz Swivel Antennas from Antenanova, both omnidirectional antennas[1]. Measurements have been performed for the first scenario along the radial white dashed line depicted in Figure 4.16a each 0.5m at a height of 0.80m. For the second and third scenario, measurements have been made for the receiver points represented in Figure 4.16b and 4.16c.

[1] For more information about the measurement equipment, see Appendix B.

Figure 4.32 shows the comparison between simulation and measurement results for the different simulation techniques, GO-only approach method and GO-UTD approach, for the three scenarios considered. Measurements were performed with 100MHz bandwidth. The measurement time at each point was 60 seconds, and the value of received power represented by each point is the highest peak of power shown by the spectrum analyzer for the considered bandwidth (MaxHold function in the spectrum analyzer of Agilent). The received power values estimated by simulation have been obtained for the same spatial samples as the real measurements, considering the corresponding cuboid in the three-dimensional mesh of cuboids in which the scenarios have been divided.

It is shown that both simulation techniques follow the trend of the real received power for the three scenarios, which is smaller when the distance between transceivers increases. Table 4.9 shows the mean error and SD between the different approaches, showing that the GO-UTD technique is more accurate for the three cases. The mean error and standard deviation is smaller for the three cases in the GO-UTD approach, with a standard deviation ranging from 0.814dB to 2.902dB, with the bigger deviation for the biggest scenario, in comparison with 2.305dB to 4.194dB of standard deviation for the GO approach. Thus, it can be concluded that measurements and simulation results are in good agreement and the accuracy is definitely better when using the GO-UTD approach. The convergence of the launching diffracted rays has been analyzed showing that an angular resolution of $\Delta\zeta_2$ yields good agreement with measurement results with and affordable simulation computational time.

Table 4.9. Mean and Standard Deviation for the different approaches considered for the three scenarios considered.

	GO approach		GO-UTD approach	
	Power Mean (dBm)	Standard Deviation (dB)	Power Mean (dBm)	Standard Deviation (dB)
Scenario 1	3.011	2.305	1.370	0.814
Scenario 2	1.285	3.586	0.047	1.670
Scenario 3	2.285	4.194	1.477	2.902
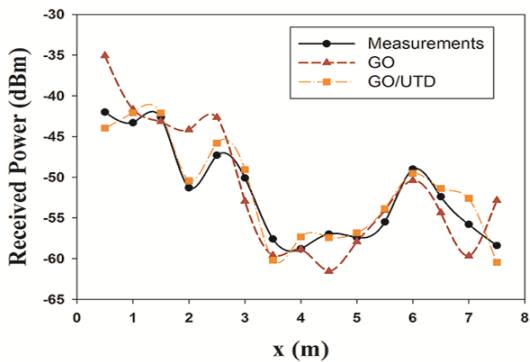
(a)
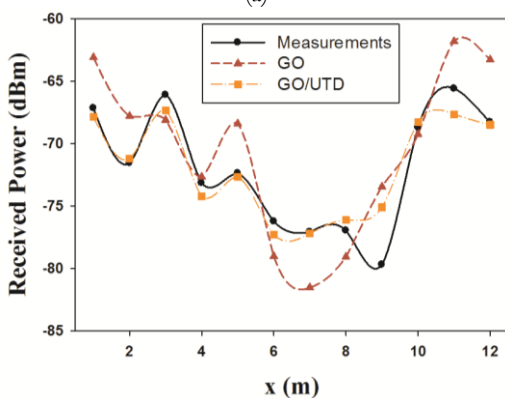
(b)
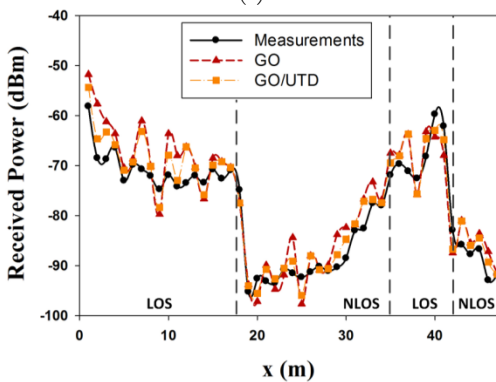
(c)

Figure 4.32. Comparison simulation versus measurements for 2.4GHz frequency in the considered scenario for the different simulation approaches. a) Scenario 1 b) Scenario 2 c) Scenario 3.

4.5 Analysis for large complex scenarios

Whereas the simulation examples in [Azp12, Azp14b, Azp14c, Azp14d, Azp14e, Naz12, Led13, Agu13, Lop14a, Lop14b] show an excellent agreement of the ray launching results with the measurement data, this section emphasizes on the outcomes when large and complex scenarios are analyzed. As it is explained in Chapter 3, the received power is calculated at each sample of the space taking into account the propagation losses through a medium (ε, μ, σ) at a distance d, with the attenuation constant α(Np/m), and the phase constant β(rad/m). The received power is calculated with the sum of incident electric vectorial fields in an interval of time Δt inside each cuboid of the defined mesh. Consequently, when vast scenarios are analyzed, significant contributions may be neglected for the transmitter at remote distances due to the fact that rays do not arrive to these cuboids. An illustration of this effect is depicted in Figure 4.33. It can be seen that depending on the angular resolution of the launching rays, for a fixed mesh of cuboids, there is a certain distance *d* from which the rays do not reach any cuboid and lead neglecting significant contributions.
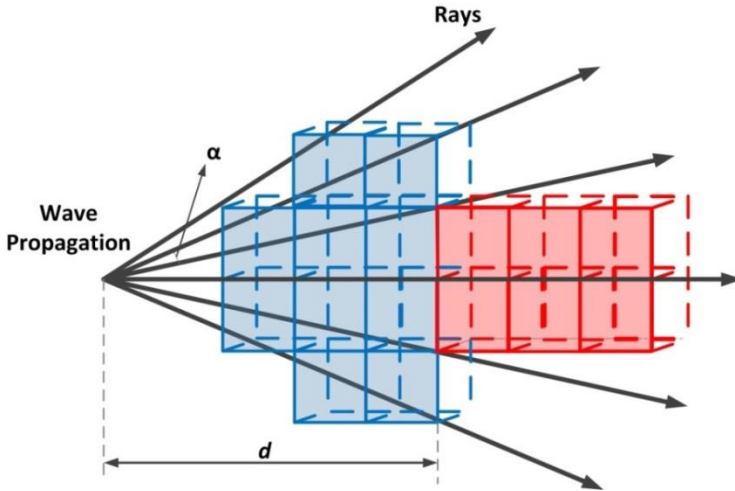

Figure 4.33. Principle of divergence for the 3D Ray Launching algorithm.

The distance *d* from which the algorithm diverges has been calculated for a Line of Sight case (LoS) and it is shown in Table 4.10 for different cuboids size. The angular resolution considered is $\Delta\Phi = \Delta\theta = 1°$ according to previous sections and reference [Azp14a].

Table 4.10. Commitment between cuboids size and distances from which rays do not reach any cuboid.

Cuboids size (m)	Distance (m) from which rays do not reach any cuboid
0.2	11.46
0.5	28.65
1	57.29
1.5	85.94
2	114.59
2.5	143.24
3	171.88

As it is shown in the following subsections, when the considered scenario is large and complex, a Non Line of Sight (NLoS) exists in most of the cases. Because of that, the previous distances shown in Table 4.10 may greatly diminish due to multipath propagation.

4.5.1 Definition of the considered scenario

In this section, an analysis of the development of the RL approach for a vast scenario has been made. The considered environment is the new Emergency Room Complex of the Hospital of Navarre, in Pamplona, Spain. A view of the new building as well as a detail image of the indoor configuration is shown in Figure 4.34.

(a)   (b)

Figure 4.34. (a) Image of the new Emergency Building, in the Hospital of Navarra, Spain (b) Detail of one of the aisles in the main specialists boxes area inside the building.

The building has a main ground floor in which most of the regular medical procedures are carried out. It consists of several zones, such as patient waiting room, intensive care unit, image diagnostics and specialist medical doctor offices. The total ground surface is ~3000m², with a very complex topology and

morphology, including different material parameters as well as sizes and shapes of rooms and hallways. On the main floor of this building, an analysis of the convergence of the 3D Ray Launching approach has been made in terms of the cuboids size of the grid considered. A schematic view of the considered scenario for simulation is represented in Figure 4.35.
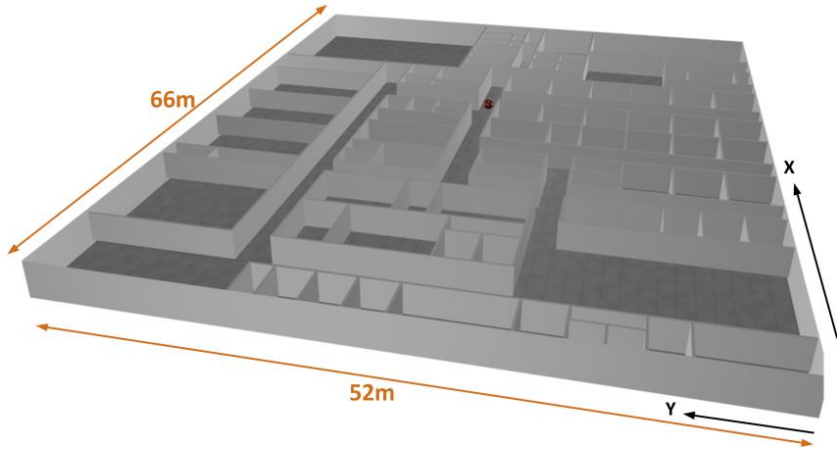

Figure 4.35. Schematic view of the whole scenario of the main floor of the New Emergency Building, in the Hospital of Navarra, Spain.

The red point in Figure 4.35 corresponds to the transmitter antenna, which is placed at the point (X=41m, Y=28m, Z=1.1m). All the elements within the scenario have been taken into account. It must be noted that the real scenario at the present time does not have furniture because is not operative yet, hence, simulations have been done without indoor furniture. The material properties for doors, windows, walls, floor and ceiling have been taken into account in the simulation model and they are the same as defined in Table 4.1 and Table 4.4 in previous sections.

4.5.2 Multipath propagation

First, an analysis of the influence of multipath propagation in the considered scenario has been made. For that purpose, the comparison of the results for the scenario with and without indoor walls has been made. Simulation parameters for both cases are shown in Table 4.11. The horizontal and vertical angle resolution have been chosen to 1º according to results in Section 4.2. Results are obtained for all samples points in the space. However, for better understanding, a radial

line of received power has been compared in the following for the empty and full scenario, which is represented in Figure 4.36.

Table 4.11. Simulation parameter for the large scenario

Ray Launching Parameters	
Frequency	2.4GHz
Transmitted Power	-10dBm
Antenna gain	5dBi
Horizontal plane angle resolution (ΔΦ)	1°
Vertical plane angle resolution (Δθ)	1°

Figure 4.36. Top view of the full schematic scenario with the location of the transmitter and the radial line for comparison.

First, simulations have been done taking into account a fixed cuboids size of 0.5m, for both scenarios. The empty scenario considered is the same scenario as Figure 4.35 but without any indoor wall. Figure 4.37 shows the estimated received power along the radial line depicted in Figure 4.36 for the empty and full scenario considering different number of reflections. It can be seen that for the full scenario (Figure 4.37b), there is a distance from the transmitter, which is around 22m, from which any ray reach further points. This is observed from the several values of -200dBm which represent that no ray has arrived to those cuboids. Thus, significant components can be neglected. On the other hand, the same

96

radial line of estimated received power is represented in Figure 4.37a for the empty scenario. In this case, it is observed that for any reflection considered, there is not a threshold distance from which the rays do not reach any cuboid. Therefore, the existence of walls inside the scenario plays an important role in the effect of multipath propagation. It must be pointed out that an analysis of the cuboids size is necessary for large scenarios because if the selection of the cuboids size is not adequate, significant components can be neglected.
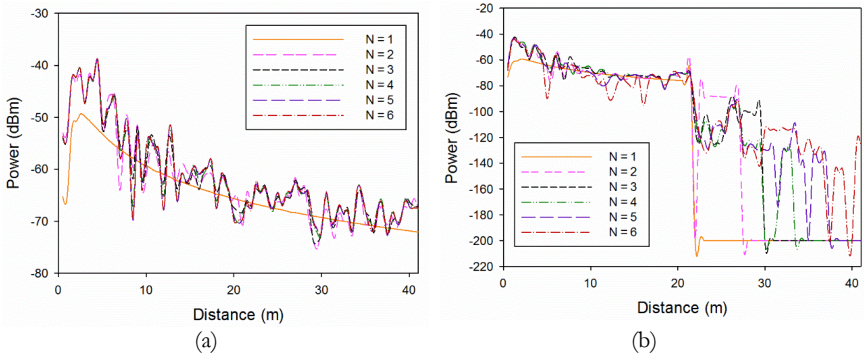

(a)

(b)

Figure 4.37. Estimated received power (dBm) along distance for different number of reflections with a fixed cuboids size of 0.5m (a) Empty scenario (b) Full scenario.
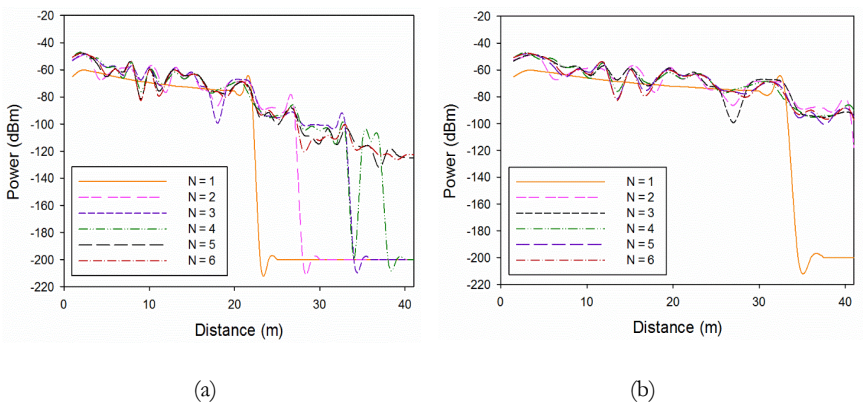

(a)

(b)

Figure 4.38. Estimated received power (dBm) along distance for different number of reflections for the full scenario (a) Cuboids size 1m (b) Cuboids size 1.5m.

Figure 4.38 shows simulation results for the same radial line depicted in Figure 4.36 for the full scenario for larger cuboids. It can be seen that the threshold distance increases as the cuboids size is also increased.

In the light of the above results, it can be conclude that an adaptive meshing is necessary in these types of scenarios, depending of the morphology, the topology and the spaciousness of the considered scenario. Because of that, an adaptive meshing has been included into the in-house developed 3D RL algorithm to obtain accurate results for large and complex scenarios. In the following subsection, the explanation of this adaptive meshing has been done as well as a comparison with measurements.

4.5.3 Adaptive meshing

In order to overcome the problem that for large and complex scenarios a fixed mesh of cuboids may lead to inaccurate results, an adaptive meshing is defined in this section. First, a campaign of measurements has been done in the real scenario to calibrate the simulation tool. With the comparison between simulation and measurements, an adequate adaptive meshing has been calculated to obtain accurate results for the whole scenario.

A campaign of measurements has been performed in the real scenario of the New Emergency Building, in the Hospital of Navarra, in Pamplona, Spain. These results provide assessment in wireless channel behavior, in order to perform adequate radio planning and an adequate adaptive meshing for the 3D RL algorithm. A transmitter antenna, connected to a signal generator at 2.4GHz has been located at the coordinates (X=41m, Y=28m, Z=1.1m) with a transmission power of -10dBm. The employed signal generator is a portable Agilent N1996A and the spectrum analyzer is an Agilent N9912 Field Fox. The antennas used are ECOM5-2400 from RS, both omnidirectional antennas[2]. Figure 4.39 shows the location for the transmitter in the simulation model and the different points of measurements which have been taken for a height of 1.1m.

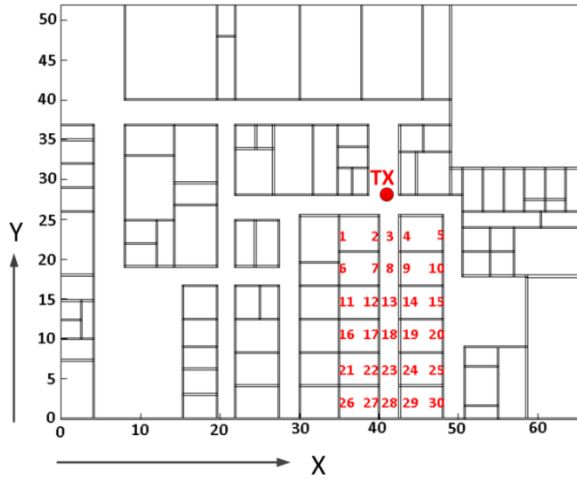[2] For more information about the measurement equipment, see Appendix B.

Figure 4.39. Measurements points within the real building of the New Emergency Building, in the Hospital of Navarra, Spain.

Figure 4.40 shows the comparison between simulation and measurement results for the measurements points depicted in Figure 4.39 for different fixed cuboids size. Measurements were performed with 100MHz bandwidth at 2.4GHz frequency. The measurement time at each point was 60 seconds, and the value of received power represented by each point is the higher peak of power shown by the spectrum analyzer for the considered bandwidth (MaxHold function in the spectrum analyzer of Agilent). The received power values estimated by simulation have been obtained for the same spatial samples as the real measurements, considering the corresponding cuboid in the three-dimensional mesh of cuboids in which the scenario has been divided.

It is observed from Figure 4.40 the evolution of the mean error between simulation and measurements versus distance. Figure 4.40a shows that cuboids of 1m size have good agreement up to a distance of 5m. Figure 4.40b matches correctly between 6 and 11m of distance from the transmitter. Figure 4.40c between 11 and 25m and Figure 4.40d from 25m ahead. Therefore, an adaptive meshing versus the distance has been implemented in the algorithm and results for the same measurements are shown in Figure 4.41, showing better agreement for all measurement points. Table 4.12 shows the mean error and SD for each case of fixed cuboids size and for the adaptive meshing, exhibiting a large decrease for the adaptive case.
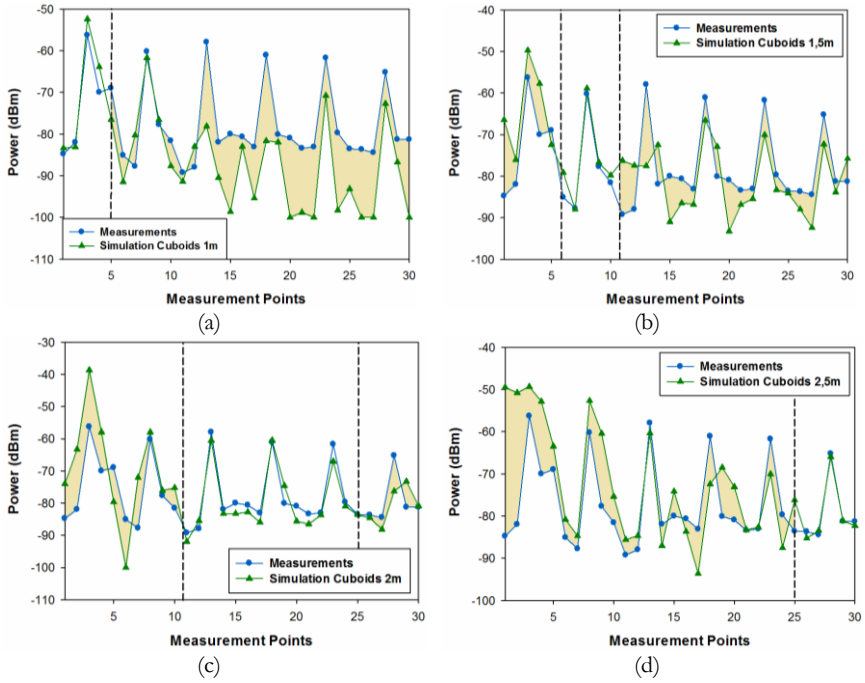
Figure 4.40. Comparison simulation versus measurements for 2.4GHz frequency (a) Fixed cuboids size of 1m (b) Fixed cuboids size of 1.5m (c) Fixed cuboids size of 2m (d) Fixed cuboids size of 2.5m.
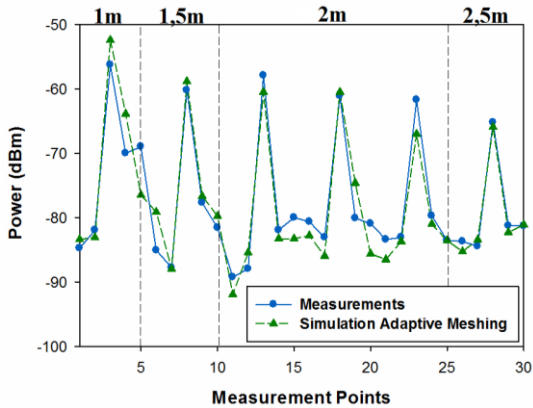

Figure 4.41. Comparison simulation versus measurements for 2.4GHz frequency with adaptive meshing.

Table 4.12. Mean Error and Standard Deviation for the different cases considered.

Cases		Mean Error (dB)	Standard Deviation
Cuboids size	1m	7.13	40.97
	1.5m	6.43	25.49
	2m	7.13	32.41
	2.5m	7.49	65.46
Adaptive meshing		2.44	4.03

Bi-dimensional planes of received power have been obtained for 1.5m height. Figure 4.42 shows the planes for different simulations of fixed cuboids size. It can be seen that for cuboids size of 1m, the received power for distances located too far away from the transmitter is not correct and an adaptive meshing is necessary. Figure 4.43 shows the bi-dimensional plane of received power for 1.5m height with the adaptive meshing, which is more accurate according with the previous measurements.

As stated previously, in Section 4.5.2, the multipath propagation is a fundamental phenomenon in this type of environment. A parameter that can grossly quantify the multipath channel is the delay spread, which shows the effects of dispersion. The delay spread has been calculated using as threshold the noise floor, with a value of -100dBm. Figure 4.44 shows the bi-dimensional planes of delay spread for 1.5m height for the whole scenario for different cases of fixed cuboids size. It is observed that in the case of 1m, the time dispersion is not very high for distances far away from the transmitter, but this can be foreseen because there are no rays reaching these cuboids. Nevertheless, for the 2.5m case, the dispersion is very high for almost every cuboid, which leads to inaccurate results. Therefore, it is demonstrated again that an adaptive meshing is necessary. Figure 4.45 shows the delay spread for the same height with the adaptive meshing, which gives accurate results. With the delay spread results, the coherent bandwidth of the channel can be calculated, leading to Bit Error Rate (BER) results, which can be very useful for capacity analysis of the radio channel.
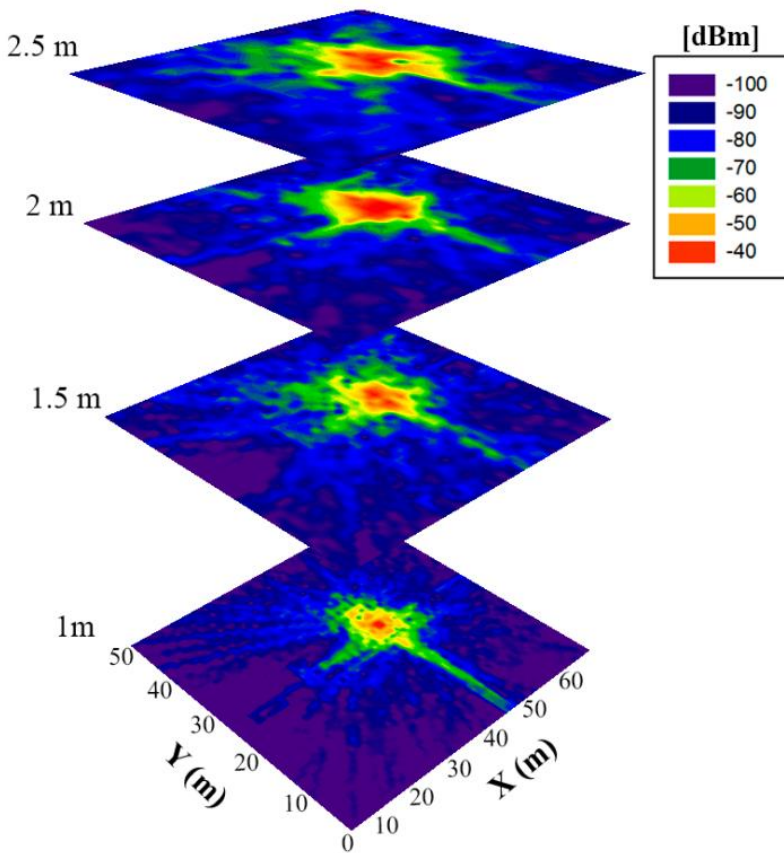
Figure 4.42. Bi-dimensional planes of received power for 1.5m of height for different cases of fixed cuboids size.
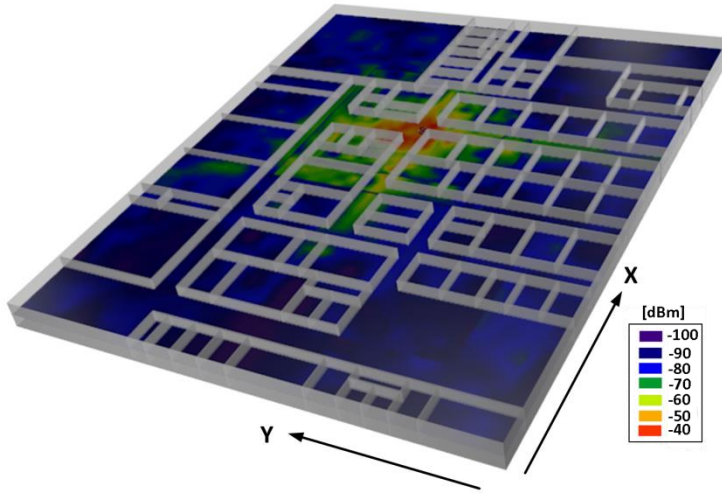
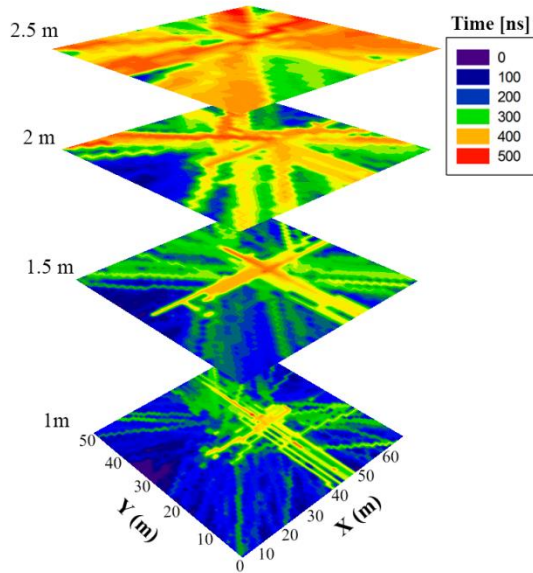**Figure 4.43**. Bi-dimensional plane of received power for 1.5m high for the adaptive meshing.

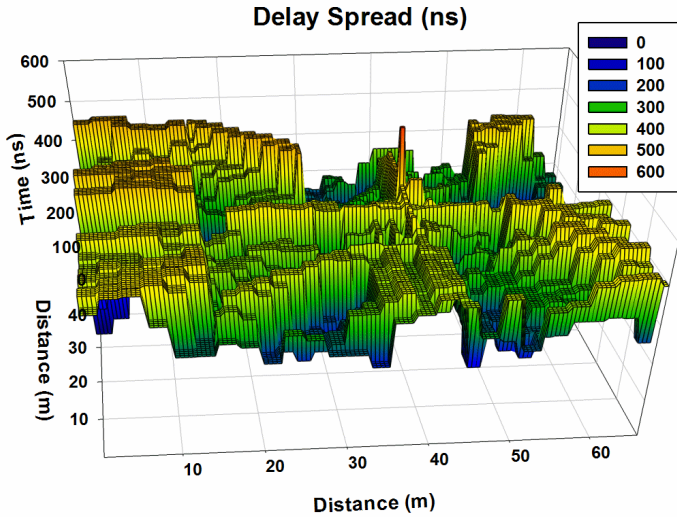**Figure 4.44**. Bi-dimensional planes of Delay Spread for 1.5m of height for different cases of fixed cuboids size.

103

Figure 4.45. Tri-dimensional plane of Delay Spread for 1.5m high for the adaptive meshing.

4.6 Summary

In this chapter, an in-depth analysis of the convergence of the in-house developed 3D RL code has been done. The different parameters which have been analyzed have been selected because they are crucial in simulation accuracy results, and a trade-off between simulation computational time and accuracy results must be achieved to obtained good results.

In order to analyze these parameters, two different types of scenarios have been assessed. First, typical office scenarios with dimensions in length lower than 30m, which we called medium scenarios, and large scenarios, with dimensions in length larger than 30m approximately. On the one hand, for the medium scenarios, the optimal parameters for the number of reflections and the angular resolution of launching rays and diffracted rays has been done, leading to the optimal parameters shown in Table 4.13. This analysis has been done taking into account simulation computational time and the accuracy of results when comparing with real measurements.

Table 4.13. Input optimal parameters in the 3D Ray Launching algorithm for medium scenarios.

Nº reflections	6
Horizontal plane angle resolution ($\Delta\Phi$)	$\pi/180$
Vertical plane angle resolution ($\Delta\theta$)	$\pi/180$
Cuboids resolution	5-15cm
Angular resolution diffracted rays	$\pi/20$
Nº reflections diffracted rays	0

On the other hand, it has been shown that when large scenarios are simulated, an adaptive meshing is necessary, because the algorithm could have divergence zones which lead to neglecting significant contributions. The adaptive meshing depends strongly on the environment. In this work, a large scenario has been analyzed with corridors and walls, but with no furniture, and the analysis and comparison with real measurements leads to the adaptive meshing shown in Table 4.14.

Table 4.14. Adaptive meshing in the 3D Ray Launching algorithm for large scenarios.

Distance	Cuboids
0-5m	1m
5-10m	1.5m
10-25m	2m
25-30m	2.5m

As a conclusion, these numerical convergence study results have led us to different optimal parameters that, depending of the dimensions of the scenario and the morphology and topology of the considered environment, could serve as a basis to obtain accurate results with an affordable simulation computational time.

Bibliography of the Chapter

[Agu13] E.Aguirre, P. López, L. Azpilicueta, J. Arpón and F. Falcone, "Characterization and Consideration of Topological Impact of Wireless Propagation in a Commercial Aircraft Environment*," IEEE Antennas and Propagation Magazine*, Vol. 55, Nº 6, December 2013.

[Azp12] L.Azpilicueta, F. Falcone, J. J. Astráin, J. Villadangos, I.J.García Zuazola, H. Landaluce, I. Angulo, A. Perallos, "Measurement and Modeling of an UHF-RFID system in a metallic closed vehicle," *Microwave and Optical Technology Letters*, vol. 54, issue 9, pp. 2123-2130, 2012.

[Azp14a] L. Azpilicueta, M. Rawat, K. Rawat, F. Ghannouchi and F. Falcone, "Convergence analysis in deterministic 3D Ray Launching radio channel estimation in complex environments," *The Applied Computational* Electromagnetic Society Journal, vol. 29, nº 4, April 2014.

[Azp14b] L. Azpilicueta, F. Falcone, J. J. Astráin, J. Villadangos, A. Chertudi, I. Angulo, A. Perallos, P. Elejoste, I. J. García Zuazola, "Analysis of Topological Impact on Wireless Channel Performance on Intelligent Street Lighting System," *Radioengineering Journal*, vol. 23, nº 1, April 2014.

[Azp14c] L. Azpilicueta, M. Rawat, K. Rawat, F. Ghannouchi and F. Falcone, "A Ray Launching-Neural Network Approach for Radio Wave Propagation Analysis in Complex Indoor Environments," *IEEE Transactions on Antennas and Propagation*, vol. 62, nº 5, pp. 2777-2786, May 2014.

[Azp14d] L. Azpilicueta, P. López-Iturri, E. Aguirre and F. Falcone, "Radio Channel characterization for Bluetooth communication systems onboard commercial aircrafts," *Microwave and Optical Technology Letters*, Vol. 56, Nº 11, November 2014.

[Azp14e] L. Azpilicueta, P. López-Iturri, E. Aguirre, I. Mateo, J. J. Astrain, J. Villadangos and F. Falcone, "Analysis of Radio Wave Propagation for ISM 2.4GHz Wireless Sensor Networks in Inhomogeneous Vegetation Environment," *Sensors*, 2014, 14, 23650-23672.

[Bal89] C. A. Balanis, Advanced engineering electromagnetics. Vol. 205. *Wiley New York*, 1989.

[Cho13] B. Choudhury, H. Singh, J. P. Bommer and R. M. Jha, "RF Field Mapping Inside a Large Passenger-Aircraft Cabin Using a Refined Ray-Tracing Algorithm," *IEEE Antennas and Propagation Magazine*, vol. 55, nº 1, pp. 276-288, 2013.

[Cui02] I. Cuiñas and M. García Sánchez, "Permittivity and conductivity measurements of building materials at 5.8GHz and 41.5GHz," *Wireless Personal Communications*, vol. 20, nº 1, pp. 93-100, 2002.

[Gri87] T. Griesser and C. A. Balanis, "Backscatter analysis of dihedral corner reflectors using physical optics and the physical theory of diffraction," *IEEE Transactions on Antennas and Propagation*, vol. 35, pp. 1137-1147, Oct. 1987.

[Led13] S. Led, L. Azpilicueta, E. Aguirre, M. Martínez de Espronceda, L. Serrano, F. Falcone, "Analysis and Description of HOLTIN Service Provision for AECG monitoring in Complex Indoor Environments," *Sensors*, vol. 13, pp. 4947-4960, April 2013.

[Lin89] H. Ling, R.C. Chou and S. W. Lee, "Shooting and bouncing rays: calculating the RCS of an arbitrarily shaped cavity," *IEEE Transactions on Antennas and Propagation*, 1989, vol. 37, pp. 194-205.

[Lop14a] P. López Iturri, E. Aguirre, L. Azpilicueta, U. Gárate and F. Falcone, "ZigBee Radio Channel Analysis in a Complex Vehicular Environment", *IEEE Antennas and Propagation Magazine*, vol. 56, Issue 4, pp. 232 – 245, Aug. 2014.

[Lop14b] P. López-Iturri, E. Aguirre, L. Azpilicueta, J. J. Astrain, J. Villadangos and F. Falcone, "Radio Characterization for ISM 2.4GHz Wireless Sensor Networks for Judo Monitoring Applications," *Sensors*, 2014,14, 24004-24028.

[Naz12] J. A. Nazábal, P. López Iturri, L. Azpilicueta, F. Falcone and C. Fernández Valdivielso. "Performance analysis of IEEE 802.15.4 compliant wireless devices for heterogeneous indoor home automation environments," *International Journal of Antennas and Propagation*, September 2012.

[Ros02] J. P. Rossi and Y. Gabillet, "A Mixed Ray Launching/Tracing Method for Full 3-D UHF Propagation Modeling and Comparison With Wide-

Band Measurements," *IEEE Transactions on Antennas and Propagation*, vol. 50, nº 4, pp. 517-523, 2002.

[Wei06] F. Weinmann, "Ray Tracing with PO/PTD for RCS modeling of large complex objects," *IEEE Transactions on Antennas and Propagation*, vol. 54, nº 6, pp. 1797-1806, 2006.

[Wei09] F. Weinmann, "UTD Shooting-and-Bouncing Extension to a PO/PTD Ray Tracing Algorithm," *The Applied Computational Electromagnetics Society Journal*, vol. 24, nº 3, pp. 281-293, 2009.

Chapter 5

Novel Hybrid Acceleration Techniques

I t has been demonstrated in the previous chapter that deterministic methods based on the RL method lead to accurate results. However, the main drawback is that the computational time can be very large depending of the required accuracy of the results. Reducing the simulation time is still a challenging problem and several acceleration techniques have been proposed in the literature to overcome this drawback. The original contribution of this chapter is the presentation of two new hybrid acceleration techniques. On one hand, a new hybrid Ray Launching-Neural Network (RL-NN) technique is presented for joint prediction of radio wave propagation using RL and NN, which is more computationally efficient as compared to the conventional RL method. This technique uses NN for modeling and storing the RL results for coverage prediction. Once NN is trained to understand RL based scenario, it allows the use of less number of launching rays in the space while power received for intermediate points can be predicted using NN. This result in computational requirements to be reduced by 80% in terms of simulation time compared with a very high-resolution fully 3D RL simulation [Azp14].

On the other hand, a novel Ray Launching-Diffusion Equation (RL-DE) approach for electromagnetic propagation analysis in complex indoor environments has also been proposed in the second part of this chapter. This technique combines the 3D RL algorithm based on Geometrical Optics (GO) and Uniform Theory of Diffraction (UTD) with the Diffusion Equation (DE)

method based on the equation of transfer. A comparison between the GO only approach, GO with edge contributions approach and the new method considering the DE has been presented for studying indoor radio wave propagation. The GO with DE method achieves accurate results when compared with measurements with a high gain in terms of computational efficiency, resulting in approximately 40% saving in simulation time when compared with the full method based on GO with UTD and DE approach [Azp15].

The chapter is organized as follows. In Section 5.2, the RL-NN approach is presented. The new method is analytically described with the geometry of the environment under consideration, following by the comparison of the neural networks considered for the new hybrid method. RL-NN results and discussion are presented in subsection 5.2.5 of this chapter.

The second part of the chapter (Section 5.3) is focused in the RL-DE approach. The new method is described, following with simulation examples and verification. Measurement results and discussion of this new method are presented in subsection 5.3.4.

5.1 Related work

As stated in previous chapters, deterministic methods based on Ray Tracing (RT) or Ray Launching (RL) techniques are the most frequently applied ones to radio coverage prediction. Historically, RL and RT were both classified as ray tracing methods, although more recently both methods are distinguished. The differences are mainly due to different approaches. RL technique principle is that the transmitter launches thousands of test rays in a solid angle and the true path is determined by looking for the rays arriving at the receiver, whereas in classical RT methods the reflected paths by walls and furniture are found by computing the image of the transmitter or of the receiver. These methods are precise but are time-consuming due to inherent computational complexity. Their combination with UTD [Kou74] is most frequently applied to radio coverage prediction [Gen09, Son99, Tay09, Son09]. The RT and RL models potentially represent the most accurate and versatile methods for urban and indoor, multipath propagation characterization or prediction.

Nevertheless, the computational time in the conventional RL, called the Shooting-and-Bouncing-Ray (SBR) method [Lin89], can be very large depending of the accuracy of the results. Reducing the simulation time is still a challenging problem and several acceleration techniques have been proposed in the literature

to overcome this drawback. The main technique focuses on reducing the number of intersections tests of the rays with the objects in the environment. This reduction is mainly done by using geometrical algorithms based on the concept of bounding volumes [Gla89, Gol87]. Bounding volumes are simple geometric objects that surround the objects of the environment in a tree-like manner. The algorithm finds the intersected wall through searching in the tree generated by the bounding volumes instead of using a brute force method. Some examples are reported in [Tor99] where the binary space is partitioned and in [Cat98] where the volumetric space is partitioned and angular Z-buffer is used. In [Sae00] several acceleration techniques to enhance data storing and processing are presented. Some authors have worked on speed-up methods by splitting the 3D problem into two 2D sub-problems [Ros02, Cor02], while the decomposition of 3D ray propagation into 2D vertical planes is proposed in [Lia98]. In [Zhe00a, Zhe00b], the environment is tessellated using rectangular and triangular meshes, respectively. A preprocessing and discretization of the database of the environment are proposed in [Hop03]. Finally, two different classes of methods for speeding up ray tracing are presented in [Deg09], aimed at reducing the size of input database and the number of rays to be handled by the algorithm.

5.2   The Ray Launching-Neural Network Approach

One of the major drawbacks of the RL method is that most of the rays emitted from the source do not reach the receiver and none of the acceleration techniques mentioned above is capable of solving this problem. However, the number of launching rays could be decreased with the aid of a trained neural network (NN) which predicts the results for intermediate rays, resulting in a significant decrease of the computational burden. In this section, we will present a new coverage prediction method based on this idea.

5.2.1 Ray Launching Simulation

As a starting step, a high resolution RL simulation has been done to achieve accurate results of the propagation channel. The results of this simulation are considered as a reference for comparing the proposed technique with current state of art. In addition, measurements have been performed in a typical indoor scenario in order to verify the high resolution RL results.

Two scenarios have been considered for the analysis. First, a canonical scenario which corresponds to with a small office on the second floor of the Electric and Electronic Department of the Public University of Navarre has

served as the set up for the experiments. Measurements have been performed in this scenario and they have been compared with simulation. A schematic view is shown in Figure 5.1 whose dimensions are 3.5m x 4m x 2.5m. The small office has two desks and one bookshelf. Objects are defined as different hexahedra in the algorithm. This basic geometric shape can be conveniently used to model any complex objects, such as tables, chairs and shelves, and placing them into the room. All the materials within the scenario have been taken into account for the simulation, like metal for the bookshelf, wood for the desks, and plasterboard for the walls, considering their dielectric constant and conductivity for the given frequency of operation.
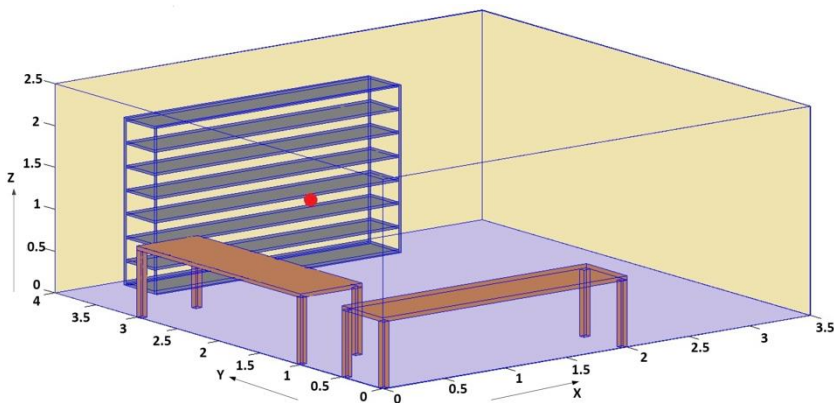

Figure 5.1. Initial scenario implemented for simulation validation.

The second considered scenario is the iRadio laboratory of the University of Calgary, which has dimensions given as 8.91m by 17.85m by 3.93m. This scenario is much more complex and bigger than the first one. A schematic view of the simulated scenario is depicted in Figure 5.2, with the typical work stations of a laboratory. The material parameters used for both scenarios at 2.4GHz frequency are provided in Table 5.1.

Table 5.1. Material Properties in the Ray Launching Simulation

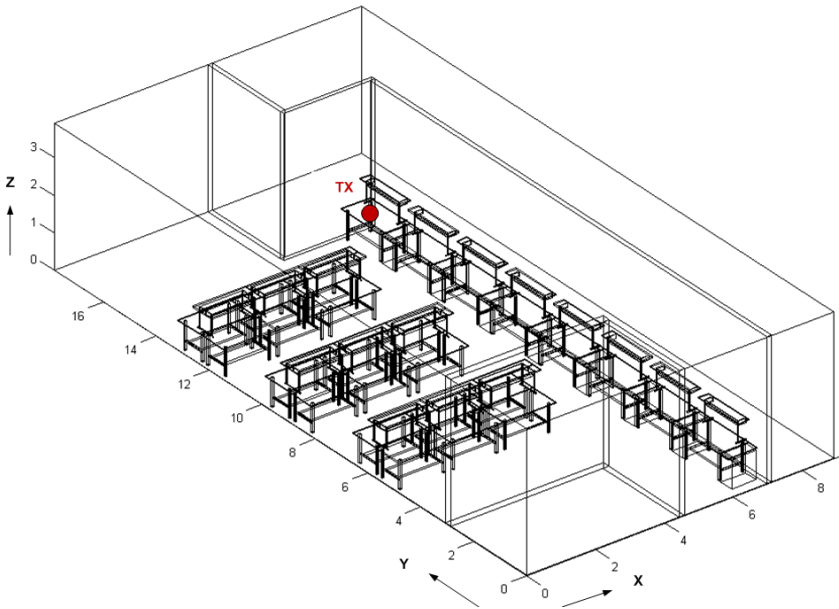| Parameters	Air	Aluminum	Wood	Plasterboard
Permittivity (ε_r)	1	4.5	2.88	2.02
Conductivity (σ)[S/m]	0	4.107	0.21	0.06

Figure 5.2. Schematic view of the considered scenario for deterministic radio channel simulation.

Table 5.2 shows the selected parameters for the high resolution RL simulation. The transmitter and receiver antennas are omnidirectional, with 5dBi gain respectively. The angular resolution in the horizontal ($\Delta\Phi$) and vertical plane ($\Delta\theta$) for the launching rays is 0.5°. The number of reflections considered in the simulation is seven. It should be noted that these parameters are not the optimum ones presented in Chapter 4, but they have been chosen because a high accuracy is required, although the simulation time could be higher.

Table 5.2. High Resolution Ray Launching Parameters

Frequency	2.4GHz
Transmitter power	0dBm
Antenna gain	5dBi
Horizontal plane angle resolution ($\Delta\Phi$)	0.5°
Vertical plane angle resolution ($\Delta\theta$)	0.5°
Reflections	7
Cuboids resolution	12cm x 12cm x 12cm

5.2.2 Multidimensional Neural Networks

For a fixed transmitter position, power decreases with respect to the distance from the transmitter and can be perceived as a nonlinear function of relative coordinates, X, Y and Z. This work proposes the use of neural network to model this multiple-input-single-output nonlinear function. In general, neural networks work on the principle that any nonlinear function can be approximated by summation of weighted nonlinear functions [Hay99]. A simple neural network contains nonlinear activation functions which map input signal into different nonlinear domains. These nonlinear outputs are multiplied by an appropriate weight and biased by a constant value (known as bias value) such that summation of these output domains is eventually equal to the required output.

An analogy can be perceived between the ray-launching scheme, where the space is segmented into 3D blocks and the power is computed for each block, and the neural network scheme where each activation function output provides nonlinear segmentation and weight/bias is adjusted to imitate computed power.

For multi-dimensional modeling, Feed-Forward NN (FFNN) and Radial Basis Function NNs (RBFNN) are used extensively. A FFNN neural network increases number of nonlinear segmentation using two layers containing activation functions. According to control theory, two transfer functions in series provide multiplication of transfer functions thus providing higher nonlinearity. A RBFNN uses a single layer with very high number of neurons with the same goal of achieving higher number of nonlinear segmentation. The working of these NNs is explained in detail in next subsection. In addition, the modeling capability of these NNs is assessed for the three cases shown in Table 5.3.

Table 5.3. High Resolution Ray Launching Parameters

Case 1) $\Delta\Phi = \pi/90$, $\Delta\theta = \pi/90$ (16,200 rays).
Case 2) $\Delta\Phi = \pi/180$, $\Delta\theta = \pi/180$ (64,800 rays).
Case 3) $\Delta\Phi = \pi/360$, $\Delta\theta = \pi/360$ (259,200 rays).

In the following, it has been discussed both NNs and their comparison from an analytical point of view.

A) Feedforward Neural Network:

FFNN contains one input layer, one hidden layer and one output layer. Figure 5.3a shows a fully connected feedforward NN. Weights are initialized randomly in the interval of [-0.8, 0.8] and converge toward their optimal values as the training proceeds.

During the forward computation, data from neurons of a lower layer (i.e., kth layer) are propagated forward to neurons in upper layer [i.e., $(k+1)$th layer]. The net input to any neuron, i, in any layer $(k+1)$ is given by [Hay99]:

$$\text{net}_i^{k+1} = \sum_{j=1}^{p} w_{ij}^{k+1} o_j^k + b_i^{k+1} \qquad (5.1)$$

Where w_{ij}^{K+1} denotes the synaptic weight connecting the jth input from the previous layer to the ith neuron of the present layer, P denotes the total number of neurons in the previous layers, and b_i^k denotes bias of the ith neuron in the kth layer. The output of neuron i at any layer (k) is calculated as:

$$o_i^k = f(\text{net}_i^k) \qquad (5.2)$$

The output of any layer works as an input to the next layer. The output layer has a linear activation function, which sums up the outputs of hidden neurons and linearly maps them to the output. The activation function, f, chosen for two hidden layers is the hyperbolic tangent, which maps nonlinearity between -1 and 1.

The goal of training is the minimization of the error between the expected value and the actual NN that was determined in the forward computation. During the forward pass, the cost function or error energy is given by:

$$\xi = \frac{1}{2N} \sum_{n=1}^{N} \{[I_{\text{out}}(n) - \hat{I}_{\text{out}}(n)]^2 + [Q_{\text{out}}(n) - \hat{Q}_{\text{out}}(n)]^2\} \qquad (5.3)$$

where ξ is total error, $I_{out}(n)$ and $Q_{out}(n)$ are the desired outputs, N denotes the total number of training samples, and $\hat{I}_{out}(n)$ and $\hat{Q}_{out}(n)$ are the outputs from output- layer neurons.

Starting with the output layer and moving back towards the input layer, the error term for the i_{th} neuron in k_{th} layer is calculated as:

$$\varepsilon_i^k = \begin{cases} t_i - o_i^k & k = \text{Output Layer} \\ \sum_{j=1}^{P} w_{ij}^{k+1} \delta_j^{k+1} & k = \text{Hidden Layer} \end{cases} \tag{5.4}$$

Where P is number of neurons in the j_{th} layer, the local gradient, δ_i^{k+1}, for the i_{th} neuron in the $(k+1)_{th}$ layer can be calculated as

$$\delta_i^k = \varepsilon_i^k f'(\text{net}_i^k) \qquad k = \text{Present Layer} \tag{5.5}$$

where $f'(net_i^k)$ is the derivative of the activation function.

With the aim of minimizing the error energy given in (5.3), the backward computation is done in batch mode to adjust the synaptic weights and biases of the network, according to the Levenberg-Marquardt algorithm [Hay99]:

$$\Delta X = [J^T(X)J(X) + \mu I]^{-1} J^T(X)e(X) \tag{5.6}$$

where μ is the gain constant, $J(X)$ is the Jacobian matrix calculated over the error matrix, e(X), with respect to X, where:

$$X = [w_{11}^1 \, w_{12}^1 ... w_{nR}^1 \, b_1^1 ... b_n^1 ... w_{11}^h \, w_{12}^h ... w_{nR}^h \, b_1^h ... b_n^h] \tag{5.7}$$

$$e(X) = [\varepsilon_x(1) \, \varepsilon_y(1) \varepsilon_z(1) ....\varepsilon_x(N) \, \varepsilon_y(N) \varepsilon_z(N)] \tag{5.8}$$

N denotes the total number of training samples, h denotes the outermost layer. A complete description of the Levenberg-Marquardt algorithm for a three-layer feedforward NN can be found in [Hay99], which is a numerical optimization of the Gauss-Newton method, where a small value of μ provides a Gauss-Newton solution and a very high value provides steepest descent solution. During initial iterations, μ is selected to be high (=.01); and, the algorithm converges swiftly according to steepest descent. After every iteration μ is divided by β (=10); and, after a few iterations, the algorithm takes the form of a second-order Gauss-Newton optimization, which avoids falling into local minima. The whole procedure is carried out repeatedly until the desired performance is attained or the NN starts failing the validation procedure, drifting away from the generalization criterion. The FFNN model had three neurons in input layer to

account for three inputs as X, Y, Z position co-ordinates and one neuron at the output layer to account for power at that co-ordinate. Figure 5.3b shows model performances in terms of absolute mean error, Standard Deviation (SD) and Normalized Mean Square Error (NMSE) with respect to number of neurons in hidden layer for the simplest case of Case 1 and number of neurons in hidden layer chosen as 15.
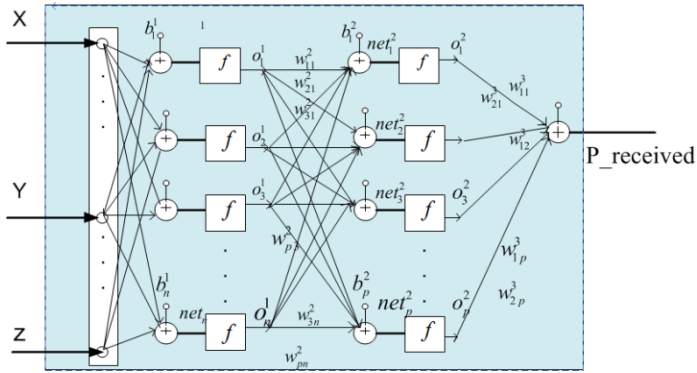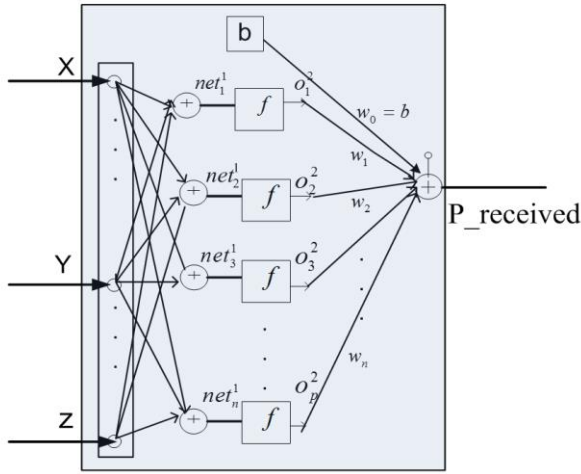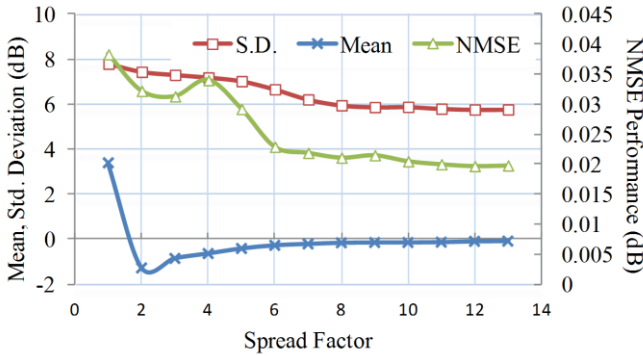

(a)
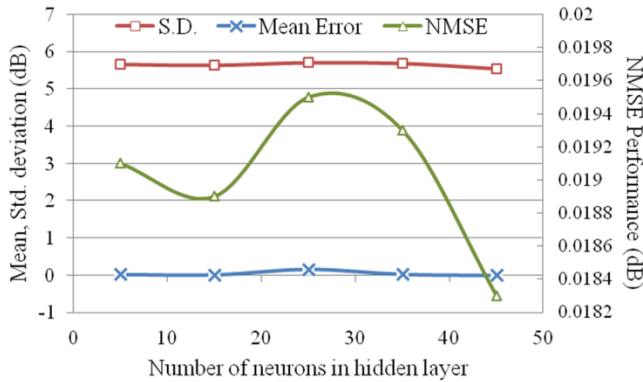
(b)

Figure 5.3. (a) Feedforward NN architecture (b) Number of hidden neurons selection for Case 1.

(a)

(b)

Figure 5.4. (a) Radial basis function architecture (b) RBFNN spread factor impact on modeling for Case 1.

B) Radial Basis Function Neural Network:

The topology of RBFNN is shown in Figure 5.4a, where only one layer of weights is to be adjusted. The training procedure works as follows [Hag94]. Computational cost of learning for RBFNN is less than FFNN as neurons are added as learning continues. Initially, the hidden layer has no neuron. The nonlinear function, $\{f_i = G(\|x - t_i\|), i = 1,2 \dots M\}$ is the Green's function defined as

$$G(\|\boldsymbol{x} - t_i\|) = \exp(-\frac{1}{2\sigma_i^2} \|\boldsymbol{x} - t_i\|^2) \qquad (5.9)$$

which is a multivariate Gaussian function with variance σ_i^2 (spread factor), where x is the input vector and {ti, i=1, 2…M} are the centers of G(.). The output of the j_{th} output node is given by

$$y(x) = W_{ij}.G(\|x - t_i\|) + b \qquad (5.10)$$

where W_{ij} are the weights and b is a bias term. The smoothness of the approximation is determined. The following steps are repeated until the mean squared error falls below goal, or the number of neurons reaches to a predefined number. The goal here is set to zero.

Step-1) The network is simulated.
Step-2) The input vector with the greatest error is found.
Step-3) A neuron is added with weights equal to that vector.
Step-4) The output layer weights are redesigned to minimize error according to least mean square method. The topology requires selection of appropriate spread factor, shown in Figure 5.4b, which is selected as 12.

5.2.3 Ray Launching modeling with NN

The implemented RL algorithm subdivides the simulation volume in uniform cuboids or blocks. In this section, each scenario in the case study is divided into a grid. The X-axis in the grid contains 146 blocks, Y-axis contains 73 blocks and Z-axis contains 33 blocks. NNs are trained for a low resolution scenario with some blocks omitted and tested for complete scenario in each case. Table 5.4 shows the modeling results for RBFNN and FFNN for the three cases. The comparisons are made in terms of total time consumption for NN training, total memory taken by processor for training including all variables as well as trained network, NMSE, SD and mean error.

It can be perceived that FFNN is efficient in terms of time while RBFNN is efficient in terms of total memory required. Due to significant saving in training time, FFNN has been chosen in this thesis for NN based modeling of RF trend. However, RBFNN can also be used according to memory or time requirement of any computing system because modeling performances in terms of NMSE, SD

and absolute mean errors are almost equivalent for both NNs. It is to be noted that processing data of 1.96GB has been modeled and saved using FFNN which requires 1.6MB memory space to train and save all data in a network.

Table 5.4. Modeling Results for FFNN and RBFNN for the three cases shown in Table 5.3.

	Case 1		Case 2		Case 3	
	FFNN	RBFNN	FFNN	RBFNN	FFNN	RBFNN
Memory Consumption (MB)	1.68	1.635	1.634	1.6322	1.633	1.612
Time Consumption (s)	403.46	3591.8	306.36	3491	305.53	3463.6
Std. Deviation (dB)	5.63	5.7655	9.89	10	5.586	5.6324
NMSE (dB)	.0189	.0198	.0543	.0553	.0164	.0165
Absolute Mean Error (dB)	.0149	.0874	.0603	.3343	.131	.1345

Once the NN based modeling has been chosen, in order to evaluate the proposed hybrid RL-NN technique, different cases for low resolution RL simulation have been tested, storing and modeling the parameters for training the data with a NN. These cases are presented in Table 5.5. Case 1 is the high resolution case and the rest are the low resolution cases. Specifically, Case 2, 3 and 4 have the same horizontal and vertical angular resolution, but with different number of reflections, whereas Case 5 presents a lower angular resolution with a higher number of rebounds.

Table 5.5. Different cases for the Ray Launching Simulation

Ray Launching High Resolution			
Case 1	$\Delta\Phi = \Delta\theta = \pi/360$	259,200 rays	N° reflections = 7
Ray Launching Low Resolution			
Case 2	$\Delta\Phi = \Delta\theta = \pi/360$	259,200 rays	N° reflections = 6
Case 3	$\Delta\Phi = \Delta\theta = \pi/360$	259,200 rays	N° reflections = 5
Case 4	$\Delta\Phi = \Delta\theta = \pi/360$	259,200 rays	N° reflections = 4
Case 5	$\Delta\Phi = \Delta\theta = \pi/180$	64,800 rays	N° reflections = 7

The high resolution RL simulation has been compared with the accuracy of the different cases of low resolution RL with FFNN. Error means and standard deviations have been calculated comparing simulation results of RL high resolution with the different cases of RL low resolution and NN. Table 5.6 shows these results, showing that the highest error mean is for Case 5. It is observed that the mean error increases considerably when the number of rays has been

decreased (Case 5). However, when the angular resolution is maintained and the number of reflections changes, there is not significant variability in the mean error.

Table 5.6. Error mean and Standard Deviation of the comparison of RL high resolution with different cases of RL low resolution and NN

	Mean Error (dB)	Standard Deviation (dB)
RL LR Case 2 + NN	0.071	5.593
RL LR Case 3 + NN	0.110	5.636
RL LR Case 4 + NN	0.288	5.969
RL LR Case 5 + NN	2.839	5.521

However, it is highly important to consider also the simulation computational time and computer consumption memory. Figure 5.5 and Figure 5.6 show simulation computational time and memory consumption for all the cases. It is observed that RL high resolution is the most demanding one in terms of time and computer memory, and the rest of the cases have fewer requirements. To better understand this statement, Table 5.7 shows the percentage of computational time and computer consumption saving for each one of the new joint prediction methods RL low resolution and NN.

Table 5.7. Computational time and computer consumption saving of RL high resolution versus different cases of RL low resolution and NN.

	Computational time saving	Computer consumption saving
RL LR Case 2 + NN	40%	29%
RL LR Case 3 + NN	64%	51%
RL LR Case 4 + NN	80%	68%
RL LR Case 5 + NN	90%	68%

It is observed that the highest computational time saving is for Case 5, when the angular resolution of launching rays has been decreased. However, considering the results of Table 5.6, the mean error for this case increases considerably. Because of that, and taking into account that the computer consumption saving is the same for Case 4 and Case 5, Case 4 has been chosen in this work for testing the new joint prediction method RL-NN.

After this analysis, in order to evaluate the proposed hybrid RL-NN technique, a low resolution RL simulation with vertical and horizontal angular resolution of $\pi/360$ and only four reflections (Case 4 of Table 5.5) has been made, storing and modeling the parameters for training the data with a NN, achieving accurate results comparable to the high resolution RL simulation as a reference technique. Results are presented in Section 5.2.3, after measurement results.
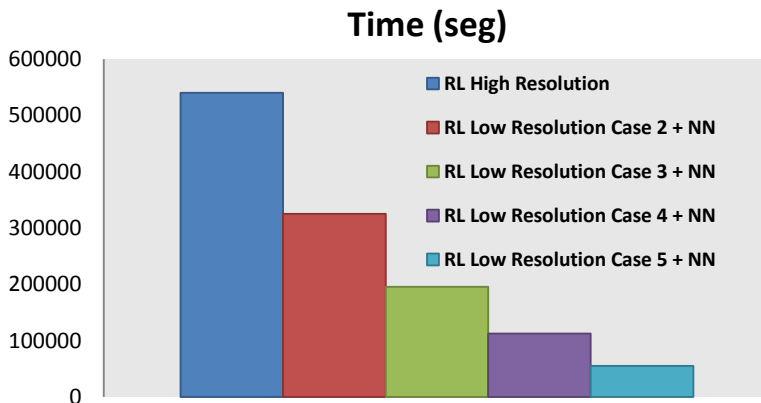

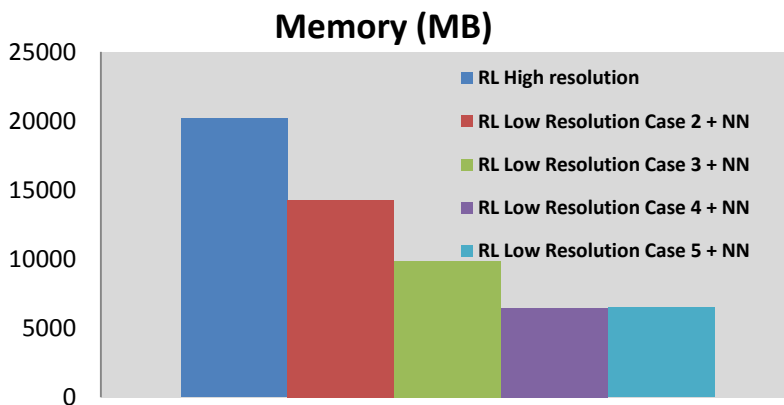**Figure 5.5**. Computational time required for the different simulations considered.


Figure 5.6. Memory consumption required in an Intel Xeon CPU X5650 @2.67GHz 2.66GHz for the different cases considered.

5.2.4 Measurement Results

In order to validate high resolution RL predictions, measurements have been performed for the first scenario depicted in Figure 5.1. The wideband measurements were performed with 100MHz bandwidth at 2.4GHz frequency, a potential situation in which Wireless Local Area Network/Wireless Personal Area Network applications and services are employed. The transceivers are from Texas Instruments, specifically the CC2530 that is a true system-on-chip (SoC) solution for IEEE 802.15.4 ZigBee. The radiation pattern of the transceivers is omnidirectional with linear polarization and 0.82dBi gain[1]. Measurements have been made with the transmitter fixed at the point XY (0.75m, 2m) with a height of 1.5m (the transmitter is depicted as a red point in Figure 5.1). The transmitter power is 0dBm.
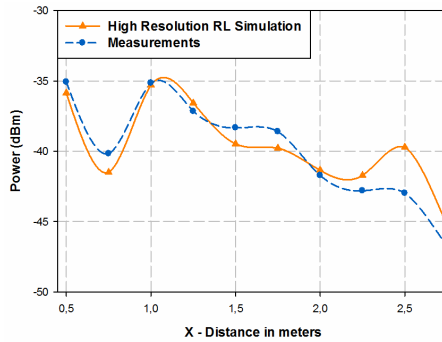
(a)
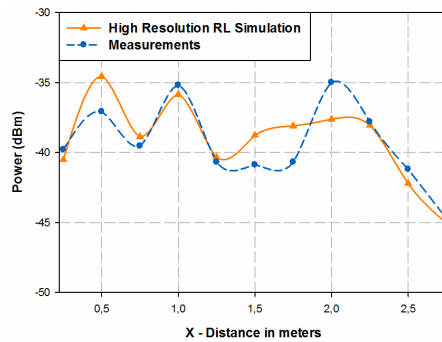
(b)

Figure 5.7. Comparison simulation versus measurements along the X-axis (a) y=1m (b) y=2m.

[1] For more information about the measurement equipment, see Appendix B.

A portable spectrum analyzer from Agilent (N9912 Field Fox) has been used for the experiments. The measurement time at each point is 60 seconds and the power value represented by each point is the higher peak of power shown by the spectrum analyzer for the considered bandwidth (MaxHold function in the 9912A Field Fox Spectrum Analyzer). Measurements have been performed for y=1m and y=2m, each 0.25m along the X-axis.

Figure 5.7 shows the comparison between simulation and measurements, exhibiting good agreement with a mean error of 0.23dB with a standard deviation of 1.65dB. The differences are mainly due to approximations made in simulation within the morphological details of the definition of the scenario, which in the case of scenarios such as this one with rich multipath components, has a significant influence.

5.2.5 RL-NN Results and Discussion

Once the RL simulation code as well as the NN algorithm has been validated, both techniques are combined in order to increase computational efficiency. This validation has been performed by comparison of RL estimation (previously compared with measurements) with the obtained NN results. Figure 5.8 shows the estimated received power corresponding to the measured scenario previously depicted in Figure 5.1. The high resolution RL results are compared with the new joint prediction method described above as RL-NN. It can be seen that the new method RL-NN follows the trend correctly, achieving a significant reduction in computational time and resources required for simulation with this new method.

Figure 5.9 and Figure 5.10 show the received power at two different heights in the indoor scenario of the iRadio Laboratory (depicted in Figure 5.2) for the full 3D High resolution RL and the proposed RL-NN technique which employs low resolution RL.
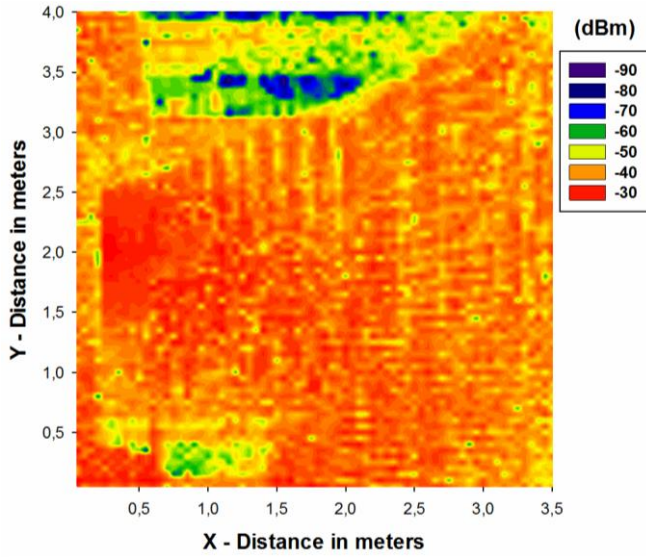
(a)
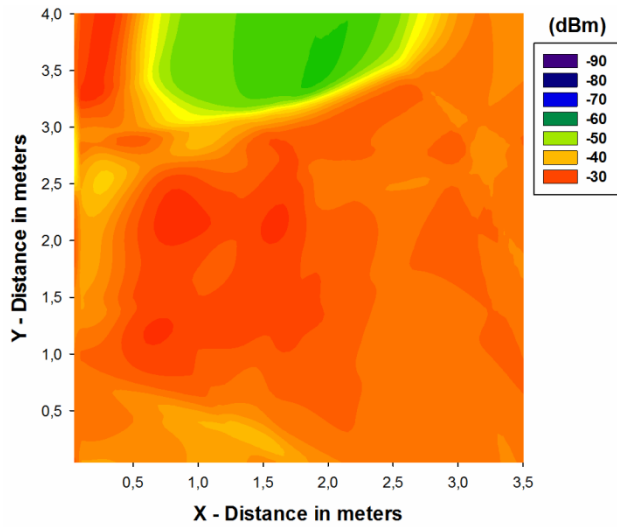
(b)

Figure 5.8. Bi-dimensional planes of estimated received power for a height of 1m in scenario of Figure 5.1 with (a) RL High Resolution and (b) RL Low Resolution and Neural Network.

125

(a)   (b)

Figure 5.9. Bi-dimensional planes of estimated received power for a height of 0.95m in scenario of Figure 5.2 with (a) RL High Resolution and (b) RL Low Resolution and Neural Network.

(a)   (b)

Figure 5.10. Bi-dimensional planes of estimated received power for a height of 1.92m in scenario of Figure 5.2 with (a) RL High Resolution and (b) RL Low Resolution and Neural Network.
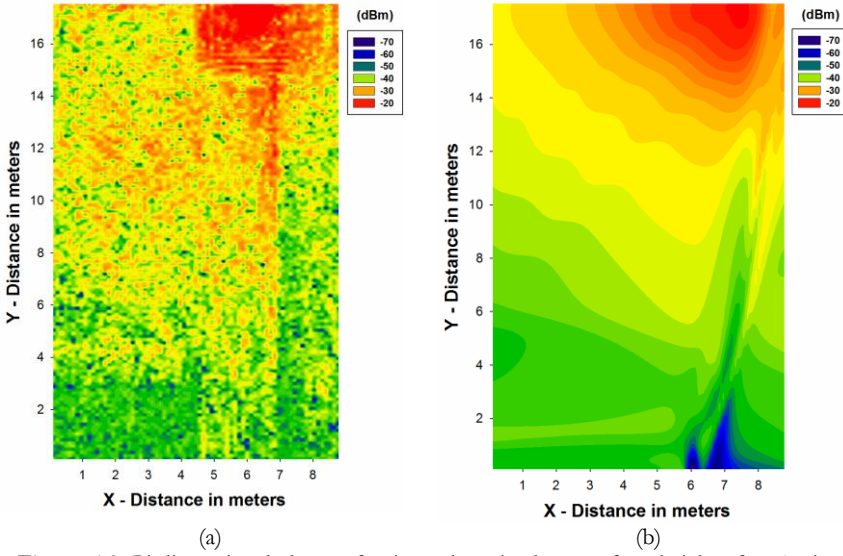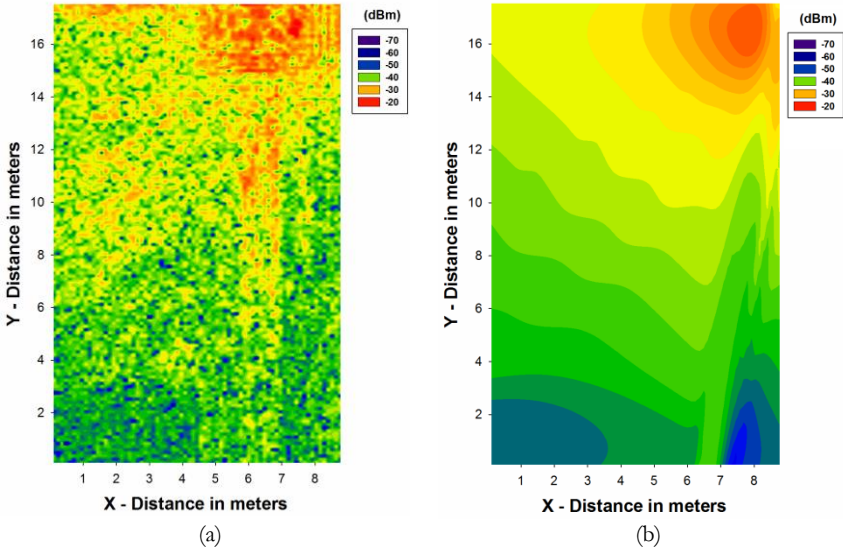
For both heights, a good agreement between the results of the proposed method and fully 3D High resolution RL is observed. A mean error of 0.07dB and 1.19dB is noticed between the results of these two techniques at 0.95m and 1.9m heights respectively. It is worth mentioning that while obtaining these results, an interaction with the different elements within the indoor scenario is considered and it is observed that the material properties of the objects (see Table 5.1) play a relevant role in the overall performance of the wireless system.

The comparison between the received power along the Y-axis, for x=2m and z=0.95m height is shown in Figure 5.11. It can be observed that even in high resolution RL, significant variations are present. This is due to multipath propagation, which is a dominant phenomenon in any indoor environment and can be characterized by the temporal dispersion of the signal and the frequency dispersion because of temporal variations of the received amplitude. Thus, the RL-NN technique also follows the trend of the high resolution RL technique.
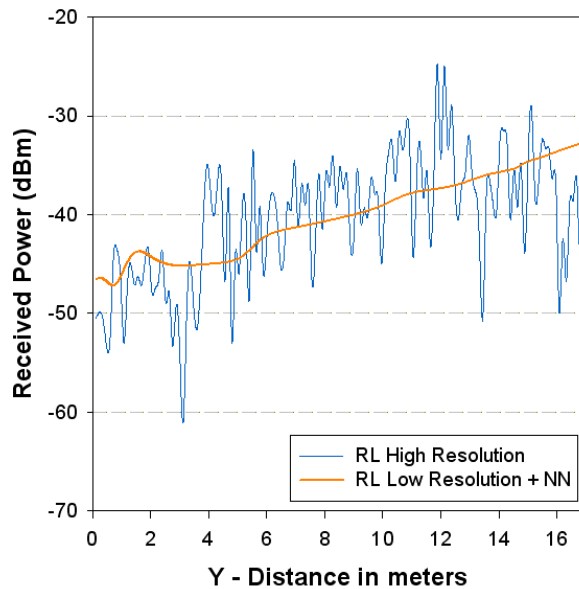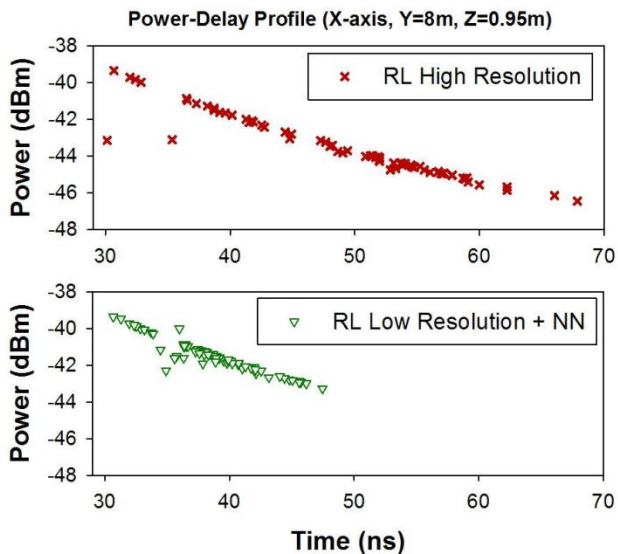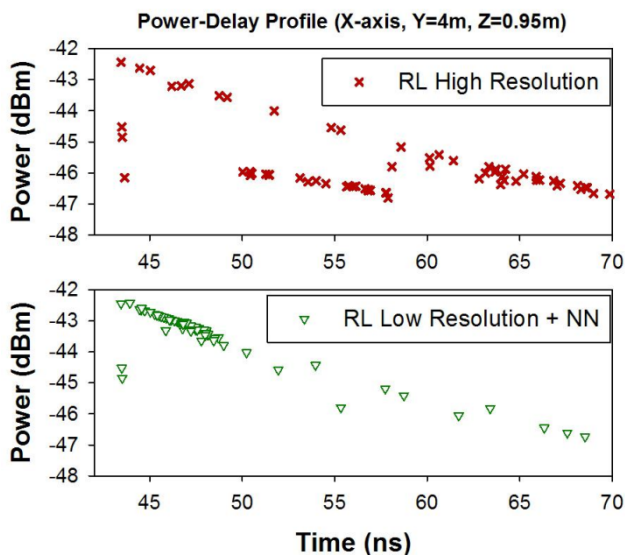

Figure 5.11. Estimated received power along the Y-axis, for X=2m and Z=0.95m, for RL High Resolution and the RL+ NN proposed technique.

127

(a)

(b)

Figure 5.12. Power-Delay Profile along the X-axis for Z=0.95m, for RL High Resolution and the RL-NN proposed technique (a) Y=8m (b) Y=4m.

To illustrate the relevance of the multipath effect in the propagation channel, the Power Delay Profile (PDP) has been predicted along the X-axis, for Y=8m and Z=0.95m (Figure 5.12a) and for Y=4m and Z=0.95m (Figure 5.12b). The PDP has been calculated for each cuboid along the X-axis, taking into account all the multipath components which arrive to the receiver cuboid, a similar procedure adopted in the case of PDP estimation by means of grid measurements [Isa05, And12]. Figure 5.12 represents the most significant component of the PDP for each sample point along the 8.7m of the X-axis of the scenario depicted in Figure 5.2. From these figures it can be seen that there are a large number of echoes in the scenario and the significant components do not have relevant variance between both methods. Figure 5.12 shows the comparison for two different cases, but the whole scenario has been characterized and compared. It is worthy to mention that the hybrid method lead to more accurate results for the first components of the multipath trajectory, as it can be seen in the depicted cases, that the tail of the PDP is not as accurate as the comparison of the first components. This is due to the fact that the proposed RL method performs the calculation in a given frequency point and hence, is inherently narrowband for a single calculation sweep. The RL-NN method provides an estimation in which a smaller amount of rays are present and therefore, the available time domain information is reduced.
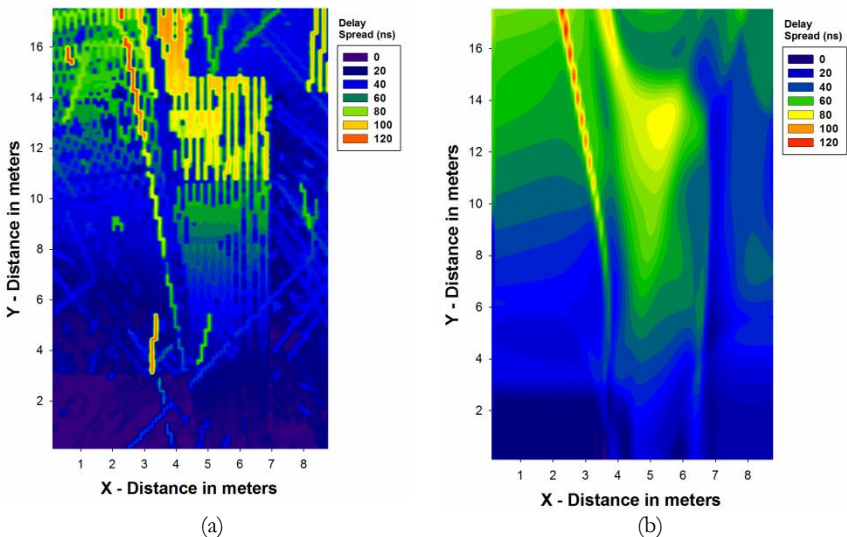

(a)   (b)

Figure 5.13. Bi-dimensional planes of estimated RMS delay spread for a height of 1.9m in scenario of Figure 5.2 with (a) RL High Resolution and (b) RL Low Resolution and Neural Network.

129

To illustrate the multipath propagation properly, the RMS delay spread has been predicted for the scenario depicted in Figure 5.2 for both simulation methods. The RMS delay spread has been calculated using as threshold the noise floor and it is shown in Figure 5.13. It can be seen that the surrounding physical environment, as well as the geometrical position of the transmitter and the receiver, have a relevant influence in time dispersion of the mobile radio channel.

The new proposed method for coverage prediction achieves a good trade-off between accuracy and computational efficiency.

Table 5.8 shows the improved performance of the new method RL-NN versus the high resolution RL method in terms of computational time and energy consumption. The CPU-time savings reported include the FFNN training in the new joint approach RL-NN. The results shown present 80% reduction in terms of simulation time compared with High Resolution RL. In addition, whole 3D space data is stored in a parametric form in terms of NN weights, which lead to a 70% less memory space used in storing the massive data. The mean error acquired with the new proposed method compared with the reference solution is 0.28dB with a standard deviation of 5.96dB. These results indicate that low resolution RL results may not fully capture fast fading phenomena. Therefore, a trade-off between computational complexity and final accuracy is present when employing this combined approach.

Table 5.8. New Joint Prediction method RL-NN

Computational time saving	80%
Computer consumption saving	70%
Mean Error	0.28dB
Standard Deviation	5.96dB

5.3   The Ray Launching-Diffusion Equation Approach

A novel and efficient deterministic approach to model radio wave propagation channels in complex indoor environments reducing computational complexity is proposed in this section. This technique combines the 3D RL algorithm based on GO and UTD with a Diffusion Equation (DE) method based on the equation of transfer. A comparison between the GO-only approach, GO with edge contributions approach and the new method considering the DE is presented for studying indoor radio wave propagation.

It is generally believed that electromagnetic waves behave diffusively in discrete random media with sufficient multiple scattering [Ish78, Ull99, Jan06]. Because of that, it is highly important to take into account the diffuse scattering when analyzing wireless electromagnetic behavior. In the literature, several methods have implemented this phenomenon in deterministic approaches. Reference [Gou07] presents an implementation of the diffuse scattering within a 3D urban propagation simulation method. A field prediction model which integrates reflection/diffraction with diffuse scattering is shown in [Deg04, Deg01, Fus08] presenting the impact of diffuse scattering on narrowband and wide-band parameters and showing that diffuse scattering plays a key role in urban propagation. Reference [Tar03] presents a novel and efficient hybrid model combining 2D site-specific model and a statistical model, to characterize the relative mean contribution of diffused scattering.

However, the computational time for the above-mentioned methods can be high depending of the accuracy of the results. Reducing the simulation time is nowadays a challenge and, because of that, several speed-up techniques have been proposed in the literature to overcome this drawback, as stated in Section 5.1 of related work.

In the light of the survey of different propagation methods, it is highly important to adopt deterministic approaches which lead to accurate results with an affordable computational simulation time. This is the original contribution of this work, which presents a novel and efficient hybrid Geometrical Optics-Diffusion Equation (GO/DE) approach to analyze radio wave propagation in complex indoor environments. Diffusion process is added to GO to account for material absorption and non-specular scattering by obstacles. This is also true of the full technique that combines diffusion process with GO and UTD. The full technique (GO/UTD/DE) is also a new approach proposed here for better accuracy, but accompanied with an inherent rise in computational time. The

explicit form of the solution to the DE, based on the equation of transfer, circumvents the much more complicated Hemholtz equation and provides a simple way to predict radio wave propagation when combined with GO methods. The novel technique GO/DE is computationally more efficient as compared to the full GO/UTD/DE technique and it shows accurate results, with an increase in a mean error of only 0.16dB. Figure 5.14 shows a scheme of the proposed work, showing the different cases which have been analyzed, with the benefits and drawbacks of each one.
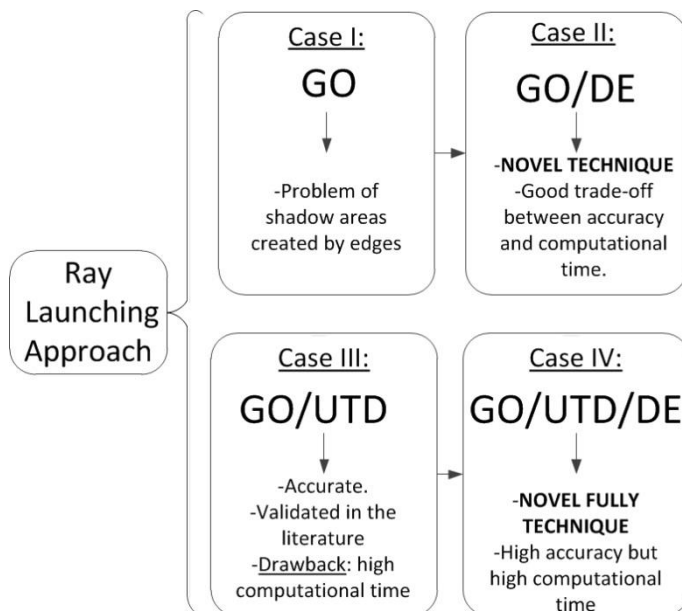

Figure 5.14. Description of the different considered approaches with the advantages and disadvantages of each one.

In the literature, the in-house developed 3D RL code based on GO/UTD has been widely validated to predict wireless propagation in closed environments [Azp12, Mor12, Naz12, Led13], interference analysis [Itu12] or electromagnetic dosimetry evaluation in wireless systems [Agu12]. It has been shown that the basis of GO/UTD predicts accurately wireless communication propagation when a complete 3D scenario is taking into account. However, as stated before, the main drawback of the algorithm is the elevated computational time needed for simulations, which can be excessive for large and highly complexity scenarios.

Because of that, in order to achieve accurate results with a manageable simulation time, a novel technique based on DE implemented in the GO-only-approach has been introduced in this work. The DE approach to predict path loss considers absorption and scattering electromagnetic phenomena due to obstacles, neglecting the edge contributions. The aim of this work is to obtain an efficient power prediction tool in order to achieve accurate results with an acceptable computational time. The novel technique GO/DE will be compared with the full technique GO/UTD/DE in terms of accuracy and simulation time required. The full technique GO/UTD/DE is also a new approach proposed by the authors which takes into account all the electromagnetic phenomena including edge diffractions. In the following sections, it is shown that the novel GO/DE technique leads to accurate results with a significant reduction of computational time required.

5.3.1 Diffusion Equation Approach

It is generally believed that electromagnetic waves behave diffusively in discrete random media with sufficient multiple scattering. In the literature, Ishimaru shows that the equation of transfer in the classical transport theory can be simplified to the diffusion equation under the assumption of uniform overall scattering [Ish78]. Xu and Janaswamy study the wave diffusion in 2D random media and describe under what circumstances a radiowave system starts to behave diffusively, showing that the area density of the embedded obstacles manifests itself to be the most important factor in determining wave diffusion [XuJ08]. In 2D, the obstacle occupational density (p_0) is equal to the ratio of the total area occupied by the obstacles to the total area of the region under consideration. It can be easily estimated from building floor plans and obstacle sectional areas.

In transport theory, results are obtained directly with statistically averaged power quantities (specific intensity), and any mathematical operation is performed in power rather than in voltage. Hence, the quantity being modeled is the mean incoherent intensity which is the quantity of interest when many obstacles are present. The transmission loss at any point under this model is the result of absorption as well as scattering by the obstacles [XuJ08]. The DE modeling is based on the concept of specific intensity which is the statistical average of the magnitude of the Poynting vector at any spatial location. The specific intensity in 2D is a function of three arguments: two spatial coordinates $\rho = (x, y) \equiv (r_a, \varphi)$, r_a being the radial distance and φ being the azimuthal angle, and one

angular coordinate ξ denoting the azimuthal direction of the average Poynting vector. After suitable normalization, the specific intensity is expressed as $I(\rho, \xi) = U_d(\rho) + \hat{s} \cdot \vec{F}(\rho)/\pi$, where $\hat{s} = \hat{x}\cos\xi + \hat{y}\sin\xi$, U_d is the average intensity (units of Watts/m) and $\vec{F}$ is the flux density vector (units of Watts/m). The relationship between the specific intensity, the average intensity and the flux vector are

$$U_d(\rho) = \frac{1}{2\pi} \int_0^{2\pi} I(\rho, s) d\xi \tag{5.11}$$

$$\vec{F}(\rho) = \frac{1}{2\pi} \int_0^{2\pi} \hat{s} I(\rho, s) d\xi \tag{5.12}$$

For a z-directed line source located at the origin and radiating power P_t per unit length, the average intensity satisfies the diffusion equation [Jan06]

$$\nabla^2 U_d - k_d^2 U_d = -\frac{P_t \rho_n \sigma_{tr}}{\pi} \delta(x)\delta(y) \tag{5.13}$$

where ∇^2 is the Laplacian operator, $\rho_n(m^{-2}) = p_0/A_0$ is the obstacle number density, A_0 is the average obstacle cross section area, $\delta(.)$ is the Dirac Delta function, $\sigma_{tr}(m)$ is the transport width of the obstacles, and $k_d = \sqrt{2\sigma_a\sigma_{tr}\rho_n}(m^{-1})$ is the diffusion coefficient, with $\sigma_a(m)$ being the absorption width of the obstacles. When the size of typical obstacles is very large compared to the wavelength, the approximation $\sigma_a \sim \sigma_g$ and $\sigma_{tr} \sim \sigma_g$ can be made, where σ_g is the geometric cross section of the obstacles per unit length. The mean excess loss is defined as the ratio of the flux density in the absence of obstacles (i.e., with $k_d = 0$) to that available in the presence of obstacles [Jan06]

$$l_{ex}^T(r_a) = \frac{F_\rho(k_d = 0)}{F_\rho(k_d)} \tag{5.14}$$

where F_ρ is the radial component of the flux density and is a measure of the power flow away from the source. The implicit relationship between U_d and $\vec{F}$ can be obtained starting from the equation of transfer. It is given by

$$\vec{F} = -\frac{\pi}{\rho_n\sigma_{tr}} \nabla U_d \tag{5.15}$$

Considering an azimuthally invariant environment, the excess loss for non-zero k_d is

$$l_{ex}^T(r_a) = \frac{1}{k_d r_a K_1(k_d r_a)} \sim \frac{e^{k_d r_a}}{\sqrt{\frac{\pi k_d r_a}{2}}}, \qquad k_d r_a \gg 1. \tag{5.16}$$

where $K_1(\cdot)$ is the modified Bessel function of the second kind of order one. Then, the excess loss on a dB scale using transport theory is

$$L_{ex}^T(r_a) \sim \frac{10\sqrt{2}\sigma_g p_0 \log e}{A_0} r_a - 5 \log\left(\frac{\pi p_0 \sigma_g r_a}{\sqrt{2} A_0}\right) \tag{5.17}$$

where σ_g (m) is the geometric cross section of the obstacles per unit length and r_a is the radial distance from the transmitter. For more details on the diffusion equation see [Jan06, XuJ08].

5.3.2 Ray Launching Modeling with Diffusion equation

Following the approach stated above, a new module based on DE, which takes into account absorption and scattering losses due to obstacles, has been developed. The DE module can be implemented in the RL algorithm both with the GO-only-approach and GO/UTD technique. The full GO/UTD/DE approach is the most accurate technique in terms that it takes into account all the electromagnetic phenomena encountered in a complex environment (reflection, absorption, diffraction and diffuse scattering). However, it takes a high computational time as it will be shown in the following sections. The novel technique GO/DE which neglects edge diffraction is described in this work achieving good results. Of course this technique ignores edge diffraction, but it is shown in the following sections that the effects of edge diffraction can be neglected when the field is averaged with respect to the random locations and orientations of the obstacles within the 3D scenario, leading to a significant reduction of simulation computational time.
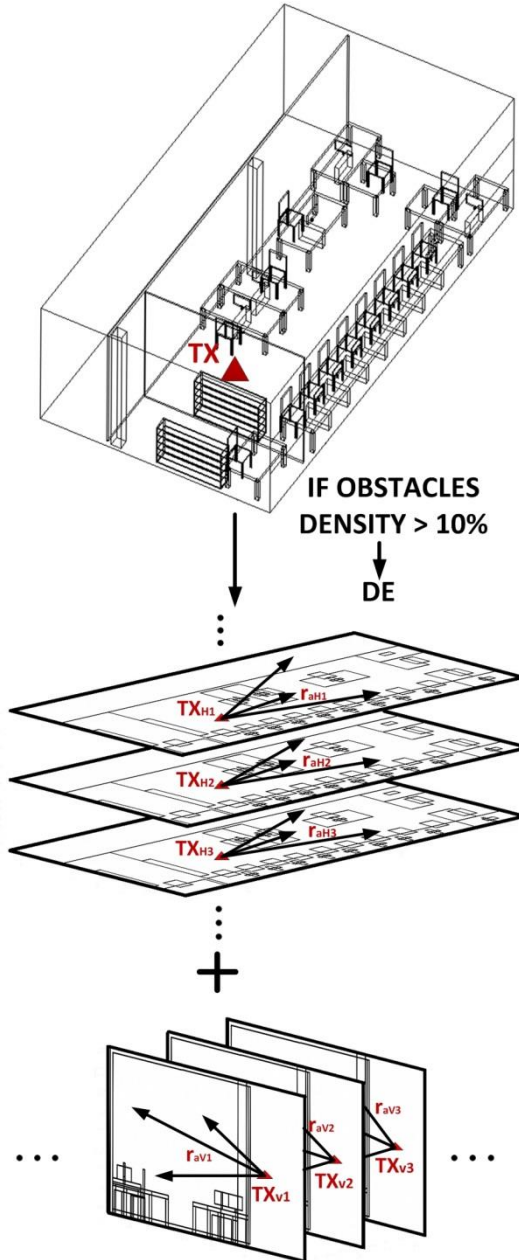
Figure 5.15. Description of the DE approach implemented in the 2D planes of the whole 3D scenario.

In [XuJ08], it has been concluded that the diffusion solutions can be applied to indoor environments if the area density of obstacles exceeds 10%. This is the key factor in order to implement the diffusion equation in the RL algorithm, in the sense that only certain planes of the whole 3D scenario have diffusive behavior. Thus, our approach consists in a decomposition of the whole 3D scenario in terms of horizontal and vertical 2D planes. Then, those 2D planes which behave diffusively (with an area density larger than 10%) are treated with the diffusion equation methodology, considering scattering and absorption losses due to the obstacles, as it is shown in Figure 5.15. As stated in Chapter 3, it is important to emphasize that a grid is defined in the space of the whole 3D scenario. Accordingly, the environment is divided into a number of cuboids of a fixed size. The cuboids size in the x, y and z-axis is defined as input parameters. Hence, the vertical and horizontal 2D planes are separated by the cuboid size, which could be different depending of the layout of the whole scenario. The obstacles density has been calculated for every 2D vertical and horizontal planes, and those with an area density larger than 10% have been treated with DE. For that purpose, it has been considered that the transmission and absorption cross sections are approximately equal to the geometric cross section because of the large size of obstacles compared to the considered wavelength [Ish78]. For each 2D horizontal and vertical diffusive plane, virtual transmitting locations TX_{Hk} and TX_{Vk}, respectively, have been calculated to apply DE. These virtual transmitters have been calculated considering the spatial sample in those diffusive 2D planes with the minimum distance (obtained through perpendicular projections) to the real transmitter in the 3D scenario. The virtual transmitting locations in the diffusive planes are then considered as the origin from which the radial distances r_a in equation (5.17) are calculated, leading to a matrix of excess losses due to scattering and absorption in the corresponding planes.

5.3.3 Simulation Examples and Verification of the Algorithm

As a starting step, several simulations of a typical office indoor scenario have been developed with the different techniques. The considered scenario is represented in Figure 5.16, which shows a three dimensional office environment with different elements, like tables of different shapes and sizes, chairs, computers and shelves. The dimensions of the scenario are 13m by 7m by 4.2m. All the elements within the scenario have been taken into account in simulation included the different walls which are also represented in the schematic view of the scenario. These obstacles have been considered with the GO-only and GO/UTD-only approaches in the complete scenario taking into account the

permittivity and conductivity of all the materials within the obstacles. In the GO/DE and GO/UTD/DE approaches, absorption phenomena by obstacles have been taken into account only with the diffusion equation, not considering the loss tangent of the materials of the obstacles in the GO and GO/UTD parts of these approaches. For the diffusive planes, the obstacle density has been considered to apply the diffusion equations in those planes, adding excess losses due to scattering and absorption. The material parameters used in the simulation are shown in Table 5.9 [Bal89, Cui02].
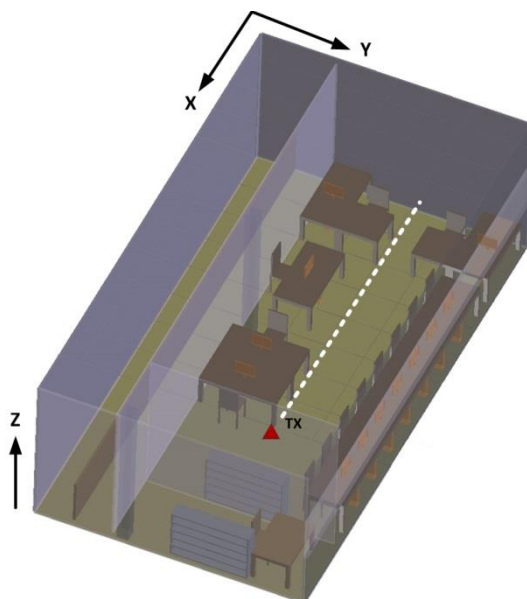

Figure 5.16. Schematic view of the considered scenario. Ceiling has not been shown for illustration.

Table 5.9. Material properties in the Ray Launching Simulation

Parameters	Permittivity (ε_r)	Conductivity (σ) [S/m]
Air	1	0
Plywood	2.88	0.21
Brick wall	4.11	0.0364
Glass	6.06	10^{-12}
Concrete	5.66	0.142
Metal	4.5	$4*10^7$
Polycarbonate	3	0.2

Table 5.10 shows the selected parameters for the GO/UTD/DE simulation. The transmitter and receiver antennas are omnidirectional, with 5dBi gain respectively. The angular resolution in the horizontal (ΔΦ) and vertical plane (Δθ) for the launching rays is 1º. The number of reflections considered in the simulation is six and the cuboids resolution is 5cm x 5cm x 5cm. In the implementation of the algorithm, reflections are combined with diffractions (i.e., a ray can undergo specular reflection and then edge diffraction). Only single diffraction is taken into account and the angular resolution of the diffracted rays is $\pi/20$, which is chosen according to the convergence analysis of diffracted rays presented in Chapter 4. The cuboids resolution leads to 84 horizontal XY-planes, 260 vertical YZ-planes and 140 vertical XZ-planes. For this particular environment, the obstacle density which exceeds 10% is present only in the horizontal planes which correspond with the tables and chairs of the scenario. These 2D horizontal planes have been treated with DE approach to obtain accurate results for those planes.

Table 5.10. High Resolution Ray Launching Parameters

Frequency	2.4GHz
Transmitter power	0dBm
Antenna gain	5dBi
Horizontal plane angle resolution (ΔΦ)	1º
Vertical plane angle resolution (Δθ)	1º
Reflections	6
Cuboids resolution	5cm x 5cm x 5cm

In order to assess the influence of the scattering in this typical complex indoor environment, different simulations have been done considering the scattering behavior with the diffusion equation modeling. A comparison between only the GO approach, the GO with edge contributions approach and the inclusion or exclusion of DE has been done. Figure 5.17 and Figure 5.18 show the comparison of the received power for the different techniques with its trend lines along the X-axis for Y=2.5m. Figure 5.17 shows the comparison between GO/UTD and GO/UTD/DE methods. It is observed in the trend lines of the figure that the inclusion of the DE method in the GO/UTD only approach leads to reduce the received power in some zones of the radial line, but it is also shown that, scattering due to obstacles, can also introduce excess gains in some spatial points. Thus, it is highly important to consider scattering phenomena in order to achieve accurate results to characterize the channel.
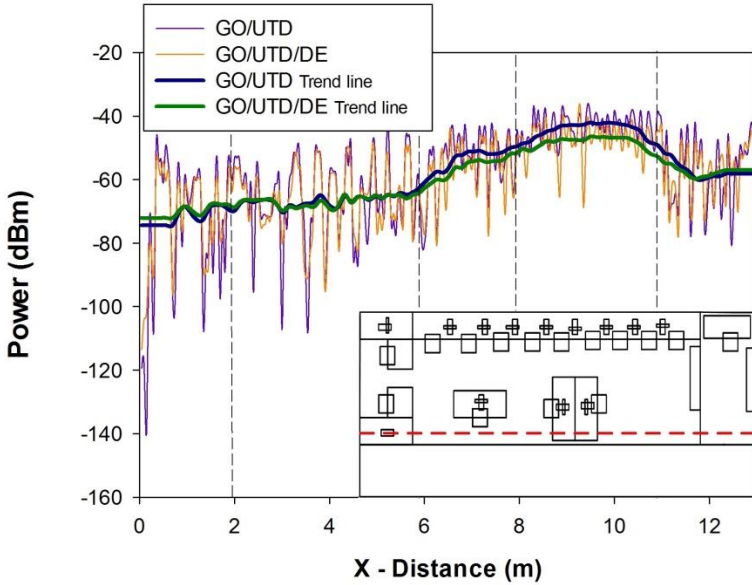
139

Figure 5.17. Comparison between radials of received power (dBm) for the GO/UTD and GO/UTD/DE approaches with its trend lines.
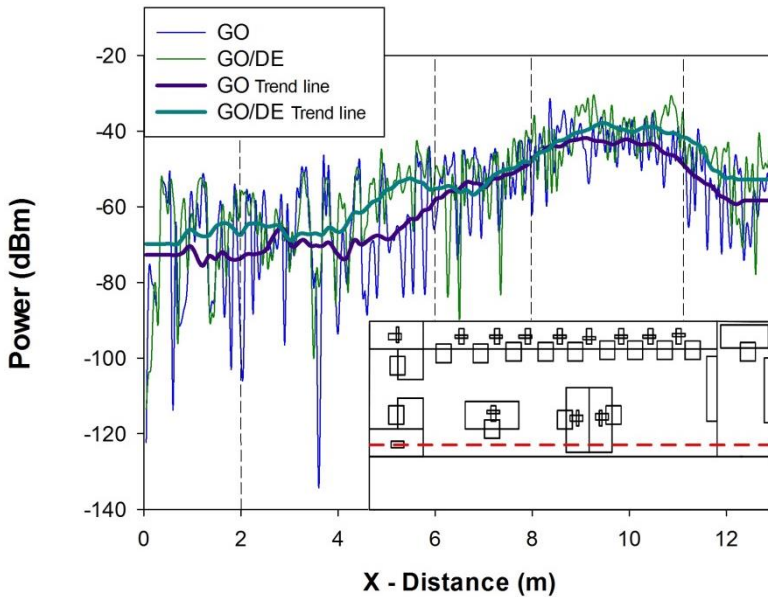

Figure 5.18. Comparison between radials of received power (dBm) for the GO only approach and the GO/DE approach with its trend lines.

Figure 5.18 shows the comparison between GO-only approach and the GO/DE technique. It can be seen that, in this case, the inclusion of DE in the GO-only approach predicts greater values of received power along most of the radial. This is because the scattering phenomenon, which is always present in practical situations, can contribute to excess gains. But it is also observed that scattering also introduces lower values of received power in some zones of the radial line (from 6 to 8 meters). The vertical dash lines in the pictures represent the different positions of the obstacles. It can be seen that these obstacles have an influence in the received power, showing more variability around the objects when the contribution of edges is considered.

5.3.4 Measurement Results and Discussion

In order to validate the results previously obtained, real measurements in the same scenario have been performed. A transmitter antenna, connected to a signal generator at 2.4GHz has been located at the coordinates (X=9.94m, Y=4.5m, Z=0.60m), depicted with a red triangle in Figure 5.16. The employed signal generator is a portable Agilent N1996A and the spectrum analyzer is an Agilent N9912 Field Fox. The antennas used are Picea 2.4GHz Swivel Antennas from Antenanova, both omnidirectional[2]. Measurements have been performed along the radial white dashed line depicted in Figure 5.16 each 0.5m at a height of 0.80m.

Figure 5.19 shows the comparison between simulation and measurement results for the different simulation techniques. Measurements were performed with 100MHz bandwidth at 2.4GHz frequency. The measurement time at each point was 60 seconds, and the value of received power represented by each point is the highest peak of power shown by the spectrum analyzer for the considered bandwidth (MaxHold function in the spectrum analyzer of Agilent). The received power values estimated by simulation have been obtained for the same spatial samples as the real measurements, considering the corresponding cuboid in the three-dimensional mesh of cuboids in which the scenarios have been divided. It is observed that results by the proposed simulation techniques, GO/DE and GO/UTD/DE, follow the trend of the measured power, which generally decays with increasing distance from transmitter. Table III shows the mean error, standard deviation and computational time of the different approaches. It is observed that with the GO/DE approach, a considerable improvement in the accuracy of the results can be achieved compared to GO and GO/UTD

---

[2] For more information about the measurement equipment, see Appendix B.

techniques, with a negligible increase of the computation time w.r.t. the GO-only approach. Besides, it can be seen that with the full GO/UTD/DE technique, a further improvement in the results can be obtained, but at the expense of a 40% increase in computation time, which becomes similar to the one of GO/UTD simulation. The computational time is of the order of minutes or hours depending on the implementation and CPU speed. Simulations have been performed in an Intel Xeon CPU X5650 @ 2.67GHz and 2.66GHz, with 64GB of RAM memory. It is observed that the characterization of the diffracted rays takes a long time, with a 40% reduction time when UTD is not considered in the model. The novel technique GO/DE permits neglecting the contribution of edges as the field is averaged with respect to the random locations and orientations of the obstacles within the 3D scenario. Because of that, a good trade-off between computational complexity and final accuracy is present when employing this combined approach, showing that the novel GO/DE technique can be accurate for an indoor environment with a considerable reduction of computational time in comparison with the full GO/UTD/DE approach.
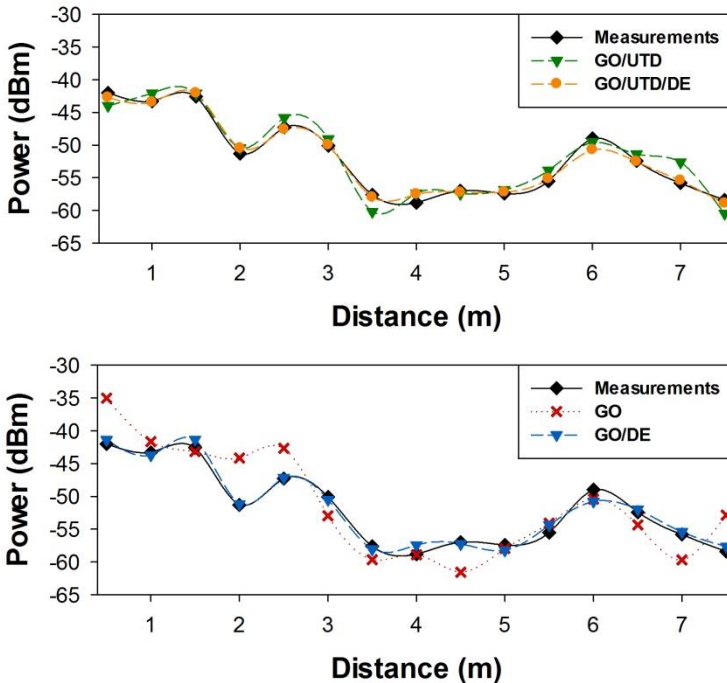

Figure 5.19. Comparison simulation versus measurements for 2.4GHz frequency in the considered scenario for the different simulation approaches.

Table 5.11. Mean Error and Standard Deviation for the different approaches.

	CASE 1	CASE 2	CASE 3	CASE 4
	GO	**GO/DE**	**GO/UTD**	**GO/UTD/DE**
Mean error (dB)	3.011	0.691	1.370	0.523
Std. Deviation (dB)	2.305	0.489	0.814	0.457
Computational Time(s)	129000	130194	217204	218398

5.4   Summary

In this chapter, two novel deterministic approaches for coverage prediction in complex indoor environments are presented. The first part of the chapter is focused in the RL-NN approach. This technique applies a NN for modeling and storing the RL results. Simulations of a real scenario have been done to compare the proposed method with a fully 3D high resolution RL as a reference solution. A difference between the results of our proposed method and the fully 3D simulation is observed. However, such difference is moderate and the results are reliable for engineering purposes. The new method achieves a high gain in terms of computational efficiency, 80% reduction in simulation time and 70% reduction in used memory space, leading to accurate results.

On the other hand, the second part of the chapter is focused in the RL-DE approach. This technique combines the 3D RL with a DE, the latter of which is based on power transport theory. The diffusion equation could be combined with GO alone or with the more accurate GO/UTD. Simulations of a real scenario have been done to compare the GO/DE method with the full GO/UTD/DE, treated as a reference solution. The GO/DE technique presents an increase in the mean error compared to the latter. However, such increase is small and the results are reliable for engineering purposes. The new GO/DE method achieves a high gain in terms of computational efficiency, 40% reduction in simulation time when compared with the full GO/UTD/DE technique.

To obviate the need for considering a set of mutually orthogonal 2D planes in the handling of excess loss by diffusion equation, a full 3D version of scattering and absorption losses by diffusion equation with anisotropic obstacle density is desirable. This is being presently considered.

The quantity that one deals with in the diffusion equation approach is the average intensity. The flux density vector is proportional to the spatial gradient of the average intensity and can be calculated from the average intensity. This

quantity is already averaged with respect to the environment. Hence, quantities such as angular spread that depend on the angular distribution of averaged power at the receiver can also be obtained from the DE approach. This will also be pursued in the future.

Bibliography of the Chapter

[Agu12] E. Aguirre, J. Arpón, L. Azpilicueta, S. de Miguel, V. Ramos and F. Falcone, "Evaluation of electromagnetic dosimetry of wireless systems in complex indoor scenarios within body human interaction," *Progress In Electromagnetics Research B*, vol. 43, pp. 189-209, 2012.

[And12] J.B. Andersen, K.L. Chee, M. Jacob and G.F. Pedersen "Reverberation and Absorption in An Aircraft Cabin with the Impact of Passenger", *IEEE Trans on Antennas and Propagation*, Vol. 60, nº 5, 2012, pp. 2472-2480, 2012.

[Azp12] L. Azpilicueta, F. Falcone, J. J. Astráin, J. Villadangos, I. J. García Zuazola, H. Landaluce, I. Angulo, A. Perallos, "Measurement and modeling of a UHF-RFID system in a metallic closed vehicle," *Microwave and Optical Technology Letters*, vol. 54, Issue 9, pp. 2126-2130, 2012.

[Azp14] L. Azpilicueta, M. Rawat, K. Rawat, F. Ghannouchi and F. Falcone, "A Ray Launching-Neural Network Approach for Radio Wave Propagation Analysis in Complex Indoor Environments," *IEEE Transactions on Antennas and Propagation*, vol. 62, nº 5, pp. 2777-2786, May 2014.

[Azp15] L. Azpilicueta, F. Falcone and R. Janaswamy, "A Novel Ray Launching-Diffusion Equation Approach for Electromagnetic Propagation Analysis in Complex Indoor Environments," *IEEE Transactions on Antennas and Propagation*, just submitted.

[Bal89]   A. Constantine Balanis. Advanced engineering electromagnetics. Vol. 205. Wiley New York, 1989.

[Cat98] M. F. Cátedra, J. Pérez, F. S. Adana, O. Gutiérrez, "Efficient ray-tracing technique for three-dimensional analyses of propagation in mobile communications: application to picocell and microcell scenarios", *IEEE Antennas and Propagat. Mag.*, vol. 40, nº 2, pp. 15-28, 1998.

[Cor02] Y. Corre, Y. Lostanlen, and Y. Le Helloco, "A new approach for radio propagation modeling in urban environment: Knife-edge diffraction combined with 2D ray-tracing," presented at the *Veh. Technol. Conf.*, Birmingham, AL, May 2002.

[Cui02] I. Cuiñas and M. García Sánchez, "Permittivity and conductivity measurements of building materials at 5.8GHz and 41.5GHz," *Wireless Personal Communications*, vol. 20, nº 1, pp. 93-100, 2002.

[Deg01] V. Degli Esposti, "A Diffuse Scattering Model for Urban Propagation Prediction," *IEEE Transactions on Antennas and Propagation Letters*, vol. 49, nº 7, July 2001.

[Deg04] V. Degli-Esposti, D. Guiducci, A. de'Marsi, P. Azzi, F. Fuschini, "An Advanced Field Prediction Model Including Diffuse Scattering," *IEEE Transactions on Antennas and Propagation*, vol. 52, nº 7, pp. 1717-1728, July 2004.

[Deg09] V. Degli-Esposti, F. Fuschini, E. M. Vitucci, and G. Falciasecca, "Speed-Up Techniques for Ray Tracing Field Prediction Models," *IEEE Transactions on Antennas and Propagation*, vol. 57, no. 5, pp. 1469-1480, May 2009.

[Fus08] F. Fuschini, H. El-Sallabi, V. Degli-Esposti, L. Vuokko, D. Guidacci, P. Vainikainen, "Analysis of Multipath Propagation in Urban Environment Through Multidimensional Measurements and Advanced Ray Tracing Simulation," *IEEE Transactions on Antennas and Propagation*, vol. 56, nº 3, March 2008.

[Gen09] G. Gennarelli and G. Riccio, "A uapo-based model for propagation prediction in microcellular environments", *Progress in Electromagnetics Research B*, vol 17, pp. 101-116, 2009.

[Gla89] S. Glassner, "An introduction to ray tracing", in Academic Press published by Morgan Kaufmann, 1989.

[Gol87] J. Goldsmith, J. Salmon, "Automatic creation of object hierarchies for ray tracing", *IEEE Comput. Graph. Appl.*, 1987, vol. 7, no. 5, pp. 14-20.

[Gou07] G. Gougeon, Y. Corre, Y. Lostanlen, "Impact of the introduction of diffuse scattering on radio channel parameters in urban environments", *EuCAP'07*, Edinburgh, November 2007.

[Hag94] M. T. Hagan and M.B. Menhai, "Training feedforward network with the Marquardt algorithm," *IEEE Trans. on Neural Net.*, vol. 5, no. 6, pp. 989-993, 1994.

[Hay99] S. Haykin. Neural Networks: A Comprehensive Foundation. Upper Saddle River, NJ: Prentice-Hall, 1999.

[Hop03] R. Hoppe, G. Woelfle, and P. Wertz, "Advanced ray-optical wave propagation modeling for urban and indoor scenarios," *Eur. Trans. Telecommun.* (ETT), vol. 14, no. 1, pp. 61-69, Jan. 2003.

[Isa05] M. Isaksson, D. Wisell and D. Ronnow, "Wide-band dynamic modeling of power amplifiers using radial-basis function neural networks," *IEEE Trans. Microw. Theory Tech.*, vol. 53, no. 11, pp. 3422–3428, Nov. 2005.

[Ish78] A. Ishimaru, Wave Propagation and Scattering in Random Media. New York: Academic, 1978, vol. 1.

[Itu12] P. L. Iturri, J. A. Nazábal, L. Azpilicueta, P. Rodriguez, M. Beruete, C. Fernández-Valdivielso and F. Falcone, "Impact of High Power Interference Sources in Planning and Deployment of Wireless Sensor Networks and Devices in the 2.4GHz frequency band in Heterogeneous Environments," *Sensors,* 2012, vol. 12, issue 11, pp. 15689-15708.

[Jan06] R. Janaswamy, "An indoor pathloss model at 60GHz based on transport theory," *IEEE Antennas Wireless Propag. Letters*, vol. 5, pp. 58-60, 2006.

[Kou74] R. G. Kouyoumjian and P. H. Pathak, "A uniform theory of diffraction for an edge in a perfectly conducting surface", *Proc. IEEE*, vol. 62, nº 4, pp. 1448-1462, 1974.

[Led13] S. Led, L. Azpilicueta, E. Aguirre, M. Martínez de Espronceda, L. Serrano, F. Falcone, "Analysis and Description of HOLTIN Service Provision for AECG monitoring in Complex Indoor Environments," *Sensors*, 2013, vol. 13, Issue 4, pp. 4947-4960.

[Lia98] G. Liang and H. L. Bertoni, "A new approach to 3-D ray tracing for propagation prediction in cities*," IEEE Trans. Antennas Propag.*, vol. 46, nº 6, pp. 853-863, June 1998.

[Lin89] H. Ling, R.C. Chou and S. W. Lee, "Shooting and bouncing rays: calculating the RCS of an arbitrarily shaped cavity", *IEEE Transactions on Antennas and Propagation*, 1989, vol. 37, pp. 194-205.

[Mor12] A. Moreno, I. Angulo, A. Perallos, H. Landaluce, I. J. G. Zuazola, L. Azpilicueta, J. J. Astráin, F. Falcone, J. Villadangos, "IVAN: Intelligent Van for the Distribution of Pharmaceutical Drugs," *Sensors*, 2012, vol. 12, pp. 6587-6609.

[Naz12] J. A. Nazábal, P. Iturri López, L. Azpilicueta, F. Falcone and C. Fernández-Valdivielso, "Performance Analysis of IEEE 802.15.4 Compliant Wireless Devices for Heterogeneous Indoor Home Automation Environments," *International Journal of Antennas and Propagation*, Hindawi Publishing Corporation, 2012.

[Ros02] J. P. Rossi and Y. Gabillet, "A mixed ray launching/tracing method for full 3-D UHF propagation modeling and comparison with wide-band measurements*," IEEE Trans. Antennas Propag.*, vol. 50, no. 4, pp. 517-523, Apr. 2002.

[Sae00] F. Saez de Adana, O. Gutiérrez Blanco, I. González Diego, J. Pérez Arriaga, and M. F. Cátedra, "Propagation model based on ray tracing for the design of personal communication systems in indoor environments," *IEEE Trans. Veh. Technol.*, vol 49, nº 6, pp. 2105-2112, Nov. 2000.

[Son09] H. B. Song, H. G. Wang, K. Hong and L. Wang, "A novel source localization scheme based on unitary esprit and city electronic maps in urban environments", *Progress In Electromagnetics Research*, vol. 94, pp. 243-262, 2009.

[Son99] H. W. Son and N. H. Myung, "A deterministic ray tube method for microcellular wave propagation prediction model", *IEEE Trans. Antennas and Propag.*, vol 47, nº 8, pp. 1344-1350, 1999.

[Tar03] J. H. Tarng, Wen-Shun Liu, Yeh-Fong Huang, Jiunn-Ming Huang, "A Novel and Efficient Hybrid Model of Radio Multipath-Fading Channels in Indoor Environments," *IEEE Transactions on Antennas and Propagation*, vol. 51, nº 3, March 2003.

[Tay09] A. Tayebi, J. Gómez, F. S. de Adana and O. Gutierrez, "The application of arrival and received signal strength in multipath indoor environments", *Progress In Electromagnetics Research*, vol. 91, pp. 1-15, 2009.

[Tor99] R. P. Torres, L. Valle, M. Domingo, S. Loredo, "An efficient ray-tracing method for radiopropagation based on the modified BSP algorithm", *IEEE Vehicular Technology Conf.* (VTS 50th), Amsterdam, Netherland, vol. 4, pp. 1967-1971, September 1999.

[Ull99] D. Ullmo and H. U. Baranger, "Wireless propagation in buildings: A statistical scattering approach," *IEEE Trans. Veh. Technol.*, vol. 48, pp. 947-955, 1999.

[XuJ08] J. Xu and R. Janaswamy, "On the Diffusion of Electromagnetic Waves and Applicability of Diffusion Equation to Multipath Random Media," *IEEE Transactions of Antennas and Propagation*, vol. 56, nº 4, April 2008.

[Zhe00a] Y. Zhengqing, M. F. Iskander, Z. Zhijun, "Fast ray tracing procedure using space division with uniform rectangular grid," *Electronic Letters*, 36 (10), pp. 895-897, 2000.

[Zhe00b] Y. Zhengqing, M. F. Iskander, Z. Zhijun, "A fast indoor/outdoor ray tracing procedure using combined uniform rectangular and unstructured triangular rids," *IEEE Antennas Propagat. Soc. Int. Symp.*, Salt Lake City, UT, vol. 2, pp. 1134-1137, July 2000.

Chapter 6

Applications

T he impact of topology and morphology of different types of complex environments is analyzed in this chapter by means of the in-house developed 3D Ray Launching (RL) code. First, an in-depth analysis of electromagnetic propagation in a typical office environment has been presented. After that, the work has been focused in more complex indoor environments, such as vehicular environments. As an example, the assessment of radio-propagation within two different types of urban buses is presented. Results show that multipath propagation plays a relevant role. Radio planning analysis within vegetation environments has also been presented in this chapter, highlighting the complexity of this type of scenarios. The use of deterministic techniques aimed to take into account the inherent complexity of the considered scenarios can aid in wireless system planning in order to minimize power consumption and increase overall system capacity. The last part of the chapter is focused in mobile channel characterization, and a Vehicle to Infrastructure (V2I) system based on Radio Frequency IDentification (RFID) is presented.

6.1 Channel characterization of different environments

The work developed in this thesis has a broad range of applications. Channel characterization of different complex environments can be assessed, as well as dosimetric analysis estimation and interference source modeling. Figure

6.1 shows a scheme of the different applications which have been developed during the work of this thesis.

Figure 6.1. Scheme of the applications developed in this thesis with the RL technique.

6.1.1 Typical office environments

In previous chapters, different typical indoor scenarios have been presented and the comparison between simulation results and real measurements has been done, showing good agreement. Therefore, once the 3D RL code has been validated, the analysis of wireless propagation in a typical office environment is made in this section. The considered scenario is a conventional office location, in which furniture, appliances, walls and doors are present. The real scenario and the implemented simulation model are depicted in Figure 6.2. The simulation parameters are presented in Table 6.1.
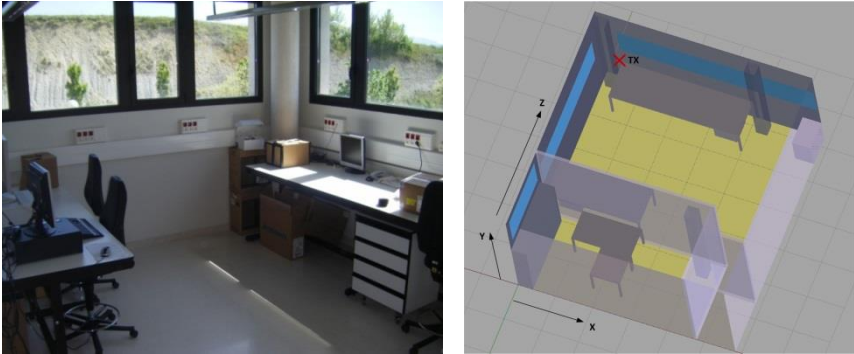
Figure 6.2. View of the real and schematic representation of the considered scenario with the transmitter point depicted with a red circle.

Table 6.1. Ray Launching Parameters

Frequency	868MHz/2.1GHz/2.4GHz
Transmitter power	0dBm
Antenna gain	5dBi
Horizontal plane angle resolution (ΔΦ)	1º
Vertical plane angle resolution (Δθ)	1º
Reflections	6
Cuboids resolution	12cm x 12cm x 12cm

First, results have been obtained for transceivers operating in the 868MHz frequency range, a possible spectral allocation for ZigBee sensors. Figure 6.3 shows the distribution of received power as a function of location for two different cut plane heights (1m and 2m). As it can be seen, power distribution is not uniform, strongly depending on the elements within the vicinity of the propagation path. More detail can be observed in Figure 6.4, in which received power levels as a function of linear distance between transmitter and receiver is depicted for different heights. There are strong variations in the received signal as a function of distance, with deviations in the order of 20dB. This is given mainly by strong multipath components which appear in indoor environments. The influence of such multipath components, which are the main reason for such strong variability, can be observed by computing Power Delay Profiles (PDPs) of the established radio links within the indoor scenarios. A schematic of the position in which the simulation power delay probes are located is shown in

Figure 6.5, whereas the results for the PDPs are given in Figure 6.6 for each one of the considered probes.
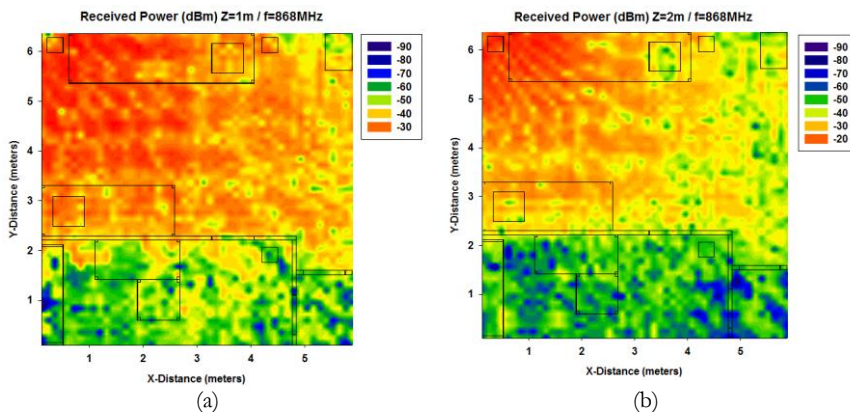

(a)   (b)

Figure 6.3. Bi-dimensional plane of received power (dBm) for 868MHz frequency (a) Z=1m (b) Z=2m.
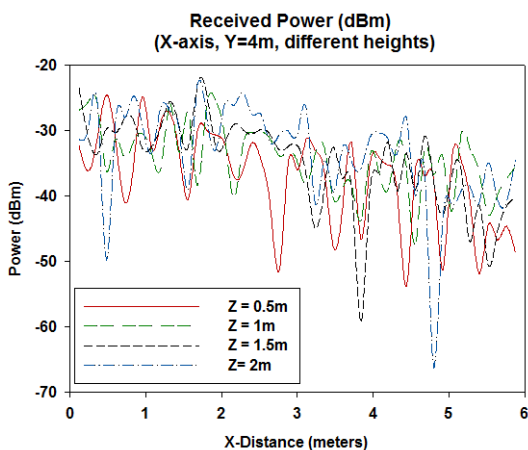

Figure 6.4. Linear distribution of received power as a function of transmitter to receiver distance in the case of employing transceivers operating at 868MHz
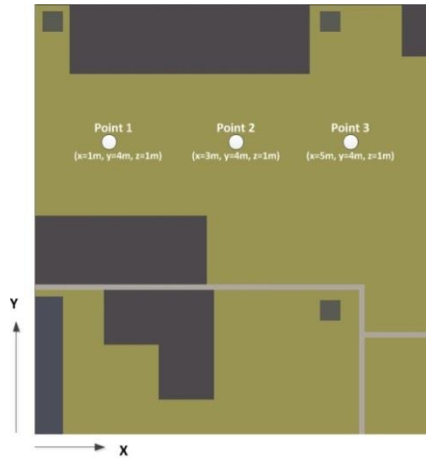
Figure 6.5. Schematic view of the considered scenario with the considered points for the PDPs.
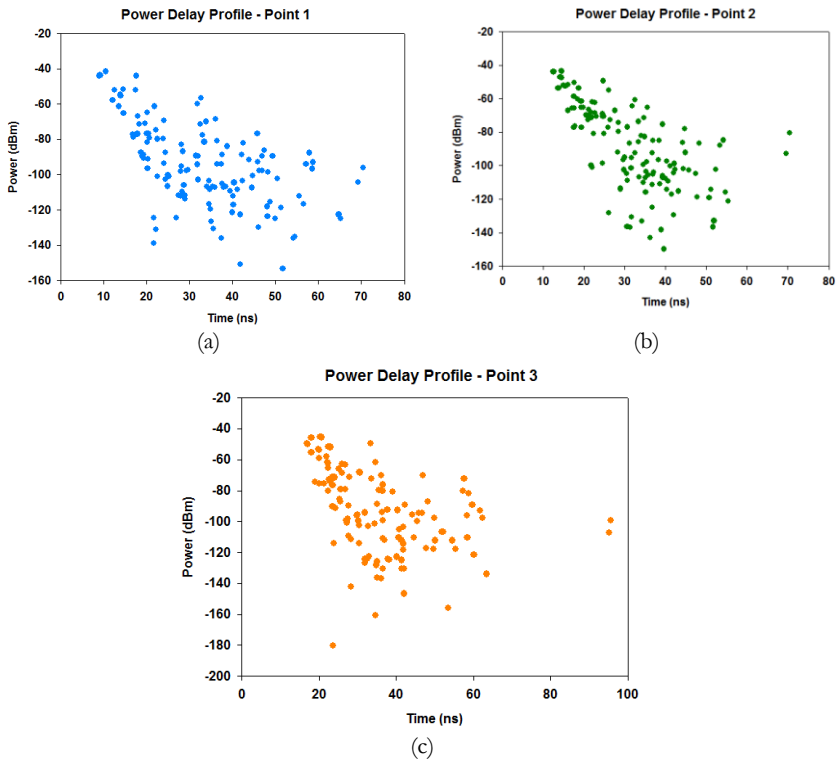

(a)

(b)

(c)

Figure 6.6. PDPs for different points in the considered scenario.

As it can be seen, a large amount of components are propagated within the scenario, given the interactions of the transmitter with the surrounding environment, mainly due to reflection and diffraction. These variations are within the order of several tens of nanoseconds, as can be derived from delay spread computations, depicted in Figure 6.7 and that once again indicates the importance of multipath components within the scenario and their relation with the topology and the morphology of the indoor environment. A simple height variation of 1 meter can substantially modify the resulting response of the wireless channel, leading to larger losses and hence, degradation of system performance.
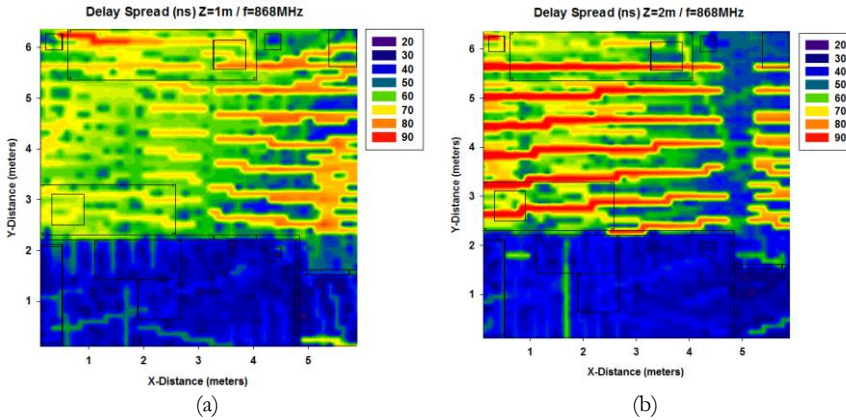

Figure 6.7. Bi-dimensional plane of Delay Spread (ns) for 868MHz frequency (a) Z=1m (b) Z=2m.

Another case has been considered, in which transceivers operating in the 2.41 GHz (i.e., Bluetooth or ZigBee sensors) are employed. The bi-dimensional power distribution planes have been obtained for two different heights, as depicted in Figure 6.8. As it can be seen, power levels are lower than in the previous case in which 868MHz frequency was employed, a consequence in the use of a higher frequency band. Moreover, the 2.4GHz band is intensively used, with larger probability of interference. Figure 6.9 shows calculation of Signal to Noise Ratio (SNR) distributions within the scenario for two different cut planes, considering potential interference sources (i.e., adjacent non coordinated WLAN networks or WPAN devices). As it can be seen, the distribution once again strongly depends on the location considered.
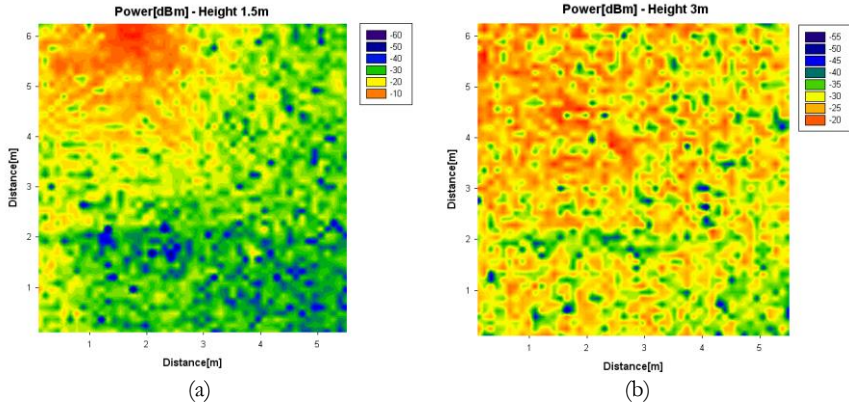
(a)   (b)

Figure 6.8. Bi-dimensional plane of received power (dBm) for 2.41 GHz frequency (a) Z=1m (b) Z=2m.
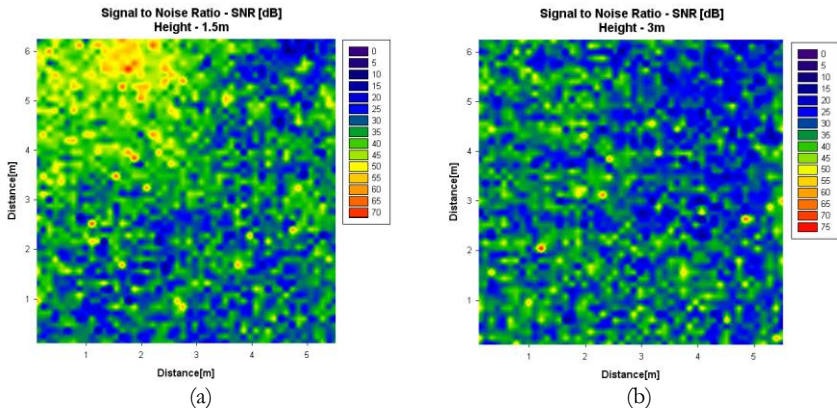

(a)   (b)

Figure 6.9. Signal to Noise Ratio for 2.41GHz frequency (a) Z=1.5m (b) Z=3m

One last case is presented, corresponding to a mobile terminal operating in the 2.1GHz band, typical of 3G and 4G systems. The bi-dimensional distribution of received power is depicted in Figure 6.10. In this case, received power levels are higher, given by the lower operating frequency. Once again, the location of the transceivers determines the received power levels and hence, the overall performance of the terminals.
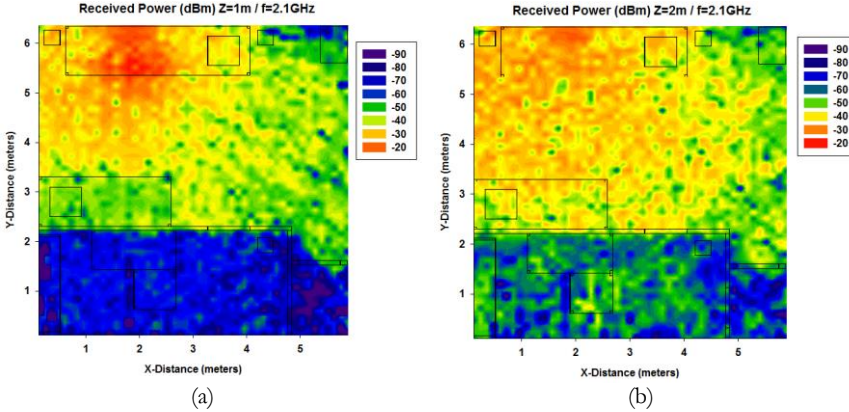
157

Figure 6.10. Bi-dimensional plane of received power (dBm) for 2.1GHz frequency (a) Z=1m (b) Z=2m.

As it can be seen from the previous results, the choice of the frequency of operation as well as the location of the devices, as a function of the scenario in which the sensors will be operating, are key parameters in order to gain into the expected overall performance. This must be carefully taken into account in order to guarantee that the received power levels will be above receiver sensitivity for a given data rate (which is usually low) to satisfy coverage/capacity requirements. Moreover, if adequate radio-planning choices are performed in the deployment of the wireless sensor network, received power levels can be maximized whilst reducing undesired interference and lowering overall power consumption.

6.1.2 Vehicular environments

With the improvement of living standards of city inhabitants, the development of information technologies applied to vehicular environments becomes highly necessary. The emerging interest in intra-vehicle applications leads to an increasing number of deployed wireless sensors inside different types of vehicles. Taking into account that a vehicle is a highly complex environment, where strong degradation effects due to multipath components and phenomena such as reflection, refraction and diffraction are present, the radio channel therefore requires and in-depth radio-propagation analysis [Has93, Fin09]. The in-house developed 3D RL code has been validated in the literature for different complex vehicular environments. For example, an in-depth propagation study for ZigBee motes operating at the ISM 2.4GHz band inside a common commercial car is presented in reference [Lop14]. Measurement results, as well as simulation results illustrate the strong influence of this complex scenario and results show

that ZigBee is a viable technology for successfully deploying intra-car wireless sensor networks. Reference [Agu13] presents the analysis of wireless propagation in an indoor commercial airplane by means of the 3D RL code, showing that these techniques can aid in wireless system planning. In addition, the assessment of an indoor wagon train has also been studied and can be found in [Azp15a]. The characterization of wireless channel impact in public transportation buses has also been analyzed and it is presented in reference [Azp15b].

6.1.2.1. Public transportation buses

In this section, as an example of application of the 3D RL code, an in-depth study within two different types of public transportation buses have been presented, emulating an operating WSN. The appropriate choice of the placement of the communication nodes, the RF frequency to use and the topology of the WSN may provide better results on communication efficiency, and therefore minimize the energy consumption of the nodes. For such reason, we tackle in this work the radio planning in different types of urban buses in order to optimize the overall systems, minimizing power consumption as well as non-desired interference levels and collisions, which are critical parameters in WSNs due to their strict energy constraints.

Figure 6.11 (left) shows the three types of urban buses which have been employed for the setup of measurements. Figure 6.11 (right) shows the internal distribution of one of the articulated vehicles. It shows the location of the metal bellows and the distribution of seats and handholds.

Figure 6.11. Vehicles used on the experimentation (left) and internal distribution of an articulated bus (right).

As it can be observed in Figure 6.11 (right), the buses considered include red seats reserved for individuals with disabilities, which have different

dimensions or are prepared to engage wheelchairs or prams. The remaining seats, turquoise blue, are destined to other passengers.

The simulation scenarios implemented for calculation by means of the in-house developed 3D RL code corresponds to the real buses shown in Figure 6.11. A view of the vehicles model developed for simulation is depicted in Figure 6.12, which corresponds with the articulated more metallic urban bus (top) and the rigid bus (bottom).

The articulated bus has two variants which correspond to two different structure materials of the vehicle. The first one has the walls, ceiling and floor made of metal, and the other is a new model lighter with less metallic parts and more plastic structures. The rigid bus has only metallic structure. All the elements within the different models of buses have been taken into account, like the different dimensions and distribution of seats, different heights, the metallic handholds and the bellows for the articulated bus model. The material parameters used in the simulation models, are presented in Table 6.2 [Bal89].

Table 6.2. Material Properties in the Ray Launching Simulation

Parameters	Air	Aluminum	Glass	Polycarbonate
Permittivity (ε_r)	1	4.5	6.06	3
Conductivity (σ)	0	$4*10^7$	10^{-12}	0.2

In addition, two new models of the articulated more metallic urban bus and the rigid bus has been created with the random presence of several persons inside them. A simplified human body model, including the dispersive nature of material organs, skin, muscle, bones and other elements has been implemented within the in-house developed 3D RL code [Agu12]. Figure 6.13 shows a view of the two models created with several human body models inside them, which have been simulated and compared with the models without persons. In next section, it is shown that the impact of persons within the vehicles has a great influence in electromagnetic radio wave propagation and it is highly important to take them into account for the implementation and development of Body Area Networks (BANs) or WSNs inside the vehicles.
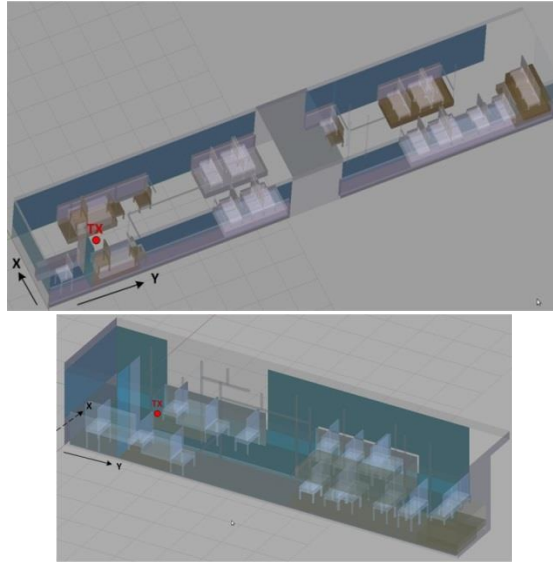
Figure 6.12. Simulation scenarios developed for calculation by means of the in-house developed 3D Ray Launching code: Articulated (top) and Rigid buses (bottom).
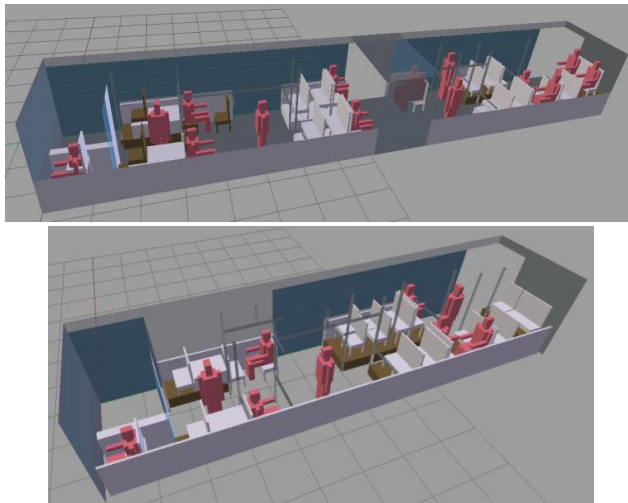

Figure 6.13. Simulation scenarios developed with the random presence of several persons inside them for calculation by means of the in-house developed 3D Ray Launching code: Articulated (top) and Rigid (bottom) buses, respectively.

161

6.1.2.2. Simulation Results

Simulations have been performed for the metallic articulated bus and rigid bus (with and without the presence of persons), with the transmitter antenna placed at the point (X=1.35m, Y=2.03m, Z=1.10m) (Case I), which is depicted with a red point in Figure 6.12. A Case II has been also considered with the transmitter antenna placed at the point (X=1.35m, Y=13.72m, Z=1.10m). Simulation parameters are shown in Table 6.2. The transmitter and receiver antennas are omnidirectional, with 5dBi gain respectively. The resolution of the cuboids and the number of reflections has been set to 10cm and 6, respectively, to balance accuracy with simulation time. Each cuboid is considered as a receiver. Moreover, the 3D RL software accepts considering diffraction phenomena or not. In this case, it has been taken into account in the simulations due to its significant effect in this propagation environment. Parameters considered in the RL simulation are a 2.4 GHz frequency, a transmission power of -10dBm, an antenna gain of 5dBi, a horizontal and vertical planes angle resolution (ΔΦ) of one degree, 6 reflections, an angular resolution diffracted rays of nine degrees and one reflection of diffracted rays.

Table 6.2. Ray Launching Parameters

Frequency	2.4GHz
Transmitter power	-10dBm
Antenna gain	5dBi
Horizontal plane angle resolution (ΔΦ)	1º
Vertical plane angle resolution (Δθ)	1º
Reflections	6
Cuboids resolution	10cm x 10cm x 10cm

A) Without the presence of human body models

As a first step, the comparison between several empirical propagation models versus the in-house 3D RL approach has been made. Figure 6.14 shows the estimated received power for different propagation models for the metallic articulated bus along the Y-axis. It can be seen that the 3D RL approach has a lot of signal variations and it is more precise than the empirical models. These models follow the trend of the RL model but they do not take into account any obstacle in their path. For a better insight of the estimated received power, Figure 6.15 shows the bi-dimensional plane of received power with the ITU-R P-

1238 empirical model. It is observed that the obtained plane is quite simple and the received power decreases linearly along the metallic articulated bus. This is because this model does not take into account any obstacle, and the bus scenario has seats, handholds and a lot of components which affect significantly the radio wave propagation. Because of that, it is highly necessary the use of deterministic methods such as the RL method which leads to more precise results with affordable computational time.
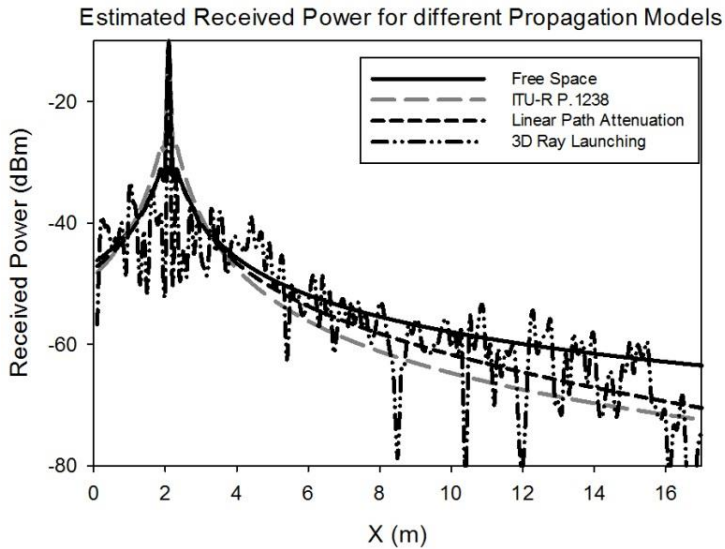

Figure 6.14. Estimated received power for different empirical propagation models and the 3D RL approach.
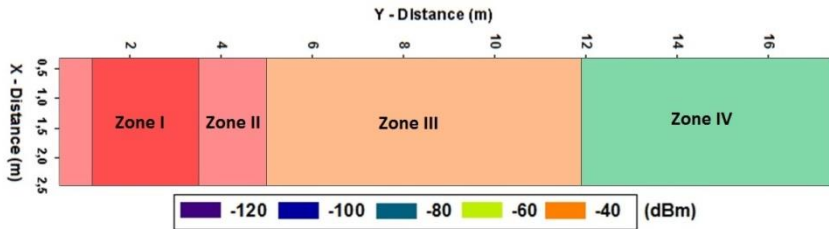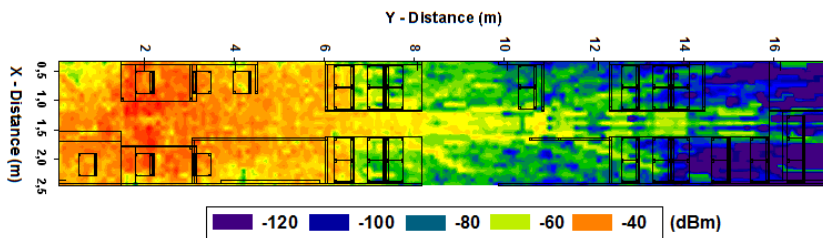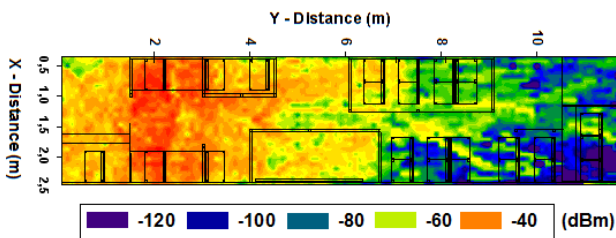

Figure 6.15. Received power (dBm) within the metallic articulated bus for 2.4GHz frequency for the empirical model ITU-R P.1238.
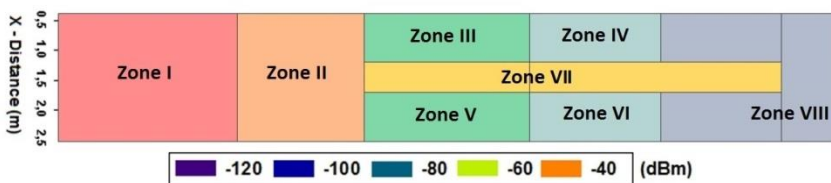
(a)

(b)

Figure 6.16. Received Power (dBm) within the different models of the buses for 2.4GHz frequency with the transmitter antenna placed at the point (X=1.35m, Y=2.03m, Z=1.10m) (a) Metallic articulated bus. (b) Rigid bus.

(a)

(b)

Figure 6.17. Received Power (dBm) divided by zones within the different models of the buses for 2.4GHz frequency with the transmitter antenna placed at the point (X=1.35m, Y=2.03m, Z=1.10m) (a) Metallic articulated bus. (b) Rigid bus.

Table 6.3. CASE I Metallic articulated bus

Zone	Area (m²)	Power Mean (dBm)	Standard Deviation (dB)	Obstacles Density (%)
I	8.28	-44.61	3.447	23.84
II	7.83	-53.54	4.59	14.15
III	3.96	-74.05	3.765	0.51
IV	3.02	-78.82	3.059	6.29
V	3.96	-73.51	3.283	6.28
VI	3.02	-80.22	2.915	14.23
VII	4.55	-81.25	9.34	0
VIII	8.88	-136.77	44.98	38.6

Table 6.4. CASE I Rigid bus

Zone	Area (m²)	Power Mean (dBm)	Standard Deviation (dB)	Obstacles Density (%)
I	4.05	-50.89	2.81	10.37
II	6.75	-43.62	5.38	21.48
III	8.10	-58.17	4.39	6.91
IV	1.70	-74.87	2.82	34.07
V	2.55	-80.68	5.05	0.95
VI	3.74	-98.67	10.83	14.6
VII	3	-74.00	7.86	32.41
VIII	1.7	-84.88	7.24	60.62

Figure 6.16 shows simulation results obtained by means of in-house developed 3D RL algorithm for received power for 2.4GHz frequency for the metallic articulated bus and the rigid bus for Case I. Power results are shown at a 2D longitudinal cut plane of 0.8 meters in height, although simulation results have been obtained for the complete simulation scenario. This height has been chosen to emulate the typical height in order that a seated person could use a wireless device. As it can be seen from the previous results, received power levels strongly depend on the location of the transceivers, a direct consequence of the impact of topology and morphology in such an indoor vehicular environment. Elements such as passenger seats produce power absorption as well as scattering, leading to increased losses. Besides, received power decreases with distance, leading to lower values of power in the final part of the articulated bus.
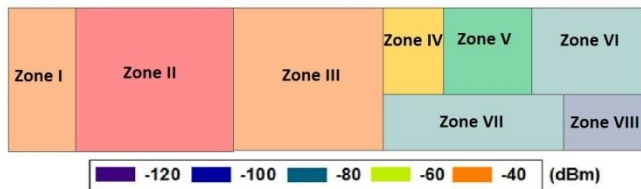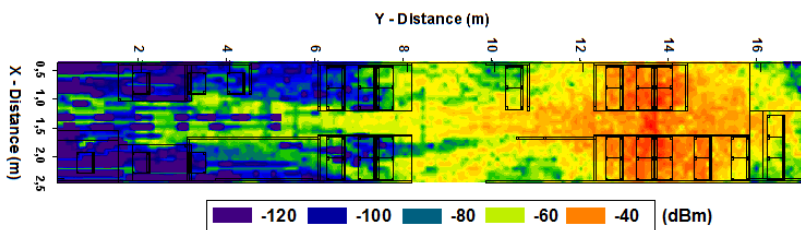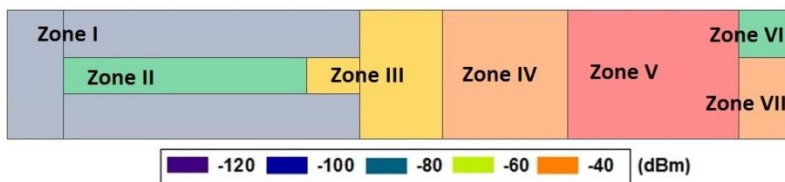
(a)
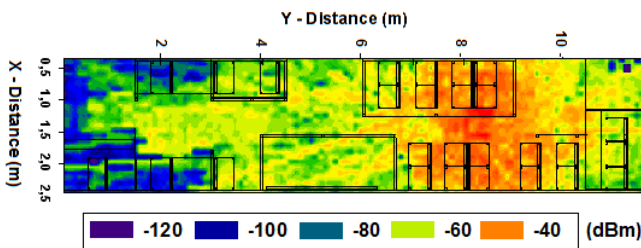
(b)

Figure 6.18. Received Power (dBm) within the different models of the buses for 2.4GHz frequency with the transmitter antenna placed at the point (X=1.35m, Y=13.72m, Z=1.10m) (a) Metallic articulated bus. (b) Rigid bus.

(a)

(b)

Figure 6.19. Received Power (dBm) divided by zones within the different models of the buses for 2.4GHz frequency with the transmitter antenna placed at point (X=1.35m, Y=13.72m, Z=1.10m) (a) Metallic articulated and (b) Rigid buses.

Table 6.5. CASE II Metallic articulated bus

Zone	Area (m²)	Power Mean (dBm)	Standard Deviation (dB)	Obstacles Density (%)
I	17.42	-107.88	32.63	21.59
II	2.55	-91.42	58.34	3.92
III	6.49	-60.67	3.16	0.92
IV	6.48	-55.66	3.98	5.63
V	9.99	-43.95	5.88	24.07
VI	1.62	-68.35	12.89	0
VII	1.84	-59.59	3.69	85

Table 6.6. CASE II Rigid bus

Zone	Area (m²)	Power Mean (dBm)	Standard Deviation (dB)	Obstacles Density (%)
I	5.85	-81.83	4.33	29.66
II	9	-62.72	1.45	4.46
III	4.05	-58.11	1.76	10.12
IV	6.75	-42.57	3.95	21.14
V	2.7	-53.24	2.63	4.52
VI	3.24	-61.96	4.05	46.12

Figure 6.17 shows the different zones of estimated received power extracted from the data of Figure 6.16. It can be seen that the morphology and the topology of the different buses play an important role in the radio planning task, obtaining different values of the mean received power depending of the obstacle density of the different zones. Table 6.3 and Table 6.4 show the different values of power mean with its standard deviation and the obstacle density of the zone considered. It can be observed that the obstacle density has a noticeable influence in the received power, but it is also highly important to take into account the area of the considered zone and the distance from the transmitter of each zone.

To gain insight into the influence that the morphology of the scenario may have in radio wave propagation, a Case II has been considered placing the transmitter antenna at the point (X=1.35m, Y=13.72m, Z=1.10m). Bi-dimensional planes of estimated received power have been obtained for the same height as Case I and they are shown in Figure 6.18. It is observed that, when the position of the transmitter antenna changes, the complete plane of estimated received power also changes, depending of the position of the obstacles and, as stated above, of the obstacle density and the distance from the transmitter. Figure

6.19 shows the same planes divided into different zones according to the mean received power, which can be very useful for radio planning purposes, with the associated tables (Tables 6.5 and 6.6), which present the data associated with the graphs.

From these results, it is shown that received power in different points of the scenarios depends greatly on the position of the transmitter, the obstacle density of the different zones and the different material properties of the obstacles. It is observed that multipath propagation is one of the most important phenomena in these types of environments, with a lot of metallic elements. Due to this fact, it is highly important to consider deterministic modelling such as RL for radio planning purposes, which permits to achieve a precise estimation of received power levels in the different parts of the transportation buses, for each transmitter antenna desired position, considering all the elements within the scenario. In terms of coverage, this analysis could lead to the optimal configuration of a WSN within the buses

As stated before, the fundamental radio electric phenomenon in this type of vehicle indoor environment is given by multipath propagation. To illustrate this fact, the PDP for the point (X=1.4m, Y= 4m, Z=0.8m) in the metallic articulated bus is depicted in Figure 6.20, exhibiting echoes in a time span of 0 to 180 ns. Time dispersion varies widely in a mobile radio channel depending on the geometrical position relationships among the transmitter, the receiver and the surrounding physical environment. Due to this fact, another parameter that can grossly quantify the multipath channel is the delay spread, which shows the effects of dispersion and is depicted in Figure 6.21 for the metallic articulated bus and the rigid bus. The delay spread has been calculated using as threshold the noise floor, with a value of -120dBm.
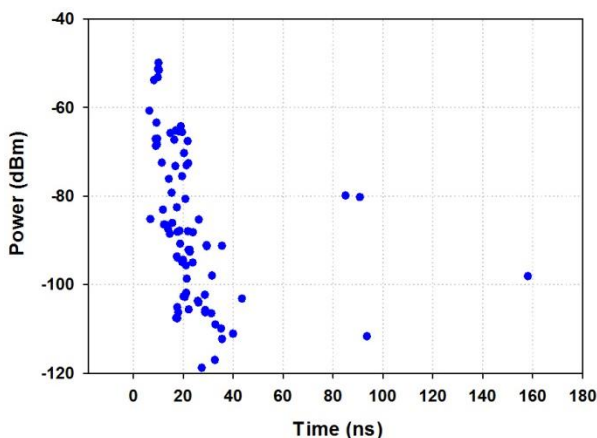

Figure 6.20. Power Delay Profile at a given cuboid, located at the point (X=1.4m, Y=4m, Z=0.8m) in the indoor metallic articulated bus.

From Figure 6.21 it can be seen that the multipath phenomenon is very different in both vehicles. The morphology and topology of the buses has a great influence in the time dispersion of the channel. It is observed that in the metallic articulated bus, the delay spread is higher in the areas near the transmitter antenna and is lower in the final part of the vehicle because the radiation power in this part is smaller due to the larger distance. However, in the rigid bus the differences between both sides of the vehicle are not as significant as the longer bus. This is due to the metallic bellow which is situated in the central part of the metallic articulated bus, which has a great influence in the behavior of multipath propagation inside the vehicles.
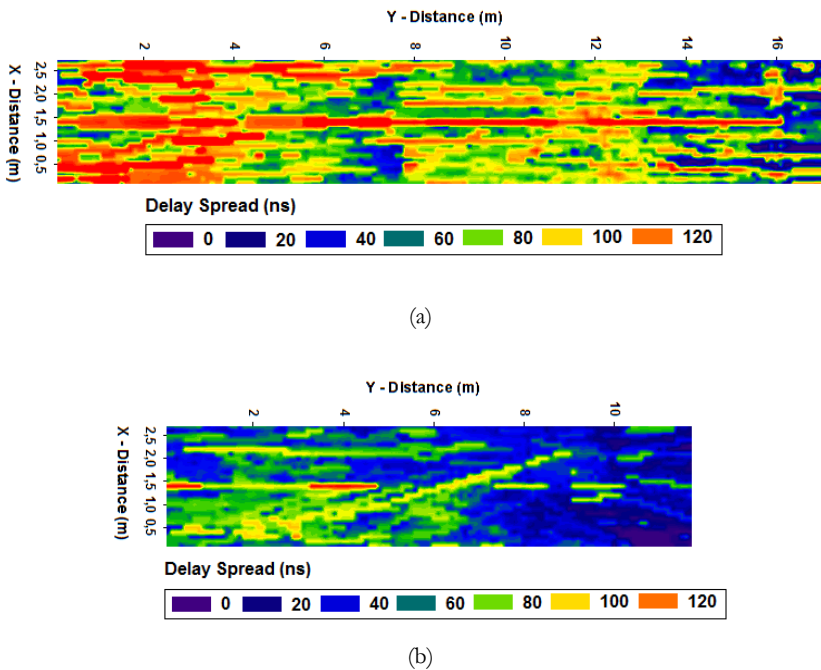

(a)

(b)

Figure 6.21. Delay Spread estimation at a bi-dimensional plane of 0.8m height (a) Metallic articulated bus. (b) Rigid bus.

B) With the presence of human body models

Simulations with the random presence of people inside the vehicles have been done in order to analyze the impact of the human bodies in the characterization of the channel for the development of BANs or WSNs within the public transportation buses. For that purpose, the vehicles modeled with

persons depicted in Figure 6.13 have been simulated with the same simulation parameters presented in Table 6.2. Figure 6.22 and Figure 6.23 show simulation results for the articulated more metallic bus (Figure 6.22) and for the rigid bus (Figure 6.23). In both figures, three cases are shown: Case I and Case II are the estimated received power for the bi-dimensional planes of 0.8m height without persons inside the vehicles (Case I) and with persons (Case II). The third case represents the difference between the two previous cases, which represents the spatial samples which are affected by the presence of persons. From both figures, it can be observed that the presence of persons (Case II) has a great impact in the estimated received power, having a widely fading channel in some spatial samples in this case than the case without persons. As mentioned above, Case III shows the comparison between the two previous cases, evidencing that the presence of passengers has a significant influence in the characterization of the channel. Accordingly, it is highly important to take into account the presence of human bodies within these types of vehicles.

From these results it can be concluded that the number of individuals is a fundamental parameter for the power distribution inside a bus. Therefore, two more simulations have been considered including more people, thus, starting from the original cases where the human occupation rate was approximately 25%, an occupation of 50% and 75% is reached for the two kinds of buses.
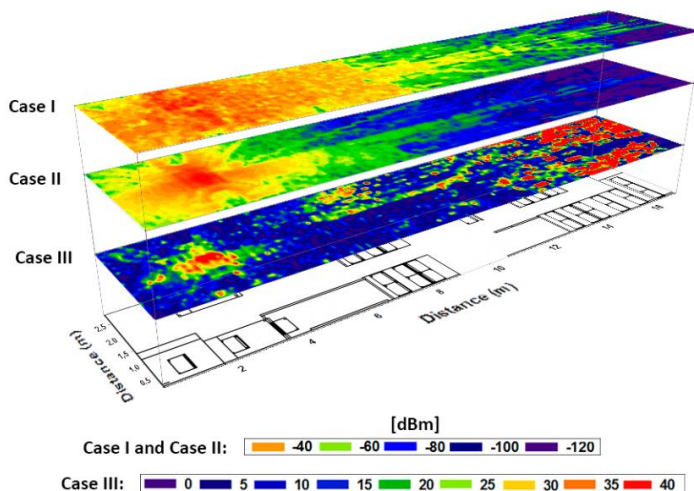

Figure 6.22. Comparison of estimated Received Power (dBm) for the bi-dimensional plane of 0.8m height for the metallic articulated bus without persons (Case I), with persons (Case II) and difference between them (Case III).
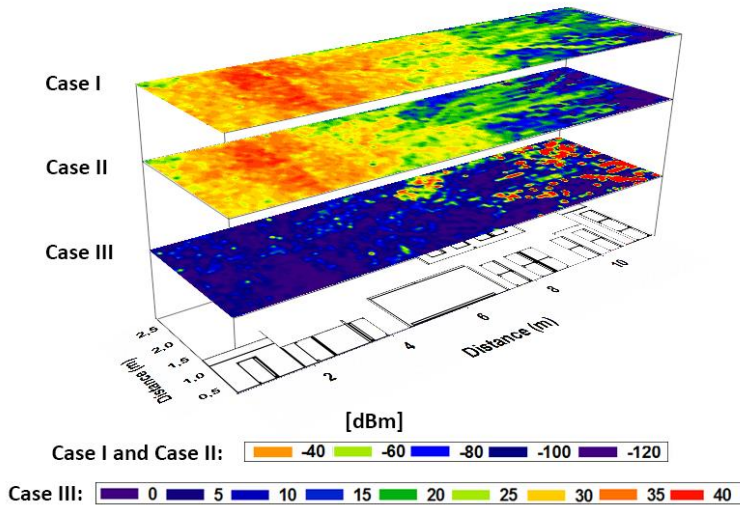
Figure 6.23. Comparison of estimated Received Power (dBm) for the bi-dimensional plane of 0.8m height for the rigid bus without persons (Case I), with persons (Case II) and difference between them (Case III).

The obtained results show that the deviation from the situation of empty vehicle grows with the inclusion of more human body models into the scenario. In the case of rigid bus the low occupation scenario (25%) gives an error of 5dB and a Standard Deviation (SD) of 21dB while the high occupation reach an error level of 7.8dB and a standard deviation of 26.6dB. The occupational difference is especially noticeable when the articulated bus is considered, with values for the three situations (in occupational ascendant order) of 9.3dB (28.5dB SD), 11.8dB (33.3dB SD) and 14dB (38.41dB SD). The fact that the bus is longer together with a larger absolute number of people leads to higher deviations comparing with empty buses. Figure 6.24 represents the considered scenario for the simulation performed for high density of human beings (75%).
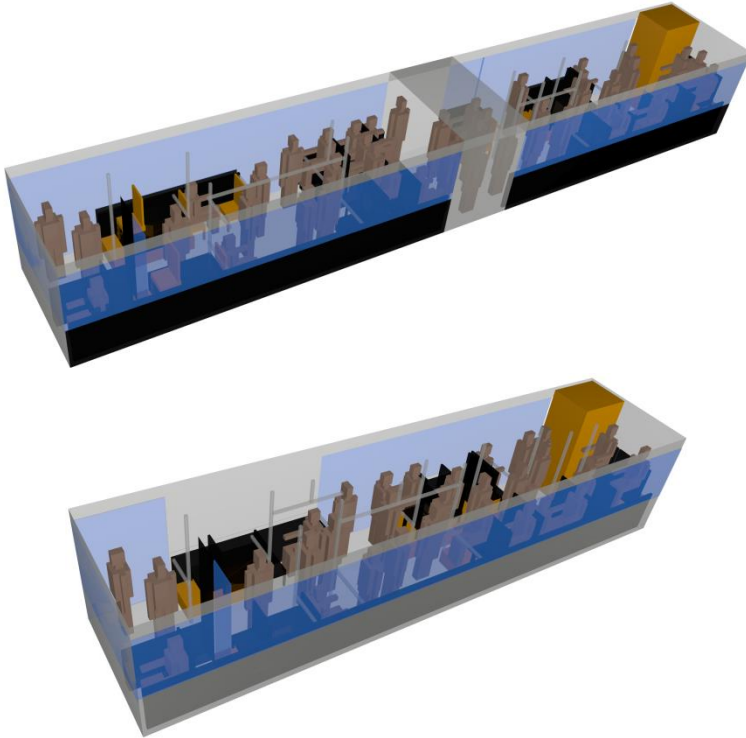
Figure 6.24. Simulation scenarios developed with the high density (75%) of human beings inside the articulated (top) and rigid (bottom) buses, respectively.

6.1.2.3. Statistical Analysis

A) Path Loss model

A widely used simple indoor path loss model is the one-slope model, based on the following expression [Rap01]:

$$PL(d) = \overline{PL}(d) + \mathrm{X}_\sigma = \overline{PL}(d_0) + 10n\log_{10}(\frac{d}{d_0}) + \mathrm{X}_\sigma \qquad (6.1)$$

where $\overline{\mathrm{PL}}(\mathrm{d_0})$ is the intercept, d is the distance from the transmitter to the receiver in meters, and n is the path loss exponent dependent on the specific

172

propagation environment indicating the rate at which PL increases with distance. In free space propagation, n equals 2. X_σ denotes shadow fading with standard deviation σ. The bars in Equation (6.1) denote the ensemble average of all possible path loss values for a given value of d.

Estimated path loss values have been calculated in the considered scenarios and compared with the lognormal distribution. From the results of received power estimated for the whole scenarios in the previous section, path loss can be predicted for each spatial point of the environment applying:

$$PL(d)[dB] = P_t[dBm] - P_r[dBm] \qquad (6.2)$$

with the antenna gains included in P_t[dBm] and P_r[dBm]. The spatial sampling with the 3D RL technique has been set to cuboids of 10cm, taking into account accuracy results and computational time of simulations. Figure 6.25 shows the scatter plot of the simulated values path loss for a height of 1.1m with respect to the transmitter-receiver separation in logarithmic scale. Additionally, the linear regression line, resulting from a Minimum Mean Square Error (MMSE) analysis, is shown, which is expressed as

$$PL(d) = 40.3 + 17.79 \log_{10}(d); \sigma = 10.22 dB \qquad (6.3)$$

The corresponding path loss exponent is n=1.779 with a standard deviation σ=10.22dB. Accordingly, n is slightly smaller than for free space propagation and lies in the range of values found for indoor radio wave propagation in office environments [Rap01, Don10, Siw98]. It can be found in the literature [Rap01] that depending of the surrounding environment, n varies between 1.6 and 3.3 and σ between 3 and 14dB.

From Figure 6.25 it can be seen that the log-normal distribution describes the random shadowing effects in the considered scenario. This phenomenon is referred to as the large-scale fading or log-normal shadowing which is caused for the slow variation in mean signal level. The considered distance for the receivers to analyze this effect has been set to the selected cuboids size, which is equivalent to three-quarters wavelength.
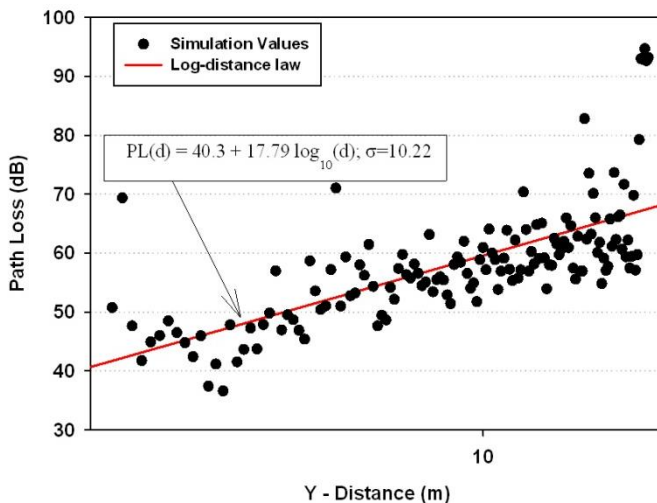
Figure 6.25. Path loss versus Tx-Rx separation with linear regression fit.

B) Small-Scale Fading Statistics

In order to verify the behavior of fast fading of the received field at different points of the considered scenario, local statistics have been calculated with the PDPs. Figure 6.26 represents the variation of received power along the Y-axis, for X=1.35m and Z=1.1m, for the metallic articulated bus depicted in Figure 6.12 (top). It is observed a great variability in the received power and it can be seen that the median value of the signal strength is monotonically decreasing with distance. The median level is subject to two major variations. One is large-scale signal variations, which has been found to be normally distributed [Siw98], as it is previously shown in Figure 6.25. The second variation is the small-scale variation due to the vector combination of multiple rays arriving at the local vicinity of the portable communications antenna. The small-scale variation which has been analyzed in the channel is referred to as flat fading, based on multipath delay spread which causes that the strength of the received signal changes with time [Rap01]. The small-scale variation for narrowband signals is distributed according to Rayleigh statistics [Rap01, Siw98]. An analysis of the small-scale fading within the metallic articulated bus has been made. The selected points for the analysis are the four points depicted with a circle in Figure 6.26. The small-scale fading has been analyzed with the PDPs for these four spatial samples, each of them with a three-quarters wavelength distance. Figure 6.27 shows the variability of signal amplitude with time for the selected points. The separation of

samples in wavelength is in agreement with the literature for small-scale analysis for indoor environments [Wee93, Jak93].
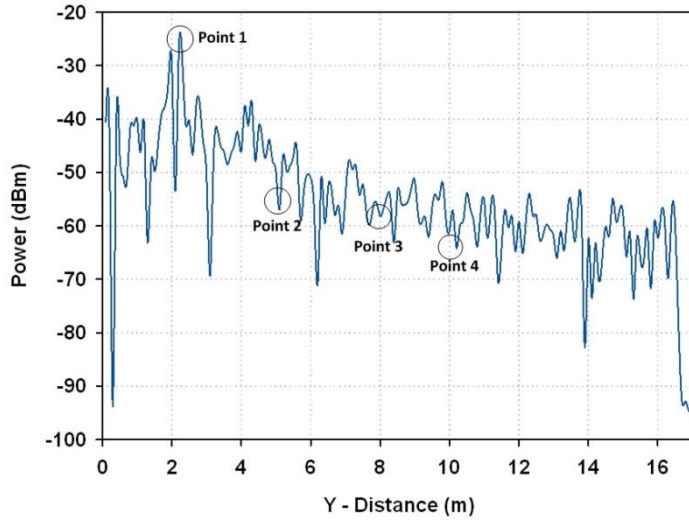

Figure 6.26. Linear distribution of Received Power (dBm) along the Y-axis, for X=1.35m and Z=1.1m, for the metallic articulated bus.
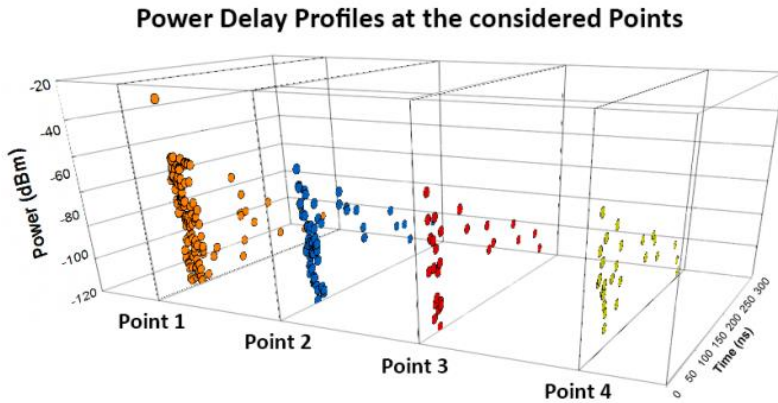

Figure 6.27. Power Delay Profiles for the four considered points selected in Figure 6.24.

These selected points have been chosen because of the different distances they have with the transmitter and the different multipath variability of each of them, as it is shown in Figure 6.27. The Cumulative Distribution Function (CDF) of the PDPs shown in Figure 6.27 for the considering points has been computed and compared against Rayleigh distribution, which is commonly used to describe small-scale fading in indoor environments [Rap01].

The Probability Density Function (PDF) of a Rayleigh distributed random variable is given by

$$p(r) = \frac{r}{\sigma^2} \exp(-\frac{r^2}{2\sigma^2}) \qquad (6.4)$$

where r is the magnitude of the received power, and σ is the standard deviation of the multipath propagation. The CDF of Rayleigh distribution is obtained via integration over the PDF.

Figure 6.28 shows the actual flat fading statistics for the selected points and its fits with Rayleigh distributions. By analyzing Figure 6.28 it can be seen that when increasing the transmitter-receiver separation distance, the standard deviation of multipath propagation decreases. This is due to the fact that since the distance has increased, the components contributing to the multipath propagation are more attenuated and more of them fall below the noise threshold, and therefore are not computed. Point 3 and Point 4 have a lower number of data due to the greater distance with the transmitter than the other considered points. Note that the small-scale analysis have been done with the PDPs shown in Figure 6.27, and only the values higher than the noise threshold level have been considered.
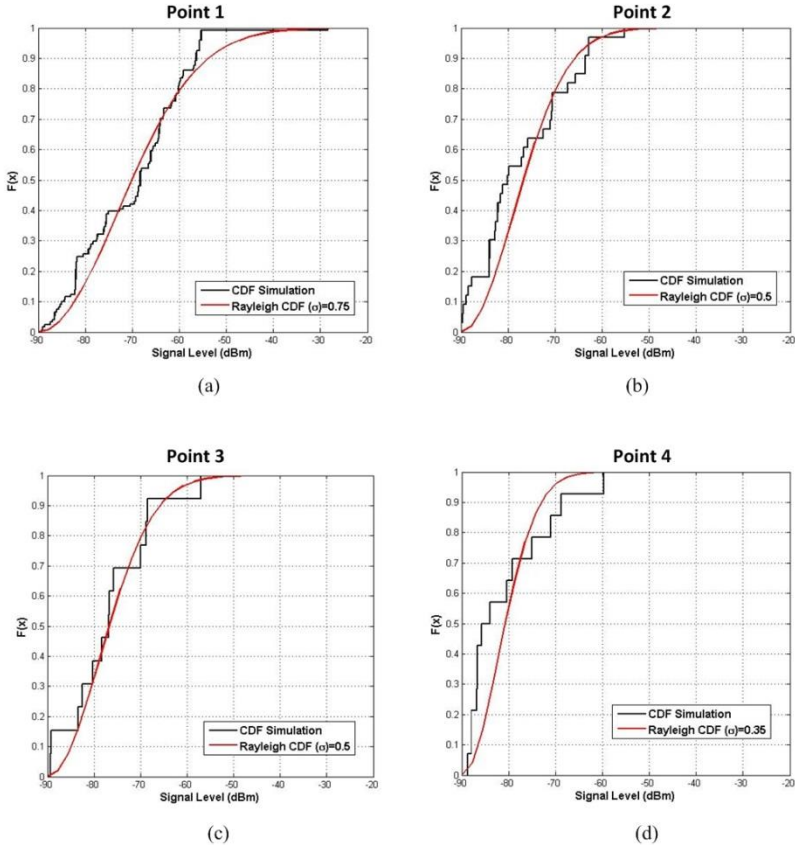
Figure 6.28. CDFs for different points of the considered scenario depicted in Figure 6.12 (top) and its matching with Rayleigh distribution.

6.1.2.4. Measurement Results

In order to validate the results previously obtained, measurements in real urban buses have been obtained. These results provide assessment in wireless channel behavior, in order to perform adequate radio planning for deployment of embarked wireless systems, such as WSNs. A transmitter antenna, connected to a signal generator at 2.4GHz has been located at the coordinates (X=1.35m, Y=2.03m, Z=1.10m) which correspond to the entrance of the bus, with a transmission power of -10dBm. The employed signal generator is a portable Agilent N1996A and the spectrum analyzer is an Agilent N9912 Field Fox. The

antennas used are ECOM5-2400 from RS, both omnidirectional antennas[1]. Figure 6.29 shows the location for the transmitter in the model created for the metallic articulated bus. Measurements have been performed along the three dashed lines depicted in Figure 6.29. In the central line, measurement points have been taken every meter at a height of 1.10 meters. For the lateral measurement lines, the bottom picture of Figure 6.29 shows a lateral view of the bus with the measurement points just above the seats, but for different heights each one depending of the morphology of the buses. Similar measurements along the three lines have been performed for the rigid bus.
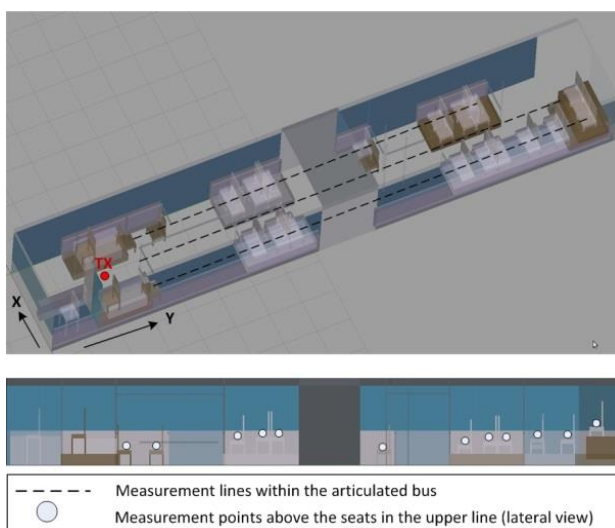

Figure 6.29. Measurement points within the metallic articulated bus model.

Figures 6.30 and 6.31 show the comparison between simulation and results for the measurement points performed along the three lines for the metallic articulated bus (Figure 6.30) and for the rigid bus (Figure 6.31) models. Measurements were performed with 100MHz bandwidth at 2.4GHz frequency. The measurement time at each point was 60 seconds, and the value of received power represented by each point is the higher peak of power shown by the spectrum analyzer for the considered bandwidth (MaxHold function in the Agilent spectrum analyzer). The received power values estimated by simulation have been obtained for the same spatial samples as the real measurements,

---

[1] For more information about the measurement equipment, see Appendix B.

considering the corresponding cuboid in the three-dimensional mesh of cuboids in which the scenarios have been divided.

The mean error between simulation and measurements for the metallic articulated bus is 0.67dB with a SD of 0.45dB, whereas the mean error between simulation and measurements for the rigid bus is 0.88dB with a SD of 0.99dB. It is shown that they exhibit good agreement and validate previous simulations results.
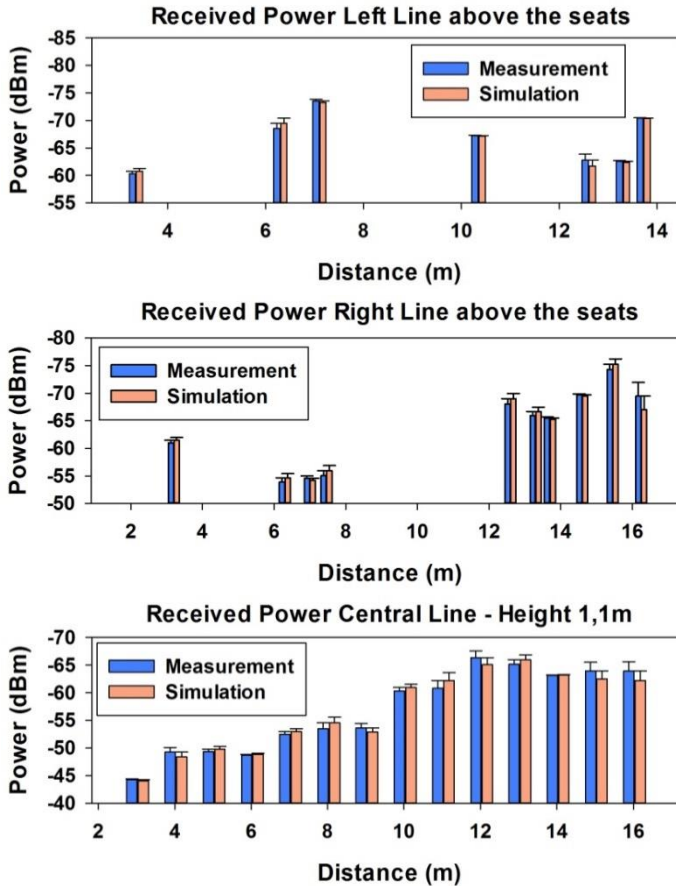

Figure 6.30. Comparison simulation versus measurements for 2.4GHz frequency in the metallic articulated bus model (top) Measurement points of left line just above the seats. (middle) Measurement points of right line just above the seats. (bottom) Measurements points of central line of the bus.

179

Figure 6.31. Comparison simulation versus measurements for 2.4GHz frequency in the rigid bus model (top) Measurement points of left line just above the seats (middle) Measurement points of right line just above the seats. (bottom) Measurements points of central line of the bus.
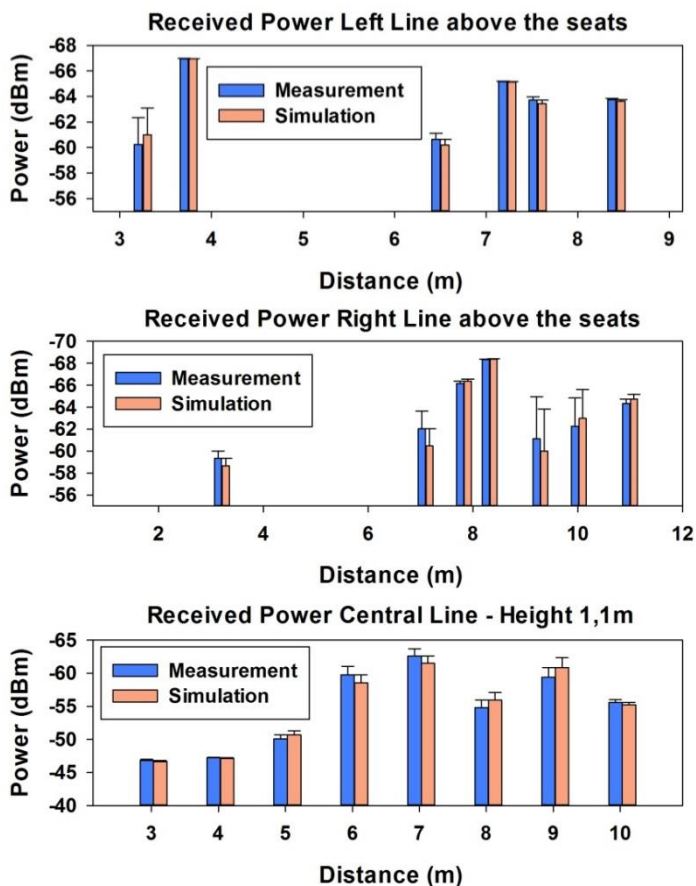
6.1.3 Vegetation environments

In this section, the radio channel characterization for ISM 2.4 GHz WSNs in an inhomogeneous vegetation environment has been analyzed. The scenario where this network is intended to operate is a combination of buildings and diverse vegetation species. To gain insight into the effects of radio propagation, a

simplified vegetation model has been developed, considering the material parameters and simplified geometry embedded in the simulation scenario.

The simulation scenario implemented for calculation by means of the in-house developed 3D RL code corresponds to the inhomogeneous vegetation environment represented in Figure 6.32, which is an outdoor location of the Campus of the Public University of Navarra.
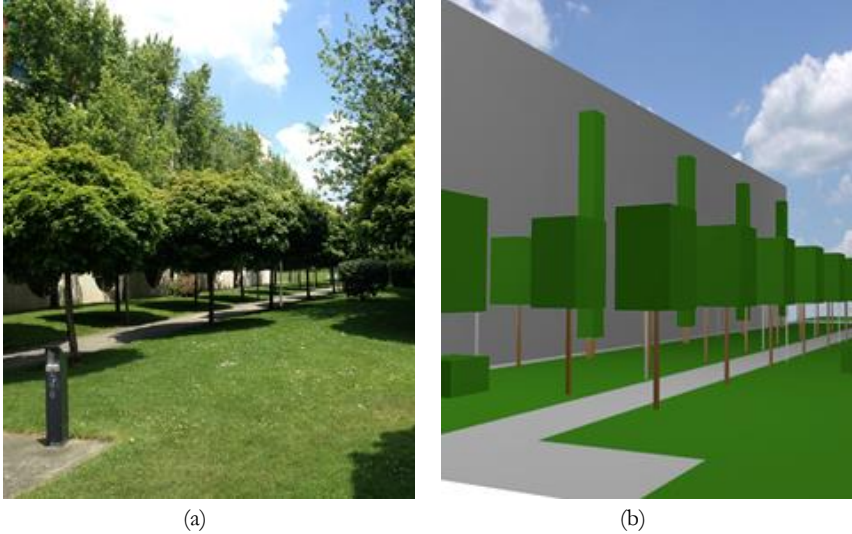

(a)   (b)

Figure 6.32. Vegetation scenario under consideration for simulation in the 3D Ray Launching algorithm (a) Real view (b) Schematic view for simulation.

A view of the complete schematic vegetation model developed for simulation is depicted in Figure 6.33 with the position of the transmitter. All the material properties for all the elements within the scenario have been considered, given the dielectric constant and the loss tangent at the frequency range of operation of the system under analysis. Due to the continuous changes of the considered environment because of the weather, it is relevant to consider different conditions for the material properties of the trees. The top portion of the tree exhibits high variability depending on the season; for example in winter, there is little foliage whereas in summer the vast totality of the volume of the top of the trees is foliage. In addition, the humidity of the wood of the trunk of the trees strongly varies depending on the weather. This has led us to consider maximum and minimum conditions for the material properties of the foliage and

the trunk of the trees. For that purpose, the values obtained in [Vya12] for the material properties of the wood and the foliage have been used. The dielectric constant and conductivity of the wood of the ash tree, which are the trees of the considered scenario is variable with the temperature, as it is shown in Equations (6.5) and (6.6) with the parameter t, and the dielectric constant and conductivity of the foliage of the trees is variable with humidity, as shown in Equations (6.7) and (6.8) with the parameter h:

$$\varepsilon_{r\,ash\,wood} = -4 * 10^{-6}t^3 + 0.0002t^2 - 0.0212t + 21.483 \qquad (6.5)$$

$$\sigma_{ash\,wood} = 3 * 10^{-7}t^3 - 0.0003t^2 - 0.004t + 7.3238 \qquad (6.6)$$

$$\varepsilon_{r\,foliage} = 137h^3 - 69.688h^2 + 23.385h + 1.4984 \qquad (6.7)$$

$$\sigma_{foliage} = 1.1541h^3 - 0.5489h^2 + 0.1669h - 0.0004 \qquad (6.8)$$
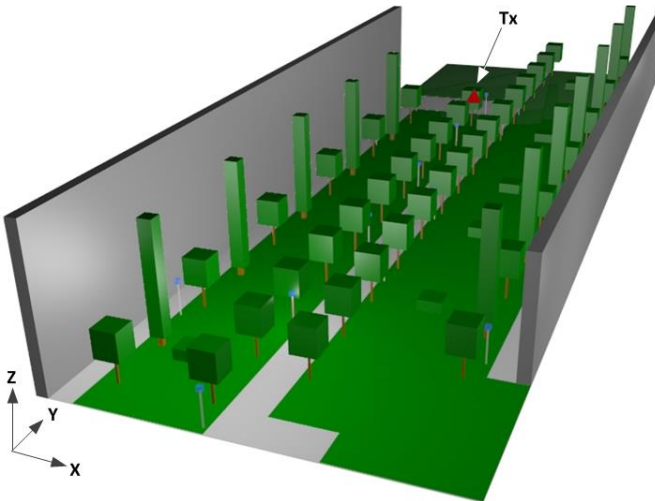

Figure 6.33. Schematic vegetation environment for simulation in the 3D Ray Launching algorithm.

To set up the dielectric constant and conductivity of the ash wood and the foliage, thresholds for the maximum and minimum humidity and temperature have been considered. These values have been fixed in the interval (0%, 30%) for the humidity and (20°, 40°) for the temperature, according to [Vya12].

Simulations have been performed for the minimum, medium and maximum values and the results shown in this work correspond to the average values for the humidity and temperature.

The material parameters used in the simulation are shown in Table 6.7 [Bal89, Cui02].

Table 6.7. Material properties in the ray launching simulation.

| Parameter	Permittivity (ε_r)	Conductivity (σ) [S/m]
Air	1	0
Concrete	5.66	0.142
Grass	30	0.01
Trunk tree	Equation (6.5)	Equation (6.6)
Tree foliage	Equation (6.7)	Equation (6.8)

For the simulations, an antenna has been placed at the point (X = 11.95 m, Y = 70.8, Z = 1.2), depicted with a red triangle in Figure 6.33. The radiating element is a wireless ZigBee mote which has been configured as a dipole, transmitting 18dBm at 2.41 GHz. Simulation parameters are shown in Table 6.8.

**Table 6.8.** Parameters in the ray launching simulation.

Frequency		2.41 GHz
Vertical plane angle resolution	$\Delta\theta$	0.5°
Horizontal plane angle resolution	$\Delta\varphi$	0.5°
Reflections		6
Transmitter Power		18 dBm
Cuboids resolution		0.5 m

6.1.3.1. Simulation Results

Once the simulation scenario has been defined, simulation results can be obtained. Figure 6.34 shows the power distribution within the considered scenario for different heights (Figure 6.34a). As it can be seen, the influence of the obstacles (like the trees and streetlights) can be easily appreciated. It is shown that the morphology as well as the topology of the considered scenario has a noticeable impact on radio wave propagation.
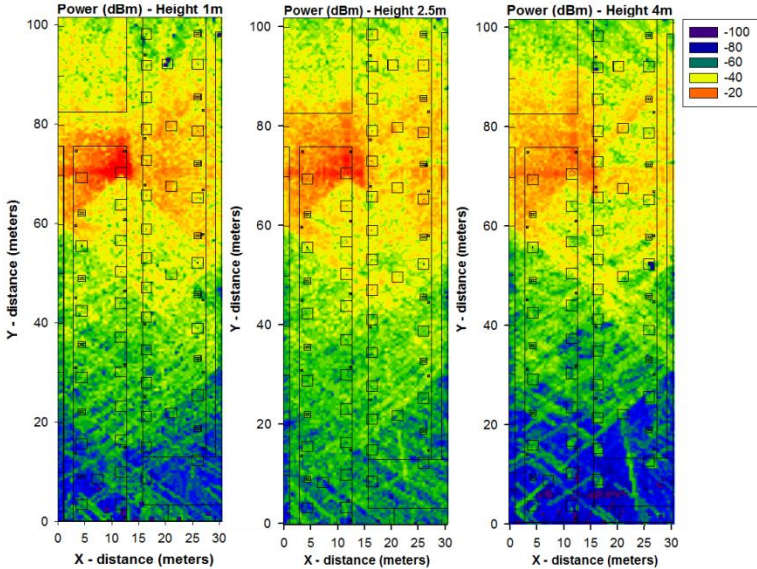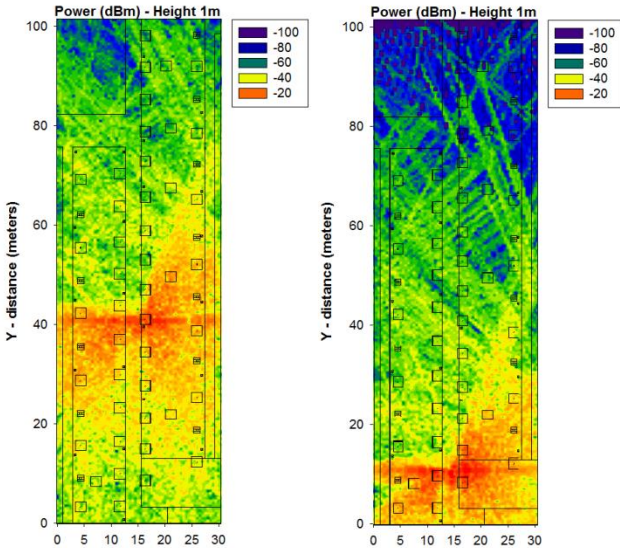
Figure 6.34. Estimation of received power (dBm) on the vegetation environment obtained by the 3D Ray Launching algorithm (a) For the transmitter antenna placed at a fixed point and for different heights (b) For two different points of the transmitter antenna for the same height.

In order to gain insight into the influence of the scenario in radio wave propagation, different locations of the transmitter antenna have been considered. Figure 6.34b represents the received power for 1m height for two different points (X = 14.7 m, Y = 41, Z = 1.2) and (X = 14.7 m, Y = 11, Z = 1.2). It is shown that the position of the transmitter antenna plays a key role in the distribution of the received power, because electromagnetic phenomena, such as reflections, diffraction and absorption due to obstacles are different depending on the environment. Therefore, this change in the overall signal levels obtained can provide with mean values of received signal but the consideration of local point values requires analysis for the specific transceivers positions employed.

Figure 6.35 depicts a linear distribution from within the transmitter-receiver range of power along the Y-axis of the considered scenario, for two different values of X, for different heights. It is observed that the distribution of power exhibits large variability due mainly to the strong influence of multipath components.
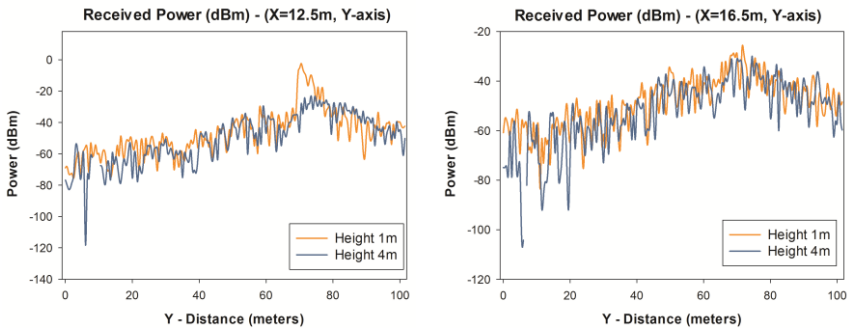

Figure 6.35. Estimation of radials of received power (dBm) along the Y-axis for X = 12.5m and X = 16.5 m for different heights.

An important radioelectric phenomenon in this type of environment is given by multipath propagation. To illustrate this fact, the PDP for the central location of the scenario has been obtained and it is shown in Figure 6.36. As it can be observed, there are several echoes in the scenario inherent to the behavior of multipath channels.
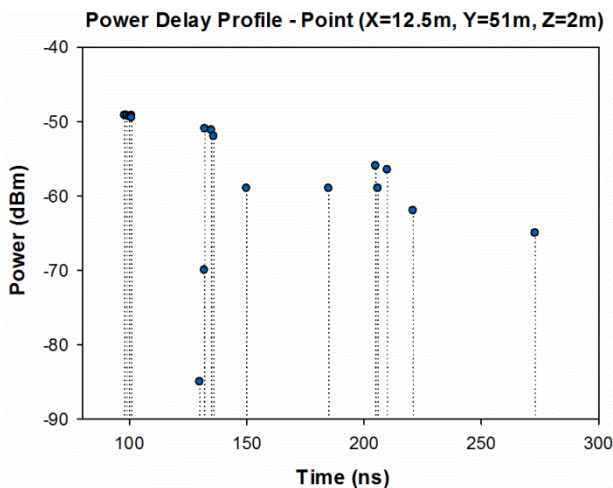
Figure 6.36. Power Delay Profile at a given cuboid, located at the central location in the considered scenario.

Time dispersion varies widely in a mobile radio channel depending on the geometrical position relationships among the transmitter, the receiver and the surrounding physical environment. Because of that, another parameter that can grossly quantify the multipath channel is the delay spread, which shows the effects of dispersion and is depicted in Figure 6.37 for the considered scenario.

The strong dependence between the observation point and received multipath components given by the complex morphology of the environment can be clearly seen. Specifically, it is observed that the Delay Spread values nearer the transmitter point are much higher than farther values. This is because at nearer points, the higher power level of the rays produced more dispersion caused by the reflections and diffractions of obstacles and metallic elements inherently presented in the environment.

In order to gain insight into the effect of topology on energy consumption, a current consumption map for the considered scenario has been obtained and is shown in Figure 6.38, for the same position of the transmitter. As it can be seen, the current consumption is strongly dependent on the location of the transceivers, as expected from the received signal variations previously shown.
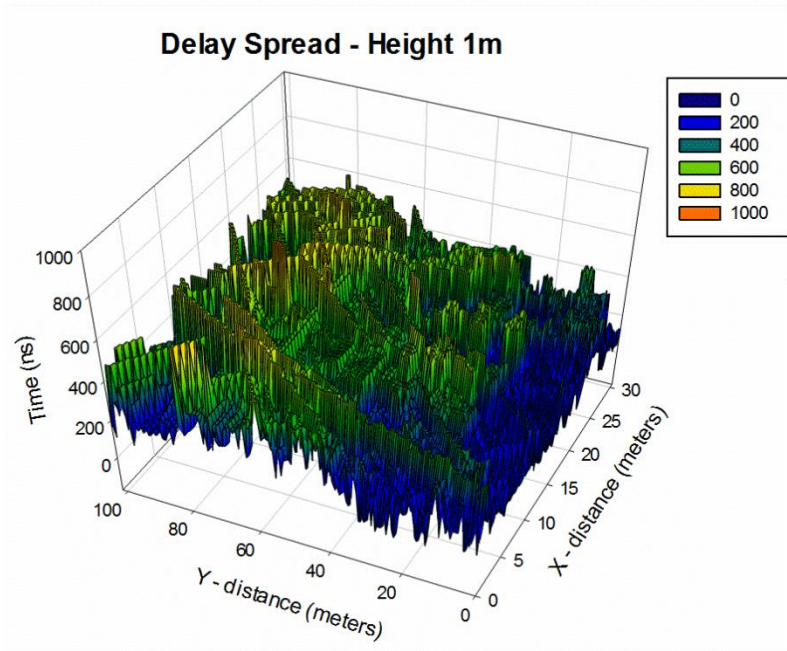
Figure 6.37. Delay Spread estimation within the considered scenario at 1 m height.
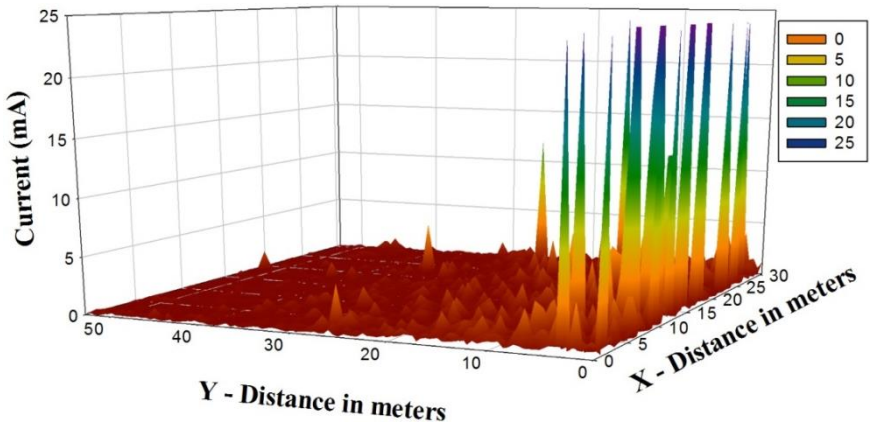

Figure 6.38. Estimation of energy consumption in terms of current values in mA.

These results can be used in order to design the optimal network layout, as a function of the number of employed nodes, the variables to transmit (and hence, the required transmission bandwidth) and the resulting sensitivity level. These previous results could be employed in combination with optimization methods in order to estimate the optimal network topology. Moreover, the density of the nodes within the network would have a clear impact on energy consumption, due to the fact that link balance limitations would be lower, since inter-node distance would also be smaller. Care should be taken however, since a larger density of nodes can also lead to increased interference levels, which could degrade system performance. This comment also applies to the case of changes in the transmitted service, associated with a certain allocated bandwidth and hence, changes in sensitivity levels.

Bit Error Rate (BER) is a key parameter that is used in assessing systems that transmit digital data from one location to another. BER expression for Quadrature Phase-Shift Keying (QPSK) modulation can be calculated, assuming Additive White Gaussian Noise (AWGN) of power density No/2, by:

$$BER_{QPSK} = Q(\sqrt{2E_b/N_0}) \qquad (6.9)$$

where $E_b = P_{RX}/R_b$. The received power (P_{RX}) has been calculated with the 3D ray launching algorithm for each spatial sample in the considered scenario. With these values, the BER has been calculated and it is shown in Figures 6.39 and 6.40, for different values of data rate (R_b) and different values of N_0. It can be seen the high variability between the different cases, with higher values of BER when N_0 is higher. In addition, it is observed the differences between the different data rates considered, leading to a lower BER for all cases with the lowest data rate considered. These results can be very helpful in order to optimize the design and deployment of a WSN depending on the modulation, the used data rate and the noise power level.
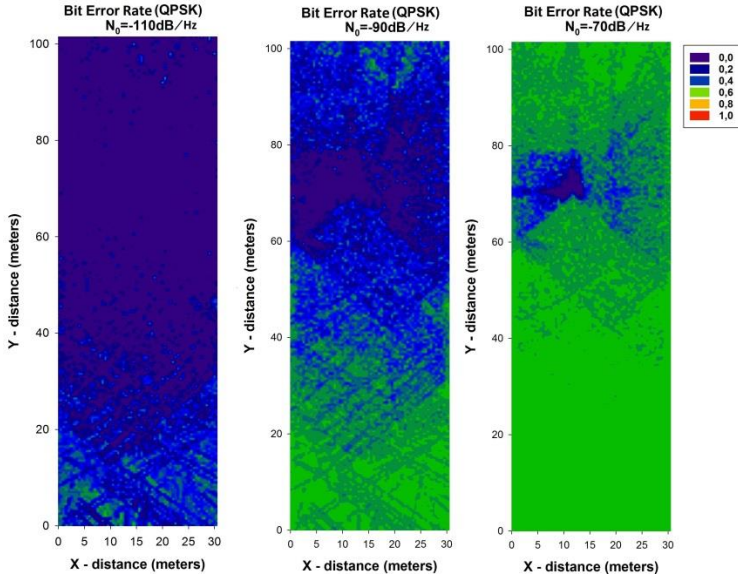
188

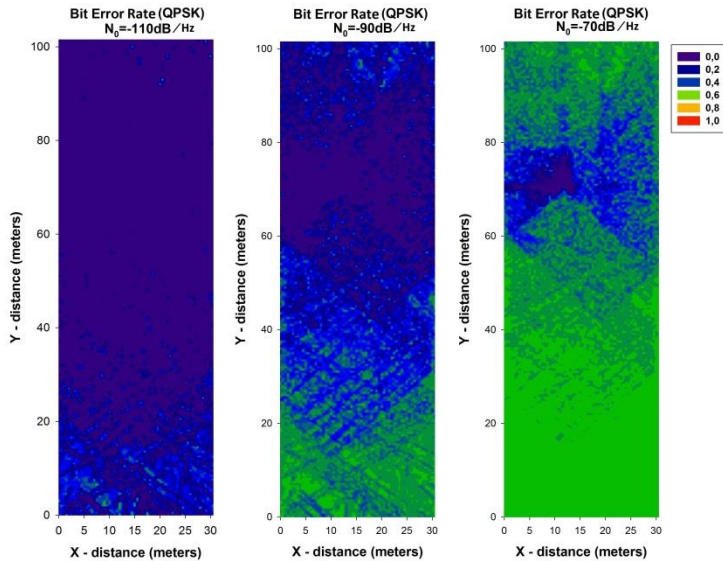**Figure 6.39.** Bit Error Rate for QPSK modulation for different values of N_0 for data rate of 250 Kbps.

Figure 6.40. Bit Error Rate for QPSK modulation for different values of N_0 for data rate of 57600 bps.

189

6.1.3.2. Radioplanning analysis

The deployment of two different communication systems (briefly described in Chapter 2) has been analyzed within the considered scenario. Firstly, the ZigBee technology has been evaluated. Specifically, the wireless devices used for simulation have been both, the XBee Pro and Xbee motes from Digi International Inc. The differences between them are mainly due to larger transmitter power of the Xbee Pro and its longer range distance. The transmitted power level considered has been reduced to the minimum default value to analyze worst case conditions. Losses due to different weather conditions and foliage have been introduced according to [Per02], adding 3 dB of losses. In addition, Bluetooth Low Energy (BLE) and classic Bluetooth have also been evaluated. BLE is an emerging wireless technology developed by the Bluetooth Special Interest Group (SIG) for short-range communications. In contrast with classic Bluetooth, BLE has been designed as a low-power solution for control and monitoring applications. The transmitted power and sensitivity for the different communication systems considered is shown in Table 6.9. It must be pointed out that the data of BLE and classic Bluetooth has been obtained from the literature [Gom12].

Table 6.9. Parameters for the different considered wireless communication systems.

	ZigBee Xbee Pro	ZigBee Xbee	Bluetooth Low Energy		Bluetooth Class 1	Bluetooth Class 2	Bluetooth Class 3
Transmitted Power (dBm)	10	10	-20	10	20	4	0
Sensitivity (dBm)	-100	-92	-93	-87	-90	-90	-90

Figure 6.41 shows the linear distributions of received power along the Y-axis for different values of X for different heights in the case of ZigBee and for one meter height in the case of Bluetooth. Figures 6.41a,b show the comparison between the received power of XBee Pro and XBee with the sensitivity of each of them.

Figure 6.41c shows the comparison between BLE with the maximum and minimum transmitted power and the higher and lower receiver sensitivity depending of which type of BLE has being used. Figure 6.41d shows the comparison between Class 1, Class 2, and Class 3 of classic Bluetooth. It can be

seen that there are some points where the signal goes down below the sensitivity level. With these values, an optimal design of the wireless sensor network coverage can be obtained, as shown in Figure 6.42.
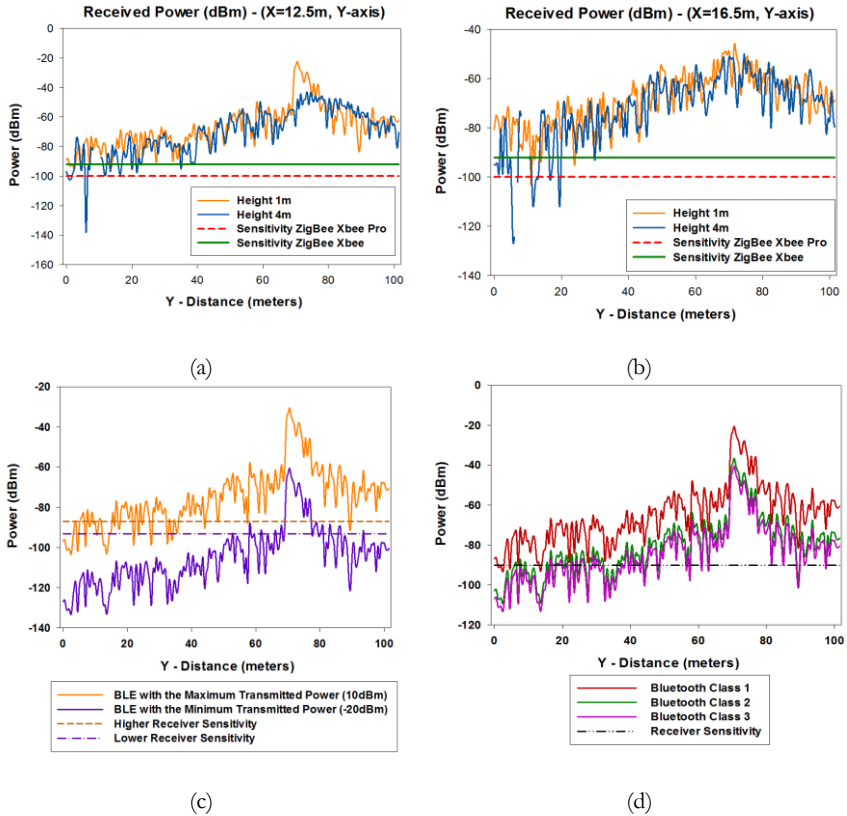
Figure 6.41. Comparison of radial of received power (dBm) along the Y-axis with the receiver sensitivity (a) ZigBee Xbee Pro and ZigBee Xbee for X = 12.5 m (b) ZigBee Xbee Pro and ZigBee Xbee for X = 16.5 m (c) BLE system (d) Classic Bluetooth.

Another important parameter to be considered when designing a WSN is capacity. Once coverage levels are satisfied, in order to have a good quality of service in the communication link, we must have adequate capacity. The channel capacity is determined by the number of users who are connected to the same communication link at the same time, the data rate of the transceivers and the number of gateways in which the information is gathered.

Figure 6.42. Radioplanning coverage for different technologies within the considered vegetation environment.
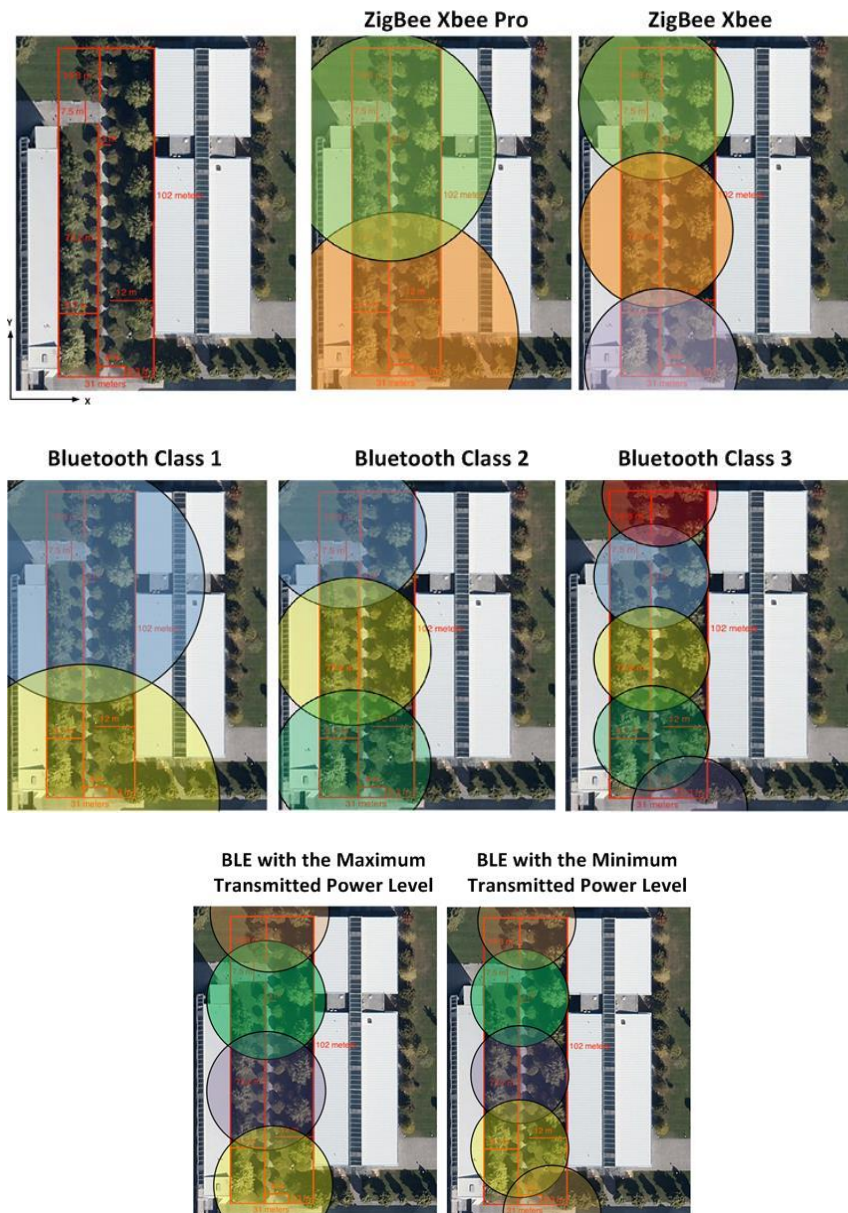
With this information, Figures 6.43 and 6.44 show the channel capacity vs. the number of users for different data rates considered and for different number of gateways. It is observed as expected that if the information is gathered with a higher number of gateways, the channel capacity increases for the same number of users, for every data rate considered.
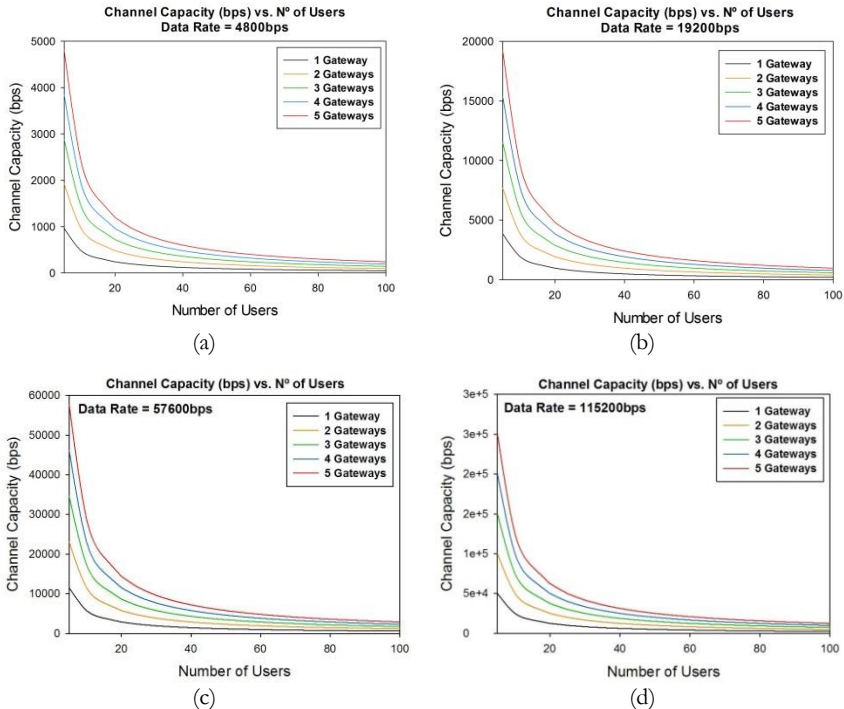
Figure 6.43. Channel capacity (bps) vs. the number of users for different number of gateways considered (a) Data Rate = 4800 bps; (b) Data Rate = 19,200 bps; (c) Data Rate = 57,600 bps; (d) Data Rate = 115,200 bps.

It is also very noticeable the great difference in the channel capacity depending of the data rate considered, showing a difference of 29,500 bps between the lowest data rate (4,800 bps) and the highest (115,200 bps) (Figure 6.44). This leads to conclude that, depending of the data rate of the transceivers and the expected number of users it is highly important to adequately set the number of gateways in the design phase.
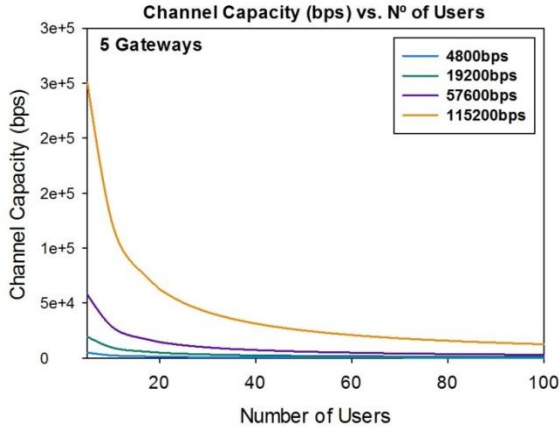
Figure 6.44. Channel capacity (bps) vs. the number of users for different data rates for five gateways considered.

6.1.3.3. Experimental Setup

An experimental setup has been set with the aim of validating the simulation results obtained previously. ZigBee technology has been chosen for emulating a WSN. Specifically, the wireless devices used for the measurements have been the XBee Pro motes from Digi International Inc[2], shown in Figure 6.45. These wireless communication devices operate in the unlicensed ISM 2.4 GHz band and the whip antenna mounted on it has an omnidirectional diagram with a gain of 1.5dBi, which has been taken into account to calibrate the measured values. For transmitting or processing received data, the motes have been connected to a PC via USB cable after being plugged into an XBee explorer unit.

Two different measurement campaigns have been carried out. In first place, the radio propagation in the vegetation environment has been characterized setting a transmitting ZigBee mote on the trunk of one of the trees, at the point indicated in Figure 6.33. The points of measurement are the rows of trees along the path, with the receiver placed inside the foliage of each tree. The received power level has been measured by means of an Agilent N9912 Field Fox portable spectrum analyzer. The omnidirectional antenna coupled to the analyzer operates at ISM 2.4 GHz band and has a gain of 5dBi. The parameters of the transmitting ZigBee mote can be seen in Table 6.10.

---

[2] For more information about the measurement equipment, see Appendix B.

Figure 6.45. The ZigBee mote used for wireless communications in the vegetation environment.

Table 6.10. Configuration of the parameters of the XBee Pro wireless devices to measure the received power level.

Transmitted Power	18 dBm (Maximum Default Value)
Transmission rate	57,600 bps
Frequency	2.41 (ZigBee Channel 12)
Measurement time	5 min

The measurement results for received power in the locations previously described can be seen in Figure 6.46, where 3D RL simulation results have also been included for comparison.

Good agreement is observed between the simulation results and the measurements. The resulting mean error for those measurement points is 1.67 dB, a low error that indicates that the proposed in-house 3D RL simulation method works properly, validating in the same way the simulation results shown in the previous sections of this work. Once the received power level for different positions within the vegetation environment has been measured and the simulation method has been validated, the second measurement campaign has been performed. The aim of these measurements is to deepen the analysis of the radio propagation in a highly complex environment such as the considered

scenario. For that purpose, the quality of the ZigBee channel has been measured. Specifically, the value of Packet Error Rate (PER) has been used as quality parameter, which indicates the percentage of transmitted packets that has been lost and do not reach properly the receiver. The position of the transmitter and the measurement points have been the same as in the previous measurement campaign. But in this case, another XBee Pro mote has been placed on the measurement points in order to implement ZigBee radio links. In addition, in this case, two different measurements have been done for each tree, one with the XBee Pro mote placed at the trunk of the tree and the second one with the mote placed in the foliage of the tree. Table 6.11 shows the configuration of the wireless mote's parameters used for measuring the PER. Notice that ACK options have been disabled to avoid packet retransmissions and the transmitted power level has been reduced to the minimum default value in order to analyze the worst case, in which the lost packet quantity will be the highest. The PER value has been calculated transmitting 100,000 packets. Two in-house developed applications based on Java, one for the transmitter and the other for the receiver, have been used in order to configure easily the parameters shown in Table 6.12, as well as to calculate the PER by reading the sequence number of the received packets.
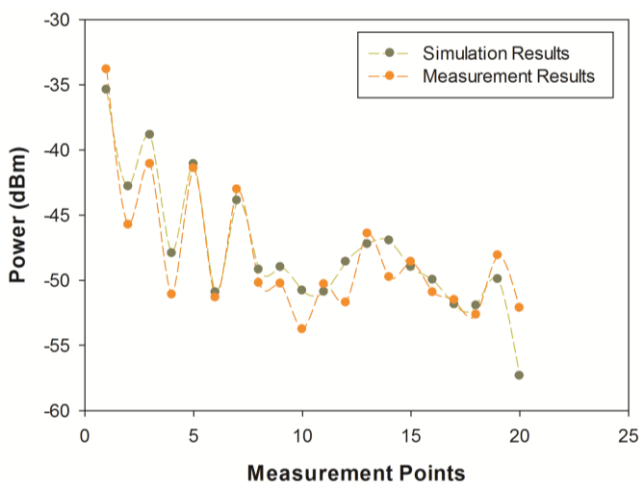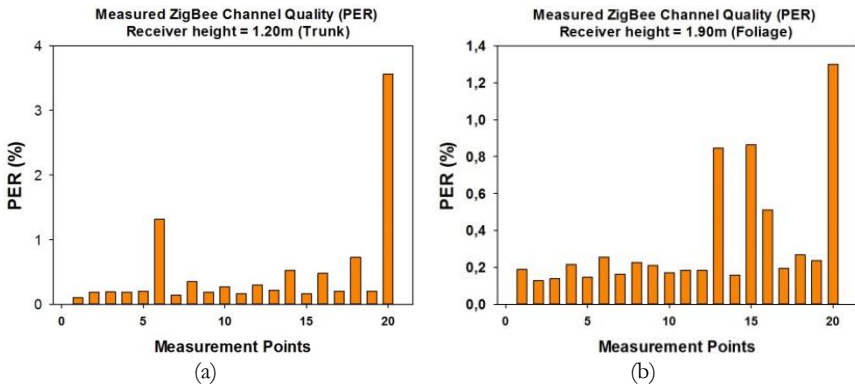

Figure 6.46. Comparison of simulation vs. measurements.

Table 6.12. Configuration of the parameters of the XBee Pro wireless devices to measure the ZigBee radio link quality.

Transmitted Power	10 dBm (Maximum Default Value)
Transmission rate	57,600 bps
Frequency	2.41 (ZigBee Channel 12)
Transmitted packet	100,000

(a)   (b)

Figure 6.47. ZigBee wireless channel quality measurements in the considered scenario (a) Receiver placed at the trunk of the tree (b) Receiver placed within the foliage of the tree.

The measured values of PER are shown in Figure 6.47. As can be seen, the values are, for every case, lower than 5%, so the number of lost packets is very low. It is worth noting that PER depends strongly (but not exclusively) on the received power level. Taking into account that the measured PER results have been obtained with the transmitted power level set to the lowest value, ACK option disabled and a quite high transmission rate (as for a real ZigBee applications lower rates are usually needed), it can be concluded that no channel quality problems in terms of packet losses would be within this kind of scenarios. This is consistent with previous power level estimations obtained in simulation as well as by direct measurement, where in all cases the values are above the threshold values for conventional QPSK modulation schemes. In this way, probability of error is low, leading to a small amount of lost packets. Furthermore, PER could be improved increasing transmitted power level, activating ACK options or reducing transmission rate.

6.2   Mobile channel modeling

6.2.1 Vehicular communications

Intelligent Transportation Systems (ITS) are currently under intense research and development for making transportation safer and more efficient. The development of such vehicular communication systems requires accurate models for the propagation channel. A key characteristic of these channels is their temporal variability and inherent non-stationarity, which has major impact on electromagnetic propagation prediction. This section investigates the channel properties of a wireless communication system within a vehicular communication environment with deterministic modeling. An analysis of the physical radio channel propagation of a UHF-RFID system for a Vehicle to Infrastructure (V2I) scattering environment is presented. A new module has been implemented in the proposed site-specific tool which takes into account the movement of the vehicles, leading to Time and Space-Frequency models.

In this work, an in-house developed 3D RL code has been used for the analysis of the behavior of an RFID system in a vehicular environment. The main contribution is that a new module has been added to the algorithm which copes with the non-stationarity of the channel. Hence, different velocities for the mobiles can be considered leading to Doppler Shift and Doppler Spread results, which give a high insight into the performance of the wireless communication system. We present the variations of received signal power within a vehicular scenario, and the power-delay-Doppler shift profile for an RFID system for vehicles. Real measurements were taken and compared to simulated values to show accuracy of the model. Statistical characterization is shown to be of the Rayleigh kind for the signal level received at the vehicle. We also introduce the feasibility of the RFID system as a function of the tag's sensitivity when the received power and the angle with respect to the reader antenna vary. The objective of the analysis is to verify how the variability and the topology of the environment affect the electromagnetic propagation for the purpose of vehicular identification and traffic congestion control. RFID readers collect information of each vehicle on the road, and send it to a central base to manage traffic. RFID is optimal to guarantee the traceability of vehicles and allows not being concerned about the security and efficiency of the system, given by automatic interrogation of the tags when passing by on the road.

A new module has been added to the in-house developed 3D RL algorithm to consider the frequency dispersive effects due to the movement of the vehicles in an ITS environment. Different velocities of the vehicles in the scenario can be considered and the Doppler shift at the receiver can be obtained by

$$f_d = \frac{v}{\lambda} cos(\psi) \qquad (6.10)$$

where ψ represents the angle between the direction of arrival of the examined propagation path and the receiver's movement.

6.2.1.1. Simulation Results

As a starting step, several simulations of a typical road scenario have been developed considering different instants of time denoted as t_i, i=1, ..., 5, for the vehicle position as shown in Figure 6.48. The considered scenario has different scatterers (trees and streetlights) on both sides of the road and the vehicle is moving at a constant velocity of 22.22m/s (80 km/hr). The road is 100m in length, with a width of 37.52m and a height of 13m. All the elements within the scenario have been taken into account in the simulation. The material properties used in the simulation are presented in Table 6.13.

Table 6.13. Material Properties in the Ray Launching Simulation

Parameters	Permittivity (εr)	Conductivity (σ) [S/m]
Air	1	0
Glass	6.06	10^{-12}
Concrete	5.66	0.142
Metal	4.5	$4*10^7$
Rubber	2.61	0
Tree	4.48	0.02

The main objective is to identify all the vehicles which go along the road with the RFID system. To achieve this goal, each vehicle is tracked using a commercial RFID tag. The transmitter antenna is placed on a streetlight on one side of the road, fixed at coordinates x=50m, y=36m, z=4m, corresponding to the red star depicted in Figure 6.48. The parameters used in the simulation are shown in Table 6.14. The frequency of operation is 868MHz (UHF-RFID Technology) with transmission rate of 106kbps and power transmission of 10dBm. The transmitter antenna is directional with linear polarization with a gain

of 7dBi and providing a 60° horizontal beam width for -3dB and 74° vertical beam width (model PATCH-A0026 from Poynting Antennas). For the receiver, an RFID generic tag is used, placed on the front part of the vehicle, with an omnidirectional radiation pattern.
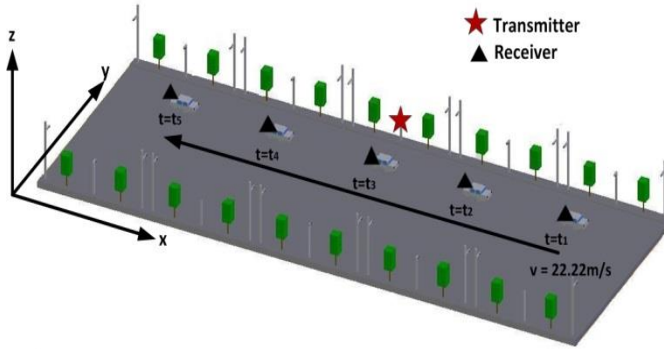

Figure 6.48. Schematic view of the considered scenario.

Table 6.14. Simulation Parameters

Frequency	868MHz
Transmitter power	10dBm
Horizontal plane angle resolution	1°
Vertical plane angle resolution ($\Delta\theta$)	1°
Reflections	6
Cuboids resolution	0.5m x 0.5m x 0.5m

Firstly, the impact of the environment within the scenario has been assessed. It is a well-known fact that the impact of different scatterers in the radio wave propagation has a great influence in the decay of the signal. Figure 6.49 shows the XY-plane of received power for the same height as the tag is placed in the vehicle (at height of 1 meter) for different instants of time. It is shown that the impact of the scatterers along the road has considerable influence on signal propagation with significant multipath interference in the scatterers' zone.
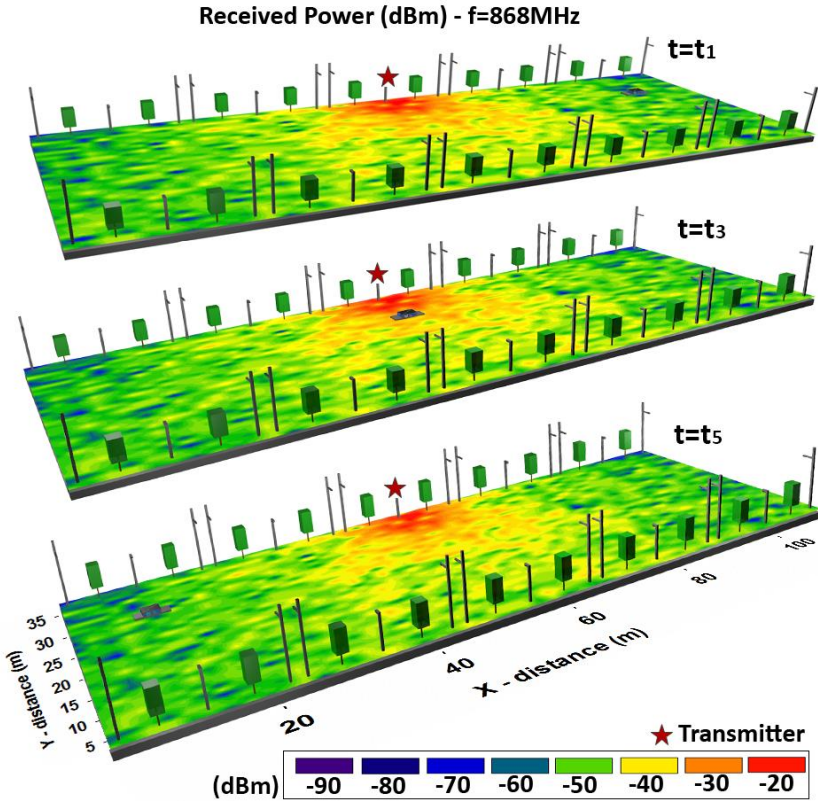
Figure 6.49. Bi-dimensional planes of estimated received power (dBm) for 1m height for t=t_1, t=t_3 and t=t_5.

It is highly important in these types of environments, which include non-stationarity elements, to consider the effects due to the movement of the vehicles. Because of that, the Doppler shift has been calculated with a constant vehicle velocity of 22.22m/s. Besides, multipath propagation has a great impact on this scenario due to the scatterers placed at both sides of the road. Figure 6.50 shows the variations of the received power for each multipath component with its Doppler shift associated for different instants of time during the movement of the vehicle. It can be seen that there is substantial variability in the received power for each component. These results can aid in the design of the antenna receivers to obtain optimal performance of the system.

To get insight into the impact of Doppler shift in the considered scenario, the Doppler Spread has been calculated for all the spatial samples of the scenario. Figure 6.51 shows the Doppler Spread for a constant velocity of 22.22m/s for the first instant of time, t_1. It is shown that the movement of the vehicle has a great impact in the frequency dispersion of the system, increasing with distance and in specific points of the considered scenario. These results are also of great aid for radio planning purposes before the deployment of a wireless communication system.
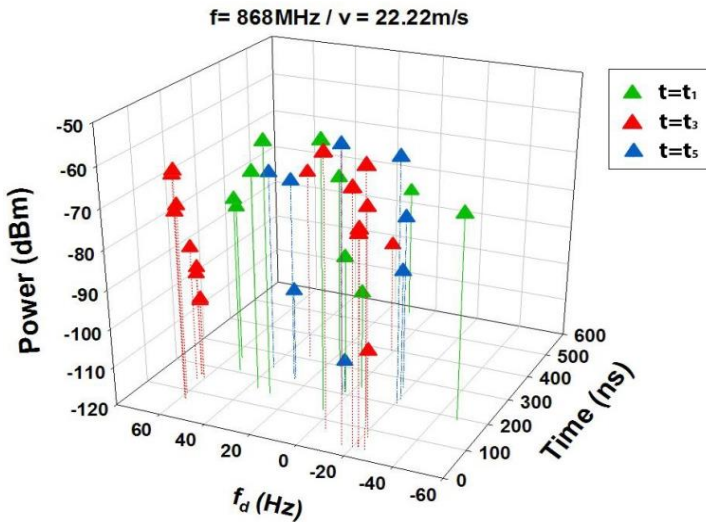

Figure 6.50. Power-Delay-Doppler Shift Profile for different instants of time during the movement of the vehicle.

6.2.1.2. Impact of the RFID system

In order to validate previous predictions, measurements in a real vehicular environment have been performed. A real scenario with similar characteristics to that of Figure 6.48 has been reproduced. A signal generator, a spectrum analyzer, and a set of antennas (used as a transmitter and a receiver) in the 900MHz frequency band have been used. The transmitter antenna has been located at coordinates x=50m, y=36m, z=4m, corresponding to the red star depicted in Figure 6.48, with a transmission power level of 10dBm. It has been placed in a streetlight in the middle of the considered scenario. The signal generator is a network analyzer Agilent N1996A configured with a minimum sweep frequency to obtain a single-frequency pulse at the output. The spectrum analyzer is an

Agilent N9912 FieldFox. The transmitter antenna PATCH-A-0026 has been used, and the receiving antenna is a monopole (model FLEXI-SMA90-868) of small dimensions to show minimal interference with the scenario[3]. The group of measurements has been done with a typical car (Mazda 3) moving along the road with a constant velocity of 22.22m/s.
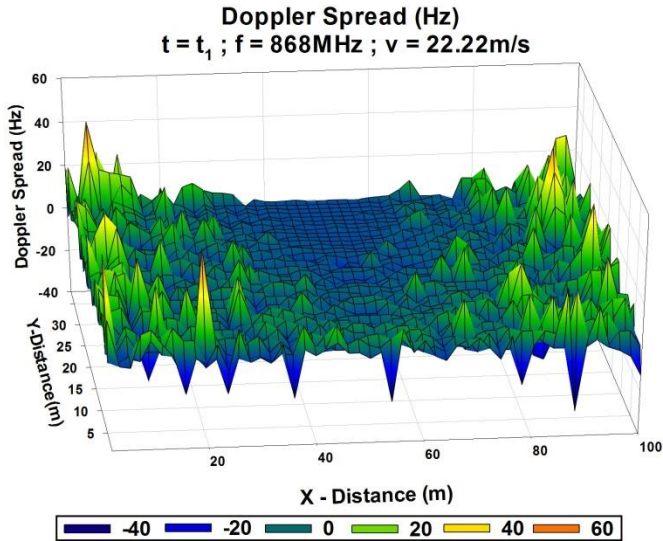

Figure 6.51. Doppler Spread (Hz) for 1m height for $t=t_1$.

Figure 6.52 (top) represents the measured spectrogram when the car with the receiver antenna moves along the road. The white dashed lines correspond with the different instants of time, which are represented in Figure 6.52 (bottom). This bottom figure represents the comparison between simulation and measurements for the chosen times. The frequency 0Hz corresponds with 868MHz in both pictures. It can be seen the effects of Doppler shift due to movement, and the good trend of the simulation technique to obtain accurate results of Doppler effects. The differences between the simulated and measured spectrogram are due mainly to the differences between the real and schematic scenario. In addition, the single-frequency pulse at the output of the signal generator had some small variations around the center frequency, due to local oscillator instability, which can produce slight mismatches between simulation

---

[3] For more information about the measurement equipment, see Appendix B.

and measurement results. Figure 6.53 shows the comparison between simulation and measurements for the received power in the car for different time instants, exhibiting good agreement, with a mean error of 0.776dB and SD of 0.782dB.
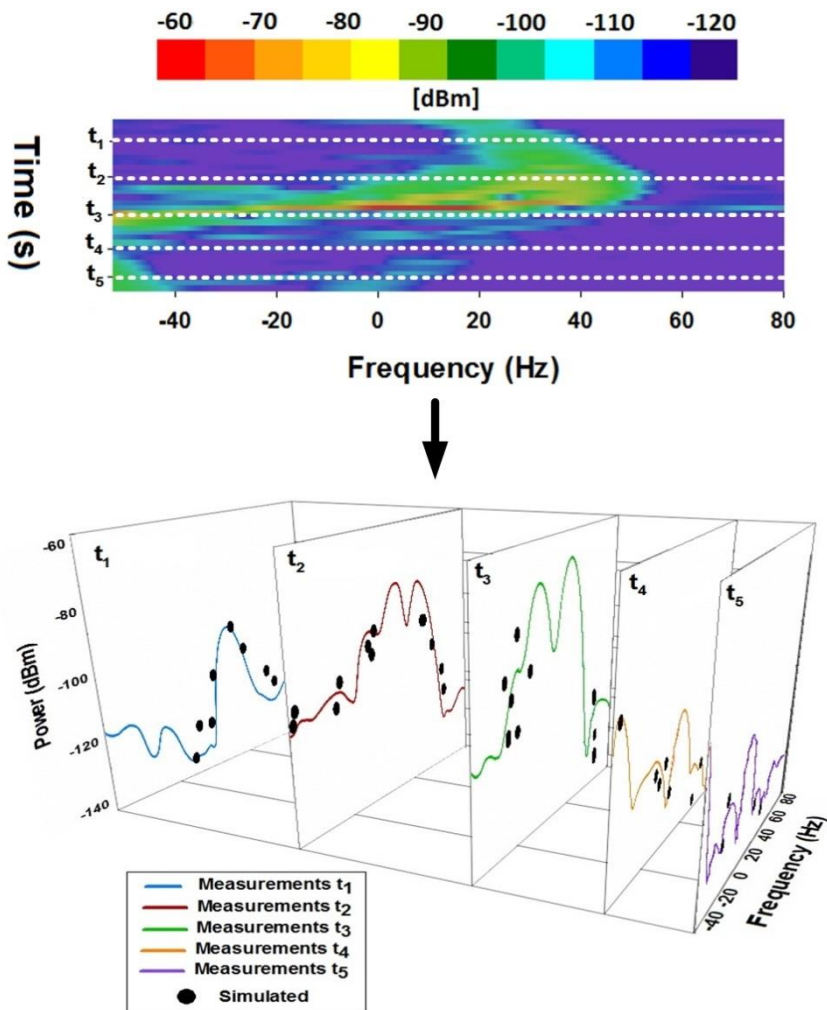

Figure 6.52. Spectrogram (top) in 868MHz when the vehicle with the receiver antenna is in movement and the transmitter is fixed in the streetlight and comparison with measurements (bottom) for different time instants.
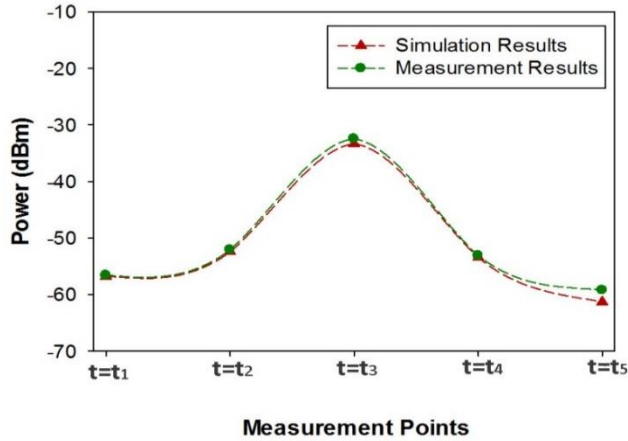
Figure 6.53. Comparison simulation versus measurements for 868MHz frequency in the considered scenario.

The next step is to consider the impact of the Doppler shift in a conventional UHF-RFID system. For that purpose, the geometry model shown in Figure 6.54 has been considered. For every instant of time, the Doppler shift worst case has been considered, and with this value the angle Φ shown has been calculated using Equation (6.9). The most common RFID systems use passive tags. Figure 6.55 shows the range of the estimated read and non-read passive tags for the UHF-RFID system considering the worst case of Doppler shift for a constant velocity of 22.22m/s. The horizontal beam width has been also represented and it is observed that in this specific environment, at instants t_1 and t_5, the tags will not be read, and the more read tags will be at instant t_3.

Figure 6.54. Geometry model considered for the calculation of the Doppler shift impact in the UHF-RFID system.

205

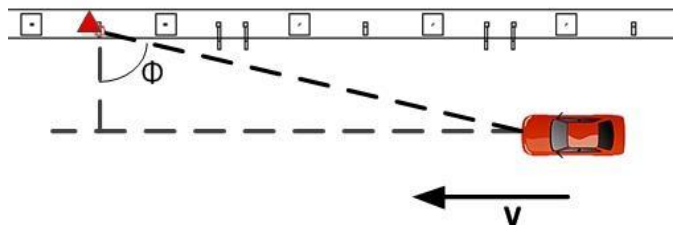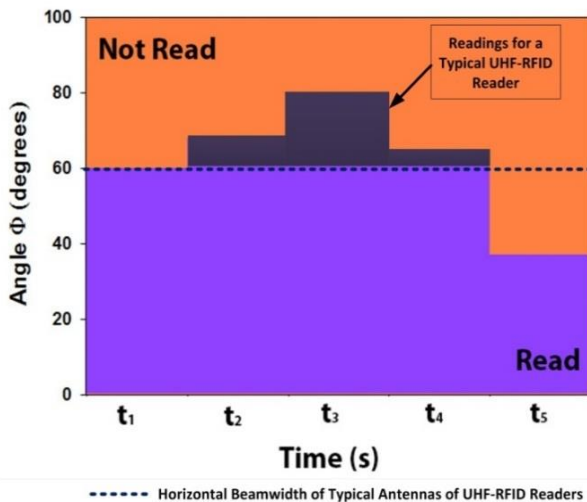**Figure 6.55.** Horizontal beam width of the transmitter antenna for a typical UHF-RFID system versus different instants of time in the considered scenario.

The basic principle of a passive UHF-RFID system is that the tags communicate with the reader by modulating its reflection coefficient to incoming radiation from the reader, i.e., modulating its scattering/radar cross section. The maximum distance at which the tag can be read by the reader is the read range. To achieve a successful read, two conditions must be satisfied. The first one is that the tag has to be powered up by the reader (the received power in the tag must be higher than the power up threshold). Secondly, the reader must be sensitive enough to pick up the backscattered modulation from the tag. With the aid of the 3D RL code, propagation losses can be estimated and become an input to a radio link budget for RFID to obtain effective read range. Therefore, the power received at the reader in the backscatter communication radio link budget has been calculated as a function of the differential reflection coefficient of the tag ($\varrho'=\varrho_1-\varrho_2$), where ϱ_1 and ϱ_2 are the 0 and 1 states of the chip reflection coefficient, respectively, which depend on the chip load [Azp12].

Figure 6.56 represents the receiver sensitivity of a typical UHF-RFID reader. It is observed that for instants t_1, t_4 and t_5, the received power is very low and the tags could not be read. At instant t_3, for all values of the tag antenna mismatch (due to usual impedance difference in the on/off states of the tag), the power received is greater than the reader sensitivity (-90dBm), so the link budget is positive and the reader could read the information from the tag. At instant t_2,

206

for values of antenna mismatch larger than 0.7, the reader could not read the tag due to the lack in power strength. In all cases, the right position of the reader and the tag play a key role in the capability of reading the tag.
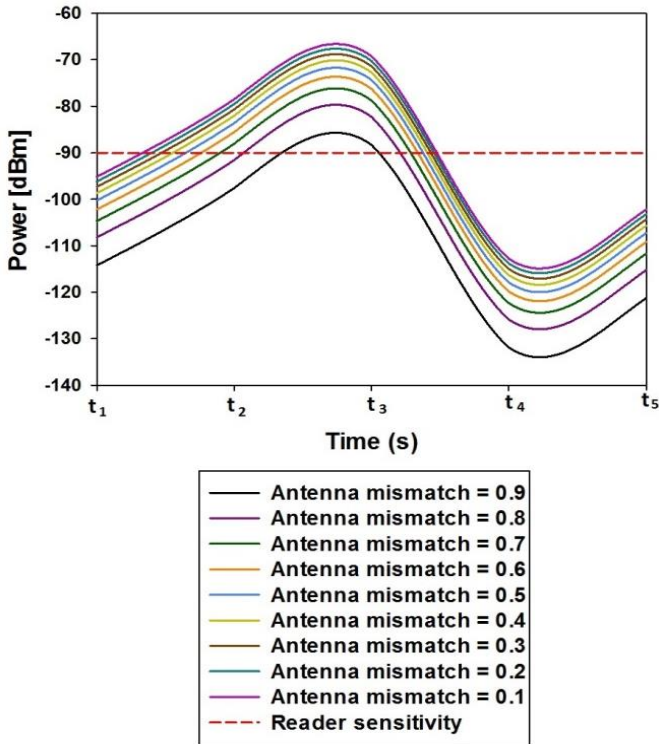
Figure 6.56. Received power in the reader in the backscatter communication radio link for different values of antenna mismatch.

6.3   Summary

In this chapter, radio propagation analysis has been made for different types of environments. First, a typical office environment has been assessed for different frequencies, emulating different wireless communication systems within it. After that, a complex vehicular environment, such as an urban bus, has been assessed, and finally an inhomogeneous vegetation environment. Results show that the morphology and the topology of these complex environments play a relevant role in electromagnetic propagation. The most important phenomenon is multipath propagation which affects significantly to the way the signal propagates through the space. With these analyses, the optimal positions for the transceivers

in wireless sensor networks can be determined, improving the overall system efficiency. Therefore, it can be concluded that the use of deterministic techniques aimed to take into account the inherent complexity of the considered scenarios can aid in wireless system planning in order to minimize power consumption and increase overall system capacity.

Bibliography of the Chapter

[Agu12] E. Aguirre, J. Arpón, L. Azpilicueta, S. de Miguel, V. Ramos, F. Falcone, "Evaluation of Electromagnetic Dosimetry of Wireless Systems in Complex Indoor Scenarios with human body interaction," *PIER B*, vol. 43, pp. 189-209, 2012.

[Agu13] E. Aguirre, P. López-Iturri, L. Azpilicueta, J. Arpón and F. Falcone, "Characterization and Consideration of Topological Impact of Wireless Propagation in a Commercial Aircraft Environment," *IEEE Antennas and Propagation Magazine*, vol. 55, nº 6, December 2013.

[Azp12] L. Azpilicueta, F. Falcone, J. J. Astráin, J. Villadangos, I. J. García Zuazola, H. Landaluce, I. Angulo, A. Perallos, "Measurement and modeling of a UHF-RFID system in a metallic closed vehicle," *Microw. Opt. Technol. Lett.* 2012, 54, 2126–2130.

[Azp15a] L. Azpilicueta, F. Falcone, J. J. Astráin, J. Villadangos, I. Salaberria, A. Perallos, R. Carballedo, I. Angulo, P. Elejoste, A. Bahillo, "Characterization of Wireless Systems for the Implementation of Context Aware Scenarios in a Railway Passenger Vehicle," *IEEE Antennas and Propagation Magazine*, just submitted.

[Azp15b] L. Azpilicueta, P. López-Iturri, E. Aguirre, J. J. Astráin, J. Villadangos, C. Zubiri, F. Falcone, "Characterization of Wireless Channel Impact on Wireless Sensor Network Performance in Public Transportation Buses," *IEEE Transactions on Intelligent Transportation Systems*, just submitted.

[Bal89] C.A Balanis, "Advanced Engineering Electromagnetics," *Wiley: New York*, NY, USA, 1989; Volume 205.

[Cui02] I. Cuiñas, M. García Sánchez, "Permittivity and conductivity measurements of building materials at 5.8 GHz and 41.5 GHz," *Wirel. Pers. Commun.* 2002, 20, pp. 93–100.

[Don10] W. Dong, G. Liu, L. Yu, H. Ding, J. Zhang, "Channel properties of indoor part for high-speed train based on wideband channel measurement", *5th International ICST Conference on Communications and Networking in China* (CHINACOM), 2010.

[Fin09] J. Fink, N. Michael, A. Kushleyev, V. Kumar, "Experimental Characterization of Radio Signal Propagation in Indoor Environments with Application to Estimation and Control," *Intelligent Robots and Systems* (IROS), St. Louis, MO, USA, 2009.

[Gom12]C. Gomez, J. Oller, J. Paradells, "Overview and Evaluation of Bluetooth Low Energy: An Emerging Low-Power Wireless Technology," *Sensors* 2012, 12, 11734–11753.

[Has93] H. Hashemi, "The Indoor Radio Propagation Channel," *Proc. IEE*, 81, pp. 943-968, 1993.

[Jak93] W.C. Jakes, "Microwave Mobile Communications," *Wiley & Sons*, 1993.

[Lop14] P. López-Iturri, E. Aguirre, L. Azpilicueta, U. Gárate and F. Falcone, "ZigBee Radio Channel Analysis in a Complex Vehicular Environment", *IEEE Antennas and Propagation Magazine*, vol. 56, Issue 4, pp. 232 – 245, Aug. 2014.

[Per02] S. Perras, L. Bouchard, "Fading characteristics of RF signals due to foliage in frequency bands from 2 to 60 GHz," *In Proceedings of the 5th International Symposium on Wireless Personal Multimedia Communications*, Honolulu, HI, USA, 27–30 October 2002; Volume 1, pp. 267–271.

[Rap01] T. S. Rappaport, Ed., Wireless Communications: Principles and Practice. *Englewood Cliffs, NJ: Prentice Hall*, 2001.

[Siw98] K. Siwiak, "Radiowave propagation and antennas for personal communications," *Artech House*, Inc., 1998.

[Vya12] V. Komarov Vyacheslav, "Handbook of Dielectric and Thermal Properties of Materials at Microwave Frequencies," *Artech House, Inc.*, 685 Canton Street, Norwood, MA 02062, ISBN-13: 978-1-60807-529-4, 2012.

[Wee93] V. Weerackody, "Characteristics of a simulated fast fading indoor radio channel*," 43rd IEEE Vehicular Technology Conf.*, 1993, pp. 231-235.

Chapter 7

Conclusions
and Future Work

This Chapter summarizes the most significant results and conclusions reported throughout this thesis. The aim of Section 7.1 is to provide a compilation of the main contributions to verify the fulfillment of the objectives proposed in Chapter 1. Furthermore, future research trends related to this work are proposed and briefly analyzed in Section 7.2.

7.1 Conclusions

Almost all the work done in this Ph.D. thesis has been based on the analysis and the application of a deterministic approach based on Ray Launching (RL) technique. This has been motivated by the growing demand of wireless communication systems and the necessity of previous radio planning before the deployment of a wireless network. In the following paragraphs, general conclusions are provided following the structure of this document.

An overview of different short-range wireless communication systems has been presented in Chapter 2. It has been explained the reasons why before the deployment of a wireless network, radio-planning analysis with an efficient propagation prediction approach becomes necessary. After that, a complete survey of different propagation models which have been used in the literature has been presented. Special attention has been paid to Ray Tracing (RT) methods which lead to a good trade-off between accuracy and computational time of simulations.

Chapter 3 has covered a detailed description of the in-house developed 3D RL code. The basis and its principle have been explained explicitly. This approach permits radio planning analysis before the implementation of a wireless system, leading to accurate results without an expensive campaign of measurements.

In Chapter 4, with the aim of using the algorithm efficiently, an in-depth analysis of the convergence of the in-house developed 3D RL code has been done. The different parameters which have been analyzed have been selected because they are crucial in simulation accuracy results, and a trade-off between simulation computational time and accuracy has been made to obtained good results. The selected parameters have been the number of reflections, the angular and spatial resolution and the number of diffracted rays.

Chapter 5 has covered two novel deterministic approaches for coverage prediction in complex indoor environments. The first part of the chapter has been focused in the Ray Launching-Neural Network (RL-NN) approach. A small difference between the results of our proposed method and the fully 3D simulation has been observed. The new method achieves a high gain in terms of computational efficiency, 80% reduction in simulation time and 70% reduction in used spaced memory, leading to accurate results. The second part of this chapter has been focused in the Ray Launching-Diffusion Equation (RL-DE) approach. The novel GO/DE technique presents a small increase in the mean error. However, the differences are moderate and the results are reliable for engineering purposes. The new GO/DE method achieves a high gain in terms of computational efficiency, 40% reduction in simulation time, leading to accurate results.

Finally, in Chapter 6, radio propagation analysis has been made for different types of environments. Results show that the morphology and the topology of these complex environments play a relevant role in electromagnetic propagation. The most important phenomenon is multipath propagation which affects significantly to the way the signal propagates along the space. With these analyses, the optimal positions for the transceivers in wireless sensor networks can be determined, improving the overall system efficiency. Therefore, it can be concluded that the use of deterministic techniques destined to consider the inherent complexity of the considered scenarios can aid in wireless system planning in order to minimize power consumption and increase overall system capacity.

In Figure 7.1, it is illustrated a general scheme of the main contributions of this thesis. On one hand, in the computational electromagnetics part, the main milestones which have been achieved along this work are presented, focusing towards a robust, efficient and enhanced electromagnetic computational tool. At the same time, on the other hand, channel characterization of different complex environments has been done for different applications. Figure 7.2 and Figure 7.3 represent a detailed description of these two paths, with the main contributions of each part represented by the published articles in top international journals and conferences.
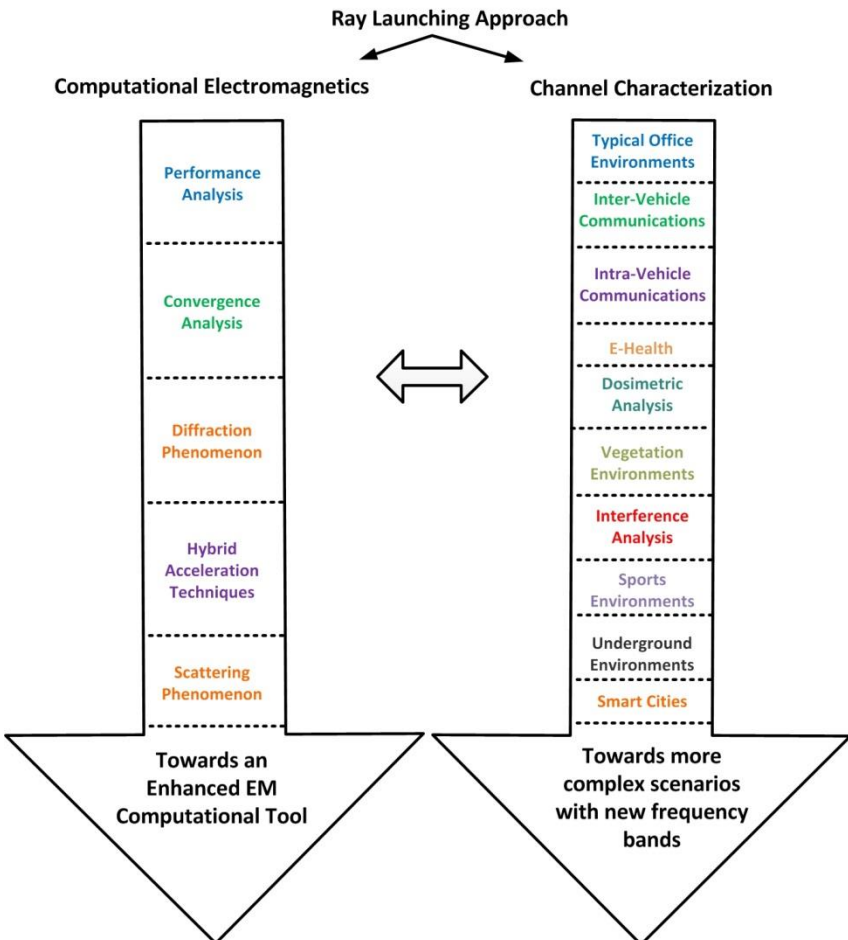

Figure 7.1. Schematic view of the main contributions of this thesis.

Ray Launching Applications

Figure 7.2. Main contributions of the Channel Characterization path.

Computational Electromagnetics
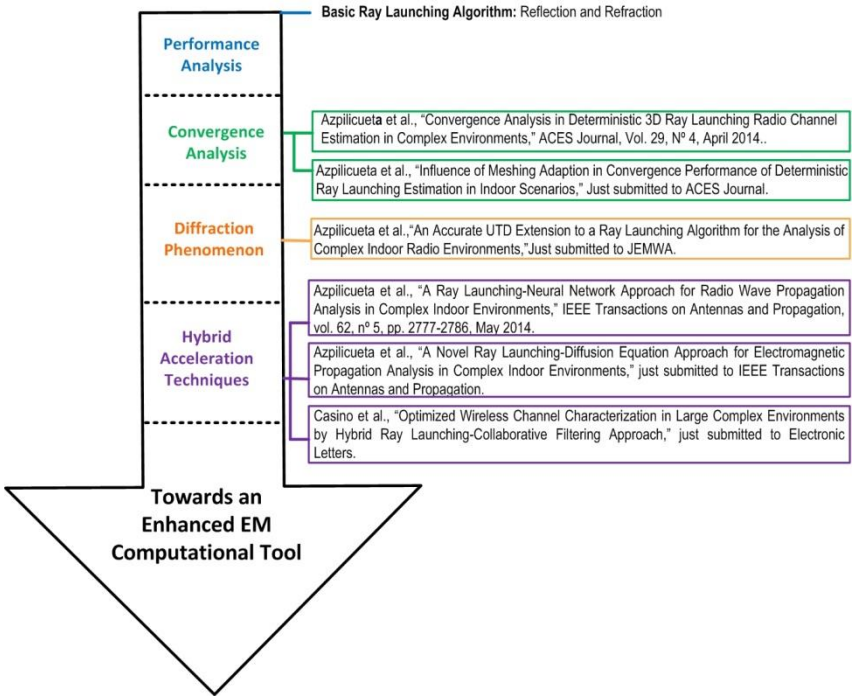
Figure 7.3. Main contributions of the Computational Electromagnetics path.

7.2 Future Work

The work carried out in this thesis leads to some future research lines. The new possible lines of work are specified below.

- In the implementation of the algorithm, the scattering phenomenon can be implemented with a new module to obtain more accurate predictions for rough surfaces. This is currently being analyzed and simulation results will be compared with real measurements in a cave environment, with a lot of rough surfaces. The hypothesis under consideration is that each rough surface element is assumed to produce a non-coherent Lambertian

spherical scattered wave. Figure 7.4 illustrates the power distribution in the diffused beam.

Figure 7.4. Polar representation of the power scattering in the diffused beam [Gou07].

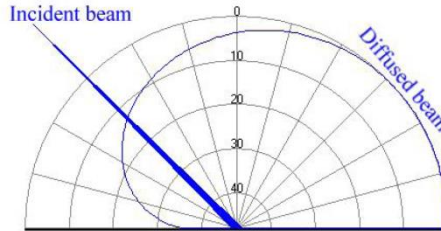- Regarding the NN acceleration technique, the aim is to probe our approach with different neural networks to analyze their performance and try to increase the efficiency of the algorithm. This analysis is currently under development to obtain better results.

- On the other hand, the DE method with the RL technique has been implemented in 2D and a future work which is now under consideration is to implement the diffusion equation three-dimensionally, to obtain more accurate results. Another work which is now being considered with the DE approach is the implementation of a no site-specific method which calculates mean values taking into account the obstacle density.

- To obtain accurate results for large scenarios with affordable computational time, a novel Ray Launching-Collaborative Filter (RL-CF) hybrid approach has been made and it is now under analysis.

- Regarding the adaptive meshing, we are working on building a database of canonical scenarios linking the different significant parameters of different environments (i.e., obstacle density, dimensions) to implement an automatic meshing in the algorithm.

- With regard to the different applications, more diverse environments could be considered, also with different obstacles densities and with human beings within them.

- A new propagation prediction method which takes into account the movement of the obstacles and the human beings is also under consideration, to emulate complex environments such as vehicular communications in large scenarios. In this sense, we will take into account the non-stationarity of the channel, considering the selective fading on time. This could be interesting also for Radar Cross Section (RCS) applications.

- Another future line is to hybridize the RL code with FDTD to obtain precise estimations of near fields. This is especially important for dosimetric analysis, when analyzing WBAN.

Bibliography of the Chapter

[Gou07]   G. Gougeon, Y. Corre and Y. Lostanlen, "Impact of the Introduction of Diffuse Scattering on Radio Channel Parameters in Urban Environments," *The Second Conference on Antennas and Propagation, EuCAP 2007*, 11-16 Nov. 2007, pp. 1-6.

Appendix A

Material Properties

Table A.1. Material Properties of Selected Materials.

Material	f(MHz)	Permittivity (ε_r)	Conductivity (σ) (S/m)
Air	868	1	0
	2400	1	0
Aluminum	868	4	$4*10^7$
	2400	4.5	$4*10^7$
Brick wall	2400	4.44	0.11
Concrete	2400	25	0.02
Fresh water	3000	20	$\sim 10^{-2}$
Glass	868	5.5	$\sim 10^{-12}$
	2400	6.06	$\sim 10^{-12}$
Grass	2400	30	$\sim 10^{-2}$
Moist soil	2400	4.8	0.98
Paper	2400	1.5-4	$3.5*10^{-3}$
Plasterboard	2400	2.02	$\sim 10^{-14}$
Plywood	2400	2.88	0.21
Polycarbonate	868	3.2	0.2
	2400	3	0.2
Polypropylene	2400	3	0.11
Polystyrene	3000	2.55	$\sim 10^{-16}$
Rubber	2400	$\sim 2.4-3$	$\sim 10^{-14}$
Seawater	3000	81	~ 4
Tree	2400	4.48	0.02
Tree foliage		(1)	(1)
Trunk tree		(1)	(1)
Wood	2400	1.4	0.021

Sources:

D. L. Sengupta and V. V. Liepa, "Applied Electromagnetics and Electromagnetic Compatibility" ISBN 0-471-16549-2, 2005 John Wiley & Sons, Inc.

C.A Balanis, "Advanced Engineering Electromagnetics," Wiley: New York, NY, USA, 1989; Volume 205.

(1) The material properties of the tree foliage and the trunk tree are variable with the temperature and humidity respectively. Values presented in the following book have been considered:

V. Komarov Vyacheslav, "Handbook of Dielectric and Thermal Properties of Materials at Microwave Frequencies," Artech House, Inc., 685 Canton Street, Norwood, MA 02062, ISBN-13: 978-1-60807-529-4, 2012.

Appendix B

Measurement Equipment Specification

Antennas

Table B.1. Selected antennas specification.

Product name	Frequency	Radiation Pattern	Gain	Illustration
Picea 2.4GHz (Antenanova)	2.4-2.5GHz	Omni Directional. Linear polarization.	1.2dBi	
ECO Series Mobile Antennas (RS)	2.4-2.5GHz	Omni Directional. Linear polarization.	5dBi	

OAN-1070 (Level One)	2.4-2.5GHz	Omni Directional. Linear polarization.	7dBi	
GPS and LTE/GSM/UMTS (Taoglas)	700MHz to 960MHz/ 1710MHz to 2200MHz	Omni Directional. Linear polarization.	3.5dBi	
FLEXI-SMA90-868 (RF Solutions)	868MHz	Omni Directional. Linear polarization.	1dBi	
LPRS Antenna 433MHz (LPRS)	433MHz	Omni Directional. Linear polarization.	1dBi	
Motorola AN480 Single Port Antenna (RFID Supply Chain)	865-956MHz	Directional. Linear polarization.	6dBi	
PATCH A-0025 (Poynting Antennas)	820-970MHz	Directional. Linear polarization.	8dBi	
PATCH A-0026 (Poynting Antennas)	820-970MHz	Directional. Circular polarization.	8dBi	

Spectrum analyzers

Table B.2. Field Fox N9912A Spectrum Analyzer specification.

Product name	Frequency Range
Agilent FieldFox RF Analyzer N9912A	100khz to 8GHz

Datasheet specification available online (2015, March 25):
http://cp.literature.agilent.com/litweb/pdf/N9912-90001.pdf

Table B.3. N1996A Agilent Spectrum Analyzer specification.

Product name	Frequency Range
N1996A Agilent CSA Spectrum Analyzer	100khz to 6GHz

Datasheet specification available online (2015, March 25):
http://www.keysight.com/en/pd-1812204-pn-N1996A/agilent-csa-spectrum-

223

ZigBee Modules

Table B.4. ZigBee RF Modules specification.

Product name	Model	Illustration
XBee/Xbee-Pro ZB RF Modules (Digi International)	XBee / XbeePro	

Datasheet specification available online (2015, March 25):
http://www.digi.com/pdf/ds_xbeezbmodules.pdf

Table B.5. Arduino Xbee Shield specification.

Product name	Model	Illustration
Arduino Xbee Shield	Libelium	

Datasheet specification available online (2015, March 25):
http://arduino.cc/en/Main/ArduinoXbeeShield

Table B.4. Arduino Uno specification.

Product name	Model	Illustration
Arduino Uno	Arduino Uno R3	

Datasheet specification available online (2015, March 25):
http://www.atmel.com/Images/doc8161.pdf

List of Publications

International Journals

1. L. Azpilicueta, P. López-Iturri, E. Aguirre, J. J. Astráin, J. Villadangos, C. Zubiri and F. Falcone, "Characterization of Wireless Transportation Systems and Intelligent Transportation Systems Magazine," *IEEE Transactions on Intelligent Transportation Systems*, in Press.

2. P. López-Iturri, P. Rodríguez-Ulibarri, E. Aguirre, L. Azpilicueta, M. Berueta and F. Falcone, "Hybrid Equivalent Source-3D Ray Launching Simulation Technique for Deterministic Estimation of Radiated Emissions of Electrical Appliances*," Journal of Electromagnetic Waves and Applications*, in Press.

3. L. Azpilicueta, P. López-Iturri, E. Aguirre, F. Falcone, "An accurate UTD Extension to a Ray Launching Algorithm for the Analysis of Complex Indoor Radio Environments," *Journal of Electromagnetic Waves and Applications*, in Press.

4. I. Angulo, E. Onieva, A. Perallos, A. Bahillo, L. Azpilicueta, F. Falcone, J. J. Astráin, J. Villadangos, "Low Cost Real Time Location System Based in Radio Frequency Identification for the Provision of Social and Safety Services," *Wireless Personal Communications*, in Press.

5. H. Baghdadi, E. Aguirre, P. López, L. Azpilicueta, J. J. Astrain, J. Villadangos, F. Falcone, "Characterization of UHF Radio Channels for Wireless Sensor Systems Embedded in Surfboards," *IEEE Antennas and Wireless Propagation Letters*, volume: PP, issue 99, doi: 10.1109/LAWP.2015.2413366, 2015.

6. E. Aguirre, P. Lopez-Iturri, L. Azpilicueta, J. J. Astrain, J. Villadangos and F. Falcone, "Analysis of Wireless Sensor Network Topology and Estimation of Optimal Network Deployment by Deterministic Radio Channel Characterization," *Sensors* 15, nº 2: 3766-3788.

7. I. J. García Zuazola, L. Azpilicueta, A. Sharma, H. Landaluce, F. Falcone, I. Angulo, A. Perallos, W. G. Whittow, J. M. H. Elmirghani, J. C. Batchelor, "Band-pass filter-like antenna validation in an ultra-

wideband in-car wireless channel," *IET Communications*, 9 pages, DOI: 10.1049/iet-com.2014.0057 , Print ISSN 1751-8628, Online ISSN 1751-8636, January 2015.

8. P. López-Iturri, E. Aguirre, L. Azpilicueta, J. J. Astrain, J. Villadangos and F. Falcone, "Radio Characterization for ISM 2.4GHz Wireless Sensor Networks for Judo Monitoring Applications," *Sensors*, 2014,14, 24004-24028.

9. L. Azpilicueta, P. López-Iturri, E. Aguirre, I. Mateo, J. J. Astrain, J. Villadangos and F. Falcone, "Analysis of Radio Wave Propagation for ISM 2.4GHz Wireless Sensor Networks in Inhomogeneous Vegetation Environment," *Sensors*, 2014, 14, 23650-23672.

10. P. López-Iturri, S. de Miguel-Bilbao, E. Aguirre, L. Azpilicueta, F. Falcone and V. Ramos, "Estimation of Radiofrequency Power Leakage from Microwave Ovens for Dosimetric Assessment at Non Ionizing Radiation Exposure Levels," *BioMed Research International*, Article ID 603260, in Press.

11. L. Azpilicueta, P. López-Iturri, E. Aguirre and F. Falcone, "Radio Channel characterization for Bluetooth communication systems onboard commercial aircrafts," *Microwave and Optical Technology Letters*, Vol. 56, Nº 11, November 2014.

12. P. López-Iturri, L. Azpilicueta, J. A. Nazábal, C. Fernández-Valdivielso, J. Soret and F. Falcone, "Analysis of Energy Consumption Performance towards Optimal Radioplanning of Wireless Sensor Networks in Heterogeneous Indoor Environments," *Radioengineering*, Vol. 23, Nº 3, September 2014.

13. I. Salaberria, A. Perallos, L. Azpilicueta, F. Falcone, R. Carballedo, I. Angulo, P. Elejoste, A. Bahillo, J. J. Astráin, J. Villadangos, "Ubiquitous Connected Train based on Train-to-Ground and Intra-Wagon Communications Capable of Providing On Trip Customized Digital Services for Passengers," *Sensors*, vol. 14, nº 5, pp. 8003-8025, 2014.

14. S. de Miguel-Bilbao, E. Aguirre, P. López-Iturri, L. Azpilicueta, J. Roldán, V. Ramos and F. Falcone, "Evaluation of Electromagnetic Interference and Exposure Assessment from s-Health Solutions based on Wi-Fi Devices," *BioMed Research International*, vol. 2015, Article ID 784362, 9 pages, 2015. doi:10.1155/2015/784362.

15. L. Azpilicueta, M. Rawat, K. Rawat, F. Ghannouchi and F. Falcone, "Convergence Analysis in Deterministic 3D Ray Launching Radio Channel Estimation in Complex Environments," *The Applied Computational Electromagnetic society Journal*, Vol. 29, Nº 4, April 2014.

16. L. Azpilicueta, M. Rawat, K. Rawat, F. Ghannouchi and F. Falcone, "A Ray Launching-Neural Network Approach for Radio Wave Propagation Analysis in Complex Indoor Environments," *IEEE Transactions on Antennas and Propagation*, vol. 62, nº 5, pp. 2777-2786, May 2014.

17. L. Azpilicueta, F. Falcone, J. J. Astráin, J. Villadangos, A. Chertudi, I. Angulo, A. Perallos, P. Elejoste, I. J. García Zuazola, "Analysis of Topological Impact on Wireless Channel Performance on Intelligent Street Lighting System," *Radioengineering Journal*, vol. 23, nº 1, April 2014.

18. J. J. Astráin, L. Azpilicueta, F. Falcone, J. Villadangos, "Analysis of Topological Influence in Air Interface Characterization of Superimposed Cluster Architectures for WSNs," *Ad Hoc & Sensor Wireless Networks*, vol. 23, pp. 1-20, 2014.

19. P. López Iturri, E. Aguirre, L. Azpilicueta, U. Gárate and F. Falcone, "ZigBee Radio Channel Analysis in a Complex Vehicular Environment", *IEEE Antennas and Propagation Magazine*, vol. 56, Issue 4, pp. 232 – 245, Aug. 2014.

20. E. Aguirre, P. López, L. Azpilicueta, S. de Miguel, V. Ramos, U. Garate and F. Falcone, "Analysis of electromagnetic dosimetric values from non-ionizing radiofrequency fields in conventional road vehicle environments," *Electromagnetic Biology and Medicine*, January 2014, doi:10.3109/15368378.2013.863782.

21. I. Sesma, L. Azpilicueta, J. J. Astráin, J. Villadangos and F. Falcone, "Analysis of challenges in the application of deterministic Wireless cannel modeling in the implementation of WLAN-based indoor location system in large complex scenarios", *International Journal of Ad Hoc and Ubiquitous Computing*, vol. 15, nº 1, pp. 171-184, 2014.

22. A. Vazquez Alejos, F. Falcone, M. Dawood, E. Aguirre and L. Azpilicueta, "Evaluation of the Brillouin precursor performance for ultrawideband intra-body technologies," *Journal of Electromagnetic Waves and Applications JEMWA*, vol. 27, issue 17, November 2013, pp. 2213-2220.

23. E. Aguirre, P. López, L. Azpilicueta, J. Arpón and F. Falcone, "Characterization and Consideration of Topological Impact of Wireless Propagation in a Commercial Aircraft Environment," *IEEE Antennas and Propagation Magazine*, Vol. 55, Nº 6, December 2013.

24. I. Angulo, L. Azpilicueta, F. Falcone, A. Perallos, U. Hernández-Jayo, A. Moreno and I. J. García Zuazola, "Towards a traceability system based on RFID technology to check the content of pallets within electronic devices supply chain," *International Journal of Antennas and Propagation*, July 2013.

25. G. Gil, M. Goyeneche, L. Azpilicueta, J. J. Astráin, J. Villadangos, F. Falcone, "Analysis of Topo-Morphological Influence of Vineyards in the Design of Wireless Sensor Networks for Smart Viticultural Management," *International Journal of Sensor Networks*, in Press.

26. E. Aguirre, J. Arpón, L. Azpilicueta, P. López, S. de Miguel, V. Ramos and F. Falcone, "Estimation of Electromagnetic Dosimetric Values from Non-Ionizing Radiofrequency Fields in an Indoor Commercial Airplane Environment," *Electromagnetic Biology and Medicine*, May 2013.

27. P. Elejoste, I. Angulo, A. Perallos, A. Chertudi, I. J. García Zuazola, A. Moreno, L. Azpilicueta, J. J. Astráin, F. Falcone, "An Easy to Deploy Street Light Control System Based on Wireless Communication and LED Technology," *Sensors*, vol. 13, pp. 6492-6523, April 2013.

28. S. Led, L. Azpilicueta, E. Aguirre, M. Martínez de Espronceda, L. Serrano, F. Falcone, "Analysis and Description of HOLTIN Service Provision for AECG monitoring in Complex Indoor Environments," *Sensors*, vol. 13, pp. 4947-4960, April 2013.

29. A.J. Bermejo, J. Villadangos, J.J. Astrain, A. Córdoba, L. Azpilicueta, U. Gárate, F. Falcone, "Ontology based Road Traffic Management in emergency situations," *Ad Hoc & Sensor Wireless Networks*, (ISSN: 1551-9899) Special Issue: Smart living technology innovations, vol. 20, nº 1-2, pp. 47-69, 2014.

30. P. López Iturri, J. A. Nazábal, L. Azpilicueta, P. Rodríguez, M. Beruete, C. Fernández-Valdivielso and F. Falcone, "Impact of High Power Interference Sources in Planning and Deployment of Wireless Sensor Networks and Devices in 2.4GHz frequency band in Heterogeneous Environments," *Sensors*, vol. 11, pp. 15689-14709, November 2012.

31. J. A. Nazábal, P. López Iturri, L. Azpilicueta, F. Falcone and C. Fernández Valdivielso. "Performance analysis of IEEE 802.15.4 compliant wireless devices for heterogeneous indoor home automation environments," *International Journal of Antennas and Propagation*, September 2012.

32. E. Aguirre, J. Arpón, L. Azpilicueta, S. de Miguel, V.Ramos, F. Falcone, "Evaluation of Electromagnetic Dosimetry of Wireless Systems in Complex Indoor Scenarios with human body interaction," *Progress In Electromagnetics Research PIER B*, vol. 43, pp. 189-209, 2012.

33. A. Moreno, I. Angulo, A. Perallos, H. Landaluce, I. García Zuazola, L. Azpilicueta, J. J. Astráin, F. Falcone, J. Villadangos, "IVAN: Intelligent Van for the Distribution of Pharmaceutical Drugs," *Sensors*, vol. 5, pp. 6587-6609, May 2012.

34. L. Azpilicueta, F. Falcone, J. J. Astráin, J. Villadangos, I.J.García Zuazola, H. Landaluce, I. Angulo, A. Perallos, "Measurement and Modeling of an UHF-RFID system in a metallic closed vehicle," *Microwave and Optical Technology Letters*, vol. 54, issue 9, pp. 2123-2130, 2012.

Book Chapters

1. S. Led, L. Azpilicueta, M. Martínez-Espronceda, L. Serrano and F. Falcone, "Operation, Analysis and Optimization of Wireless Sensor Devices in Health Oriented Monitoring Systems," *Mobile Health, Springer International Publishing*, 2015, 5, 245-263.

2. F. Falcone, L. Azpilicueta, J. J. Astrain, J. Villadangos, "Radioelectric Channel Modeling and Impact on Global Wireless System Design," *Cognitive Networks: Applications and Deployment*, CRC Press, Taylor & Francis, 2014.

3. Ramos, V.; García-Santesmases, P.; De Miguel-Bilbao, S.; García, J.; Roldán, J.; Falcone, F.; Azpilicueta, L.; Marcos, M. D.; Bardasano, J. L.; Úbeda, A.; Martínez, M. A.; Cid, M. A.; Chacón, L.; Trillo, M. A.; García-Santesmases, M.; Ed. Ramos, V., "Innovación tecnológica para la salud y la seguridad electromagnética personal". *Unidad de Investigación en Telemedicina y e-Salud Instituto de Salud Carlos III*, Madrid, 2013.

International Conferences

1. L. Azpilicueta, P. López-Iturri, E. Aguirre, F. Falcone, "Convergence evaluation of deterministic 3D ray launching approach in complex environments," *IEEE International Symposium on Antennas and Propagation and North American Radio Science Meeting*, 19-24 July 2015, Vancouver, BC, Canada.

2. P. López-Iturri, S. de Miguel-Bilbao, E. Aguirre, L. Azpilicueta, V. Ramos, F. Falcone, "Dosimetric Assessment of Radiofrequency power leakage from microwave ovens in complex scenarios," *IEEE International Symposium on Antennas and Propagation and North American Radio Science Meeting*, 19-24 July 2015, Vancouver, BC, Canada.

3. P. López-Iturri, E. Aguirre, L. Azpilicueta, F. Falcone, "Performance Analysis of Heterogeneous Wireless Networks in Complex Indoor Scenarios," *IEEE International Symposium on Antennas and Propagation and North American Radio Science Meeting*, 19-24 July 2015, Vancouver, BC, Canada.

4. E. Aguirre, S. de Miguel-Bilbao, P. López-Iturri, L. Azpilicueta, J. Roldán, V. Ramos, F. Falcone, "Exposure Assessment from s-Health Solutions based on WLAN/WBAN systems," *IEEE International Symposium on Antennas and Propagation and North American Radio Science Meeting*, 19-24 July 2015, Vancouver, BC, Canada.

5. J. J. Martínez, P. López-Iturri, E. Aguirre, L. Azpilicueta, C. Patsakis, A. Papageorgiou, A. Solanas, F. Falcone, "Analysis of Wireless Sensor Network Performance Embedded in Motorcycle Communication System," *IEEE International Symposium on Antennas and Propagation and North American Radio Science Meeting*, 19-24 July 2015, Vancouver, BC, Canada.

6. E. Aguirre, P. López-Iturri, L. Azpilicueta, Silvia de Miguel-Bilbao, V. Ramos and F. Falcone, "Deterministic 3D Ray Launching EMF/Human Body Interaction Estimation in Complex Scenarios," *COST Action BM1309 EMF-MED, Workshop on EMF Interaction with Excitable Issues*, Madrid, 4-6 March 2015.

7. E. Aguirre, P. López-Iturri, L. Azpilicueta and F. Falcone, "Characterization of Wireless Channel Response in In-Vehicle Environments," *IEEE 14th Mediterranean Microwave Symposium*, December 12-14 2014, Marrakech, Morocco.

8. P. López-Iturri, E. Aguirre, L. Azpilicueta, C. Fernández-Valdivielso, I. Matías, F. Falcone, "Analysis of Efficient Dense Wireless Sensor Network Deployment in Smart City Environments," *IEEE SENSORS* 2014, Valencia Conference Centre, Valencia, Spain, November 2-5, 2014.

9. E. Salinero, L. Azpilicueta, E. Aguirre, P. López-Iturri, J. J. Astráin, J. Villadangos, F. Falcone, "Channel Characterization in Indoor Wireless Sensor Network Deployment in Commercial Environment," *IEEE International Symposium on Antennas and Propagation USNC-URSI Radio Science Meeting*, July 6-11, 2014, Memphis, Tennessee, USA.

10. A. León, L. Azpilicueta, E. Aguirre, P. López-Iturri, F. Falcone, "Topological Dependence in the Performance of Deterministic Wireless Channel Estimation," *IEEE International Symposium on Antennas and Propagation USNC-URSI Radio Science Meeting*, July 6-11, 2014, Memphis, Tennessee, USA.

11. T. Laborra, L. Azpilicueta, P. López-Iturri, E. Aguirre, F. Falcone, "Estimation of Wireless Coverage in Complex Cave Environments for Speleology Applications," *IEEE International Symposium on Antennas and Propagation USNC-URSI Radio Science Meeting*, July 6-11, 2014, Memphis, Tennessee, USA.

12. P. López-Iturri, E. Aguirre, L. Azpilicueta, S. de Miguel-Bilbao, V. Ramos, F. Falcone, "Assessment of Electromagnetic Dosimetric values from Non-Ionizing Radiofrequency Sources in a Conventional Road Vehicle," *IEEE International Symposium on Antennas and Propagation USNC-URSI Radio Science Meeting*, July 6-11, 2014, Memphis, Tennessee, USA.

13. H. Baghdadi, E. Aguirre, P. López-Iturri, L. Azpilicueta, J. J.Astráin, J. Villadangos, F. Falcone, "Analysis of Radiopropagation of Wireless Trasnceivers in Surfboards," *IEEE International Symposium on Antennas and Propagation USNC-URSI Radio Science Meeting*, July 6-11, 2014, Memphis, Tennessee, USA.

14. E. Aguirre, M. Flores, L. Azpilicueta, P. López-Iturri, F. Falcone, V. Ramos, A. Solanas, "Implementing Context Aware Scenarios to Enable Smart Health in Complex Urban Environments," *IEEE International Symposium on Medical Measurements and Applications*, June 11-12, 2014, Lisbon, Portugal.

15. L. Azpilicueta, P. López-Iturri, E. Aguirre, I. Mateo, J. J. Astráin, J. Villadangos, F. Falcone, "Analysis of Radio Wave Propagation for ISM 2.4GHz Wireless Sensor Networks in Inhomogeneous Vegetation Environments," *International Electronic Conference on Sensors and Applications*, 1-16 June 2014.

16. E. Aguirre, P. López-Iturri, L.Azpilicueta, J. J. Astráin, J. Villadangos, F.Falcone, "Analysis of Wireless Sensor Network Topology and Estimation of Optimal Network Deployment by Deterministic Radio Channel Characterization," *International Electronic Conference on Sensors and Applications*, 1-16 June 2014.

17. P. López-Iturri, E. Aguirre, L. Azpilicueta, J. J. Astráin, J. Villadangos, F. Falcone, "Radio Characterization for ISM 2.4GHz Wireless Sensor Networks for Judo Applications," *International Electronic Conference on Sensors and Applications*, 1-16 June 2014.

18. E. Aguirre, P. López-Iturri, L. Azpilicueta, S. de Miguel, V. Ramos, F. Falcone, "Dosimetric Assessment for Non-Ionizing ISM 2.4GHz Wireless Systems in a Commercial Passenger Aircraft," *8th European Conference on Antennas and Propagation (EuCAP 2014)*, The Hague, The Netherlands, 6-11 April 2014.

19. L. Azpilicueta, J. J. Astráin, J. Villadangos and F. Falcone, "Impact of Wireless Sensor Network Cluster Architecture in Wireless Channel Performance," *8th European Conference on Antennas and Propagation (EuCAP 2014)*, The Hague, The Netherlands, 6-11 April 2014.

20. L. Azpilicueta, J. A. Nazábal, C. Fernández Valdivielso, I. Matías and F. Falcone, "Impact of wireless sensor networks in the advancement of ambient intelligent and Smart cities," *International Conference on New Concepts in Smart Cities Smart Mile 2013*, Vigo, Spain, December 2013.

21. I. Angulo, E. Onieva, A. Perallos, I. Salaberria, L. Azpilicueta, F. Falcone, J. J. Astráin, J. Villadangos, "Low Cost & Easy to Deploy Real Time Location System Based in Radio Frequency," *7th International Conference on Ubiquitous Computing* & *Ambient Intelligence* (UCamI 2013), Costa Rica, 2-6 December 2013.

22. I. Salaberria, A. Perallos, L. Azpilicueta, F. Falcone, R. Carballedo, I. Angulo, P. Elejoste, J. J. Astráin, J. Villadangos, "Towards a Train-to Ground and Intra-Wagon Communications Solution Capable of Providing On Trip Customized Digital Services for Passengers," *7th*

International Conference on Ubiquitous Computing & *Ambient Intelligence* (UCamI 2013), Costa Rica, 2-6 December 2013.

23. S. de Miguel-Bilbao, J. García, E. Aguirre, L. Azpilicueta, F. Falcone, V. Ramos, "Assessment of statistical distribution of exposure to electromagnetic fields from social alarm devices," *XIII Mediterranean Conference on Medical and Biological Engineering and Computing (MEDICON 2013)*, Sevilla, Spain, 25-28 September 2013.

24. L. Azpilicueta, "Characterization of Wireless Propagation in Complex Indoor Scenarios," *The 14th IEEE International Symposium on a World of Wireless, Mobile and Multimedia Networks, IEEE WoWMoM 2013*, Madrid, Spain, 4-7 June 2013.

25. P. López-Iturri, J. A. Nazábal, L. Azpilicueta, C. Fernández and F. Falcone, "Impact and Characterization of the Microwave Oven Power Leakage on 802.15.4 Networks," *2013 IEEE International Symposium on Antennas and Propagation and USNC-URSI National Radio Science Meeting*, Orlando, Florida, USA, 7-13 July 2013.

26. C. Rivares, L. Azpilicueta, P. López, J. A. Nazábal and F. Falcone, "Influence of Human Body and Indoor Scenarios in On-body Wireless Communication Systems," *2013 IEEE International Symposium on Antennas and Propagation and USNC-URSI National Radio Science Meeting*, Orlando, Florida, USA, 7-13 July 2013.

27. E. Aguirre, L. Azpilicueta, S. de Miguel, V. Ramos, F. Falcone, "Role of Material Changes and Topological Influence in Deterministic Estimation of Dosimetric Values in Complex Indoor Scenarios," *2013 IEEE International Symposium on Antennas and Propagation and USNC-URSI National Radio Science Meeting*, Orlando, Florida, USA, 7-13 July 2013.

28. C. Zubiri, L. Azpilicueta, J. J. Astráin, J. Villadangos and F. Falcone, "Analysis of Topo-Morphological Impact in Indoor Wireless Sensor Network Deployment in Urban Transport Buses," *2013 IEEE International Symposium on Antennas and Propagation and USNC-URSI National Radio Science Meeting*, Orlando, Florida, USA, 7-13 July 2013.

29. S. Led, Leire Azpilicueta, E. Aguirre, M. Martínez de Espronceda, L. Serrano, F. Falcone, "Analysis of AECG Monitoring Wireless Channel Performance in Indoor Environments," *2013 IEEE International Symposium on Antennas and Propagation and USNC-URSI National Radio Science Meeting*, Orlando, Florida, USA, 7-13 July 2013.

30. P. López-Iturri, J. A. Nazábal, L. Azpilicueta, C. Fernández-Valdivielso, F. Falcone, "Impact of the microwave oven power leakage on 802.15.4 networks," *7th European Conference on Antennas and Propagation (EuCAP 2013)*, Gothenburg, Sweden, 8-11 April 2013.

31. E. Salinero, L. Azpilicueta, F. Falcone, "Topological Analysis of Performance of ZigBee Systems in Commercial Environments," *7th European Conference on Antennas and Propagation (EuCAP 2013)*, Gothenburg, Sweden, 8-11 April 2013.

32. P. Elejoste, A. Perallos, A. Chertudi, I. Angulo, A. Moreno, L. Azpilicueta, J. J. Astráin, F. Falcone, J. Villadangos, "Easily Deployable Streetlight Intelligent Control System based on Wireless Communication," *6th International Sympsosium on Ubiquitous Computing and Ambient Intelligence (UCAml 2012)*, Vitoria, Diciembre 2012.

33. E. Aguirre, J. Arpón, L. Azpilicueta, S. de Miguel, V. Ramos, F. Falcone, "Impact of Realistic Human Body Interaction in Indoor Wireless System Evaluation," *Progress in Electromagnetic Research Symposium (PIERS 2012)*, Moscow, Russia, 19-23 August 2012.

34. J. Arpón, E. Aguirre, L. Azpilicueta, S. de Miguel, V. Ramos, F. Falcone, "Assesment on Electromagnetic Spectrum within Large Enclosed Vehicles," *Progress in Electromagnetic Research Symposium (PIERS 2012)*, Moscow, Russia, 19-23 August 2012.

35. E. Aguirre, J. Arpón, L. Azpilicueta, V. Ramos, F. Falcone, "Evaluation of Dosimetry of Wireless Systems in Complex Indoor Scenarios with Human Body Interaction," *2012 IEEE International Symposium on Antennas and Propagation and USNC/URSI National Radio Science Meeting*, Chicago, Illinois, USA, 8-14 July 2012.

36. S. Larripa, A. Satóstegui, L. Azpilicueta, F. Falcone, "Estimation of Wireless Coverage for Utilities in Complex Tunnel Environments," *2012 IEEE International Symposium on Antennas and Propagation and USNC/URSI National Radio Science Meeting*, Chicago, Illinois, USA, 8-14 July 2012.

37. A. Satóstegui, S. Larripa, L. Azpilicueta, F. Falcone, "Impact of Morphology in the Estimation of Power Delay Profiles in Future Indoor Femtocell Scenarios," *2012 IEEE International Symposium on Antennas and Propagation and USNC/URSI National Radio Science Meeting*, Chicago, Illinois, USA, 8-14 July 2012.

38. J. Arpón, E. Aguirre, L. Azpilicueta, V. Ramos, F. Falcone, "Analysis of Dosimetry Estimation in Large Enclosed Vehicles," *2012 IEEE International Symposium on Antennas and Propagation and USNC/URSI National Radio Science Meeting*, Chicago, Illinois, USA, 8-14 July 2012.

39. L. Azpilicueta, J. J. Astráin, H. Landaluce, I. Angulo, A. Perallos, J. Villadangos, F. Falcone, "Analysis of an UHF-RFID System in a Metallic Closed Vehicle," *6th European Conference on Antennas and Propagation (EuCAP 2012)*, Prague, March 2012.

40. L. Lenín Trigueros, L. Azpilicueta, C. del Río, F. Falcone, "Topological and Morphological Influence in the Performance of MIMO Techniques in Complex Indoor Scenarios," *6th European Conference on Antennas and Propagation (EuCAP 2012)*, Prague, March 2012.

41. L. Azpilicueta, J. Becerra, F. Falcone, S. de Miguel, V. Ramos, "Impact of Material Changes in Electromagnetic Dosimetry Estimation of Complex Indoor Scenarios," *6th European Conference on Antennas and Propagation (EuCAP 2012)*, Prague, March 2012.

42. A. Moreno, H. Landaluce, I. Angulo, A. Perallos, I.J. García Zuazola, L. Azpilicueta, J. J. Astráin, F. Falcone, J. Villadangos," Intelligent Van Based on Wireless Technologies for Pharmaceutical Drugs Traceability and Incidences Reporting," *V International Sympsosium on Ubiquitous Computing and Ambient Intelligence* (UCAml 2011), México, Diciembre 2011.

43. V. Torres, L. Azpilicueta, A. Estévez, M. Beruete, F. Falcone, "Analysis of Topology and Morphology Influence in Indoor Millimeter Wave Wireless Networks," *IEEE International Microwave Workshop Series on Millimeter Wave Wireless Networks* (IEEE IMWS 2011), Sitges, Barcelona, Septiembre 2011.

Spanish National Conferences

1. E. Aguirre, P. López-Iturri, L. Azpilicueta, F. Falcone, "Ingurune konplexuen azterketa dosimetrikoa 3D Ray Launching Simulazio metodoaren bidez eta giza gorputzaren eredua erabiliz," *First Conference for Basque Researchers IkerGazte 2015*, 13-15 May 2015, Durango, Spain.

2. P. López-Iturri, E. Aguirre, L. Azpilicueta, F. Falcone, "Haririk Gabeko Komunikazio Sistemen Azterketa Ingurune Konplexuetan 3D Ray Launching Metodo Deterministaren bidez," *First Conference for Basque Researchers IkerGazte 2015*, 13-15 May 2015, Durango, Spain.

3. E. Salinero, L. Azpilicueta, P. López-Iturri, E. Aguirre, F. Falcone, "Caracterización del Canal Radioeléctrico en Grandes Superficies Comerciales," *XXIX Simposium Nacional de la Unión Científica Internacional de Radio (URSI 2014)*, Valencia, Septiembre 2014.

4. T. Laborra, E. Aguirre, P. López-Iturri, L. Azpilicueta, J. J. Astráin, J. Villadangos and F. Falcone, "Sistema de Comunicación en Tiempo Real Basado en WSN para Aplicaciones Espeleológicas," *XXIX Simposium Nacional de la Unión Científica Internacional de Radio (URSI 2014)*, Valencia, Septiembre 2014.

5. H. Baghdadi, E. Aguirre, P. López-Iturri, L. Azpilicueta, J. J. Astráin, J. Villadangos, F. Falcone, "Caracterización Radioeléctrica de Sistemas Inalámbricos Embebidos en Tablas de Surf," *XXIX Simposium Nacional de la Unión Científica Internacional de Radio (URSI 2014)*, Valencia, Septiembre 2014.

6. E. Aguirre, L. Azpilicueta, P. López, C. Zubiri, J. J. Astráin, J. Villadangos, F. Falcone, "Caracterización Radioeléctrica de Sistemas Inalámbricos Embarcados en Autobuses Urbanos", *XXVIII Simposium Nacional de la Unión Científica Internacional de Radio (URSI 2013)*, Santiago de Compostela, Septiembre 2013.

7. L. Azpilicueta, P. López, E. Aguirre, U. Gárate, F. Falcone, "Análisis del Canal Radioeléctrico en un Entorno Vehicular Complejo," *XXVIII Simposium Nacional de la Unión Científica Internacional de Radio (URSI 2013)*, Santiago de Compostela, Septiembre 2013.

8. P. López, L. Azpilicueta, E. Aguirre, S. de Miguel, V. Ramos, F. Falcone, "Análisis Dosimétrico de las Fugas de Hornos Microondas," *XXVIII Simposium Nacional de la Unión Científica Internacional de Radio (URSI 2013)*, Santiago de Compostela, Septiembre 2013.

9. T. Cantabrana Martínez, V. Garrido Calvo, L. Azpilicueta, J. J. Astráin, J. Villadangos, F. Falcone, "Análisis del Canal Radioeléctrico en el Interior de Vagones de Transporte en el Sector Ferroviario", *XXVII Simposium Nacional de la Unión Científica Internacional de Radio (URSI 2012)*, Elche, Septiembre 2012.

10. V. Garrido Calvo, T. Cantabrana Martínez, L. Azpilicueta, J. J. Astráin, J. Villadangos, F. Falcone, "Caracterización del Canal Radioeléctrico aplicado a la interconexión de vagones de tren," *XXVII Simposium Nacional de la Unión Científica Internacional de Radio (URSI 2012)*, Elche, Septiembre 2012.

11. G. Gil, J. J. Rodríguez, L. Azpilicueta, J. J. Astráin, J. Villadangos, F. Falcone, "Análisis de la influencia topológica en la implantación de redes de sensores vitivinícolas," *XXVII Simposium Nacional de la Unión Científica Internacional de Radio (URSI 2012)*, Elche, Septiembre 2012.

12. P. López-Iturri, J. A. Nazábal, L. Azpilicueta, C. Fernández-Valdivielso, F. Falcone," Impacto de la potencia de fuga de hornos microondas en redes 802.15.4," *XXVII Simposium Nacional de la Unión Científica Internacional de Radio (URSI 2012)*, Elche, Septiembre 2012.

13. J. Arpón, E. Aguirre, L. Azpilicueta, S. de Miguel, V. Ramos, F. Falcone, "Evaluación dosimétrica en el entorno de interior de un avión," *XXVII Simposium Nacional de la Unión Científica Internacional de Radio (URSI 2012)*, Elche, Septiembre 2012.

14. E. Aguirre, J. Arpón, L. Azpilicueta, S. de Miguel, V. Ramos, F. Falcone, "Evaluación dosimétrica de sistemas inalámbricos en entornos interiores con interacción del cuerpo humano," *XXVII Simposium Nacional de la Unión Científica Internacional de Radio (URSI 2012)*, Elche, Septiembre 2012.

15. L. Azpilicueta, J. J. Astráin, H. Landaluce, I. Angulo, A. Perallos, J. Villadangos, F. Falcone, "Análisis de funcionamiento de un sistema RFID en un entorno vehicular cerrado," *XXVI Simposium Nacional de la Unión Científica Internacional de Radio (URSI 2011)*, Leganés, Madrid, Septiembre 2011.

16. P. López, J. A. Nazábal, L. Azpilicueta, G. Martínez, R. García, Jesús Soret, J. Torres, J. Martos, C. Fernández-Valdivielso, F. Falcone, "Analysis of Performance of Wireless Sensor Networks in Heterogeneous Indoor Environment," *XXVI Simposium Nacional de la Unión Científica Internacional de Radio (URSI 2011)*, Leganés, Madrid, Septiembre 2011.

FE DE ERRATAS

Tesis Doctoral: "Characterization of Wireless Propagation in Complex Indoor Environments"

Siguiendo las recomendaciones de los revisores externos, se ha revisado el documento original de la tesis realizando las siguientes modificaciones:

Recomendaciones del Dr. Ramakrishna Janaswamy:

1.- En la Figura 1.1 se presentan las principales contribuciones del candidato a la tesis doctoral, junto con las aplicaciones. La Figura 1.2 representa sólo las principales contribuciones de la tesis.

2.- Se ha reemplazado "proposed work" con "work done" al final de la página 3.

3.- Se ha añadido las unidades de la sensibilidad en la Tabla 2.1.

4.- La Figura 2.2 se ha modificado, indicando correctamente los nodos coordinadores.

5.- Se ha reemplazado "suffered" con "experienced" en la página 17.

6.- Se ha cambiado a_t por A_t en la Ecuación 2.3.

7.- Se ha reemplazado "promise" por "promising technique"

8.- La referencia [Lon68] se ha modificado en la página 33.

9.- Se ha reemplazado "him" con "it" en la página 47.

10.- Se ha modificado la Ecuación 3.1 incluyendo dos ángulos.

11.- El término "Convergence Analysis" se ha reemplazado por "Numerical Convergence Study" a lo largo de la tesis para reflejar más explícitamente que lo que se está haciendo es comparaciones numéricas detalladas conforme variamos los diferentes parámetros.

12.- En la Tabla 4.2 se indica que una resolución angular de 2 grados corresponde a 16.200 rayos lanzados.

13.- Se ha explicado más detalladamente la expresión "linear radials" en la página 64.

14.- A continuación de la Figura 4.12 se explica por qué se produce un aumento no lineal del tiempo de simulación respecto al número de reflexiones considerado.

15.- Se ha modificado la conductividad del metal en la Tabla 4.4.

16.- En la página 81, se clarifica el significado de los ángulos zeta_1 y zeta_2.

17.- Se indica en la página 82 el significado del tamaño de los obstáculos difractivos y cómo se han escogido.

18.- En la página 97, se indican los trade-offs entre tamaño de cuboides y precisión de los resultados obtenidos.

19.- Se han añadido las unidades de la conductividad en la Tabla 5.1.

20.- Se ha modificado la línea 3 en la página 124.

21.- Se ha modificado la Ecuación 5.12.

22.- Los colores de las Figuras 6.15, 6.17 y 6.19 se han modificado para que pueda verse con más claridad las diferentes zonas de potencia recibida.

23.- En la página 170, se indica la definición del porcentaje de ocupación de personas.

24.- En la página 178, se han explicado que cuando tenemos menos componentes multitrayecto, los valores recibidos tienen más variaciones, y por ello la Desviación Estándar aumenta.

25.- Las unidades de N_0 en las Figuras 6.39 y 6.40 se han modificado.

26.- El rango de los ejes verticales de las Figuras 6.43(a) y 6.43(b) se han cambiado a 5,000 y 20,000 respectivamente.

Recomendaciones del Dr. Luis M. Correia:

1.- En la página 1, párrafo 3, se han modificado las referencias de COST231 y Walfish-Bertoni.

2.- En la página 12, Tabla 2.1, se han añadido las unidades de la sensibilidad.

3.- En la página 24, ecuación 2.1, se ha corregido Gr.

4.- En la página 24, ecuación 2.3, a_t se ha modificado por A_t.

5.- En la página 25, se han modificado las expresiones matemáticas para que su representación sea más adecuada.

6.- En la página 25, se ha revisado la Ecuación 2.5.

7.- En la página 35, Tabla 2.2, se ha diferenciado entre los modelos Okumura, Hata y COST-231 para evidenciar que son adecuados para entornos diferentes.

8.- En la página 49, Figura 3.5 se ha revisado el algoritmo de simulación.

9.- En la página 63, en el párrafo 1 se indica la posición de la antena transmisora.

10.- En la página 63, Tabla 4.3, se ha modificado cm por cm3.

11.- En la página 66, Figura 4.4, se ha especificado las unidades de la Desviación Estándar.

12.- En la página 70, se ha explicado más detalladamente el análisis de los resultados, siguiendo las indicaciones del revisor.

13.- En la página 79, párrafo 2, se ha especificado explícitamente la orientación de la antena.

14.- En la página 81, Tabla 4.7, se ha modificado el número de dígitos decimales para la Desviación Estándar, poniendo 2, al igual que la Media.

15.- Se ha realizado una comparación numérica entre los métodos GO y GO con UTD en el apartado de resultados de medida.

16.- En la página 119, último párrafo, se indica la metodología que se ha utilizado para el cálculo de los errores.

17.- En la página 124, párrafo 2, el error medio se refiere a los dos casos (a y b).

18.- En la página 130, párrafo 3, se hace referencia a dos casos: si queremos sólo capturar las pérdidas de propagación y si queremos también capturar el "fading".

19.- El símbolo de producto se ha modificado a lo largo de todo el documento, siguiendo la recomendación del revisor.

20.- El inglés se ha revisado a lo largo de toda la tesis, siguiendo la recomendación indicada.

21.- Se ha revisado que todas las ecuaciones matemáticas estén definidas la primera vez que aparecen en el texto.